Low-frequency wave propagation in an ice-covered Arctic Ocean

Modeling with the spectral element package SPECFEM2D

Jenny Lundahl

Thesis submitted for the degree of
Master of Geosciences
Geophysics and Geodynamics
60 credits

Department of Geosciences
Faculty of Mathematics and Natural Sciences

UNIVERSITY OF OSLO

June 1, 2022

2022

Low-frequency wave propagation in an ice-covered Arctic Ocean. Modeling with the spectral element package SPECFEM2D.

Supervisors: Prof. Valerie Maupin (UiO), Dr. Marianne Lanzky Kolstrup (FFI) and Dr. Trond Jenserud (FFI)

http://www.duo.uio.no/

Printed: Reprosentralen, Universitetet i Oslo

Preface

This thesis was submitted to the Department of Geoscience at the University of Oslo, as part of a two-year master's program in Geophysics. The submitted work represents 60 ECTS credit points. The thesis was proposed by the Norwegian Defence Research Establishment (FFI) and conducted under supervision by Prof. Valerie Maupin (UiO), Dr. Marianne Lanzky Kolstrup (FFI), and Dr. Trond Jenserud (FFI).

Abstract

The significance of sea ice on acoustic wave propagation in the Arctic Ocean is extensively investigated, yet not completely understood. The Arctic sea ice is characterized by ice roughness and ice ridges and to properly model this complex geometry is often a challenge for numerical wave propagation tools. The open-source spectral element package SPECFEM2D is a powerful tool for wave propagation problems in laterally varying domains and can handle coupled fluid-solid domains. In this thesis, SPECFEM2D is used to model low-frequency deep-water wave propagation in an ice-covered Arctic Ocean. Using the axisymmetric version of the software and a point source at the symmetry axis enables simulations with a realistic 3D geometrical spreading at a moderate computational cost. Simulations are performed for a 50 Hz source located at 30 m depth in models with an absorbing bottom at 500 m depth and a propagation range of 4 km. Different models of laterally varying ice-water interfaces are implemented. Ice roughness is modeled with a Gaussian power spectrum with correlation length of 19.1 m and RMS roughness of 0.6 m. Ice ridges of 4.9 and 7.1 m depth are also introduced. Results are compared for a uniform, a linearly increasing and a realistic upwards refracting sound velocity profile in the water. The results suggest that a relatively thin ice layer, whether rough or not, with or without ridges, only impacts Arctic transmission loss at 50 Hz and 30 m depth to a minor extent over shorter ranges. Instead, the sound velocity profile in the water is shown to be the most important parameter controlling acoustic transmission loss at 30 m depth. The wave field in the ice layer itself is much weaker than in the water but is shown to be more impacted by the presence of lateral ice thickness variations.

Acknowledgements

First of all, I would like to thank my supervisor Professor Valerie Maupin at University of Oslo. I am truly grateful for all her invaluable support and guidance during my work with this thesis, for offering so much of her time and expertise, for all her feedback and for always being there to answer all my questions. It would not have been possible without her.

I am also deeply grateful to my supervisors at the Norwegian Defence Research Establishment (FFI), Marianne Lanzky Kolstrup and Trond Jenserud, for offering their time and sharing their knowledge. I especially want to thank them both for all their valuable feedback and advice in the writing progress, and for providing help with model validations. I highly appreciate it all.

I also want to express my gratitude to Gaute Hope for taking his time to answer my e-mails and share helpful explanations and information with me, and to Quentin Brissaud for his kindness in sharing his Fortran script with me and by so, helping me to implement an external velocity profile in my thesis.

My dear friends are not to be forgotten. Thank you all, for your moral support, your positivity, for all your pep talks, and for always motivating me. You know who you are. I am so thankful for each and every one of you.

Finally, I would like to thank my family, for always being there for me. I am truly blessed to have such a warm, loving, and supportive family.

Contents

Chapter 1 1

Introduction 1

1.1. A brief introduction to underwater acoustics 1

1.2. Sea ice in the Arctic Ocean 2

1.3. Acoustic wave propagation in the Arctic Ocean 3

1.4. Numerical methods for acoustic wave propagation 4

1.5. Objectives 6

1.6. Structure of the thesis 6

Chapter 2 8

Theoretical background 8

2.1. The wave equation 8

2.1.1. Solid region 8

2.1.2. Fluid region 8

2.1.3. Initial and boundary conditions 9

2.2. The weak form of the wave equation 10

2.2.1. Solid region 10

2.2.2. Fluid region 11

2.3. Spectral elements approximation 12

2.3.1. Defining the mesh 13

2.3.2. Lagrange polynomials and Gauss-Lobatto-Legendre points 14

2.3.3. Numerical integration 17

2.3.4. The Newmark method 18

2.3.5. Courant-Friedrichs-Lewy stability criterion 19

2.4. Axisymmetric 2.5D simulations 19

2.4.1. The axisymmetric domain and coordinate system 20

2.5. Perfectly matched layers 22

2.6. Transmission loss 22

Chapter 3 23

Defining the model 23

3.1. Brief description of the general model parameters 23
3.2. Attenuation and Quality factors 23
3.3. Transmission loss 25
3.4. Depth-dependent sound velocity profiles 25
3.4.1. A linearly increasing sound velocity profile 26
3.4.2. An Arctic sound speed profile from CTD-data 26
3.5. Ice ridges 28
3.6. Ice roughness 29
3.7. Ice models in the simulations 30
3.7.1. Plain models 30
3.7.2. Ice models with ice ridges and ice roughness 31
Chapter 4 33
Implementation and validation 33
4.1. Spectral element parameters 33
4.2. Source function 33
4.3. Meshing with the internal mesher 34
4.4. Stability and points per wavelength 35
4.5. Validation against OASES and an exact solution 35
4.5.1. Validation of the domain dimensions 36
4.5.2. Validation of attenuation in the ice layer 42
4.5.3. Time step and stability 43
Chapter 5 44
Results 44
5.1. Simulations with a homogeneous velocity profile 45
5.1.1. Model 1 – water only 45
5.1.2. Model 2 - a range-independent ice layer 47
5.1.3. Model 3 - a range-dependent ice layer 50
5.1.4. Comparison between the three models 50
5.1.5. Transmission loss 52
5.2. Simulations with a linearly increasing sound velocity profile 53
5.3. Simulations with an Arctic sound speed profile 56

5.4. Simulations with ice roughness and ice ridges 59
5.4.1. A smooth ice model with two ice ridges 60
5.4.2. A rough ice model with two ice ridges 68
5.4.3. The effect of ice roughness and ice ridges 72
5.4.4. The effect of the sound velocity profile 77
Chapter 6 81
Discussion 81
6.1. Modeling acoustic wave propagation in an ice-covered Arctic Ocean with SPECFEM2D 81
6.1.1. Implementing ice roughness and ice ridges in SPECFEM2D 81
6.1.2. Reflections from the absorbing boundary 83
6.2. Comparison to the shallow water models in Collis et al. (2016) 84
6.3. The effect of ice ridges on acoustic wave propagation 87
6.4. The effect of ice roughness (and ice ridges) 89
6.5. The effect of the sound velocity profile 91
6.6. Modeled acoustic wave propagation within the ice layer 92
6.7. In the aspect of Arctic climate change 93
6.8. Suggestions for future work 95
Chapter 7 96
Conclusion 96
References 98
Appendix A 102
A.I. The bulk modulus in a plain strain case 102
A.II. The quality factor in a plain strain case 103
A.III. The image solution used for model validation 104
Appendix B 106
B.I. 2D vs 2.5D simulations 106
B.I.I. Model 1 - water only 106
B.I.II. Model 2 - a range-independent ice layer 108
B.I.III. Model 3 - a range-dependent ice layer 110
B.II. Additional figures 111

Chapter 1
Introduction

1.1. A brief introduction to underwater acoustics

In the ocean, acoustic waves have the most efficient propagation of all kinds of radiation (Urick, 1983, p. 1) and sound, therefore, has a wide spectrum of applications in underwater environments. Underwater acoustics has a long history of use. As early as 1827 sound velocity was measured in Lake Geneva, Switzerland, by Colladon and Strum (1827), as the possibly earliest quantitative measurement (Urick, 1983, pp. 1-6). The interest in underwater acoustics increased during the world wars, and a great number of important discoveries and concepts of underwater acoustics originate from that time (Urick, 1983, pp. 1-6). Today acoustic wave propagation is used for various purposes. Monitoring whales (Patris et al., 2019), studying acoustic waves generated by seismic events (Bottero, 2018), locating underwater mines and objects by their scattering properties (Tesei et al., 2002), and measuring temperature changes in the Arctic Ocean (Mikhalevsky & Gavrilov, 2001) are some examples. It can also be used to monitor long-term changes in the Arctic sea ice cover through the relation between long-range low-frequency propagation loss and seasonal changes in ice thickness Gavrilov and Mikhalevsky (2006).

In Arctic, wave propagation has been of interest since the Cold War, when American and Russian nuclear submarines were deployed in the area (Hutt, 2012). The earliest acoustic research in the Arctic Ocean was mostly carried out, or sponsored, by military research institutions, and the first research papers (e.g., Buck & Greene, 1964; Mellen, 1966; Mellen & Marsh, 1963) were published in the 1960s (Hutt, 2012). How even small water temperature changes can greatly impact sound refraction was discovered in the years between the two world wars (Urick, 1983, pp. 1-6). This is very relevant in the Arctic Ocean, where acoustic wave propagation is characterized by an upwards refracting sound speed profile and continuous wave interaction with the rough sea ice cover (Hutt, 2012; Jensen et al., 2011, p. 27; Mikhalevsky, 2001; Urick, 1983, pp. 169-171).

Today a wide spectrum of research in underwater acoustics has been conducted in the Arctic Ocean. While it is widely known that the upwards refracting velocity profile and the overlaying ice cover both influence acoustic wave propagation in the area, the full effect of the ice layer is not fully understood (e.g., Jensen et al., 2011). It is therefore a topic for multiple research papers. Collis et al. (2016) and Li et al. (2021) studied the influence of an ice layer on shallow-water low-frequency wave propagation, and the effect of ice thickness and elasticity on long-range reverberation was studied by Frank and Ivakin (2018). LePage and Schmidt (1994) modeled the additional transmission loss induced by ice roughness for low-frequency propagation, while ice roughness and its effect on high-frequency long-range propagation was studied by Hope et al. (2017). The impact of ice ridges on acoustic propagation has been investigated (e.g., Diachok, 1976; Fricke, 1993), as well as their geometry and properties (e.g., Davis & Wadhams, 1995; Metzger et al., 2021; Strub-Klein & Sudom, 2012). Ballard (2019) studied

the effect of an ice layer on acoustic wave propagation in 3D and considered effects caused by ice ridge keels, such as diffraction of sound in shadow zones, horizontal focusing, and defocusing.

1.2. Sea ice in the Arctic Ocean

As already mentioned, wave propagation in the Arctic Ocean is strongly influenced by its upwards refracting sound velocity profile and repetitive wave interactions with the sea ice (Jensen et al., 2011, p. 27). The Arctic region is subject to a rapid climate change, and as reported in the third chapter of the IPCC *Special Report on the ocean and cryosphere in a changing climate, Chapter 3: Polar regions* (Meredith et al., 2019), the surface air temperature in the Arctic region has, with a probability of 66-100%, increased more than double of the global average during the last 20 years. This impacts the ice cover, both in extent and thickness, and the sea ice extent decreases during all months of the year. As the sea ice layer is also thinned out, there is a current change in the age of the Arctic ice, where thick ice of at least 5 years of age has decreased up to 90 % since 1979. Most ice situated in the Arctic is now younger and thinner ice. Thus, the extent of multi-year ice has decreased in the Arctic basin (Stroeve & Notz, 2018), and Lindsay and Schweiger (2015) showed that the annual average mean thickness of the ice in the Arctic basin has decreased from 2.12 to 1.41 m between 2000-2012 (Figure 1).

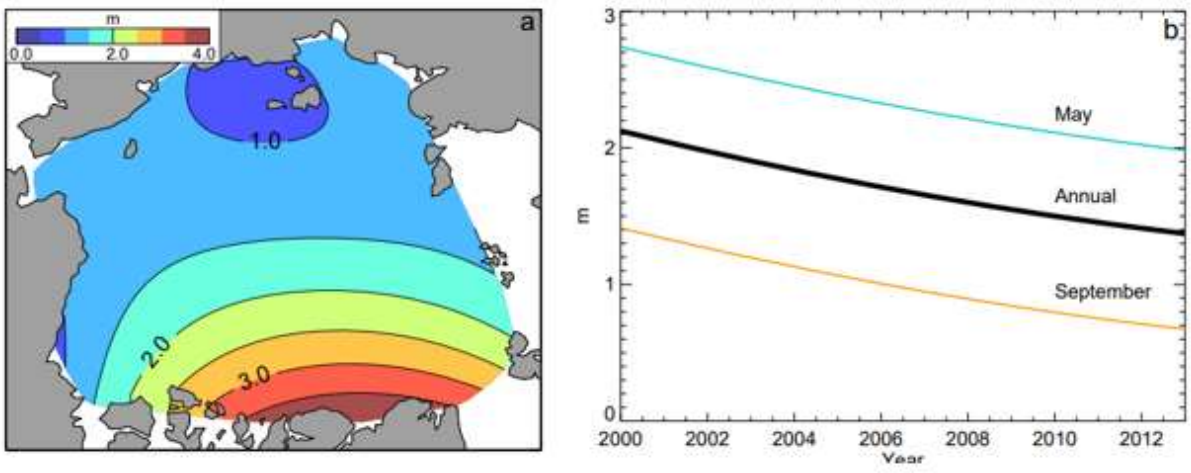

Figure 1. *Figure from Lindsay and Schweiger (2015). Figure 1a shows the annual mean thickness in the Arctic region during 2000-2012, and Figure 1b shows the mean ice thickness in May, September, and on an annual basis.*

The age and thickness of the sea ice are related, as older multi-year ice is thicker than younger ice (Maslanik et al., 2007). This also affects the ice ridges in the region (Wadhams & Toberg, 2012). Ice ridges result from ice deformation due to winds and ocean currents. Although an ice ridge often is formed by both shear and pressure forces, two different ice ridges can be distinguished by their respective creational forces (Davis & Wadhams, 1995). A pressure ridge is created by two colliding ice sheets, where the younger ice sheet is crushed and forced above and below the older one. The largest amount of crushed ice is forced below the older ice sheet, creating a triangular underwater shape with a small hill on the upper side. A shear ridge is created by ice sheets moving parallel to each other causing an ice debris to develop. However, it is common to refer to all ice ridges as pressure ridges (Davis & Wadhams, 1995).

The ice characteristics are different for old and young sea ice. Wadhams and Toberg (2012) used data collected in 2007 from the Beaufort Sea and Ellesmere Island to distinguish the differences between ice ridges in multi-year ice and first-year ice. They observed that ice ridges in multi-year ice were deeper and had less steep sides (mean slope angle 25.2°), while ice ridges in first-year ice were found to be shallower and steeper (mean slope angle of 27.5°). The features of the ice ridges were also observed to be different, and first-year ice ridges were found to consist of many smaller blocks of ice, a triangular cross-section, and a constant profile alongside the ridge. Multi-year ridges were instead found to often have a more irregular shape alongside the ridge, as it had been broken up into larger detached blocks of smooth, solid ice. Wadhams and Toberg (2012) could also observe more ice ridges in multi-year ice than in first-year ice. A reduction of multi-year ice in the Arctic Ocean will therefore affect both the number and characteristics of the ice ridges in the area. By analyzing over 64000 pressure ridge profiles, Metzger et al. (2021) could present a new concave cross-section profile for an average pressure ridge. This new profile will be used to implement ice ridges in the thesis.

1.3. Acoustic wave propagation in the Arctic Ocean

The Arctic water masses consist of a cold upper layer with low salinity, a cold intermediate layer with increasing salinity, and a warmer, saline layer of Atlantic water, above the Arctic deep water (Metzner et al., 2020; Nummelin et al., 2016). The sound velocity profile is a function of temperature, salinity, and pressure. This creates a vertical profile with a steep velocity gradient in the upper water layer where the sound velocity increases as both the salinity and temperature increases with depth. At greater depths, the sound velocity instead increases by increasing pressure, and the velocity gradient become less steep (Jensen et al., 2011, pp. 3, 27). This characteristic upwards refracting sound speed profile creates a very efficient acoustic propagation channel, enabling efficient long-range acoustic propagation in the Arctic, as seen in Figure 2. One important feature of this channel of effective sound propagation is that it works as a bandpass filter, where higher frequencies are rapidly attenuated at the rough sea ice interface, and mainly lower frequencies are caught in the sound channel (Hutt, 2012; Urick, 1983, pp. 169-171). Attenuation rapidly increases for frequencies above 30 Hz, and approximately 15-30 Hz is the range of most efficient wave propagation in the Arctic Ocean (Urick, 1983, pp. 169-171). However, those values originate from older findings, and as the climate in the Arctic Ocean has changed significantly during the last decades (Meredith et al., 2019), wave propagation has also changed. Long-range wave propagation is still only possible for low frequencies, but the decreased extent of multi-year ice and its deeper ice ridges allows higher frequencies to propagate greater distances than before (Worcester & Ballard, 2020).

As the acoustic waves continuously interact with the sea ice, the characteristics of the ice layer influence acoustic wave propagation (e.g., Fricke, 1993; LePage & Schmidt, 1994), and the scattering loss by the rough sea interface strongly affects the long-range transmission loss in the Arctic Ocean (Gavrilov & Mikhalevsky, 2006; Yang, 1989). Long-range low-frequency propagation is impacted by seasonal variations in the Arctic sea ice cover, such as changes in ice roughness and ice thickness (Gavrilov & Mikhalevsky, 2006). Hope et al. (2017) found that the primary cause for acoustic propagation loss at high frequencies was the roughness of the ice cover, and increased loss for all incidence angles was

observed when a rough and smooth ice layer was compared. Also, ice parameters such as porosity, brine content, and the ability of the ice layer to withstand stress and strain influence acoustic wave propagation (Worcester & Ballard, 2020).

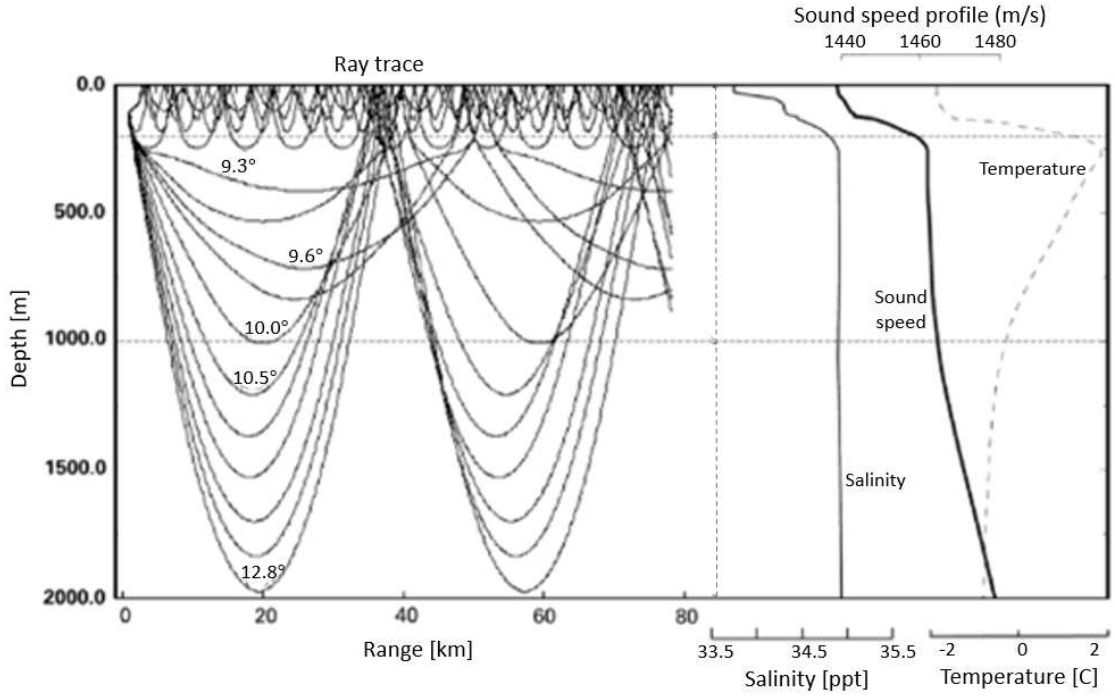

Figure 2. *Modified figure from Mikhalevsky (2001), showing a ray trace for a source at 100 m depth. The temperature and salinity profiles used to calculate the sound speed profile in the figure were measured in the eastern Arctic Ocean in 1994. Waves of lower grazing angles are efficiently trapped in a channel below the sea ice.*

1.4. Numerical methods for acoustic wave propagation

In this thesis, acoustic wave propagation in the Arctic Ocean is numerically modeled in a coupled fluid-solid domain with the open-source package SPECFEM2D (Tromp et al., 2008), available at the Computational Infrastructure for Geodynamics website (https://geodynamics.org). SPECFEM2D is a spectral element method implemented in Fortran2003 software for wave propagation simulations, full waveform imaging, and adjoint tomography. The package is comprehensive and efficient in elastic, acoustic, viscoelastic, and poroelastic domains, with the linearized Euler approximation for acoustic domains (Centre national de la recherche scientifique & Princeton University, 2021). Dimitri Komatitsch and Jean-Pierre Vilotte at Institute de Physique du Globe (IPGP) in Paris, France, first developed SPECFEM2D during 1995-1997, after attending a lecture highlighting the benefits of the Legendre spectral element methods, given by Professor Yvon Maday from Centre national de la recherche scientifique (CNRS) and the University of Paris. Dimitri Komatitsch then continued to develop the package during 1998-2005, at Harvard University, USA, Caltech, USA, and CNRS and the University of Pau, France. It has thereafter been developed further by a whole team of contributors (Centre national de la recherche scientifique & Princeton University, 2021).

Different numerical methods have been used to model acoustic wave propagation in the Arctic Ocean over the years. Fricke (1993) used a 2D finite difference method to model long-range low-frequency (10-100 Hz) wave propagation to investigate ice scattering loss from ice ridges. Collis et al. (2016) presented a range-dependent parabolic solution for modeling acoustic wave propagation in an ice-covered ocean. Parabolic equation approximations are often used in underwater acoustic wave propagation applications. Compared to other numerical methods, they are simple and fast for range-dependent problems (Xu et al., 2016), and can efficiently handle changing material properties along the propagation directions. However, two criteria must be fulfilled before implementing the parabolic equation. First, waves propagating at small horizontal angles must be the most important feature for long-range acoustic propagation, and second, the backscattered energy must be considered small enough compared to the forward scattered energy to be neglected (Thomson & Brooke, 2008). In addition, many parabolic equation methods are not able to handle elastic materials such as ice (e.g., Collins, 1993).

The finite difference method has the challenge that the free surface is not implicitly solved (Igel, 2016b). Simon et al. (2018) instead used the finite element method to model acoustic wave propagation and reverberation in ice-covered water. The free surface condition is implicitly solved in the finite element method and the method is very well adapted to complex geometries. The equations are solved within the domain elements, which facilitates the calculations to be performed in matrix systems. However, a large set of linear equations must be solved (Igel, 2016a). Another method widely used for a variety of wave propagation problems is the spectral element method. Nowadays, it is one of the most common numerical methods for wave propagation in seismic settings (Igel, 2016b) and it is very efficient in both fluid and solid regions (Bottero, 2018; e.g. Komatitsch et al., 2000; Komatitsch et al., 2002).

The spectral element method was initially introduced in fluid dynamics in the mid-late 1980s (Maday & Patera, 1989; Patera, 1984) and was first implemented for elastic wave propagation problems in the mid-1990s (Faccioli et al., 1996; Priolo et al., 1994; Seriani & Priolo, 1994). The great benefit of the spectral element method, namely a diagonal mass matrix, was first introduced by Komatitsch and Vilotte (1998). They implemented the specific choice of Lagrange polynomials as the local basis functions and Gauss-Lobatto-Legendre points as both interpolation and integration points. The great benefit of the diagonal mass matrix is that it enables explicit extrapolation of the scheme, without having to solve a large set of linear equations. This leads to a decreased computational cost, and it becomes very suitable for parallel implementation (Igel, 2016b; Komatitsch & Vilotte, 1998).

The spectral element method has several strengths and utilizes benefits from several of the other numerical methods. A finite difference scheme is used when advancing in time, and alike the finite element method, the free-surface condition is implicitly solved. As the finite element method, it allows unstructured tetrahedral and hexahedral grids, and thus, is very efficient for modeling of complex geometries. Another great benefit of the spectral elements method, inherited by the pseudo-spectral method, are the spectral convergence properties where the convergence rate of the approximation towards the exact solution has an exponential form. This asset is used on a local level, approximating the wave equation by interpolation of the Lagrangian basis functions within each element (Igel, 2016b).

The complex geometry of Arctic sea ice is highly variable along the propagation direction, and is distinguished by complicated dynamics, such as ice roughness and ice ridges (e.g. Jensen et al., 2011, p. 307). Implementing a realistic, rough sea ice layer can be challenging for many numerical tools, where

e.g. the wavenumber integration package OASES (Schmidt & Jensen, 1985) uses a statistical method requiring the RMS variations to be small compared to the wavelength and therefore cannot fully approximate the ice roughness (Hope et al., 2017). The open-source package SPECFEM2D (Tromp et al., 2008) uses the spectral element method, and is very well adapted to solve the weak formulation of the wave equation in a fluid-solid domain (Chaljub et al., 2003; Chaljub et al., 2007). The 2.5D axisymmetric version of SPECFEM2D, developed by Bottero (2018) for his PhD-thesis, was shown to be very efficient in fluid-solid domains. Regular 2D Cartesian simulations model waves generated by line sources perpendicular to the 2D plane. These non-physical out-of-plane sources artificially changes both physical properties and amplitudes in the simulation, which might cause errors in the interpretation. Those effects can be avoided by using a 2.5D model instead, which allows for geometrical spreading and a point source in a cylindrical system by locating the source on the symmetry axis and rotating a 2D domain around it. Thus, an axisymmetric 2.5D simulation with 3D geometrical spreading can be obtained at a moderate computational cost (Bottero, 2018).

1.5. Objectives

The main objective of this thesis is to implement an ice layer above a water layer in the axisymmetric 2.5D version of SPECFEM2D to model acoustic wave propagation in a coupled solid-fluid domain, imitating the deep ice-covered Arctic Ocean. Although the 2.5D version of SPECFEM2D has been proven to be very efficient for wave propagation modeling in fluid-solid domains, an ice layer has never been modeled on top of a water layer with this numerical tool. The benefit of a point source and 3D geometrical spreading at a moderate cost make SPECFEM2D very attractive for underwater acoustic wave propagation. The aim is to investigate if SPECFEM2D could be a suitable numerical tool for such simulations in the hope of finding out if it can be an asset for further studies on acoustic wave propagation in the Arctic Ocean.

To do this, two subsidiary objectives are specified. Collis et al. (2016) present predicted transmission loss curves for their elastic parabolic solution, using three different models with a 50 Hz source and a receiver at 30 m depth. The first subsidiary objective is to set up three models comparable to those used in Collis et al. (2016) and to compare the influence of sea ice on acoustic wave propagations between the models obtained in this thesis and the models presented in Collis et al. (2016).

The next subsidiary objective is to introduce more complex sea ice interfaces by implementing ice roughness and ice ridges in the models. The purpose is both to find out how wave propagation domains with more complex ice layers are modeled in SPECFEM2D and to study the effect of ice ridges and ice roughness on acoustic wave propagation.

1.6. Structure of the thesis

This first introductory chapter has provided an insight into the characteristics of acoustic wave propagation in the Arctic Ocean and introduced some numerical methods commonly used for underwater wave propagation problems, with emphasis on the spectral element method. The motivation

and objective of this thesis have also been described. Chapter 2 presents the theoretical mathematical background for the spectral element method in a coupled solid-fluid domain, and Chapter 3 describes the model setup and introduces model parameters. Both sound velocity profiles and ice models are presented. Chapter 4 gives a description of how the model is implemented into SPECFEM2D and describes the validation of the model against the seismo-acoustic propagation model OASES and an exact solution. The results achieved by the simulations in the study are presented in Chapter 5 and discussed and compared in Chapter 6. Uncertainties and valuable experiences are also addressed in Chapter 6, together with suggestions for further work. A conclusion of the work is given in Chapter 7.

Chapter 2
Theoretical background

2.1. The wave equation

This section is based on the work of Chaljub et al. (2007), for the seismic wave equation in a regional setting. In a regional setting the considered scale is so small that the Earth's rotation and gravity can be neglected. This section will present one formulation of the wave equation for solid regions and one potential formulation for fluid regions in the domain.

2.1.1. Solid region

To start with, the elastic wave equation for a solid medium in a regional setting may be expressed as:

$$\rho \ddot{\boldsymbol{u}} = \nabla \cdot \boldsymbol{T}(\boldsymbol{u}) + \boldsymbol{f} \tag{1}$$

where $\boldsymbol{T}(\boldsymbol{u})$ is the Lagrangian incremental stress tensor, $\boldsymbol{u}$ the Lagrangian perturbation of displacement, ρ the density, $\boldsymbol{f}$ the source and the two dots denote time differentiation twice. Stress and strain can be related by Hooke's Law, which relates the stress tensor $\boldsymbol{T}_{ij}(\boldsymbol{u})$ to infinitesimal strain $\boldsymbol{\varepsilon}(\boldsymbol{u})$ by:

$$\boldsymbol{T}_{ij}(\boldsymbol{u}) = c_{ijkl}\boldsymbol{\varepsilon}_{kl}(\boldsymbol{u}) \tag{2}$$

$$\boldsymbol{\varepsilon}(\boldsymbol{u}) = \frac{1}{2}(\nabla \boldsymbol{u} + \nabla^T \boldsymbol{u}) \tag{3}$$

where the elastic tensor is denoted c_{ijkl}. Inserting Equation (2) and (3) into Equation (1), leads to the full expression of the elastic wave equation in a regional setting:

$$\rho \ddot{\boldsymbol{u}} = \nabla \cdot \left(c_{ijkl} \left[\frac{1}{2}(\nabla \boldsymbol{u} + \nabla^T \boldsymbol{u}) \right] \right) + \boldsymbol{f} \tag{4}$$

2.1.2. Fluid region

If Equation (4) is used for wave propagation in both solid and fluid regions, problems will arise as the wave equation gets too many degrees of freedom in the fluid region, where shear wave velocity is zero. This will cause artificial oscillations to emerge and grow without control in the simulation. Therefore, a potential formulation is defined within the fluid regions instead.

In the fluid region the stress tensor takes the form:

$$\boldsymbol{T}(\boldsymbol{u}) = -\delta p\boldsymbol{I} = \rho c^2(\nabla \cdot \boldsymbol{u}\boldsymbol{I}) \tag{5}$$

where c denotes the compressional wave speed, δp the Lagrangian pressure perturbation, and $\boldsymbol{I}$ the identity matrix. The source term is initially ignored. Putting Equation (5) into Equation (1) leads to an expression for the acoustic wave equation in a regional setting (Chaljub et al., 2007):

$$\rho\ddot{\boldsymbol{u}} = \nabla(\rho c^2 \nabla \cdot \boldsymbol{u}) \tag{6}$$

The displacement field of the acoustic wave equation in Equation (6) can be expressed in terms of a scalar potential χ as:

$$\boldsymbol{u} = \frac{1}{\rho}\nabla(\chi) \tag{7}$$

For a density not varying with time, a double differentiation in time leads to:

$$\ddot{\boldsymbol{u}} = \frac{1}{\rho}\nabla(\ddot{\chi}) \tag{8}$$

By replacing $\ddot{\boldsymbol{u}}$ on the left side of the acoustic wave equation in Equation (6) with the expression obtained in Equation (8), and expressing $\boldsymbol{u}$ on the right side of Equation (6) with the scalar potential in Equation (7) an expression of the acoustic wave equation in terms of scalar potential is obtained:

$$\ddot{\chi} = \rho c^2 \nabla \cdot \left(\frac{\nabla(\chi)}{\rho}\right) \tag{9}$$

The choice of potential in Equation (7) and the equation for the stress tensor in Equation (5), results in an expression for the pressure as $dP = -\ddot{\chi}$. Lastly, a point source located at $\boldsymbol{x}_s$ is added to Equation (9), and the final expression for the wave equation, for a fluid with density either constant or slowly varying in space, in the acoustic domain becomes (e.g. Bottero, 2018):

$$\ddot{\chi} = \rho c^2 \nabla \cdot \left(\frac{\nabla(\chi)}{\rho}\right) + f(t)\delta\boldsymbol{x}_s \tag{10}$$

2.1.3. Initial and boundary conditions

To solve Equations (4) and (10), initial and boundary conditions must also be specified. The initial condition states that the medium is at rest at time zero, by $\boldsymbol{u} = \dot{\boldsymbol{u}} = 0$ and $\chi = \dot{\chi} = 0$ for the solid and fluid region, respectively. The external boundaries of the domain are the free surface and the absorbing boundaries. As the traction is zero at the free surface, the stress vanishes at this point and thus, the free surface is enforced. Hooke's law must be adapted at the absorbing boundaries as all energy is absorbed at this point (Chaljub et al., 2007). The absorbing boundary conditions on the external boundaries of the

model are modeled by perfectly matched layers, further described in *Chapter 2.5. Perfectly matched layers*.

In addition to the regular external boundary conditions, the internal boundary conditions must also be considered at the interface between the solid and fluid region Ω_{FS}, to provide a relation between the waves traveling in the elastic and the acoustic parts of the domain. The internal boundary conditions states that tangential slip must be allowed at the fluid-solid interface, and that only the normal component of the displacement and stress will be continuous across the boundary. Accordingly, the kinematic condition for continuity of normal displacement should be used at the fluid-solid interface (Assi & Cobbold, 2016; Chaljub et al., 2007), expressed with Equation (8) for the displacement in the fluid domain (Chaljub et al., 2007):

$$\boldsymbol{u} \cdot \hat{\boldsymbol{n}}|_{\Omega_{FS}} = \left(\left[\frac{1}{\rho}\nabla(\chi)\right] \cdot \hat{\boldsymbol{n}}\right)|_{\Omega_{FS}} \tag{11}$$

The normal vector $\hat{\boldsymbol{n}}$ is here defined to be positive in the same direction as the axis. Another internal boundary condition that must be taken into account is the traction at the fluid-solid interface, where the normal stress must be continuous across the interface (Chaljub et al., 2007):

$$\boldsymbol{T}(\boldsymbol{u}) \cdot \hat{\boldsymbol{n}}\,|_{\Omega_{FS}} = \ddot{\chi}\hat{\boldsymbol{n}} = -dP \tag{12}$$

2.2. The weak form of the wave equation

This chapter addresses the weak form of the wave equation in the solid and fluid region, and is also based on the work by Chaljub et al. (2007). The weak form of the wave equation is presented for the fluid and solid region.

2.2.1. Solid region

The weak form of the elastic wave equation in Equation (1) is obtained by multiplying with an arbitrary spatial-dependent test function $\boldsymbol{v}$ and integrating over the domain. The weak form of the wave equation in a solid region, V_S, becomes (Chaljub et al., 2007; Igel, 2016b):

$$\int_{V_S} \rho\ddot{\boldsymbol{u}} \cdot \boldsymbol{v}\ dV = \int_{V_S} \nabla \cdot \boldsymbol{T}(\boldsymbol{u}) \cdot \boldsymbol{v}\ dV + \int_{V_S} \boldsymbol{f} \cdot \boldsymbol{v}\ dV \tag{13}$$

Following the procedure in Chaljub et al. (2007), the divergence of the stress tensor integrated by parts leads to the following expression:

$$\int_{V_S} \nabla \cdot \boldsymbol{T}(\boldsymbol{u}) \cdot \boldsymbol{v}\ dV = -\int_{V_S} \boldsymbol{T}(\boldsymbol{u}) \cdot \nabla\boldsymbol{v}\ dV + \int_{\Omega_{int}} \boldsymbol{T}(\boldsymbol{u}) \cdot \hat{\boldsymbol{n}} \cdot \boldsymbol{v}\ dS \tag{14}$$

Here Ω_{int} includes all interfaces; the free surface Ω_{sur}, the fluid-solid interface Ω_{FS} and the absorbing boundaries Ω_{abs}:

$$\int_{\Omega_{int}} \boldsymbol{T}(\boldsymbol{u}) \cdot \hat{\boldsymbol{n}} \cdot \boldsymbol{v}\ dS = \int_{\Omega_{sur}} \boldsymbol{T}(\boldsymbol{u}) \cdot \hat{\boldsymbol{n}} \cdot \boldsymbol{v}\ dS \int_{\Omega_{FS}} \boldsymbol{T}(\boldsymbol{u}) \cdot \hat{\boldsymbol{n}} \cdot \boldsymbol{v}\ dS + \int_{\Omega_{abs}} \boldsymbol{T}(\boldsymbol{u}) \cdot \hat{\boldsymbol{n}} \cdot \boldsymbol{v}\ dS \tag{15}$$

The integral on the absorbing boundaries and the free surface equal zero, and Equation (15) will be reduced to:

$$\int_{\Omega_{int}} \boldsymbol{T}(\boldsymbol{u}) \cdot \hat{\boldsymbol{n}} \cdot \boldsymbol{v}\ dS = \int_{\Omega_{FS}} \boldsymbol{T}(\boldsymbol{u}) \cdot \hat{\boldsymbol{n}} \cdot \boldsymbol{v}\, dS = \int_{\Omega_{FS}} \ddot{\chi} \hat{\boldsymbol{n}} \cdot \boldsymbol{v}\, dS \tag{16}$$

The right-hand side of Equation (16) is obtained by using the boundary condition for traction in Equation (12), which states that the normal stress must be continuous over the fluid-solid interface.

Thus, when solving the wave equation in the solid region the potential of the displacement in the fluid region is used to express the boundary conditions at the solid-fluid interface, and the wave equation to be solved in the solid region becomes:

$$\int_{V_S} \rho \ddot{\boldsymbol{u}} \cdot \boldsymbol{v}\ dV = -\int_{V_S} \boldsymbol{T}(\boldsymbol{u}) \cdot \nabla \boldsymbol{v}\ dV + \int_{\Omega_{FS}} \ddot{\chi} \hat{\boldsymbol{n}} \cdot \boldsymbol{v}\, dS + \int_{V_S} \boldsymbol{f} \cdot \boldsymbol{v}\, dV \tag{17}$$

2.2.2. Fluid region

To obtain an expression for the weak form of the wave equation expressed by potentials in the fluid regions, the procedure in Chaljub et al. (2007) will be followed as well. Thus, the weak form of the acoustic wave equation (Equation (9)) is obtained by taking the integral over the fluid region, V_F, and multiplying it with an arbitrary potential w on both sides:

$$\int_{V_F} \frac{1}{\rho c^2} \ddot{\chi} w\, \mathrm{d}V = \int_{V_F} \nabla \cdot \left(\frac{\nabla(\chi)}{\rho} \right) w\, \mathrm{d}V \tag{18}$$

The stress tensor is integrated by parts and becomes:

$$\int_{V_F} \nabla \cdot \left(\frac{\nabla(\chi)}{\rho} \right) w\, \mathrm{d}V = -\int_{V_F} \left(\frac{\nabla(\chi)}{\rho} \right) \cdot \nabla w\, \mathrm{d}V + \int_{\Omega_{int}} \left(\frac{\nabla(\chi)}{\rho} \right) \cdot \hat{\boldsymbol{n}}\, w\, \mathrm{d}V \tag{19}$$

As in the solid region, the interfaces Ω_{int} includes all interfaces; the free-surface Ω_{sur}, the fluid-solid interface Ω_{FS} and the absorbing boundaries Ω_{abs}:

$$\int_{\Omega_{int}} \left(\frac{\nabla(\chi)}{\rho}\right) \cdot \hat{\boldsymbol{n}}\, w \; dS \;=\; \int_{\Omega_{sur}} \left(\frac{\nabla(\chi)}{\rho}\right) \cdot \hat{\boldsymbol{n}}\, w \; dS \;\int_{\Omega_{FS}} \left(\frac{\nabla(\chi)}{\rho}\right) \cdot \hat{\boldsymbol{n}}\, w \;\; dS + \int_{\Omega_{abs}} \left(\frac{\nabla(\chi)}{\rho}\right) \cdot \hat{\boldsymbol{n}}\, w \;\; dS \tag{20}$$

As the stress vanishes at the free-surface and the integral of the absorbing boundaries equals zero, Equation (9) becomes:

$$\int_{V_F} \frac{1}{\rho c^2} \ddot{\chi} w \, \mathrm{d}V \;=\; \int_{\Omega_{FS}} \left(\frac{\nabla(\chi)}{\rho}\right) \cdot \hat{\boldsymbol{n}}\, w \, \mathrm{d}S - \int_{V_F} \left(\frac{\nabla(\chi)}{\rho}\right) \cdot \nabla w \, \mathrm{d}V \tag{21}$$

The internal kinematic boundary condition for continuity of normal displacement across the fluid-solid interface, Equation (11), is applied to take the solid-fluid interfaces into consideration in the fluid region. Equation (18) becomes:

$$\int_{V_F} \frac{1}{\rho c^2} \ddot{\chi} w \, \mathrm{d}V \;=\; \int_{\Omega_{FS}} (\boldsymbol{u}) \cdot \hat{\boldsymbol{n}}\, w \, \mathrm{d}S - \int_{V_F} \left(\frac{\nabla(\chi)}{\rho}\right) \cdot \nabla w \, \mathrm{d}V \tag{22}$$

Adding the source, the weak form of the acoustic wave equation becomes (e.g. Bottero, 2018):

$$\int_{V_F} \frac{1}{\rho c^2} \ddot{\chi} w \, \mathrm{d}V \;=\; \int_{\Omega_{FS}} (\boldsymbol{u}) \cdot \hat{\boldsymbol{n}} w \, \mathrm{d}S - \int_{V_F} \left(\frac{\nabla(\chi)}{\rho}\right) \cdot \nabla w \, \mathrm{d}V + \frac{1}{\rho c^2} f(t) w(\boldsymbol{x}_s) \tag{23}$$

In this way, the fluid and solid regions are coupled by using one of the two internal boundary conditions in each domain. The wave equation in the solid region is solved by using the boundary condition for traction, Equation (12), enforcing a continuous normal stress across the fluid-solid interface. In the fluid region, the kinematic boundary condition for a continuity of normal displacement across the fluid-solid interface, Equation (11), is used.

2.3. Spectral elements approximation

The spectral element method is a powerful and commonly used tool to model wave propagation formulated in its weak form, as presented in the previous sections. The model domain is divided into elements, where a set of Lagrange polynomials as basis functions are defined with the purpose of function interpolation to approximate the unknown functions $\boldsymbol{u}$ and χ. The collocation points are set to be Gauss-Lobatto-Legrende points for both the interpolation and integration scheme, leading to the benefit of a diagonal mass matrix invertible without having to solve a large set of linear equations. In

this section, the procedure for the spectral elements approximation is explained by mainly following the method in Chaljub et al. (2007), where a more extensive explanation can be found.

2.3.1. Defining the mesh

First, the whole domain V is divided into a mesh of a chosen number of elements V^e. The elements are not necessarily simple cubes or tetrahedra but can have different shapes so that they can be adapted to the geometry of the studied structure and its interfaces. Figure 3 shows an example of a mesh created in SPECFEM2D.

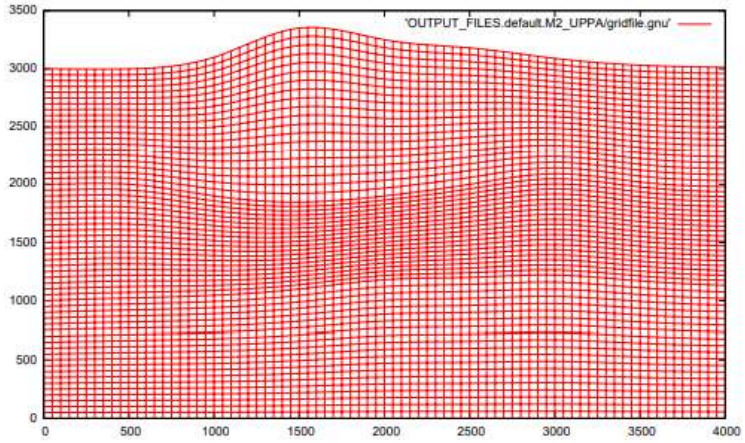

Figure 3. *Figure from the SPECFEM2D User Manual Version 7.0 (Centre national de la recherche scientifique & Princeton University, 2021), showing an example of a mesh created by the internal mesher in SPECFEM2D.*

Dividing the domain into a chosen number of elements ease the calculations of the integrals as the global coordinates are mapped into a reference interval $[-1,1]$ where the calculations are performed for each element. The meshing is done so that the elements V^e in the mesh can be invertible mapped from the global domain into a squared reference interval, $\Lambda = [-1,1]$:

$$V^e = \boldsymbol{F}^e(\Lambda) \tag{24}$$

Here the mapping $\boldsymbol{F}^e$ is controlled by a collection of control nodes n_a, which are defining a shape function N_a for the mapping. The shape functions are normally linear or quadratic, making the maximum number of control nodes to be 9 in a 2D simulation. The mapping can be expressed as (Chaljub et al., 2007):

$$\boldsymbol{x}^e = \boldsymbol{F}^e(\boldsymbol{\zeta})\ 1 \approx \sum_{a=1}^{n_a} N_a(\boldsymbol{\zeta})\boldsymbol{x}_a^e \tag{25}$$

Here $\boldsymbol{x}^e$ is the global vector on each element V^e,and $\boldsymbol{\zeta}$ is the local vector on the reference interval Λ, so that the global vector $\boldsymbol{x}_a^e$ for each control node $\boldsymbol{\zeta}_a$ can be mapped into the reference interval as $\boldsymbol{x}_a^e = \boldsymbol{F}^e(\boldsymbol{\zeta}_a)$. The control nodes $\boldsymbol{\zeta}_a$ are defined as $N_a(\boldsymbol{\zeta}_b) = \delta_{ab}$. A visualization of the mapping is shown in Figure 4.

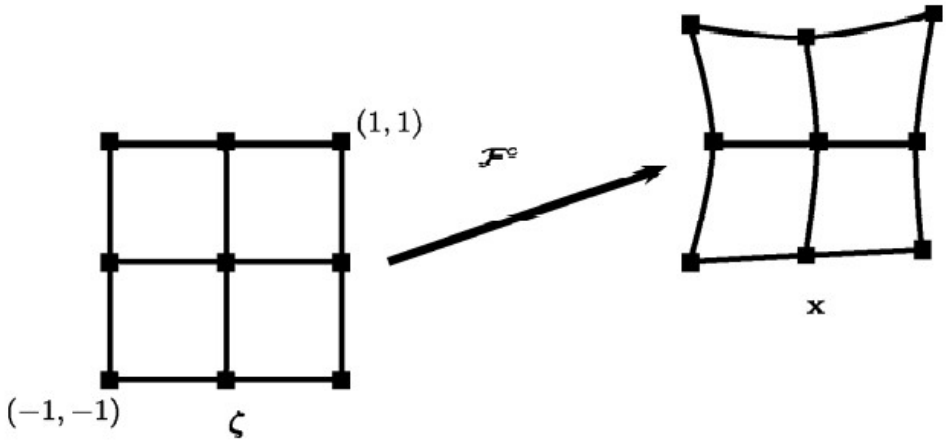

Figure 4. *Figure from Chaljub et al. (2007), showing an example of the mapping in a 2D domain with 9 control nodes. The control nodes* $\boldsymbol{\zeta}$ *are the local vector in the element and* $\boldsymbol{x}$ *the global vector in the domain.*

As explained in Chaljub et al. (2007), it is important to take the shape and topography of the domain into consideration when constructing the mesh of the domain. Interfaces or other sharp variations must be placed at the element boundaries, as smooth functions are used for approximation within the elements, and consequently sharp variations can only exist at element boundaries. Another aspect that is important to take into consideration is the element size. The element size must be adapted to the shape of the domain so that interfaces in the domain can be approximated in a decent manner. The mesh should also be designed so that the wavelengths are modeled approximately evenly within the domain. It is wise to avoid oversampling of the wavelengths as this will require an unnecessary amount of both calculation time and memory. Also, the time-step in the simulation is based on the Courant-Friedrichs-Lewy stability criterion (Section *'2.3.5. Courant-Friedrichs-Lewy stability criterion'*). The choice of element size will affect the distance used to determine an appropriate time step for the simulation, which must be kept in mind when creating the mesh.

2.3.2. Lagrange polynomials and Gauss-Lobatto-Legendre points

The displacement and potential in Equation (23) and Equation(17) are approximated in each element of the domain by a basis of Lagrange polynomials. The Lagrange polynomial of degree N is written as (Igel, 2016b; Langtangen & Mardal, 2019) .

$$l_i^N = \prod_{j=0, j\neq i}^{N} \frac{\xi - \xi_j^N}{\xi_i^N - \xi_j^N} \tag{26}$$

A great benefit of the Lagrange polynomials is that l_i^N is equal to 1 at ξ_i^N, and zero at the other ξ_j^N collocation points on the reference interval $\Lambda = [-1,1]$ for a polynomial of degree N (Chaljub et al., 2007; Igel, 2016b):

$$l_i^N\left(\xi_j^N\right) = \delta_{i,j} \qquad \forall(i,j) = \{0, \dots, N\}^2 \tag{27}$$

Here $\delta_{i,j}$ is the Kronecker delta. For the spectral element method, the collocation points are chosen as a set of $N+1$ Gauss-Lobatto-Legendre (GLL) points. The GLL points have the benefit of including the outer boundaries of the reference interval, which is beneficial for the calculations of continuity conditions between elements (Chaljub et al., 2007). The distance between the GLL points is non-uniform, but the distribution of points is denser towards the boundaries for higher orders of polynomials. The higher the order is, the smaller the distance between the points becomes (Igel, 2016b). The non-uniform distribution is designed such that the polynomial does not exceed 1 on the whole reference interval $\Lambda = [-1,1]$. Sets of GLL points for different order of N are shown in Figure 5, where the $N+1$ GLL points for $N = 4$ are colored red.

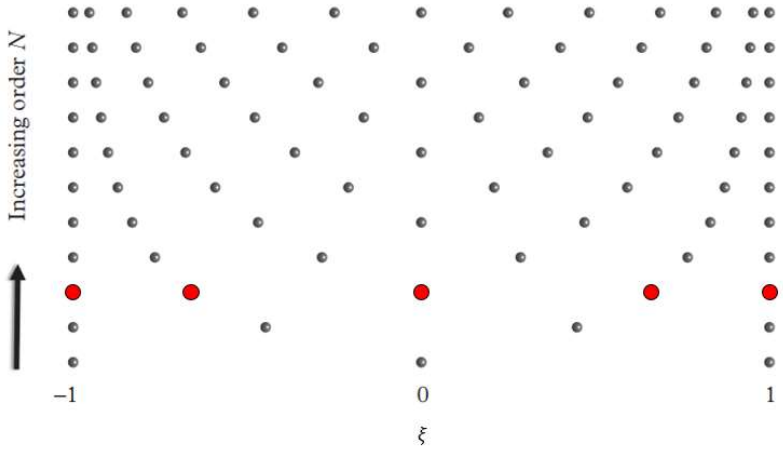

Figure 5. *GLL points for different polynomial orders shown on a reference interval* $\Lambda = [-1,1]$. *The* $N+1$ *GLL points for polynomial order* $N = 4$ *are colored red. Modified figure from Igel (2016b).*

Thus, $N+1$ Lagrange polynomials of order N will be exactly interpolated on the $N+1$ GLL collocation points in the reference interval. Figure 6 shows the 5 Lagrange polynomials for order $N = 4$ on the reference interval.

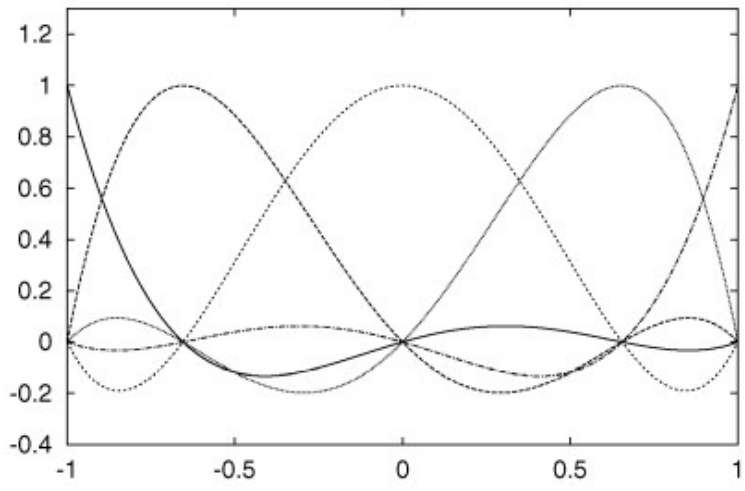

Figure 6. $N+1$ *Lagrange polynomials for degree* $N = 4$ *shown on the reference interval* $\Lambda = [-1,1]$. *Note that the polynomial never exceeds 1 and that it equals zero on all collocation points but one of the* 5 *GLL points. Figure from Chaljub et al. (2007).*

In 2D, a set of GLL collocation points is defined to combine the Lagrange interpolants in both directions (Figure 7). A set of GLL points is defined as $\boldsymbol{\zeta}_{ij}^{N} = \left(\xi_i^N, \xi_j^N\right)$, where the corresponding Lagrange interpolants are $l_{i,j}^{N}(\boldsymbol{\zeta}) = l_i^N(\xi) l_j^N(\eta)$. Here, the local vector on the reference square is $\boldsymbol{\zeta} = (\xi, \eta)$.

Each element e has a set of collocation points defined as $\boldsymbol{x}_{i,j}^{e,N} = \boldsymbol{F}^e(\boldsymbol{\zeta}_{i,j}^{N})$. For a discrete displacement vector $\tilde{u}$ and $\boldsymbol{x} = \boldsymbol{F}^e(\boldsymbol{\zeta})$ the interpolation formula can be presented as (Chaljub et al., 2007):

$$\tilde{u}_\alpha(\boldsymbol{x}) = \tilde{u}_\alpha^e(\boldsymbol{\zeta}) = \sum_{i=0}^{N}\sum_{j=0}^{N} \tilde{u}_a^e(\boldsymbol{\zeta}_{ij}^N) l_{i,j}^N(\boldsymbol{\zeta}) = \sum_{i=0}^{N}\sum_{j=0}^{N} \tilde{u}_a(\boldsymbol{x}_{ij}^{e,N}) l_{i,j}^N(\boldsymbol{\zeta}) \tag{28}$$

where (i,j) are the local indices of the collocation points within each element. The Lagrange basis functions are only defined on the reference interval within each element and the approximation of the weak form of the wave equation within each element can be obtained by summing up all the basis functions and suitable coefficients within each element (Igel, 2016b).

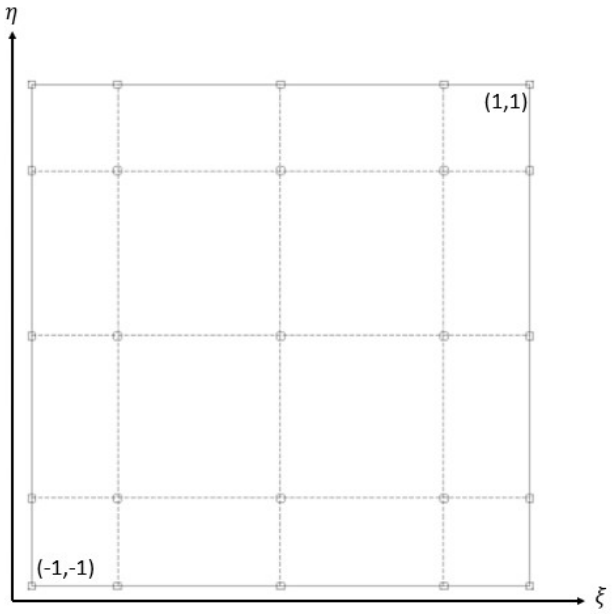

Figure 7. *The GLL points in a local reference interval in a 2D domain for order* $N = 4$. *Modified figure from Chaljub et al. (2007).*

The total number of local points within the domain is $N_L = E \times (N+1)$ for E number of elements. The local points on the edges or corners of the elements will belong to more than one element and must only be counted once when counting the total number of global points N_G in the domain. For a grid point within element e with local indices (i,j), the global index of the grid point will be denoted $n(e,i,j)$, for $n \in [1, N_G]$. For grid points located within the element, the shape functions will be defined as $\phi_n(\boldsymbol{x}) = l_{i,j}^N(\boldsymbol{\zeta})$ on V^e. For grid points which belongs to more than one element, so that the grid point also belongs to element e' and has a global index $n(e',i',j') = n(e,i,j)$, the shape functions must be extrapolated into the other element as $\phi_n(\boldsymbol{x}) = l_{i',j'}^N(\boldsymbol{\zeta})$ on $V^{e\prime}$ (Chaljub et al., 2007).

This makes it possible to define both a local and a global vector, $\widetilde{\boldsymbol{U}}_L$ and $\widetilde{\boldsymbol{U}}_G$ with dimensions $d \times N_L$ and $d \times N_G$ respectively, which both holds the values of the displacement at the collocation points. The local and global vector are related through the Boolean connectivity matrix $\boldsymbol{Q}$ as $\widetilde{\boldsymbol{U}}_L = \boldsymbol{Q}\widetilde{\boldsymbol{U}}_G$. By taking the transpose of $\boldsymbol{Q}$, the values of the displacement in the local vector can be assembled into the global vector (Chaljub et al., 2007). When assembling the contributions, the values of the shared grid points must be summed up, so that only one value belongs to each grid point (Igel, 2016b).

2.3.3. Numerical integration

The weak form of the wave equation, Equation (17) and (23) which features integrals, are numerically calculated and weighted at the GLL collocation points. The weighting is done with the integrals of the Lagrange interpolants at the GLL collocation points (Chaljub et al., 2007; Igel, 2016b).

The integral of any function f, defined on the squared 2D reference interval, can be approximated by the quadrature formula (Chaljub et al., 2007):

$$\int_{\Lambda} f(\boldsymbol{\zeta})\, \boldsymbol{d\zeta} = \sum_{i=0}^{N} \sum_{j=0}^{N} \omega_i^N \omega_j^N f(\xi_{ij}^N) \tag{29}$$

where the weights are $\omega_i^N = \int_{\Lambda} l_i^N \, d\xi$. As previously mentioned, the choice of GLL points as collocation points for both interpolation of the Lagrange polynomials (*2.3.2. Lagrange polynomials and Gauss-Lobatto-Legendre points*) and integration is an important feature of the spectral element method. This specific choice results in a diagonal mass matrix (Equation (32), and it is not necessary to deal with many linear equations to extrapolate the scheme explicitly (Chaljub et al., 2007; Igel, 2016b). Using the left-hand side of Equation (17) as an example of the required integration, the displacement $\ddot{\boldsymbol{u}}$ can be expressed on the polynomial basis functions ϕ_n as (Igel, 2016b):

$$\ddot{\boldsymbol{u}}(\boldsymbol{x}, t) = \sum_{n=1}^{N} \ddot{\boldsymbol{u}}_n\,(t) \phi_n(\boldsymbol{x}) \tag{30}$$

The spectral elements method uses the Galerkin principle, and the arbitrary test functions $\boldsymbol{v}$ are expressed by the same polynomials that are used to approximate the field, i.e. Lagrange polynomials (Igel, 2016b):

$$\boldsymbol{v}(\boldsymbol{x}) = \phi_{n'}(\boldsymbol{x}) \tag{31}$$

Using Equation (30) and (31) to express the integral in the left-hand side of Equation (17) leads to:

$$\int_{V_S} \rho(\boldsymbol{x})\, \boldsymbol{u}(\ddot{\boldsymbol{x}}, t) \cdot \boldsymbol{v}\; dV = \sum_{n=1}^{N} \left(\int_V \rho(\boldsymbol{x})\, \phi_n(\boldsymbol{x}) \phi_{n'}(\boldsymbol{x}) dV \right) \ddot{\boldsymbol{u}}_n(t) \tag{32}$$

Here, the integral term on the right-hand side is the mass matrix $M_{n'n}$, which is the scalar matrix of the polynomial basis and test functions. Those polynomial shape functions are defined as $\phi_n(\boldsymbol{x}) = l_{i,j}^N(\boldsymbol{\zeta})$ and $\phi_{n'}(\boldsymbol{x}) = l_{i',j'}^N(\boldsymbol{\zeta})$, for the grid points of global indices $n = n(e, i, j)$ and $n' = n(e', i', j')$ in element e and e', respectively. Using the shape functions, the mass matrix can be expressed on the local reference interval (Chaljub et al., 2007):

$$M_{n'n} = \int_{\Lambda} \rho(\boldsymbol{\zeta}) l_{i,j}^N(\boldsymbol{\zeta}) l_{i',j'}^N(\boldsymbol{\zeta})\, J^e(\boldsymbol{\zeta})\, \boldsymbol{d\zeta} \tag{33}$$

where J^e is the Jacobi determinant from the invertible mapping. By using the quadrature formula in Equation (25), Equation (33) can be rewritten to:

$$M_{n'n} = \int_{v^e} \rho(\xi_{ij}^N)\delta_{ii'}\delta_{jj'}\omega_i^N\omega_j^N J^e(\xi_{ij}^N) \tag{34}$$

Because the Lagrange interpolants, as described above, satisfies $l_i^N(\xi_j^N) = \delta_{i,j}$, the mass matrix will only have a value where $n = n'$ and be zero elsewhere, and thus, the mass matrix becomes diagonal. The same procedure must be followed for the rest of the terms in Equation (17) and in Equation (23). Thereafter, the spectral element problem can be set up as a matrix system of differential equations (Chaljub et al., 2003; Chaljub et al., 2007). In the solid region this can be expressed as:

$$\boldsymbol{M}_s\ddot{\boldsymbol{u}}(t) = -\boldsymbol{K}_s\boldsymbol{u}(t) + \boldsymbol{C}^{SF}\ddot{\boldsymbol{\chi}}(t) + \boldsymbol{F}^{EXT}(t) \tag{35}$$

where $\boldsymbol{M}_s$ is the mass matrix, $\boldsymbol{K}_s$ the stiffness matrix, $\boldsymbol{F}^{EXT}$ the external source and $\boldsymbol{C}^{SF}$ the coupling matrix of the solid-fluid boundary on the solid side. $\boldsymbol{u}$ and $\boldsymbol{\chi}$ are global vectors for displacement in the solid region and potential in the fluid region, respectively. The dots denote time differentiation.

In the fluid region, the matrix system can be expressed as:

$$\boldsymbol{M}_F\ddot{\boldsymbol{\chi}}(t) = -\boldsymbol{K}_F\boldsymbol{\chi}(t) + \boldsymbol{C}^{FS}\boldsymbol{u}(t) + \boldsymbol{F}^{EXT}(t) \tag{36}$$

Here are $\boldsymbol{M}_F$, $\boldsymbol{K}_F$ and $\boldsymbol{F}^{EXT}$ the same as above but for the fluid region, and $\boldsymbol{C}^{FS}$ is the coupling for the fluid-solid boundary on the fluid side (Chaljub et al., 2007).

Equation (35) and (36) uses the scalar potential for displacement χ, defined in Equation (7). The scalar potential for velocity can be defined as $\phi = \dot{\chi}$, so that we have $\dot{\phi} = \ddot{\chi}$. Time differentiation of Equation (36) and using the scalar potential for velocity gives:

$$\boldsymbol{M}_F\ddot{\boldsymbol{\phi}}(t) = \boldsymbol{C}^{FS}\dot{\boldsymbol{u}}(t) - \boldsymbol{K}_F\boldsymbol{\phi}(t) + \boldsymbol{F}^{EXT}(t) \tag{37}$$

Adapting Equation (35) to the new variable leads to:

$$\boldsymbol{M}_s\ddot{\boldsymbol{u}}(t) = \boldsymbol{C}^{SF}\dot{\boldsymbol{\phi}}(t) - \boldsymbol{K}_s\boldsymbol{u}(t) + \boldsymbol{F}^{EXT}(t) \tag{38}$$

2.3.4. The Newmark method

The meshing and use of Lagrange polynomials only affect the space representation of the functions, not their time-dependence. The Newmark time-stepping method will be used for the numerical integration of Equation (37) and Equation (38) in time. As the matrix system in both the fluid and solid parts have a similar structure in terms of time derivation, a global vector $\boldsymbol{q} = (\boldsymbol{u}, \boldsymbol{\phi})$ can be defined. The Newmark time-stepping scheme progresses in time by a mapping system, where a vector $\boldsymbol{q}$ is mapped for time $t_n = n\Delta t$ as $(\boldsymbol{q}_n, \dot{\boldsymbol{q}}_n) \rightarrow (\boldsymbol{q}_{n+1}, \dot{\boldsymbol{q}}_{n+1})$ (Chaljub et al., 2007). The Newmark time-stepping scheme can then be expressed as (Chaljub et al., 2007; Komatitsch et al., 2000):

$$\boldsymbol{M}\ddot{\boldsymbol{q}}_{n+1} - \boldsymbol{C}\dot{\boldsymbol{q}}_{n+1} + \boldsymbol{K}\boldsymbol{q}_{n_{+1}} = \boldsymbol{F}^{\boldsymbol{EXT}}_{n+1} \tag{39}$$

where $\boldsymbol{M}$ is the mass matrix, $\boldsymbol{C}$ the coupling matrix between the interfaces, $\boldsymbol{K}$ the stiffness matrix, $\boldsymbol{F}^{\boldsymbol{EXT}}$ the vector of external forces, and the dot denotes time differentiation as earlier. The Taylor expansion-based time-stepping scheme for $\boldsymbol{q}_{n+1}$, $\dot{\boldsymbol{q}}_{n+1}$ and $\ddot{\boldsymbol{q}}_{n+1}$ is given by (Chaljub et al., 2003; Chaljub et al., 2007):

$$\ddot{\boldsymbol{q}}_{n+1} = \boldsymbol{M}^{-1}(\boldsymbol{C}\dot{\boldsymbol{q}}_{n+1} - \boldsymbol{K}\boldsymbol{q}_{n_{+1}} + \boldsymbol{F}^{\boldsymbol{EXT}}_{n+1}) \tag{40}$$

$$\boldsymbol{q}_{n+1} = \boldsymbol{q}_n + \Delta t\dot{\boldsymbol{q}}_n + \Delta t^2\left[\left(\frac{1}{2} - \beta\right)\ddot{\boldsymbol{q}}_n + \beta\ddot{\boldsymbol{q}}_{n+1}\right] \tag{41}$$

$$\dot{\boldsymbol{q}}_{n+1} = \dot{\boldsymbol{q}}_n + \Delta t[(1-\gamma)\ddot{\boldsymbol{q}}_n + \gamma\ddot{\boldsymbol{q}}_{n+1}] \tag{42}$$

Here $\beta \in [0,0.5]$ and $\gamma \in [0,1]$ are the only parameters that need to be chosen. To obtain second order accuracy, a centered scheme is required to update the velocity. This can only be done by choosing $\beta = 0$ and $\gamma = 0.5$, leading to the explicit central method (Chaljub et al., 2007).

2.3.5. Courant-Friedrichs-Lewy stability criterion

The Newmark time-stepping scheme is conditionally stable for a maximum time step determined by the Courant-Friedrichs-Lewy (CFL) criterion. The CFL criterion assures that the speed at which the information travels through the domain is not so fast that the information skips a collocation point in the duration of one time step. The appropriate time step can be expressed by (Chaljub et al., 2007):

$$\Delta t \leq C\left(\frac{\Delta h}{c}\right)_{min} \tag{43}$$

where c is the P-wave velocity, C a constant which should be chosen between 0.3 and 0.5, and Δh the distance between two neighboring GLL points (Chaljub et al., 2007). Thus, the CFL criterion determines the maximum time step from the maximum velocity and the minimum distance between two GLL points to ensure that no information is lost.

2.4. Axisymmetric 2.5D simulations

The weak form of the wave equation in the axisymmetric 2.5D simulations is expressed in cylindrical coordinates (r, θ, z). The domain, and any important feature of the domain, is considered symmetric around the axis where $r = 0$, which makes all information of interest independent of θ. However, numerical problems may arise on the symmetry axis because $r = 0$ in this point and all elements in contact with the symmetry axis will be affected by a singularity $\frac{1}{r}$. There are several ways to solve this problem. One alternative is to use a higher numerical integration accuracy for elements close to the

symmetry axis and to move all affected elements slightly away from the axis. However, this will cause problems for the source location, which needs to be at the symmetry axis to avoid a line source type. Another alternative, which is the one that is applied, is to use a different quadrature for the integration (Bottero, 2018).

2.4.1. The axisymmetric domain and coordinate system

The cylindrical coordinates used in the axisymmetric 2.5D simulation are shown in Figure 8. The position vector $\boldsymbol{x}$ will take the shape $\boldsymbol{x} = r\hat{\boldsymbol{r}} + z\hat{\boldsymbol{k}}$, and an arbitrary vector $\boldsymbol{q}$ will be expressed in cylindrical coordinates as (Bottero, 2018):

$$\boldsymbol{q} = q_r(r,\theta,z,t)\hat{\boldsymbol{r}} + q_\theta(r,\theta,z,t)\hat{\boldsymbol{\theta}} + q_z(r,\theta,z,t)\hat{\boldsymbol{k}} \tag{44}$$

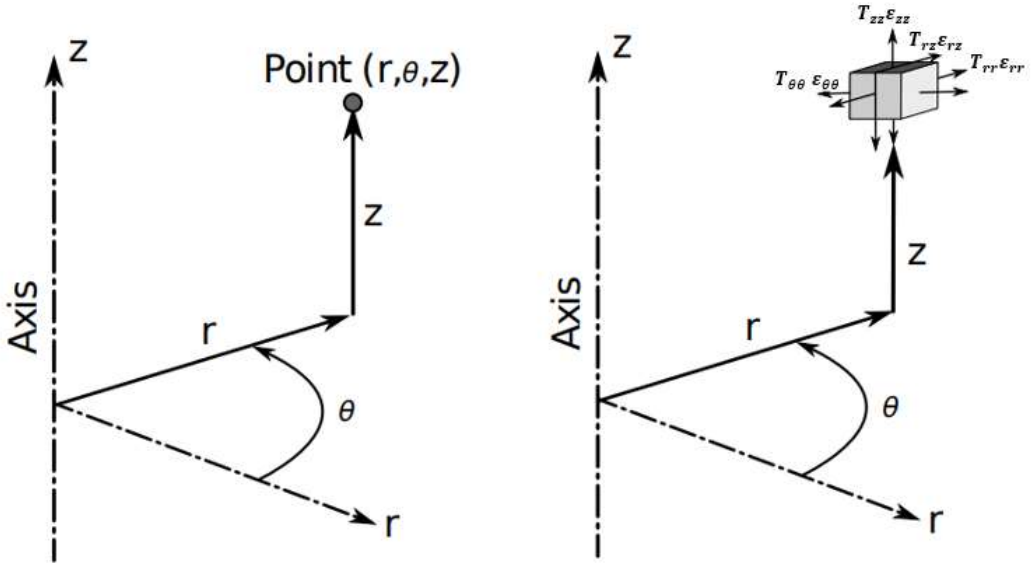

Figure 8. *Modified figure from Bottero (2018) showing the cylindrical coordinate system and a box with the different directions of stress* $\boldsymbol{T}$ *and strain* $\boldsymbol{\varepsilon}$.

The 2.5D domain is created by considering a 2D domain rotated around the axis where $r = 0$, creating a 3D domain, fully symmetric around the symmetry axis, as shown in Figure 9. As mentioned, this assumed symmetry around the symmetry axis removes the dependence of θ for all quantities within the domain and, thus, make the θ component of the displacement zero. This also applies for the source term. However, the component for out-of-plane stress, $\boldsymbol{T}_{\theta\theta}$, will be kept.

When applying the spectral element method to a 2.5D axisymmetric domain, all elements which are not in contact with the symmetry axis can be calculated on the GLL points as in a regular 2D simulation. However, all elements with grid points in contact with the symmetry axis (black dots in Figure 10) must be treated differently.

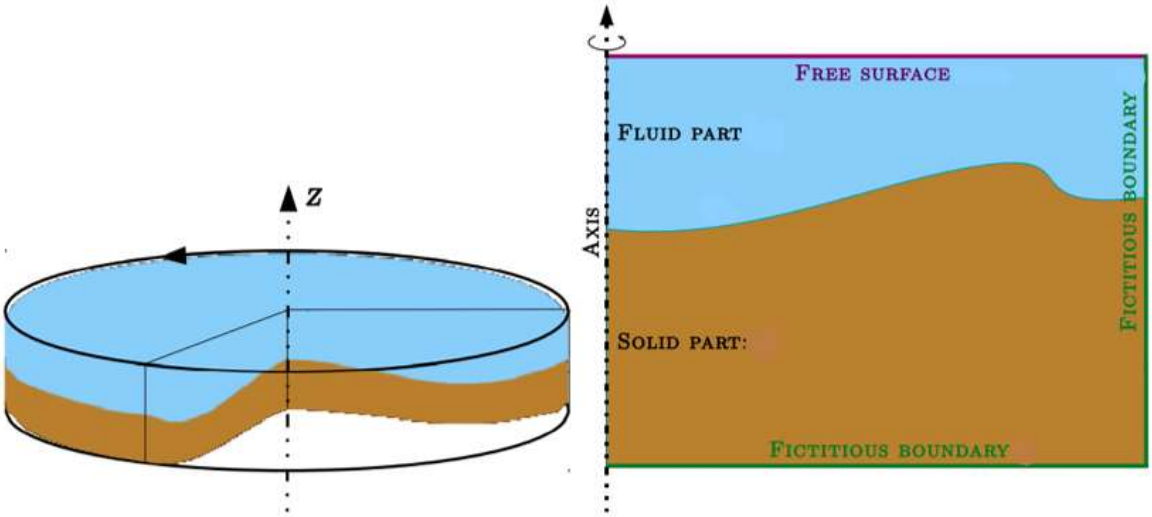

Figure 9. *Modified figure from (Bottero, 2018). The 2.5D simulations builds upon a 2D domain rotated around the symmetry axis, creating an axisymmetric 3D domain.*

All elements in contact with the symmetry axis will have grid points with the factor $r = 0$. This will cause problems solving the integrals in the local coordinate system due to $rd\xi d\eta$ becoming zero with cylindrical coordinates, leading to $0 = 0$ equations when mapping between global and local coordinates for $\xi_0^N = -1$ on the symmetry axis. Therefore, the elements touching the symmetry axis acquire a new quadrature for the integration, namely the Gauss-Lobatto-Jacobi (GLJ) quadrature on $\Lambda_{GLJ} = (0,1)$. The vertical direction is left untouched, only applying the GLJ points in the horizontal ξ-direction (Bottero, 2018).

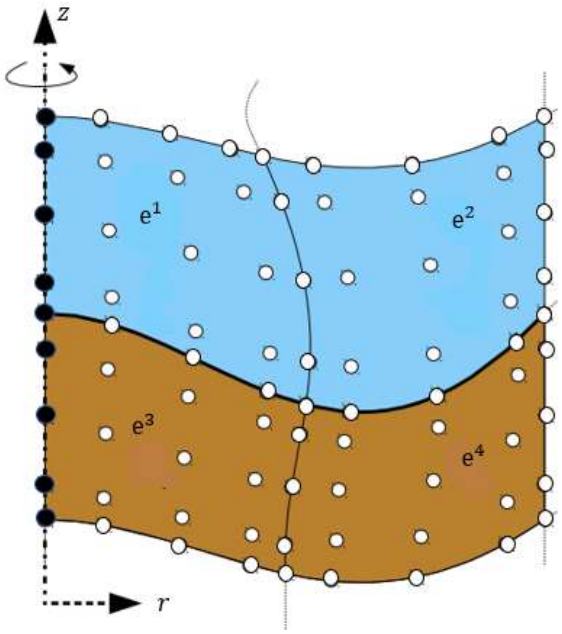

Figure 10. *Modified figure from Bottero (2018) showing the collocation points for polynomial order of $N = 4$ for 4 elements, where element e^1 and e^2 are in a fluid region and element e^3 and e^4 are in a solid region. The elements located on the symmetry axis are colored black. The figure is also showing that some local points within each element will be shared between more than one element, hence the contribution for this global point must be a summation of all contributions from the local points as explained in Chapter 2.3.2. Lagrange polynomials and Gauss-Lobatto-Legendre points.*

2.5. Perfectly matched layers

When solving problems in unbounded domains by numerical methods, it is necessary to crop the unbounded domain by an artificial boundary. On the artificial boundary, some form of absorbing boundary conditions is prescribed, such that waves reaching the boundary of the computational domain does not cause artificial reflections that disturbs the simulation. The concept of creating an absorbing layer that surrounds the computational domain and absorbs all waves at the boundaries without any reflection was introduced by (Berenger, 1994) as a perfectly matched layer, PML.

For wave simulations performed in a finite, regional setting PMLs are very important to avoid artificial reflections at the boundaries in order to simulate an unbounded domain. PMLs can be implemented as an extension of the domain. In this extended layer the solution of the wave equation will be a plane wave, whose amplitude decays exponentially with a frequency-independent factor with increasing distance away from the domain (Chaljub et al., 2007; Komatitsch & Tromp, 2003). The reflections will not be completely eliminated, but they will become small enough to be neglected for most frequencies and incident angles (Assi & Cobbold, 2016).

2.6. Transmission loss

As an acoustic wave is propagating through a medium, the acoustic intensity decreases due to geometrical spreading. In addition, some energy will also be lost due to attenuation. Transmission loss is a way to evaluate the loss due to both phenomena (Jensen et al., 2011, p. 14). As explained in Bottero (2018), transmission loss curves or maps are often convenient when quantifying the energy within acoustic models, where the signal can contain sharp variations due to heterogeneity or challenging geometry of the model domain. Transmission loss curves or maps are frequency-dependent measures of the energy within a model, normally calculated in the frequency domain. Transmission loss can be calculated as (e.g. Bottero, 2018):

$$TL(\boldsymbol{x}) = -10\, log \frac{E(\boldsymbol{x})}{E_0} \tag{45}$$

where the energy of the source is E_0, and $E(\boldsymbol{x})$ is the instantaneous energy field in the fluid and solid domain integrated over the considered duration time.

Chapter 3
Defining the model

3.1. Brief description of the general model parameters

The aim is to simulate acoustic wave propagation in a coupled solid-fluid domain representing a deep ice-covered Arctic Ocean. In order to focus on the wave interactions with the ice-cover, without the complication of sea floor interactions, the water layer is modeled as a half-space. To handle the resulting unbounded domain, an artificial boundary is introduced, where absorbing boundary conditions are implemented to avoid reflections from the edges of the domain. The domain will be elongated, stretching over 4 km horizontally with a depth of 100-500 m.

The ice models are set up as following. First, one model with a simple ice layer of constant thickness and one model with an ice layer of linearly decreasing thickness is set up. Thereafter, concave ice ridges are implemented using an average cross-section profile presented in Metzger et al. (2021). Finally, an ice roughness profile built from the characteristic correlation length in Hope et al. (2017), calculated from an ice segment in the Nansen Basin, is implemented in the ice models with ice ridges. Additionally, one simple model with water only is also be set up. The elastic ice parameters used in this section (Table 1) are the same as in Collis et al. (2016). The ice parameters will be kept constant through all simulations. Attenuation in the ice layer will be implemented in most, but not all, simulations. The water will be assumed to be non-attenuating for all simulations.

	SOLID REGION
COMPRESSIONAL VELOCITY v_P	3500 m/s
SHEAR VELOCITY v_S	1800 m/s
DENSITY ρ	900 kg/m^3

Table 1. *The elastic ice parameters used in all simulations.*

Different sound velocity profiles are used in the water. Initially, a homogeneous sound velocity profile is used. Then, a simple upwards refracting sound velocity profile is introduced, and lastly, a more realistic Arctic sound speed profile created from CTD-data collected in the Arctic Ocean (Chierici et al., 2021) is implemented. In the first two cases, the density profile will be constant, while it will be depth-dependent for the simulations using the realistic Arctic sound speed profile.

3.2. Attenuation and Quality factors

In SPECFEM2D, attenuation is given as bulk and shear quality factors. As part of the results will be compared to the results in Collis et al. (2016), the same attenuation as in their paper is used in this thesis. In Collis et al. (2016), the attenuation parameters for the ice layer are $\alpha_p = 0.3\ dB/\lambda$ and $\alpha_s = 1\ dB/\lambda$. The water layer is assumed to be non-attenuating in all simulations. This section describes how to

convert attenuations in dB/λ to bulk and shear quality factors. As the simulation is performed in a 2.5D domain, constructed by a 2D domain rotated around the symmetry axis, the plain strain formulation of the bulk modulus is used. The plain strain case differs from the 3D convention due to the lack of strain in the third direction. More details are given in Appendix A.I. and A.II.

The attenuations are given in dB/λ, and the relation between the attenuation in dB/λ and the quality factor is given by (Jensen et al., 2011, p. 244):

$$\alpha = 40\pi \frac{1}{2Q} \log(e) \approx \frac{27.29}{Q} \tag{46}$$

Here Q is the quality factor, which quantifies the amount of lost energy in a medium during one cycle. The relation between the s-wave quality factor Q_s and the shear quality factor Q_μ is (Seth & Wysession, 2003, pp. 119-212):

$$\frac{1}{Q_s} = \frac{1}{Q_\mu} \tag{47}$$

The expression for the p-wave quality factor Q_p is more complicated and depends on both the bulk quality factor Q_κ, the s-wave velocity v_s, the p-wave velocity v_p and the shear quality factor:

$$\frac{1}{Q_p} = \left(\frac{v_s}{v_p}\right)^2 \frac{1}{Q_\mu} + \left(1 - \left(\frac{v_s}{v_p}\right)^2\right) \frac{1}{Q_\kappa} \tag{48}$$

Equation (48) combined with Equation (46) gives an expression for the attenuation:

$$\alpha_p = \left(\frac{v_s}{v_p}\right)^2 \alpha_\mu + \left(1 - \left(\frac{v_s}{v_p}\right)^2\right) \alpha_\kappa \tag{49}$$

Here, $v_p = \sqrt{\frac{M}{\rho}} = \sqrt{\frac{\lambda+2\mu}{\rho}} = \sqrt{\frac{\kappa+\mu}{\rho}}$, and $M = \rho v_p^2 = \lambda + 2\mu$ is the P-wave modulus. $\kappa = \lambda + \mu$ is the bulk modulus for a 2D plain strain domain (Mavko et al., 2020, p. 38). Using Equation (46) to find the shear quality factor for the ice layer to use in the simulations:

$$Q_{\mu,S} = \frac{27.29}{\alpha_s} = \frac{27.29}{1} = 27.29 \tag{50}$$

The bulk attenuation is found through Equation (49), which inserted in Equation (46) gives the bulk quality factor for the simulations:

$$Q_{\kappa,S} = \frac{27.29}{\alpha_\kappa} = \frac{27.29}{0.0483} = 565.01 \tag{51}$$

The water layer is as said assumed to be non-attenuating, which is implemented by using a large quality factor; $Q_{\kappa,F} = Q_{\mu,F} = 9999$.

3.3. Transmission loss

The transmission loss presented in this thesis is calculated with the script '*computeTL.py*' (Bottero, 2015) with some minor changes made to adapt it to multiple receiver sets and to avoid command line input arguments. The script uses Equation (45) in Section '*2.6. Transmission loss*' to calculate the loss, where $E(\boldsymbol{x})$ is the discrete Fourier transform of the amplitude, and E_0 is the reference amplitude measured at the reference frequency by interpolation. All transmission loss curves are calculated for the reference frequency $50\ Hz$, also used as the dominant source frequency. The reference amplitude used to normalize the curve is measure from the first receiver in each receiver set. As the transmission loss is calculated from the total seismogram, the contribution of all waves recorded at each receiver is included.

3.4. Depth-dependent sound velocity profiles

The distribution of sound velocity in the ocean affects the propagation pattern of acoustic waves. The sound speed profile is a function of temperature, salinity, and pressure. In the Arctic Ocean, the lowest sound velocities are found in the top of the water column, and the vertical sound velocity profile increases with depth as salinity, temperature and pressure increases with increasing water depths (Jensen et al., 2011, pp. 3, 27). This increase in velocity with depth results in an upwards refracting sound speed profile in the whole water column, characteristic of the Arctic Ocean (Hutt, 2012; Mikhalevsky, 2001; Urick, 1983, pp. 169-171).

In the built-in velocity profile in SPECFEM2D, a velocity and density are assigned to separate regions with different material properties. Therefore, the velocity and density profile within each region becomes homogeneous. However, external profiles can be used instead by setting the choice of model parameter to '*external*'. Then, implementing a depth-dependent velocity and density profile where the values vary with depth within the same region, requires reading in an external profile. In this thesis, this was achieved by creating a text file containing the different depths and the corresponding velocities and densities, and then writing a subroutine '*define_external_model.f90*' which reads in the velocity text file. The subroutine thereafter assigns those values to the corresponding elements in the domain.

The subroutine is written with the scripts '*define_external_model.f90*' (Komatitsch & Tromp, 2017) and '*routine_define_external_model.f90*' by Quentin Brissaud (personal communication, October 7, 2021) as a basis, where the latter was received in an e-mail from the author. The scripts are combined and modified to fit the models in this thesis. The subroutine first reads in and stores all external values for depth, velocity, and density, and thereafter loops through all elements and GLL points in the domain. All points which are located within the water layer are assigned the velocity and density that corresponds to the point where the depth in the domain is closest to the depth read in from the external velocity profile. All points in the ice are assigned to constant values, $v_{p,E} = 3500\ m/s$, $v_{s,E} = 1800\ m/s$ and $\rho_E = 900\ kg/m^3$.

3.4.1. A linearly increasing sound velocity profile

The first upwards refracting sound velocity profile introduced in the simulations, is a simplified profile with velocities linearly increasing with depth. The same velocity range as in Collis et al. (2016) is used, and the sound velocity profile increases from $v_{p,F} = 1482\ m/s$ at the surface to $v_{p,F} = 1525\ m/s$ at the bottom of the domain. The density profile is constant, $\rho_F = 1000\ kg/m^3$.

3.4.2. An Arctic sound speed profile from CTD-data

An Arctic sound speed profile is built with data from Chierici et al. (2021), collected by the cruise HK2018707 aboard the Research Vessel Kronprins Haakon, as part of the Nansen LEGACY project. Data collected at latitude 83.1303 and longitude 31.7093 was chosen to create the Arctic sound speed profile. The data consists of 12 measurements measured at the station SICE1 on August 17th, 2018 (Table 2). The total bottom depth in the area is 3827 m, but the data was collected between 10.4 and 499.7 m depth. There is no direct measurement of the sound speed, but as salinity, temperature and pressure are major parameters controlling the sound velocity, those will be used to calculate the profile.

Yr	M	D	Hr	Lat [deg.N]	Lon [deg.E]	Max depth [m]	Depth [m]	Pre [dBar]	Sal [pss-78]	Temp [deg.C]
2018	8	17	0	83,13033333	31,70933333	3827	493,7265722	499,651	34,93	1,5196
2018	8	17	0	83,13033333	31,70933333	3827	395,8486388	400,503	34,9233	1,8
2018	8	17	0	83,13033333	31,70933333	3827	297,1209153	300,542	34,9167	1,9511
2018	8	17	0	83,13033333	31,70933333	3827	197,6646636	199,892	34,8995	2,0742
2018	8	17	0	83,13033333	31,70933333	3827	147,7137763	149,36	34,8743	2,0721
2018	8	17	0	83,13033333	31,70933333	3827	119,1505274	120,47	34,8158	1,6829
2018	8	17	0	83,13033333	31,70933333	3827	89,1009248	90,081	34,7115	0,9301
2018	8	17	0	83,13033333	31,70933333	3827	59,42768551	60,077	34,4211	-1,693
2018	8	17	0	83,13033333	31,70933333	3827	40,84559575	41,29	34,3569	-1,706
2018	8	17	0	83,13033333	31,70933333	3827	29,50679191	29,827	34,2035	-1,6371
2018	8	17	0	83,13033333	31,70933333	3827	18,97260421	19,178	33,6457	-1,4977
2018	8	17	0	83,13033333	31,70933333	3827	10,32840677	10,44	33,4183	-1,4344

Table 2. *The raw data collected by HK2018707 August 17th, 2018 (Chierici et al., 2021) used to create the Arctic sound speed profile for the simulations.*

First, the water column profiles were extrapolated to fully cover the area from 0 to 515 m depth. Then, the 4 measurements collected between 10.3 m and 40.8 m depth were used to extrapolate the dataset from 10.3 m depth to the surface. To extrapolate the profile from 493.7 m depth to 515 m depth, the two last measurements in the data set, collected at 395.8 and 493.7 m, are used.

The profile was extrapolated by using a least squares polynomial fit to find the polynomial coefficients with the NumPy module '*numpy.polyfit*' after which '*numpy.poly1d*' was used to construct the polynomial. The extrapolated depth, pressure, salinity and temperature profiles stretching from 0 m to 515 m depth were thereafter interpolated with the SciPy module '*scipy.interpolate.interp1d*' to create continuous arrays to be used further on.

The density profile is calculated from the CTD-measurements following EOS80 as described in (Fofonoff & Millard Jr, 1983), which with a complex formula calculates the density in kg/m^3 as a function of practical salinity, temperature, and pressure. The ESO80 is valid for practical salinities in the range $[0,42]$, temperatures in range $[-2°C, 40°C]$ and pressure in range $[0\ \text{dBar}, 10000\ \text{dBar}]$.

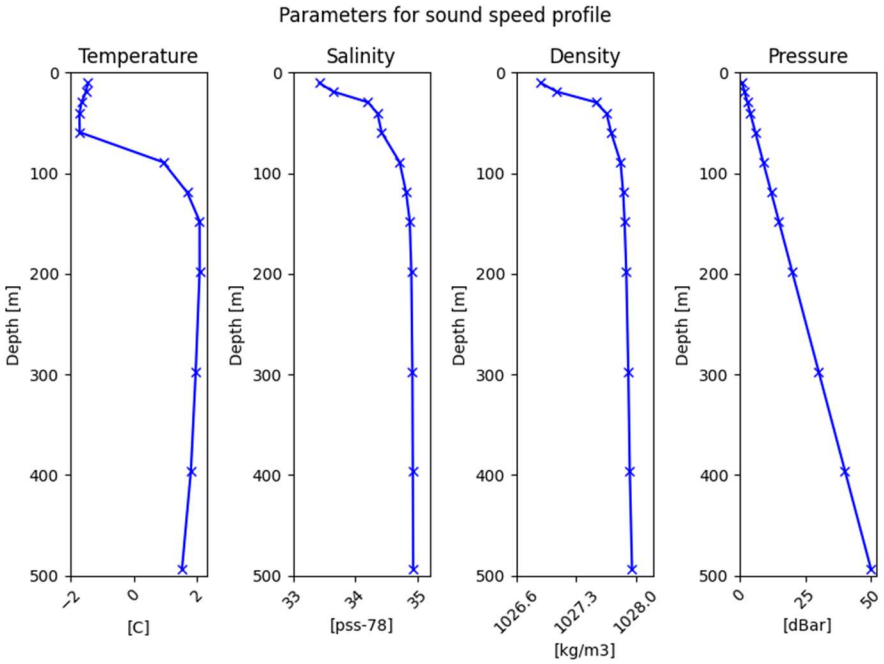

Figure 11. *Water column profiles for temperature [°C], salinity [pss-78], density [kg/m^3] and pressure [dBar] used to calculate the Arctic sound speed profile used in the simulations.*

The Arctic sound speed profile was calculated from the water column data shown in Figure 11, by (Brekhovskikh & Lysanov, 2003, p. 1):

$$c = 1449.2 + 4.6T - 0.055T^2 + 0.00029T^3 + (1.34 - 0.01T)(S - 35) + 0.016z \qquad (52)$$

Here is T temperature in °C, S salinity in parts per thousands and z depth in meters. The resulting Arctic sound speed profile is shown in Figure 12.

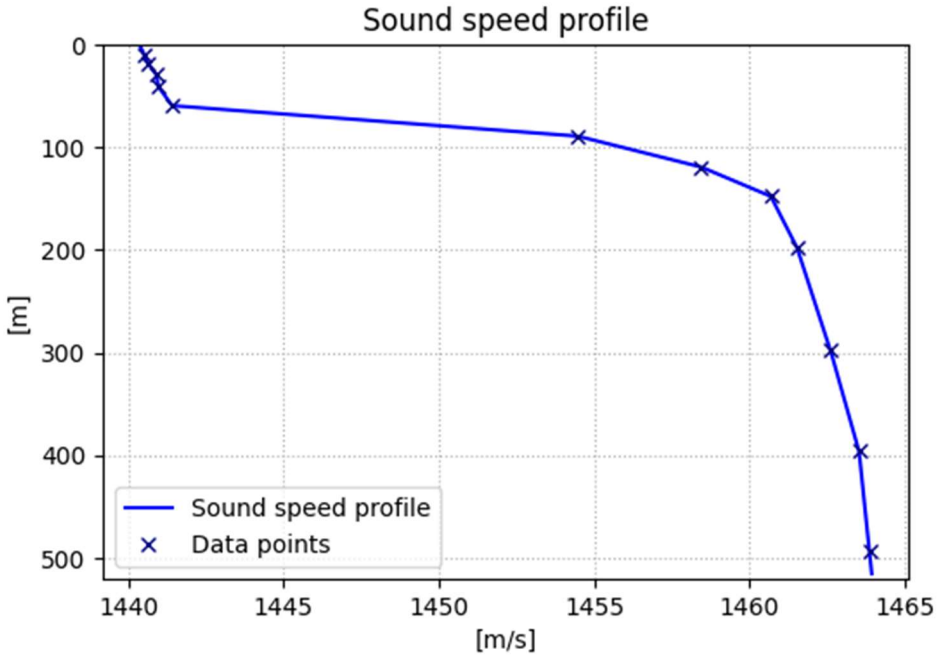

Figure 12. *The Arctic sound speed profile resulting from the data in Table 2.*

Figure 13 shows the homogeneous (blue line), the linearly increasing (pink line) and the Arctic sound speed profile (light blue) used in the simulations.

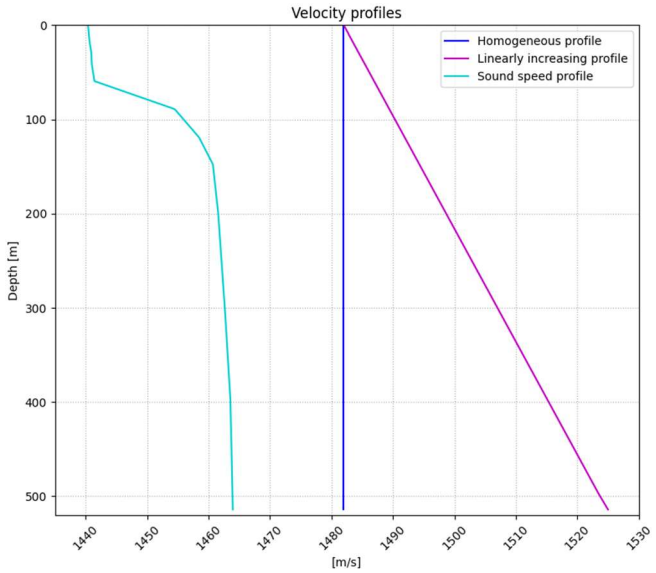

Figure 13. *The three velocity models used in the simulations.*

3.5. Ice ridges

The sea ice in the Arctic Ocean affects acoustic propagation in the area. The amount of thicker multi-year ice has decreased during later years and most of the sea ice in Arctic is now thinner, younger ice (Meredith et al., 2019) and the annual mean thickness has decreased from 2.12 to 1.41 m during 2000-2012 The characteristics of ice ridges in multi-year and first-year ice differ, and the ridges in younger ice are found to be shallower and steeper (Wadhams & Toberg, 2012).

The ice ridge model in the thesis will be based on the work by Metzger et al. (2021), using their profile for an average pressure ridge cross-section. They analyzed more than 64 000 ice ridge profiles identified from upward-looking sonars set up in the Chukchi and Beaufort Sea in the years from 2009 to 2013 and found that the average shape of an ice ridge is more concave or cusped, in contrast to the previously generally modeled triangular shape. The concavely shaped idealized profile of an average pressure ridge of Metzger et al. (2021) shown in Figure 14 will be used in this thesis.

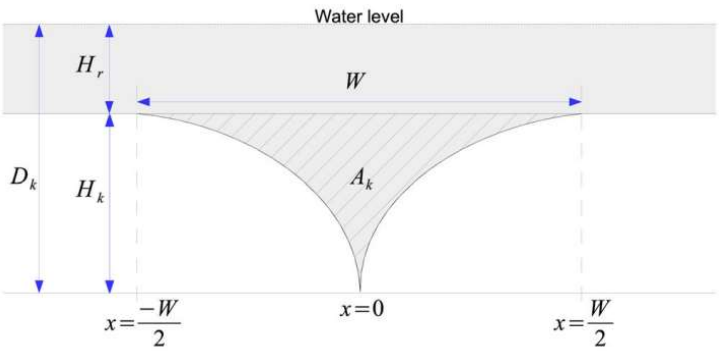

Figure 14. *The cross-section of a pressure ridge. Figure from Metzger et al. (2021).*

In Figure 14, H_r is the depth of the level ice surrounding the ice ridge, H_k the maximum depth below the level ice, A_k is the area of the cross-section of the ice ridge below the level ice and W is the width.

Metzger et al. (2021) fitted a curve to this average shape of a concave ice ridge cross-section profile $D(x)$ with:

$$D(x) = H_r + H_k e^{-(\frac{H_r}{\lambda}x)} \tag{53}$$

Here λ is a characteristic scale and x, which is taken to be positive in the equation, is the distance away from the tip of the ridge. Metzger et al. (2021) have also created a table summarizing the ridge keel and profile fitting parameters for their statistical fit to observations. The models will partly be based on those numbers.

3.6. Ice roughness

The sea ice cover in the Arctic Ocean impacts wave propagation as the upwards refracting sound speed profile causes the acoustic wave to interact continuously with the underside of the ice, and ice roughness will therefore be implemented in the models. The upper ice surface, where ice is in contact with air, is chosen to be kept smooth in all models, and instead, the focus will be on implementing a rough water-ice interface. When the ice interface is mentioned further on, it refers to the ice-water interface in case nothing else is explicitly said. When mentioning depth, it always refers to the depth of the whole domain, where zero depth is at the free surface.

The main ice roughness model is built based on the work by Hope et al. (2017). They investigated how sea-ice roughness impact acoustic propagation in a long-range setting and the suitability of the seismo-acoustic wavenumber integration package OASES (Schmidt & Jensen, 1985) to model this. For this purpose, they gathered statistical data to model the sea ice roughness, and therefore calculated the characteristic correlation length for a segment of ice in the Nansen basin, at 84.1°N and 25.2°E. The data they used was collected in 2005 by upwards-looking sonars, distributed by the National Snow and Ice Data Center (National Snow and Ice Data Center, 1998). They found the characteristic correlation length to be 19.1 m, with a corresponding RMS value of 1.52 m and a mean thickness of 2.4 m.

Hope et al. (2017) performed simulations in OASES, which requires the RMS value to be small compared to the wavelengths. Therefore, the real RMS value of 1.52 m was too high, and instead they used an RMS value of 0.6 m. Hope et al. (2017) point out that this RMS is an underestimate, even if melting seasons, a thinning of the sea ice, and a decrease in multi-year ice in the region since the measurements they used were made in 2005 makes a somewhat lower RMS value likely.

The main ice roughness model in this thesis is built with the characteristic correlation length found by Hope et al. (2017). Also, the same RMS value of 0.6 m is used. As this RMS value was numerically suitable for OASES, it will be assumed to work well in SPECFEM2D too. Hope et al. (2017) performed their simulations in OASES, which model ice thickness as a Gaussian function around the mean. Therefore, the roughness amplitude spectrum for the rough ice model in this thesis is generated with a Gaussian power spectrum:

$$f(k) = \sqrt{A_0 e^{\frac{-(2\pi L)^2 k^2}{2}}} \tag{54}$$

Here A_0 is amplitude, L the characteristic correlation length and k wavenumber. Then, the inverse Fourier transform of the power spectrum is also a Gaussian:

$$F(x) = \frac{1}{2\pi L} A_0 e^{-\frac{x^2}{2(2\pi L)^2}} \tag{55}$$

The spectrum was then created in python as a complex wave spectrum with an amplitude equal to the amplitude spectrum in Equation (54) and a random phase. An inverse Fourier transform is applied with the NumPy module '*numpy.fft.ifft*'. Finally, the autocorrelation of the profile has been calculated to verify it satisfies Equation (55).

The rough ice interface is created simply by adding the ice roughness to the smooth ice interface. To avoid very thin ice, all points where the ice thickness of the rough ice layer became less than 1 m were redefined to be 1 m.

3.7. Ice models in the simulations

Introducing an ice layer to the models practically means to introduce a layer at which the acoustic waves can be reflected, transmitted, and refracted. The impedance in a medium depends on its material properties in terms of density and velocity and determines the amount of reflection and transmission at the interface (Rossing, 2007, pp., p. 211-212). The amount of reflection and transmission at an ice-water interface depends on the frequency of the wave and the material properties of the ice interface (Diachok, 1976). Along with a simple model consisting of only one water layer, various ice models will be introduced in the simulations to investigate the effect different water-ice interfaces have on acoustic propagation, both in the ocean and in the ice layer itself.

3.7.1. Plain models

For the first part of this thesis, three simple models are introduced. The first model (Model 1) consists of an infinite water layer only, i.e., a fluid half space. The second model (Model 2) consists of one range-independent 3 m thick ice layer above a fluid half space. Finally, the third model (Model 3) has a range-dependent ice layer with a thickness linearly decreasing with 0.25 m per km, from 3 m thickness on the left-hand side of the domain to 2 m thickness on the right-hand side of the domain, above a fluid half space. This is the same ice configuration as used in Collis et al. (2016). However, the sea floor in Collis et al. (2016) is removed in this thesis, in order to focus on sound interactions with the sea ice, without the disturbances from bottom reflected sound. The absence of a sea floor is not unrealistic, since the upwards refracting sound speed profile in the Arctic Ocean means that there is usually little bottom interaction (e.g., Jensen et al., 2011, p. 140).

3.7.2. Ice models with ice ridges and ice roughness

Two ice models containing two ice ridges with different maximum ridge keel depths are created, and the location of the deeper and shallower ice ridge will be varied. One half cross-section of each ridge is created at a time with Equation (53), and the full ridge cross-section is created by mirror-imaging the first part. Consequently, the ice models are symmetric around the ridge keel. The values chosen in Equation (53) are based on the statistical values in Metzger et al. (2021).

The two ice ridges are located 996 m and 2992 m from the source. Each ice ridge is created with Equation (53), and the whole ice model in the domain is created by concatenating the multiple sections of ice. This results in an ice model containing two ice ridges and a smooth ice-water interface. The rough ice models are created as explained in Section *'3.6. Ice roughness',* with a correlation length of 19.1 m and an RMS value of 0.6 m. Because the roughness is created with a random phase and the full ice model is built by concatenating the ice sections surrounding each ice ridge, there is one roughness profile for the first and one roughness profile for the second part of the domain. The autocorrelation functions associated with the ice roughness profile for the first and second part of the domain are shown in Figure 15.

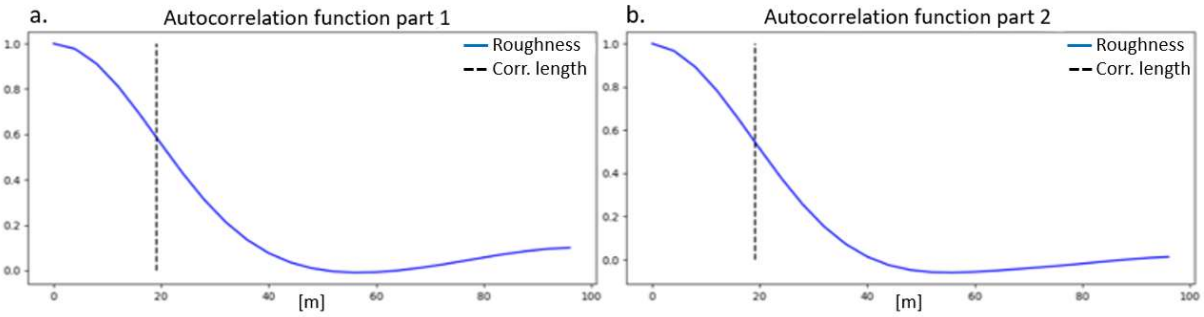

Figure 15 *The autocorrelation function for the spectrum used to create the ice roughness in the models. Figure 6a. shows the autocorrelation function for the first part and Figure 6b. for the second part of the domain.*

The deeper ice ridge has a maximum depth below the level ice of $H_k = 5.1$ m and a characteristic scale $\lambda = 39.8$. The shallower ridge has a maximum depth below level ice of $H_k = 2.9$ m and a characteristic scale $\lambda = 19.6$. Thus, the deepest ridge is 7.1 m deep, while the shallower ridge has a total depth of 4.9 m. The thickness of the level ice around the ridge is chosen to be the same for both ridges, $H_r = 2$ m. This is a much lower value than what is given in the statistical values in Metzger et al. (2021), but because the region of interest for the imitated domain is the nearby surroundings of the Nansen Basin in the Arctic Ocean a thinner level ice is chosen. The mean thickness for the ice segment that Hope et al. (2017) used to find the characteristic correlation length (Section '*3.6. Ice roughness*') was 2.4 m. The amount of old multi-year ice in the Arctic Ocean is decreasing, and more first-year ice covers the ocean nowadays. Along with the decreasing age of the Arctic sea ice, the ice thickness decreases (Maslanik et al., 2007; Stroeve & Notz, 2018; Wadhams & Toberg, 2012).

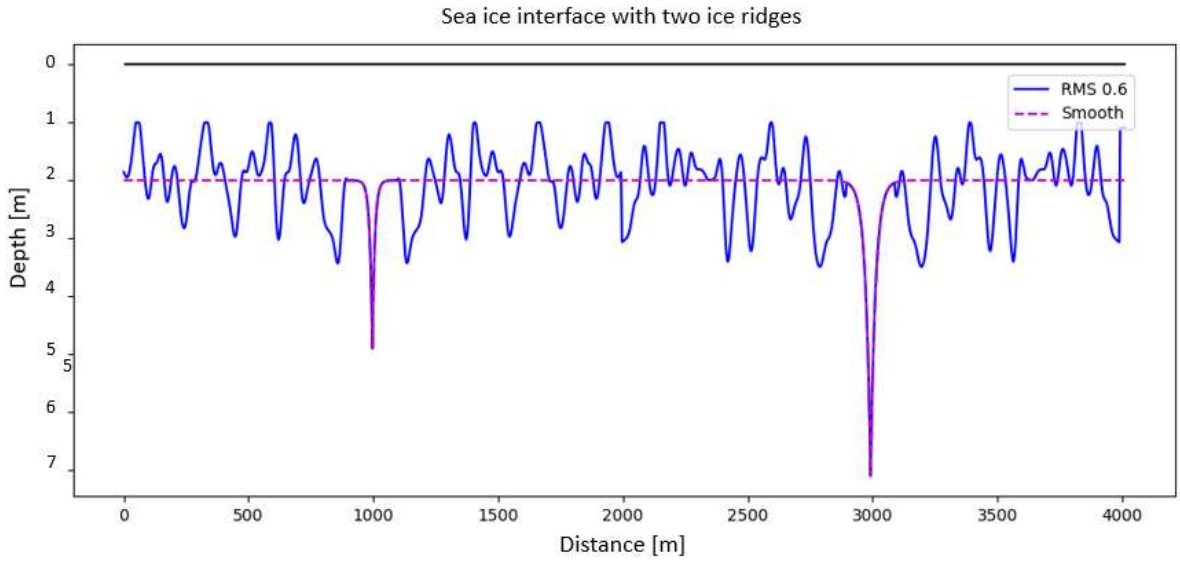

Figure 16. *The ice model with a shallower (4.9 m) ice ridge 996 m into the domain and a deeper (7.1 m) ice ridge at 2992 m for a model with a smooth (dashed pink line) and a rough (blue solid line) ice-water interface. The symmetry around the ridge keel tips is clearly visible.*

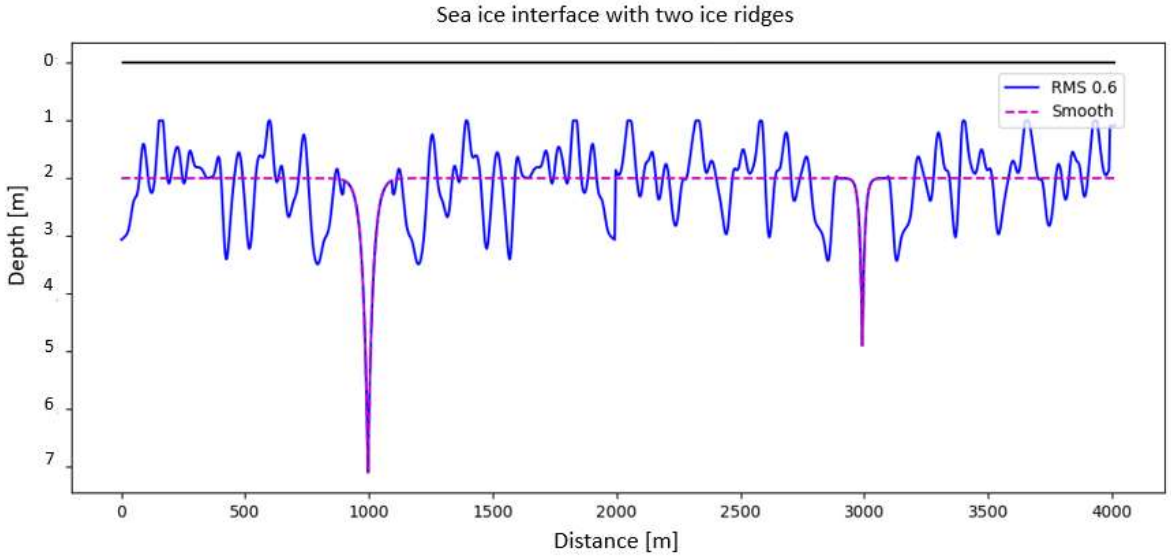

Figure 17. *Ice models as in Figure 16, but with opposite location of the deeper respectively shallower ice ridge.*

A total of 4 ice models with ice ridges are created. Two models, one with a smooth and one with a rough ice interface, have the shallow ice ridge in the first part and the deeper ridge in the second part of the domain (Figure 16). For the other two models, the only difference is that the ridge locations are reversed (Figure 17). As the rough ice models were created by adding ice roughness to the smooth ice interfaces after the ice ridges were already created, the total depth of the ice ridges could differ between the smooth and rough ice models. To avoid this, the ice roughness was removed 50 m before and after each ice ridge. This also ensured that the ice thickness did not become too thin in close connection to the ridges. This can be seen in Figure 16 and Figure 17, as the blue and pink lines coincides around the ridge keels.

Chapter 4
Implementation and validation

The aim is to model the acoustic wave propagation in the coupled solid-fluid domain imitating the Arctic Ocean with the open-source spectral elements package SPECFEM2D. The 2.5D version developed by Bottero (2018) is mainly used for the simulations.

4.1. Spectral element parameters

All simulations are forward simulations with a second order Newmark time-stepping scheme. 9 control nodes per element are used to characterize the model geometry, and the SPECFEM2D default value of polynomial degree 4, and thus, 5 GLL points in each direction are used in the simulations (Centre national de la recherche scientifique & Princeton University, 2021). The PML thickness, given in a number of elements, was set to 5. Most of the simulations are done in 2.5D, which is easily switched on by changing the axisymmetric parameter to true in the input parameter file. However, a few simulations were initially performed in 2D.

4.2. Source function

The source in all simulations is located within the water and is specified by its displacement potential. A Gaussian is chosen for the source time function. As we have $dP = -\ddot{\chi}$ (see Section *'2.1.2. Fluid region*'), the choice of a Gaussian time function for the source leads to a Ricker wavelet for the pressure seismograms. The standard definition of a Ricker is used in SPECFEM2D, given as (Centre national de la recherche scientifique & Princeton University, 2021):

$$R(t) = (1 - 2(\pi f_0 t)^2)e^{-(\pi f_0 t)^2} \tag{56}$$

where the dominant frequency of the source is denoted f_0. The corresponding Gaussian function is then defined as:

$$G(t) = -\frac{e^{-(\pi f_0 t)^2}}{2(\pi f_0)^2} \tag{57}$$

A dominant source frequency of $f_0 = 50\,Hz$ and an amplification factor of 10^9 is used for all simulations.

The source in the axisymmetric 2.5D simulations must be placed on the symmetry axis to be a point source. If the source is placed elsewhere in the domain, it will instead take a circular shape, as the 2D

domain is rotated around the symmetry axis (Centre national de la recherche scientifique & Princeton University, 2021). The source in the 2D simulation is a line source.

4.3. Meshing with the internal mesher

The mesh is created with the internal mesher in SPECFEM2D. The range of the domain and number of elements in the horizontal direction is defined within the input parameter file. The depth of the domain and the number of elements in the vertical direction is defined within the interface input file, as well as the number of vertical layers. The interfaces defining the boundaries of each layer are defined by a chosen number of sets of (x, z) points. Each interface must be defined with increasing values in the horizontal direction.

Therefore, the total number of horizontal elements is the same everywhere in the domain, as well as the total number of vertical elements. The number of vertical elements can vary within each layer. It is recommended to use a rather regular grid in the simulations to ensure that the sampling of the wavelength is relatively consistent in the domain (Chaljub et al., 2007). This is both to avoid unnecessarily large memory use and CPU time from oversampling, and because the grid size directly affects the choice of time step determined by the Courant-Friedrichs-Lewy stability criterion.

The different regions in the domain are defined within the input parameter file as areas of a certain type of material property, where the material type is defined by assigning a material type to a set of element grid cells. The velocity, density, and attenuation parameters in the simulations will be defined in two ways in this thesis. Some simulations will use homogeneous velocity and density profiles defined by the built-in velocity model in SPECFEM2D. Then, the parameters of a material type are defined within the input parameter file and uniformly read into the whole set of elements assigned to this material type. Some simulations will use an external velocity profile, and the parameters are instead read in from an external file and the GLL points are assigned a value one by one, creating a depth-depending profile. In this case an external depth-dependent velocity and density profile will be assigned to the water layer, whilst the velocity and density profile in the ice layer will be kept constant. The attenuation profiles will be constant in the whole domain, as defined in Section *'3.2. . Attenuation and Quality factors*'.

As the number of horizontal elements is the same in the whole domain and the number of vertical elements in each layer is defined within two interfaces, this can somewhat narrow the ability to fully adjust the grid size to large velocity variations in the domain. It will also affect layers that have sharp variations in thickness horizontally, as the number of elements will be the same within the whole layer and the grid cells affected by large thickness variations will be stretched or compressed at those locations.

In SPECFEM2D, the perfectly matched layers are turned on or off within the input parameter file. The thickness of the absorbing layers is given in a number of elements, which means the total thickness of the layer will be given by multiplying the number of PML elements by the length of the element grid cell in the direction of question. The perfectly matched layers are located within the defined domain. The length, depth, and number of elements corresponding to the chosen absorbing layers must be added to the domain dimensions if one wishes to keep the desired domain dimensions after perfectly matched

layers are activated. In 2D simulations, the perfectly matched layers must be placed on the bottom, left and right side of the domain to simulate a boundless domain, while in the 2.5D simulations they must be placed on the bottom and right side only.

4.4. Stability and points per wavelength

The Newmark time-stepping method is conditionally stable with the Courant-Friedrichs-Lewy (CFL) criterion as explained in Section *'2.3.5. Courant-Friedrichs-Lewy stability criterion'*. The global maximum CFL stability condition is calculated from the maximum P-wave velocity in the model and the minimum distance between two GLL-points. The minimum distance between two collocation points in a simulation where $N = 4$ is 17.27 % of the shortest edge of the smallest grid cell in the simulation. In SPECFEM2D, The CFL criterion is recommended to be around or below 0.5.

The number of points per wavelength can be used to control how well the chosen mesh samples the wave field. The recommended threshold value is 4.5 points per S-wavelength in solid media and 5.5 points per P-wavelength in fluid media. If the number of points per wavelength exceeds those values, the program will use unnecessary memory and CPU time, while less points than the recommended threshold value will result in poor calculations (Centre national de la recherche scientifique & Princeton University, 2021).

Simulations in 2.5D will require approximately 25 % more points per wavelength in comparison to a 2D simulation due to the different quadrature that is used (Centre national de la recherche scientifique & Princeton University, 2021), which then would be approximately 5.6 points per S-wavelength in an elastic region and 6.9 points per P-wavelength in an acoustic region.

4.5. Validation against OASES and an exact solution

The intention of the first part of the project was to build a domain and three models using the same dimensions and parameters as in Collis et al. (2016), who used a domain with a 100 m thick water layer over a 10 km range to obtain results for predicted transmission loss curves. The source in their experiment was a 50 Hz source placed at 30 m depth, and the transmission loss curves were calculated for a receiver at 30 m depth. They used three models; one model with a water layer only, one model with a 3 m thick ice layer, and one model with an ice layer with a thickness linearly decreasing from 3 m thickness to 0.5 m thickness over 10 km.

Therefore, three models similar to the ones used in Collis et al. (2016) were set up; one model with only water (Model 1), one model with a range-independent ice layer of 3 m thickness (Model 2) and one model with a range-dependent ice layer (Model 3). The models are described in Section '*3.7.1. Plain models'*. However, the sea floor is removed in this thesis and is instead replayed by an absorbing layer. Also, the horizontal range was shortened down to 4 km. This was done to decrease the simulation domain, and as the results in Collis et al. (2016) show a stable trend from a little before 4 km and throughout the rest of their domain a range of 4 km appeared to be a good choice.

Model 1 and Model 2 are used to validate SPECFEM2D against the wavenumber integration package OASES and an exact solution. Trond Jenserud at the Norwegian Defence Research Establishment (FFI) contributed with the reference curves obtained by simulations in OASES and calculations of the exact solutions. Those were compared to the results obtained in SPECFEM2D (Figure 18, Figure 19, Figure 24, and Figure 27).

The exact solution used to validate the models is an image (ray) solution for a fluid half-space with a pressure free upper boundary, in which the wave field is represented by the discrete arrivals of reflections from the boundaries. More details are given in Tolstoy and Clay (1966) and in Appendix A.III. '*The image solution used for model validation*'.

4.5.1. Validation of the domain dimensions

As explained in Section '*4.3. Meshing with the internal mesher*', the choice of grid size in the horizontal direction will affect the choice of grid size in the vertical direction, as the aim is a regular mesh with somewhat rectangular or squared cells as standard for a uniform domain without any sharp changes in the vertical layers. The grid size was chosen to be somewhat 3x3 m due to an ice thickness of between 2 m and 3 m in Model 2 and Model 3. However, some elements are slightly stretched or compressed when the ice thickness decreases with distance in Model 3. In Model 1 and Model 2 the grid will be 3x3 m.

The initial choice of the domain was 4000x100 m, including the PMLs, making the domain consist of 1333 elements in the horizontal direction and 33 elements in the vertical direction. As the PMLs are included in this domain and the simulation were run with a PML thickness of 5, the outer 5 elements on the bottom and right side of the domain constituted the absorbing layer. The models were run with the parameters presented in Table 3 and a source with a dominant frequency of 50 Hz at 30 m depth. The attenuation was set to zero for the initial runs.

	FLUID REGION	SOLID REGION
COMPRESSIONAL VELOCITY v_P	1482 m/s	3500 m/s
SHEAR VELOCITY v_S	-	1800 m/s
DENSITY ρ	1000 kg/m^3	900 kg/m^3

Table 3. *Parameters for the simulations.*

Comparing the results obtained in SPECFEM2D to the reference curves from OASES and the image (ray) solution, the results were observed to be very accurate up to approximately 500 m range, after which an extra pulse behind the main pulse became visible. Additionally, this extra pulse was observed to grow with increasing distance.

The first attempt to find out what caused this distortion was to change the grid size to a finer and coarser grid, to check whether numerical dispersion could be the reason. The domain dimensions were kept the same, but the absorbing layer was moved outside of the domain. This is because the thickness of the absorbing layer depends on the grid sizes, and to keep the domain the same when trying different grid sizes, this was necessary. First, Model 1 was run with a finer grid size of 1x1 m, which only caused the

noise pulse to become worse. Running it with a coarser grid size, 5x5 m and 10x10 m, did not improve the result either.

The next attempt was to keep the grid size 3x3 m as before but instead extend the depth of the domain. This was done as it was suspected that the extra pulse could be caused by a reflection from the absorbing layer at the bottom of the domain. Extending the domain depth to 200 m depth, with 67 elements in the vertical direction excluding the 5 absorbing elements, did improve the result but was not enough. However, for 500 m depth, with 167 elements in the vertical direction excluding the 5 absorbing elements, the result was very good at x = 1910.5 m when comparing them to the exact solution. Figure 18 shows the wave pulse recorded at a seismogram at 30 m depth 1910.5 m into the domain for different depths.

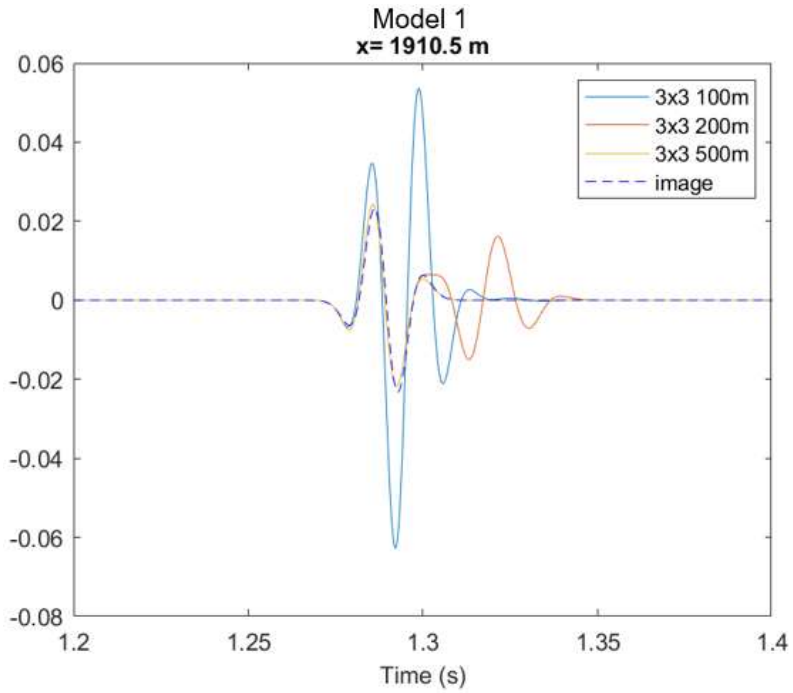

Figure 18. *The wave pulse for a seismogram at 30 m depth 1910.5 m into the domain for a domain with 3x3 m grid cells for 100 (blue), 200 (orange) and 500 (yellow) m depth, compared the image solution (dashed). The wave pulse significantly improves with increasing depth of the domain. Figure from Trond Jenserud, Norwegian Defence Research Establishment, based on simulations from SPECFEM2D and the image solution (personal communication, March 17, 2022).*

By increasing the receiver range to 2955 m (Figure 19) an extra pulse arriving after the main pulse was observed, while the main pulse had the correct shape. This extra pulse is interpreted as the reflection from the PML. For shallower models, this noise pulse interferes with the main pulse to create the observed pulse distortion in Figure 18.

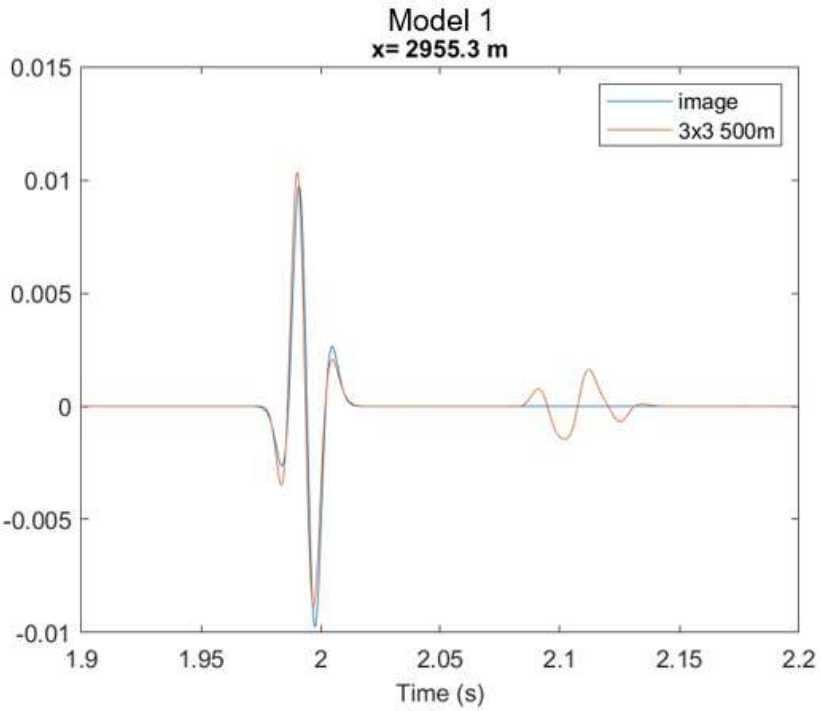

Figure 19. *The pulse at x = 2955.3 m for Model 1 (orange line) with only water in a 500 m deep domain compared to the exact solution (blue line). The extra pulse arriving after the main pulse is still small but is increasing in amplitude with propagation distance. Figure from Trond Jenserud (personal communication, March 17, 2022).*

The imperfect behavior of the PML is visualized in Figure 20 and Figure 21, which show the wave field figures created in SPECFEM2D for $t = 1.40$ and $t = 2.09$ s, respectively.

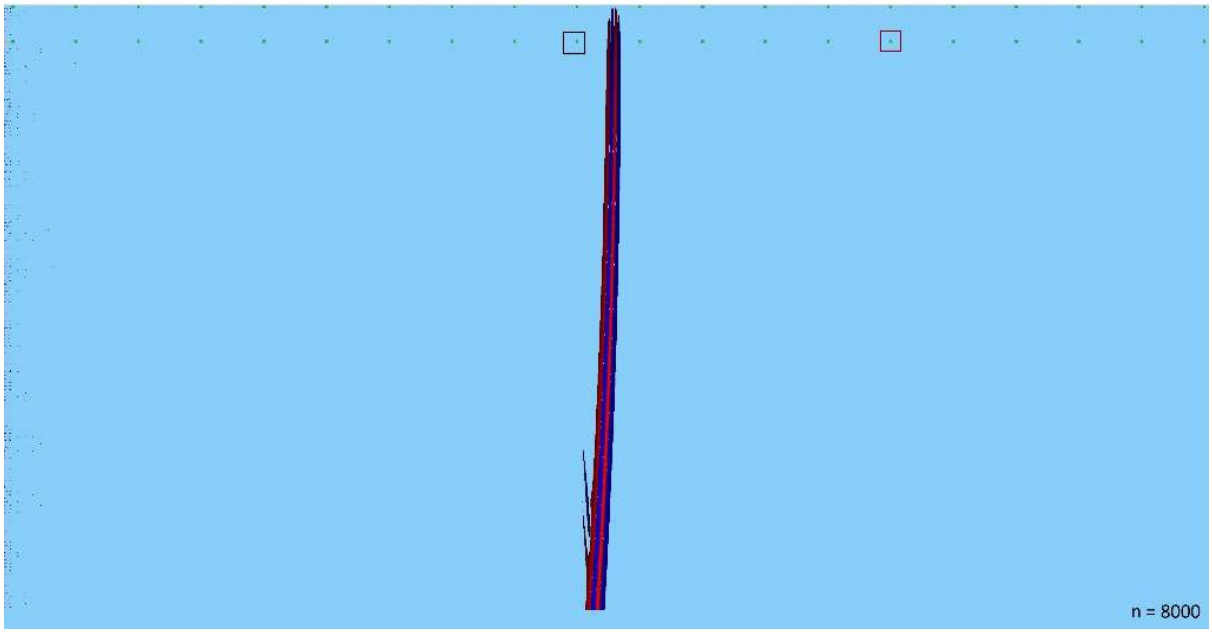

Figure 20. *Figure created by SPECFEM2D as part of the output, showing the wave field in pressure for Model 1 at time* $t = 1.40$ *s. A small reflection is visible at the bottom. The black square shows the receiver at* $x = 1910.5$ *m, and the red square the receiver at* $x = 2955.3$ *m. Note that there is no scale for the pressure.*

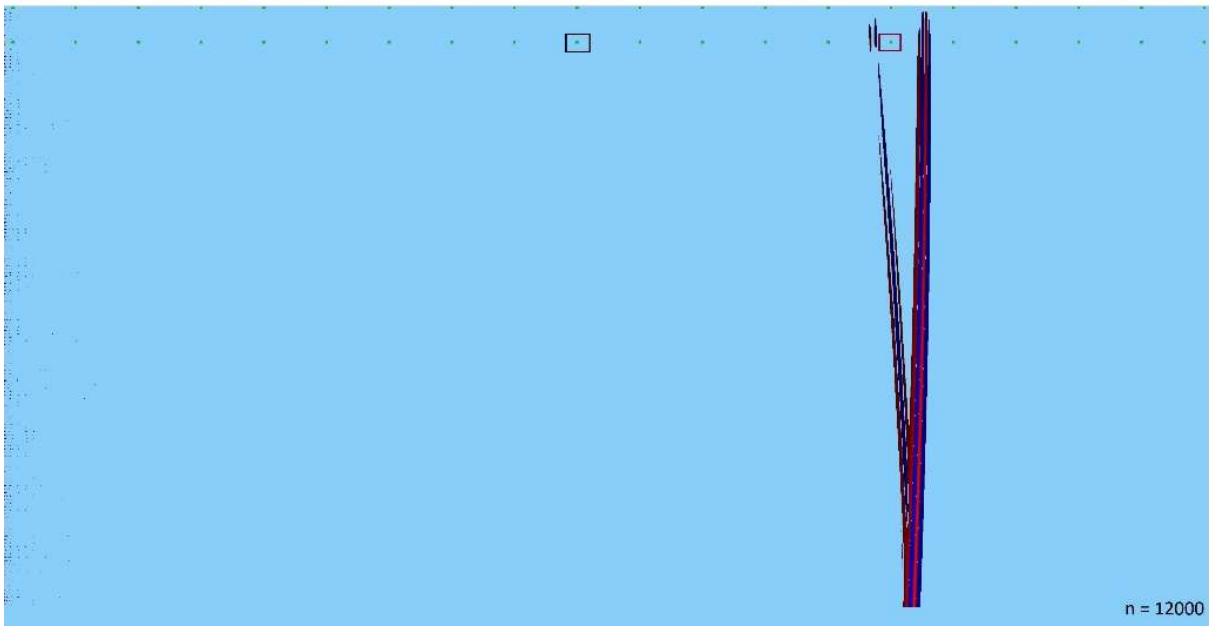

Figure 21. *The wave field as in Figure 20 , but for* $t = 2.09$ *s. The reflection from the bottom has grown larger, relative to the main wave propagating directly through the water.*

A small reflection growing from the bottom of the wave can be observed already halfway into the domain, and the reflection is observed to continue to grow with increasing distance. The model domain is very elongated, and the wave is propagating almost parallel with the bottom boundary. Despite the efficiency of the perfectly matched layers in most situations, they do not seem to fully remove the reflections in this case, and this appears to be the most likely explanation for the noise pulse growing with distance in the simulations. Adding a sea floor might have helped solve the problem with bottom reflections from the absorbing layer, since the reflections from the sea floor might mask the weaker reflection from the absorbing layer. However, absorbing layers were used to remove the wave interactions at the sea floor to focus on the wave interactions with the sea ice layer. Also, the aim is to model wave propagation in the deep Arctic Ocean, and a depth of approximately 4 km would be required. This would significantly increase the domain and the calculation time.

Figure 22 shows the transmission loss for Model 1 at 30 m depth for a domain with 100 m and 500 m depth. The transmission loss curves are observed to correspond to each other until about 500 m into the domain, where they start to deviate. The loss curve for the domain with 500 m depth is decaying smoothly until about 2.3-2.4 km from the source, where it becomes uneven. This corresponds to what is observed in Figure 19 and Figure 21, where the extra pulse is growing in amplitude at the same time as we see a stronger reflection from the bottom of the domain. Figure 23 shows the wave field at time $t = 2.70$, showing how the reflection has reached the surface and is reflected downwards again. This might be what causes the irregularity in the last part of the transmission loss curve in Figure 22.

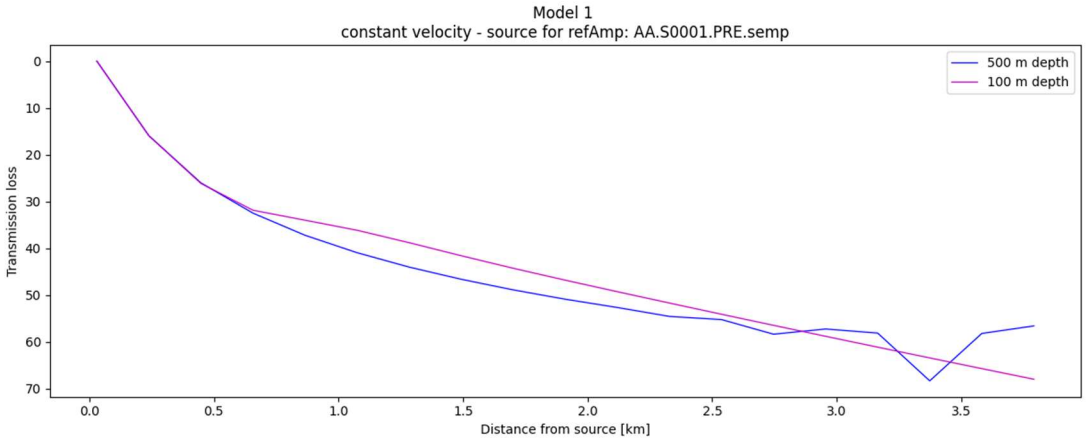

Figure 22. *The transmission loss for the domain with 100 m depth (pink) and 500 m depth (blue), for Model 1. For the 100 m deep model (pink line), a sharp change in the curve is observed right after 500 m. For the 500 m deep model (blue line), the curve decreases smoothly until approximately 2.5 km, after which it becomes more irregular.*

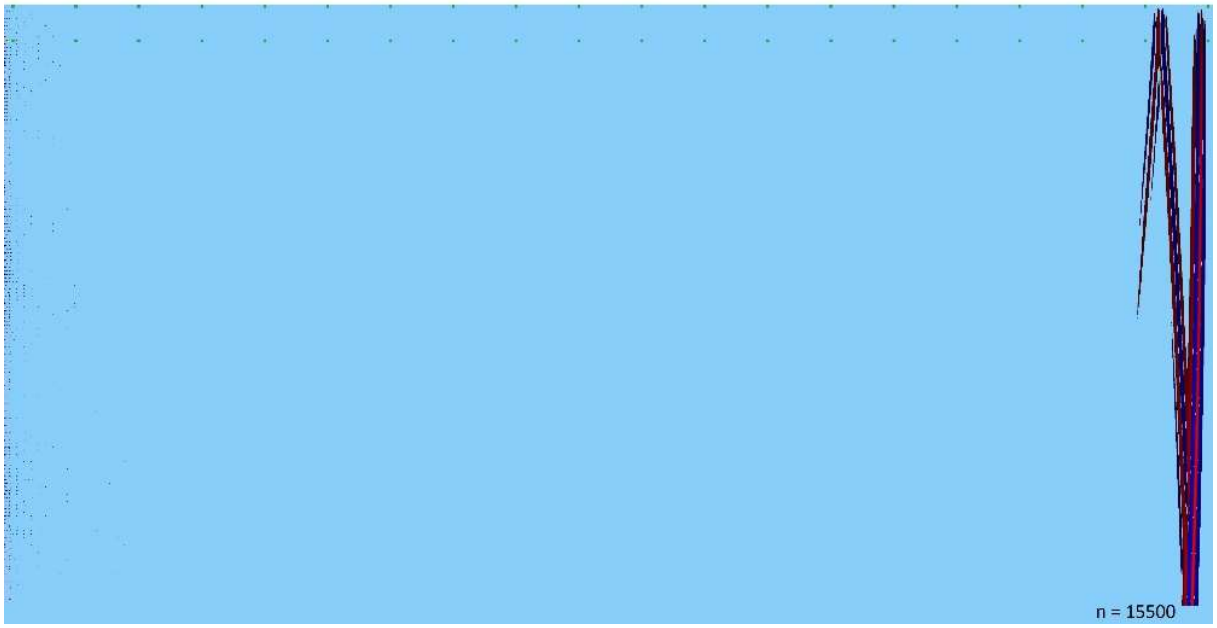

Figure 23. *The wave field for Model 1, here at time* $t = 2.70$ *s. The reflection has grown to reach the surface and is reflected downwards again.*

Model 2 also shows good correspondence between SPECFEM2D and OASES. Figure 24 shows that the wave form is correct, but there are some smaller deviations in both time and amplitude. The amplitude in OASES simulation is slightly larger for the pulse of the wave refracted from the wave propagating within the ice layer (first arrival) and seems to be slightly low for the wave pulse of the wave propagating directly through the water (second arrival), compared to the results obtained with SPECFEM2D. There also is a small pulse arriving later, just before 1.5 s in the SPECFEM2D model, which could be the extra pulse shown in Figure 19. Figure 25 shows the wave field in Model 2 at time $t = 1.34$ s. The wave propagating within the ice layer is approaching the last receiver, while the wave propagating directly through the water just passed the 10^{th} receiver at this point.

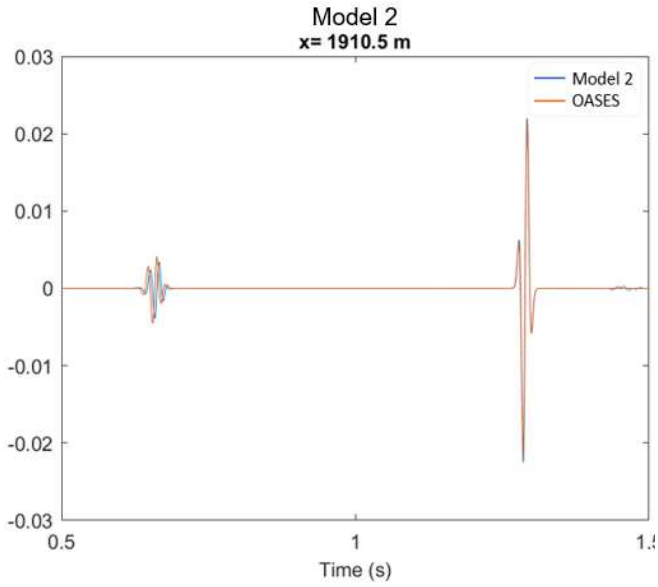

Figure 24. *Seismogram for Model 2 (blue line) compared to results obtained with OASES (orange line) for a domain of 500 m depth with a grid size of 3x3 m grid cells. Figure from Trond Jenserud based on the simulations in SPECFEM2D compared to results obtained with OASES (personal communication, March 17, 2022).*

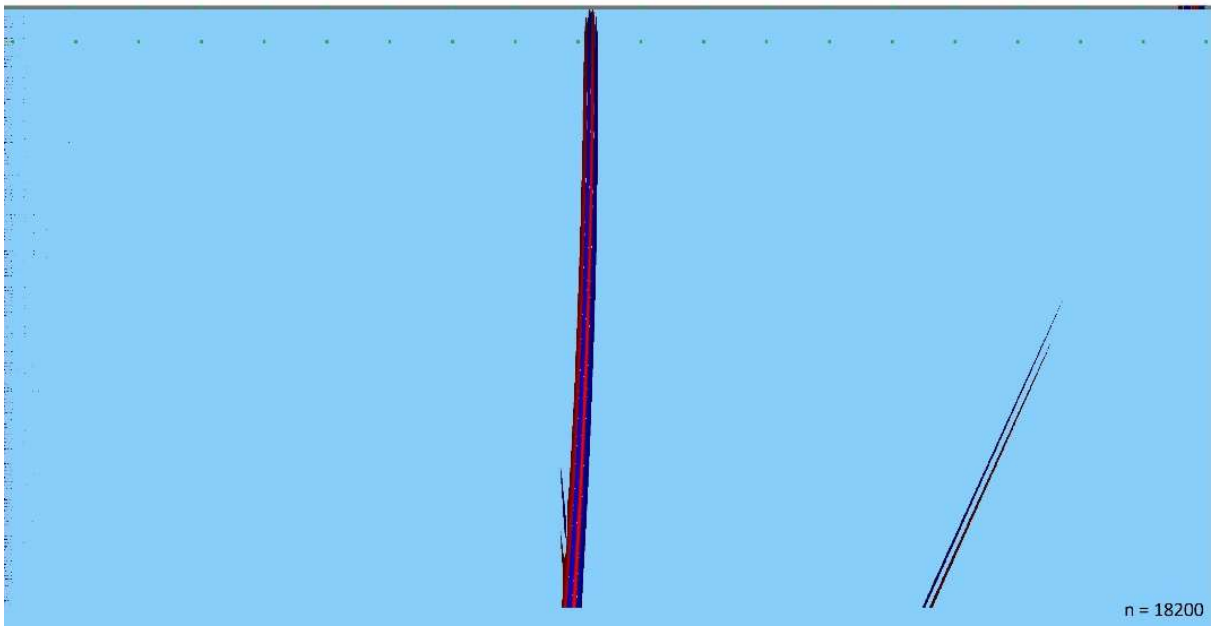

Figure 25. *The wave field for Model 2 at time* $t = 1.34$. *The wave propagating directly through the water has just past the 10th receiver located at* $x = 1910.5$ *m. The wave propagating within the ice layer has almost reached the end of the domain.*

The final domain (Figure 26) that will be used in the simulations has a water layer of 500 m above the absorbing boundary. It is chosen to be 4015x515 m and consists of 1338 elements in the horizontal direction and 172 elements in the vertical direction, including the absorbing boundaries. The element thickness of the absorbing layer is set to 5 elements, so the outer 5 elements of the bottom and right side of the 2.5D domain will be perfectly matched layers. Therefore, the actual domain size is 4000x500 m with 1333 horizontal and 167 vertical elements, when the PMLs are excluded. This size of a domain has shown to give good results when compared to the exact solution for Model 1, and to the OASES results for Model 2 until approximately 2000 m into the domain, after which the arising extra pulse must be kept in mind.

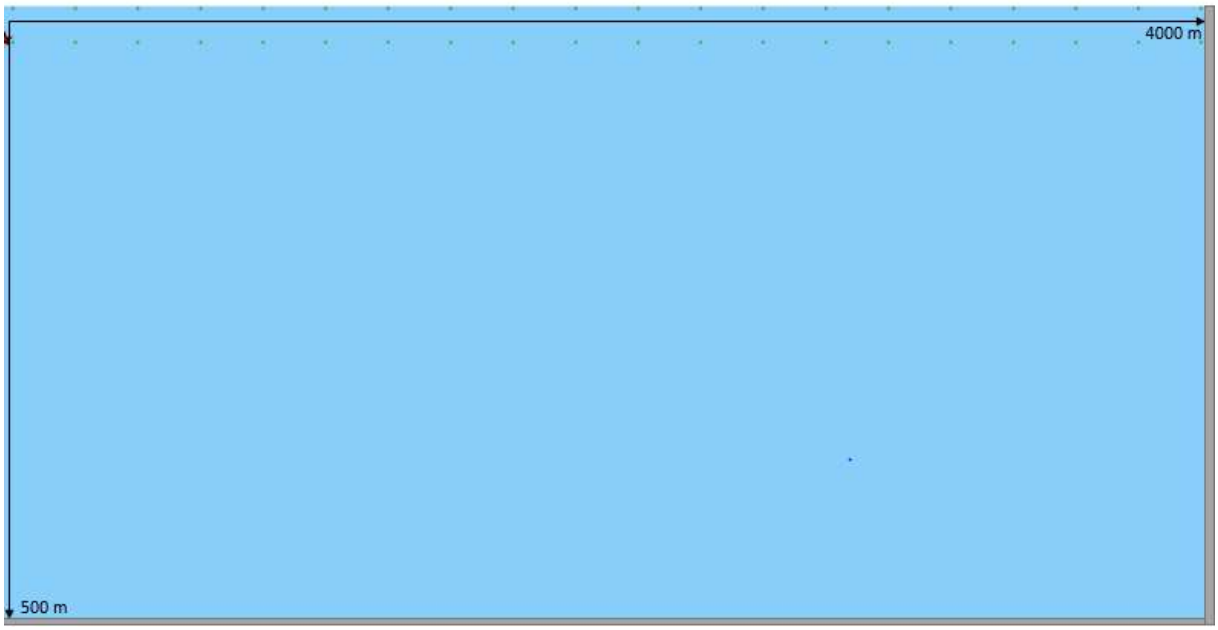

Figure 26. *The final domain for the simulations, here shown with only one water layer. The red star on the symmetry axis is the source and the green dots the receivers. The grey areas mark the perfectly matched layers, which are 5 elements or approximately 15 m thick.*

4.5.2. Validation of attenuation in the ice layer

Attenuation is implemented in the ice layer with a compressional attenuation of $\alpha_P = 0.3\ \mathrm{dB}/\lambda$ and a shear attenuation of $\alpha_S = 1\ \mathrm{dB}/\lambda$. The water layer is assumed to be non-attenuating. Figure 27 compares the output in SPECFEM2D and OASES for a receiver located at 30 m depth 1910.5 m into the domain. There is a fair agreement between the wave pulses in SPECFEM2D and OASES for the pulse of the acoustic wave propagating directly through the water layer (second arrival), even though there is a slightly smaller amplitude in the OASES simulation. The amplitude of the wave refracted from the wave propagating in the ice layer (first arrival) appears to be of the approximately same amplitude, but it arrives slightly later in SPECFEM2D. The difference is, however, small.

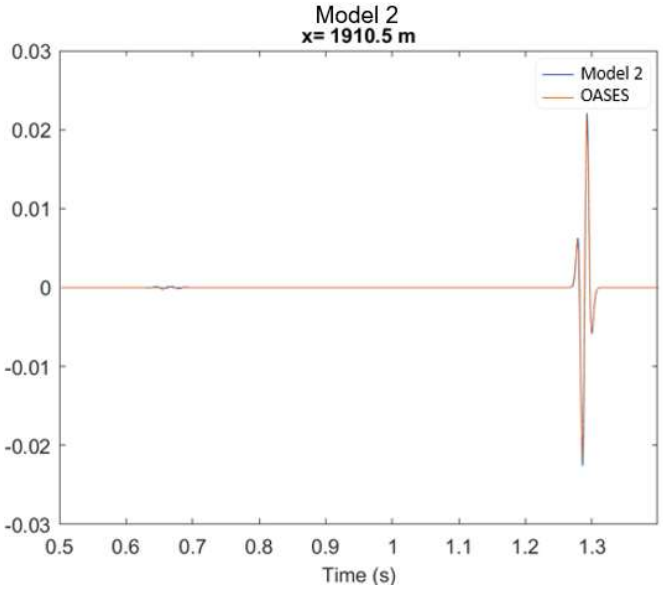

Figure 27. *Seismogram for Model 2 (blue line) compared to the OASES (orange line) simulation the 500 m deep domain. The first arrival at approximately 0.65 s is the refraction from the wave propagating through the ice layer, and the second arrival is the wave propagating directly through the water layer. Figure from Trond Jenserud (personal communication, March 17, 2022).*

4.5.3. Time step and stability

In SPECFEM2D, the global CFL-criterion (Section '2.3.5. Courant-Friedrichs-Lewy stability criterion') is calculated from the maximum P-wave velocity, and a CFL-threshold-criterion is defined as 0.95 times the global CFL-criterion. The local CFL-value inside the elements is compared to the threshold value, where instability is marked for all areas with a local CFL-value above the threshold value. Thus, for a model with only water all local CFL-values will be above the threshold and an instability is indicated in the whole domain, even though this is not the case.

The maximum time step suggested in SPECFEM2D was chosen in the simulations. Attempts to change the time step were made. However, this often caused the simulations to terminate in error, although the CFL value was seemingly within the recommended value of around or below 0.5. The minimum number of points per wavelength is well above the recommended minimum values for all simulations, which should ensure that the wave field is properly sampled. As the number of time steps per wavelength is above the recommendations, the simulations might be slightly more costly in memory and CPU time. However, because the ice layer is quite thin the choice of grid size within the ice layer was somewhat limited, and those mesh dimensions was chosen to keep the grid fairly rectangular.

Chapter 5
Results

All results in this Chapter are presented in terms of pressure. The source level in SPECFEM2D is somewhat arbitrary, therefore only the relative differences between the different cases are considered. The figures visualizing the wave field show normalized pressure. The domain is 4000 m in the horizontal direction and 500 m in the vertical direction, consisting of 1333 horizontal and 167 vertical elements with the perfectly matched layer excluded, as described in Section *'4.5.1. Validation of the domain dimensions'* (Figure 26). The source is an acoustic pressure with a Gaussian source time function. The dominant source frequency is 50 Hz.

The simulations are run on a virtual computer, which reports that it utilizes a 64 bits Intel(R) Xeon(R) Gold 6248 CPU @ 2.50 GHz, on the operative system Red Hat Enterprise Linux 7.9. In SPECFEM2D, it is possible to select postscripts figures as part of the output. A higher computational time was observed when this was selected. The reported CPU times in this thesis are given for simulations without postscripts as part of the output if nothing else is explicitly written.

The results are presented as follows. In the first section, the results for one model with a water layer only, one model with a range-independent ice layer of 3 m thickness, and one model with a range-dependent ice layer with linearly decreasing thickness are presented. A homogeneous sound velocity profile is used in these simulations. The second section presents the results for the same ice models, but with a simplified upwards refracting sound velocity profile with a linearly increasing velocity. The third section presents the results obtained when a more realistic Arctic sound speed profile, obtained from CTD-data, is implemented. Finally, in the fourth section, the results for models with different configurations of ice roughness and ice ridges are presented.

Some simulations were performed with both the 2D and axisymmetric 2.5D version of SPECFEM2D to compare the results. As those simulations were performed early in the progress, and the extra pulse from the absorbing boundary was still unknown, there are uncertainties to those results, and they will not be included in this section nor be discussed at a later stage. A relative comparison between those results is given in Appendix '*B.I. 2D vs 2.5D simulations*'. All results presented in this Chapter are 2.5D simulations.

The waves considered are visualized in Figure 28. The wave propagating directly through the water layer is referred to as the 'acoustic wave'. If an ice layer is present, some energy is transmitted from the acoustic wave into the ice layer, and the wave recorded by the receiver within the ice layer will be referred to as the 'transmitted acoustic wave'. The wave propagating through the ice layer will be referred to as the 'elastic P-wave', while the refraction of the elastic P-wave into the water layer will be referred to as the 'head wave'.

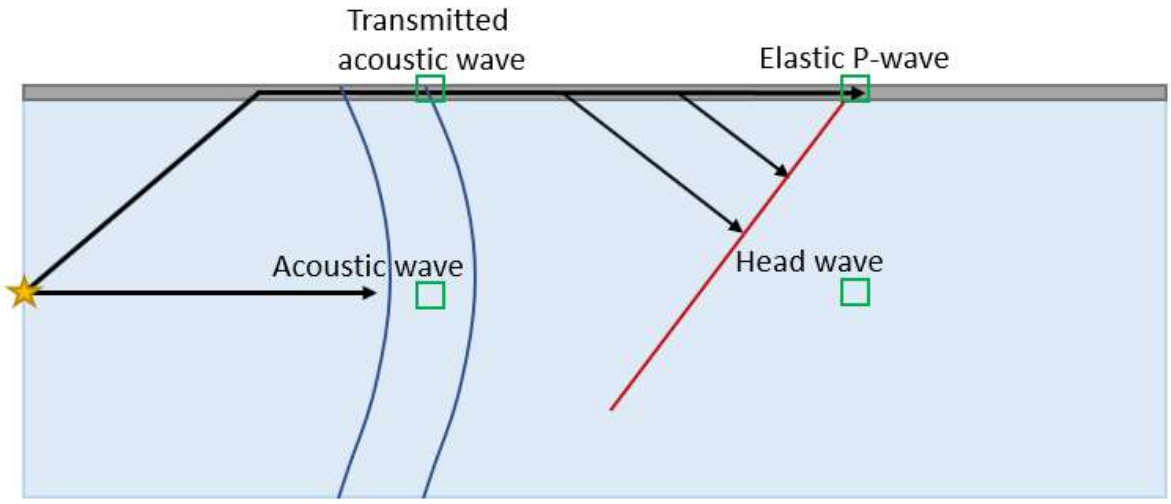

Figure 28. *Figure of the main waves considered. The acoustic wave is propagating directly in the water layer and the transmitted acoustic wave is transmitted into the ice layer above. The elastic P-wave is the fastest wave in the domain, generating a head wave in the water layer. The source is denoted by a yellow star and the squares receivers.*

5.1. Simulations with a homogeneous velocity profile

This section presents the results obtained with a simple homogeneous velocity profile in the water layer. The elastic parameters in the ice layer are the same as previously introduced (Section *3.1. Brief description of the general model parameters'*). The parameters of the simulations in this section are summarized in Table 4. Two receiver sets are utilized, one placed at 1.5 m depth within the ice layer and one placed in the water layer at 30 m depth. There are 20 receivers in each set, evenly placed between 30 and 4000 m. The source is located at 30 m depth, at the symmetry axis.

	ACOUSTIC REGION	ELASTIC REGION
COMPRESSIONAL VELOCITY v_P	1482 m/s	3500 m/s
SHEAR VELOCITY v_s	-	1800 m/s
DENSITY ρ	1000 kg/m^3	900 kg/m^3
COMPRESSIONAL ATTENUATION α_p	-	0.3 dB/ λ
SHEAR ATTENUATION α_s	-	1.0 dB/λ

Table 4. *Parameters for the simulations with a homogeneous velocity profile.*

5.1.1. Model 1 – water only

Model 1 consists of one water layer only. The simulation uses a time step of $dt = 1.744 \cdot 10^{-4}$ s and a total of $N = 18000$ time steps. Postscripts were written out during the simulation, and the total simulation time was 2 h 30 min. Figure 29 shows the wave field in pressure at $t = 0.087$ s, and the wave field at $t = 1.308$ s, approximately 1900 m into the domain, is shown in Figure 30. The figures show a simple wave front where the free-surface condition of zero pressure can be observed at the surface as the wave amplitude is reduced to zero at this point. A reflection from the surface is observed in Figure

29, which merges with the other wave as the wave propagates. There is some slight noise at the symmetry axis, and some reflections from the bottom are visible at the lower part of the wave.

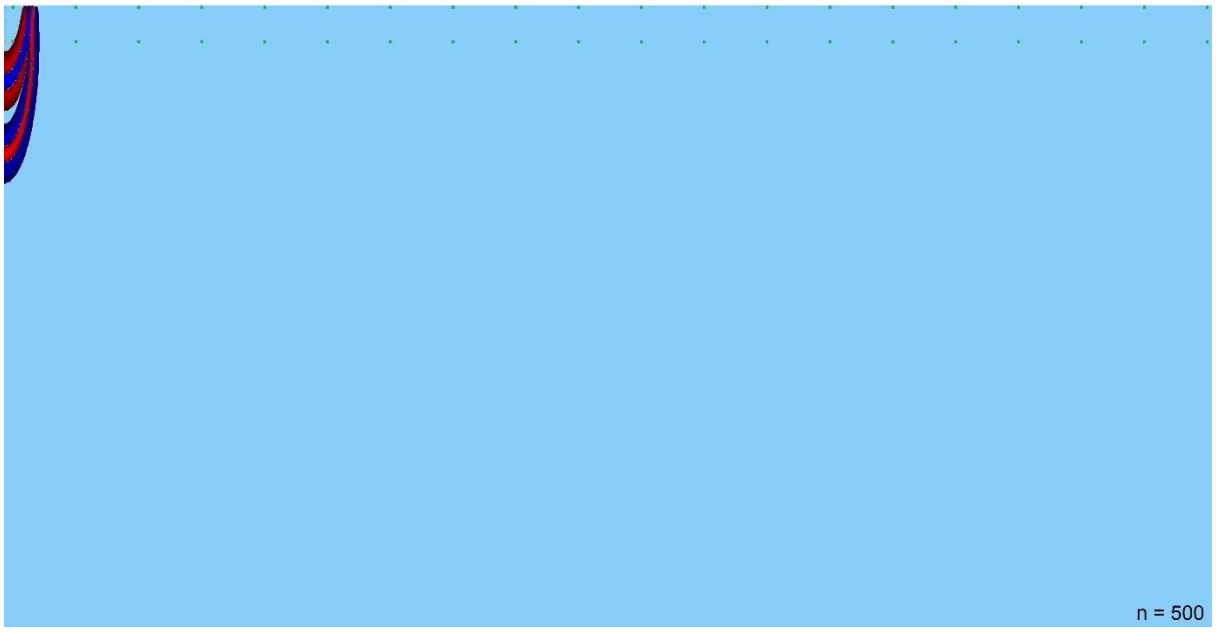

Figure 29. *Figure created in SPECFEM2D as part of the output, showing the wave field in pressure without scale, at* $t = 0.087$ *s. The receivers are shown by the green dots and the source by the yellow dot, barely seen at 30 m depth on the symmetry axis.*

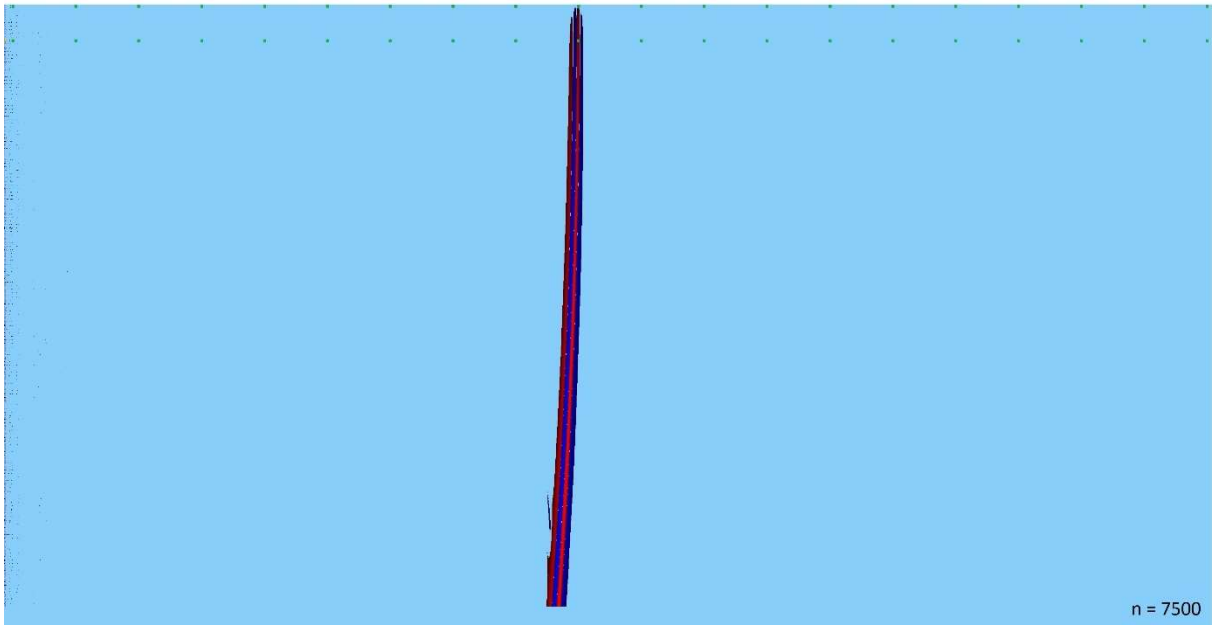

Figure 30. *The wave field of Model 1 as in Figure 29, but at* $t = 1.308$ *s.*

Seismograms recorded at the 10th receiver, at $x = 1910.5$ m, are shown in Figure 31 for a receiver located at 1.5 m depth (Figure 31a) and 30 m depth (Figure 31b). The acoustic wave arrives at approximately 1.3 s. It can be noted that the amplitude is smaller at 1.5 m depth in accordance with the free-surface condition of zero surface pressure. Smaller oscillations follow the wave pulse of the acoustic wave, probably caused by numerical noise. The small pulse arriving just before 1.5 s is likely the noise pulse generated by the reflection at absorbing layer in the bottom of the domain, discussed in Section *'4.5.1. Validation of the domain dimensions'*.

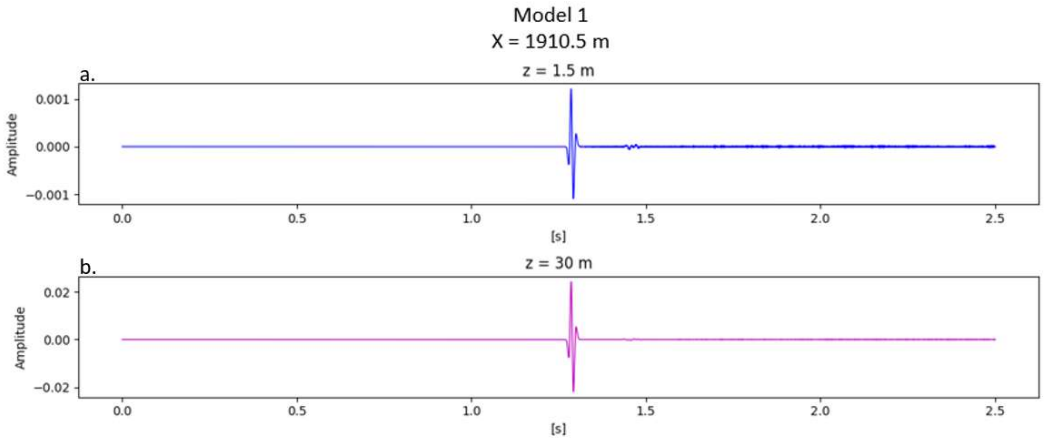

Figure 31. *Seismogram from the 10th receiver, located at $x = 1910.5$ m, at 1.5 m depth (blue) and 30 m depth (pink). The vertical scales differ as the amplitude significantly decreases towards the surface, according to the free-surface condition of zero surface pressure.*

5.1.2. Model 2 - a range-independent ice layer

Model 2 has a 3 m thick homogeneous ice layer above 497 m of water. The time step in the simulation was $dt = 7.374 \cdot 10^{-5}$ s over a total of $N = 39000$ time steps. The CPU time was 2 h 53 min. The wave field at $t = 0.088$ s is visualized in Figure 32. In addition to the acoustic wave, an elastic P-wave is observed in the ice layer along with a head wave, refracted from the elastic P-wave down into the water layer. The head wave can be observed in the visualization of the wave field at $t = 0.221$, in Figure 33. The wave field at $t = 0.678$ is shown in Figure 34. The elastic P-wave has reached the 10th receiver at $x = 1910.5$ m. The head wave in the water is so small at this point that it is not visible in this figure.

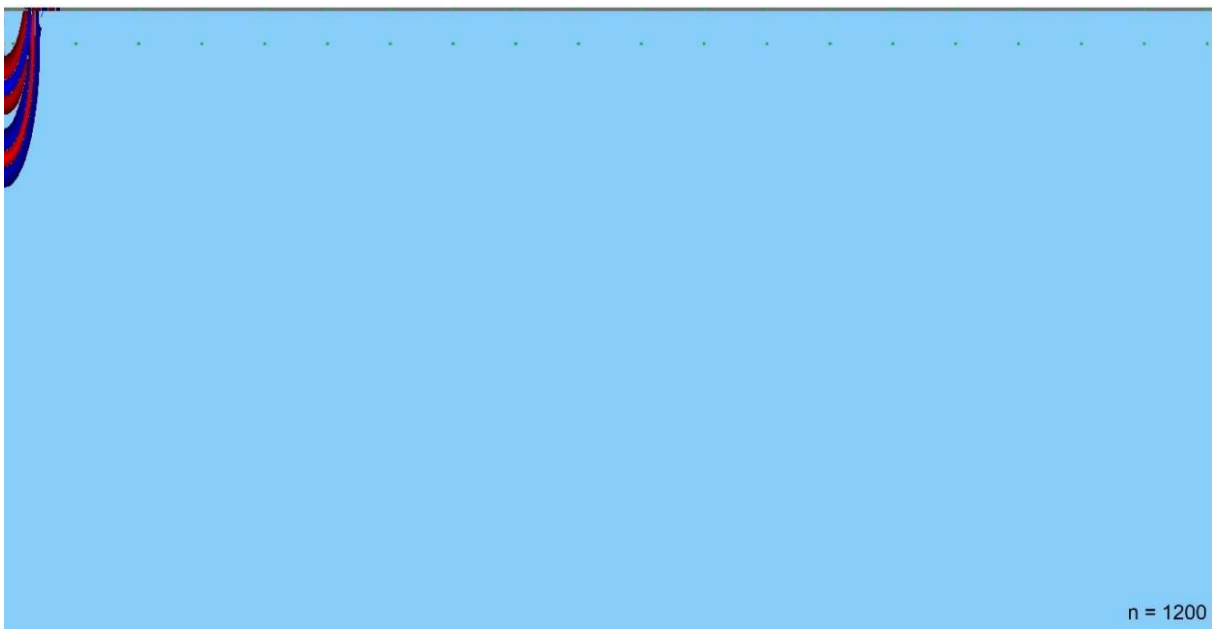

Figure 32. *The wave field in pressure for Model 2 at $t = 0.088$ s. The elastic P-wave can be observed within the ice layer.*

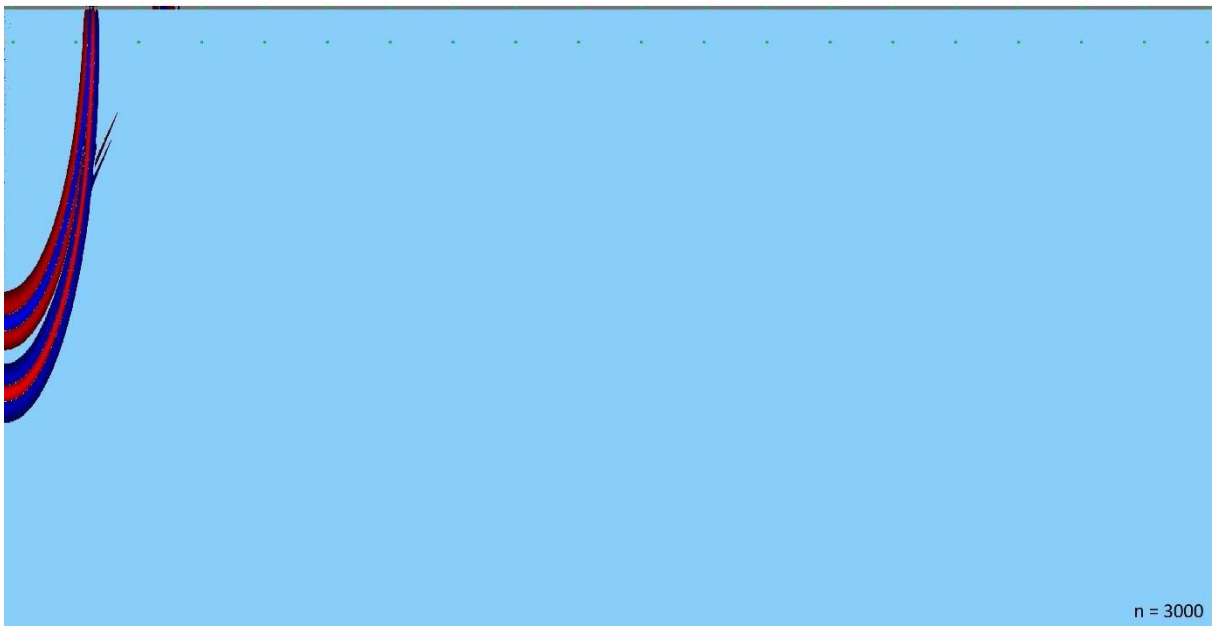

Figure 33. *The wave field for Model 2 as in Figure 32, but at* $t = 0.221$ *s.*

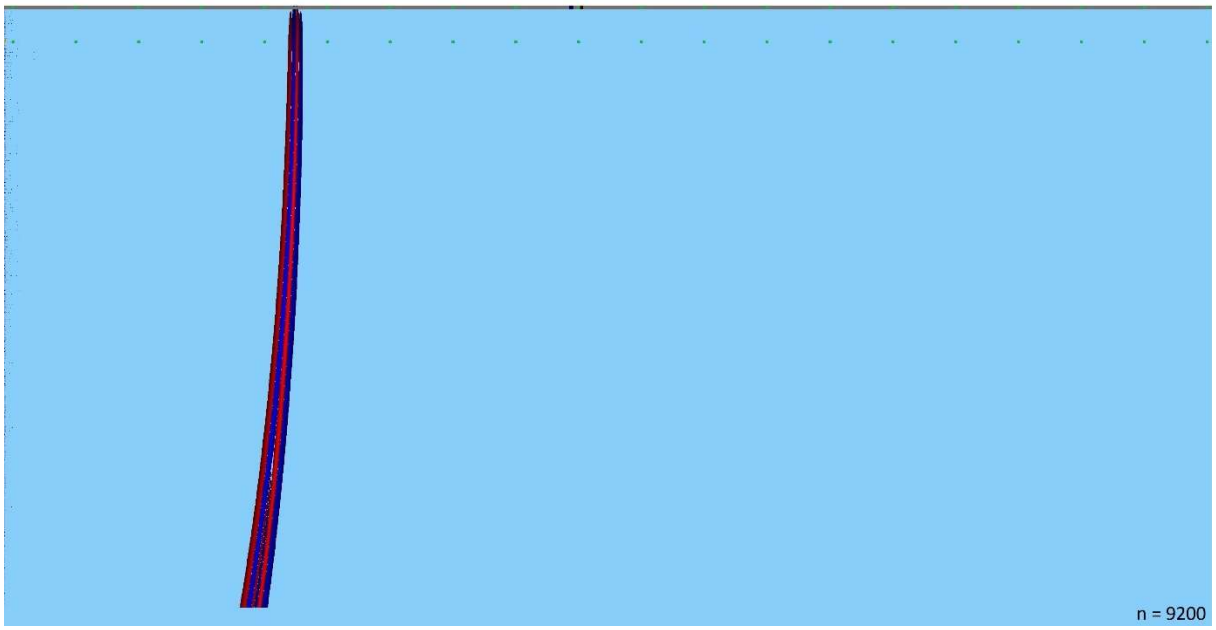

Figure 34. *The wave field of Model 2 as in Figure 32 and Figure 33, but at* $t = 0.678$ *s.*

Simulations were also performed without attenuation in the ice layer to observe its effect on wave propagation in the model. Without attenuation in the ice layer, the CPU time was slightly less, 2 h 45 min. Figure 35a shows the wave pulse at $x = 1910.5$ m at 30 m depth for one case with attenuation (blue lines) and one without attenuation (pink lines). A large difference in amplitude of the head wave (approx. 0.65 s) is observed, the amplitude is significantly smaller when attenuation is implemented. This is expected as more energy is attenuated in the ice in this case. The acoustic wave appears unaffected by the attenuation in the ice layer. The amplitude difference between the acoustic wave and the head wave is large, whether there is attenuation implemented in the ice layer or not. A time delay in the arrival time of the head wave is observed for the attenuating model (Figure 35b).

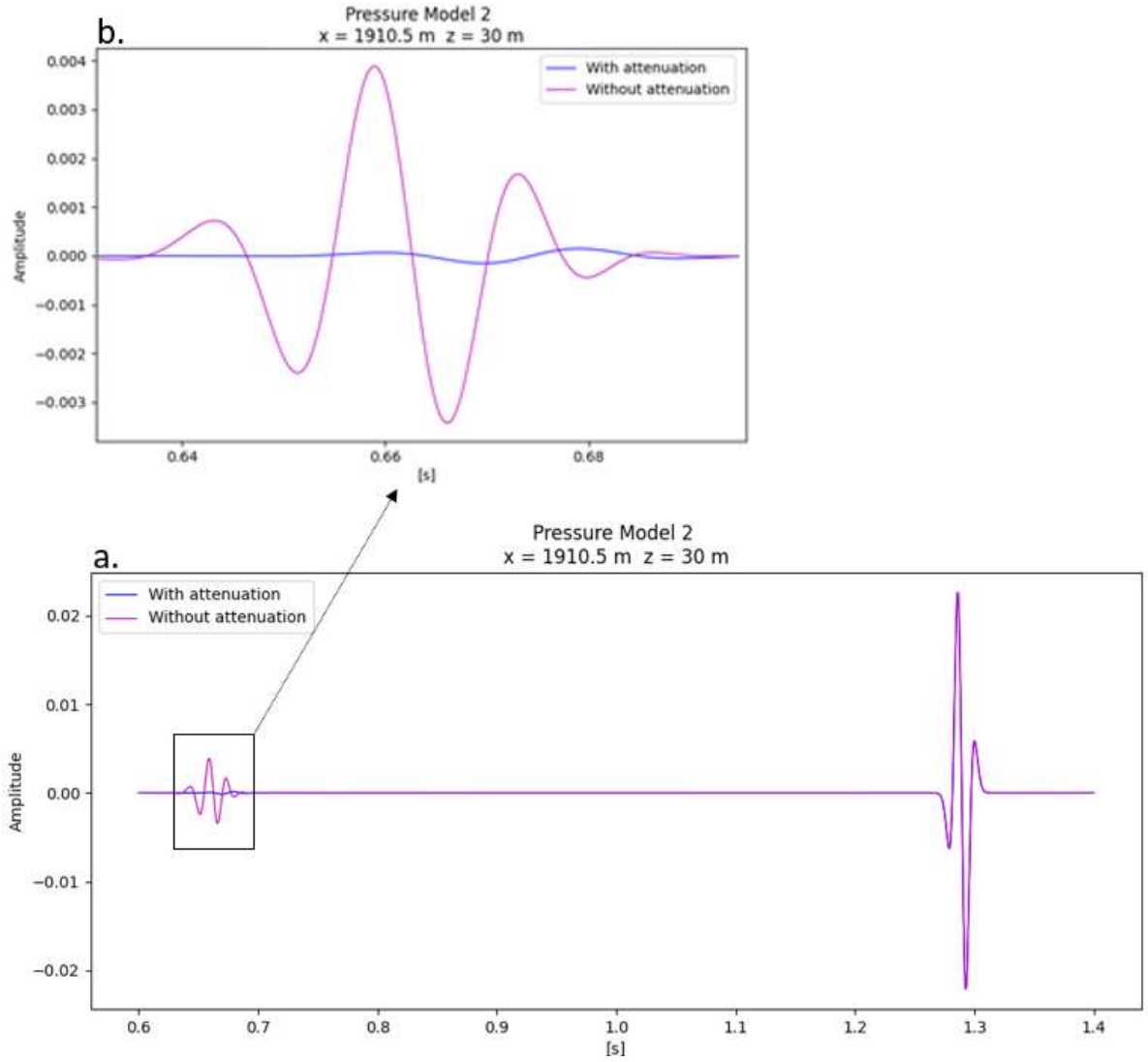

Figure 35. *Seismograms from the 10th receiver, at $x = 1910.5$ m and 30 m depth. The wave pulse of the head wave is observed at approximately 0.65 s and the acoustic wave at approximately 1.3 s, for one model with attenuation in the ice layer (blue lines) and one without (pink lines). Figure 35b shows the head wave between 0.62 and 0.72 s.*

The seismogram from the receiver located at 1.5 m depth within the ice layer at $x = 1910.5$ m is shown in Figure 36. It is worth noting the significant difference in amplitude between the elastic P-wave (approx. 0.6s) and the transmitted acoustic wave (approx. 1.3 s), which increases in the absence of attenuation. The delay in arrival time for the elastic P-wave is clearly shown. The transmitted acoustic wave appears unaffected by the attenuation within the ice layer in terms of amplitude. There is an opposite polarity of the elastic P-wave (Figure 36) and the head wave (Figure 35b).

An advantage of applying attenuation in the ice layer is that it appears also to attenuate some of the numerical noise. This is observed in Figure 37, which show the transmitted acoustic wave for attenuating ice (blue lines) and non-attenuating (pink lines) ice. Note that the amplitudes are very small, and the simulation appears to be close to noise level, but an improvement is still clearly visible.

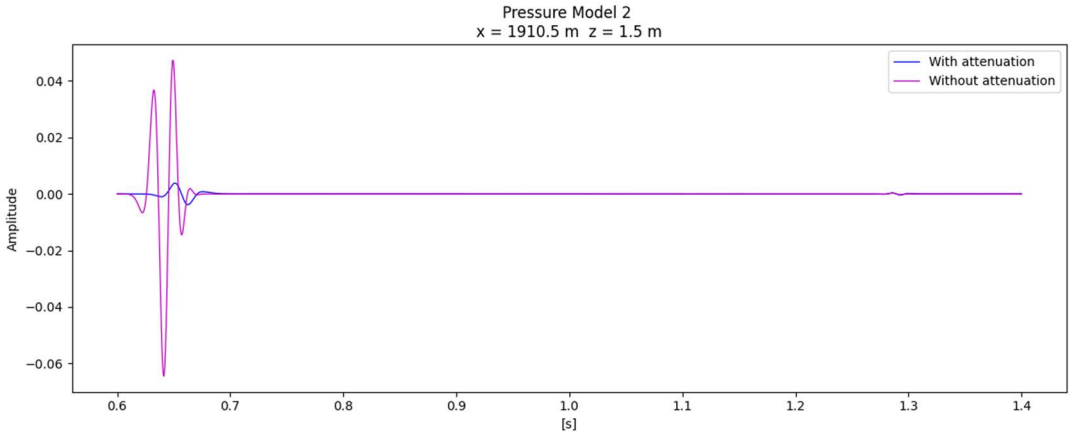

Figure 36. *Seismogram from the 10th receiver, located at 1.5 m depth within the ice layer at* $x = 1910.5$ *m.*

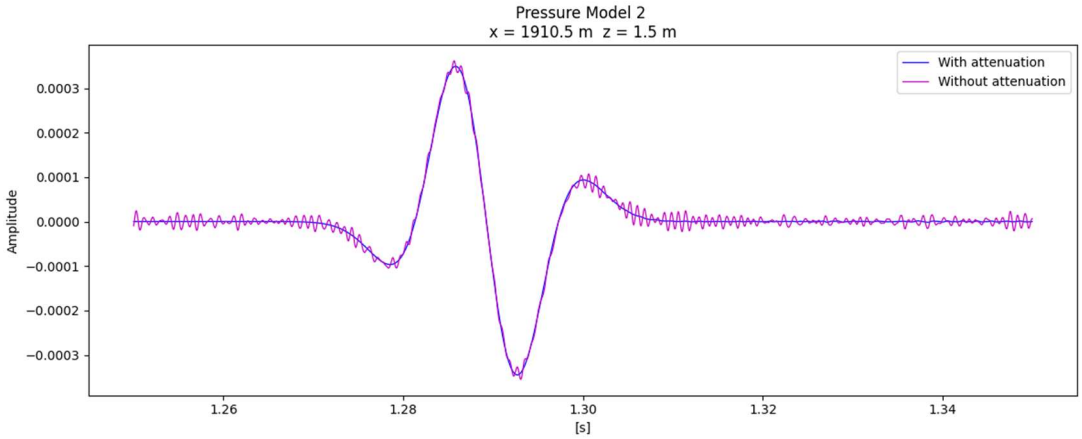

Figure 37. *Zoom in on Figure 36 between 1.25 and 1.35 s showing the wave pulse of the transmitted acoustic wave.*

5.1.3. Model 3 - a range-dependent ice layer

Model 3 has a range-dependent ice layer, linearly decreasing from 3 m thickness by 0.25 m/km throughout the domain. The simulation was run $dt = 4.994 \cdot 10^{-5}$ over $N = 57500$ time steps, and the CPU time was 4 h 12 min. The model was also run without attenuation in the ice layer. As the results with a non-attenuating ice layer were very similar to what has already been presented in the previous section, those results will not be included here. However, the CPU time was slightly less without attenuation; 3 h 56 min. Model 3 has shown only minor differences compared with Model 2 (3 m thick ice), both on the wave field visualizations and the seismograms. Therefore, the results for Model 3 will not be presented separately, but instead in comparison with the other two models in the following section.

5.1.4. Comparison between the three models

Figure 38 shows the seismograms for all three models at 30 m depth at $x = 1910.5$ m, with the head wave shown separately in the upper left corner. The head wave is observed to have a slightly larger

amplitude for Model 2 (range-independent ice), which has approximately 0.5 m thicker ice than Model 3 (range-dependent ice) at this location. The amplitude of the acoustic wave is observed to have a slightly larger amplitude in the absence of an ice layer, but the difference (approx. 0.0016) is very small.

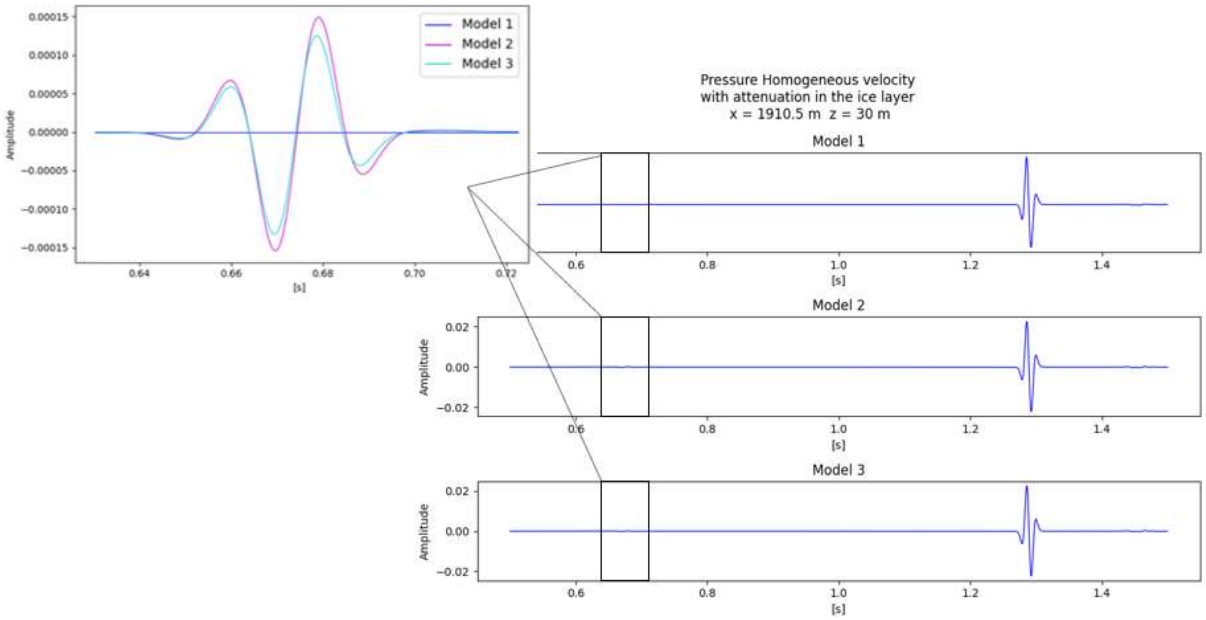

Figure 38. *Seismograms recorded at 30 m depth at* $x = 1910.5$ *m, for all three models. The figure in the upper left corner shows a zoom in on the head wave, where Model 1 is shown in blue, Model 2 in pink, and Model 3 in light blue.*

In Figure 39, the seismograms recorded at 1.5 m depth are shown for all models, at $x = 1910.5$. A larger amplitude of the elastic P-wave is observed for Model 3 than for Model 2. This is the opposite of what is observed for the head wave (Figure 38). The transmitted acoustic wave (approx. 1.3 s in Figure 39) is observed to have larger amplitudes for Model 2 than for Model 3. Note that for Model 1, Figure 39 shows the wave pulse of the acoustic wave only, as this model only contains water.

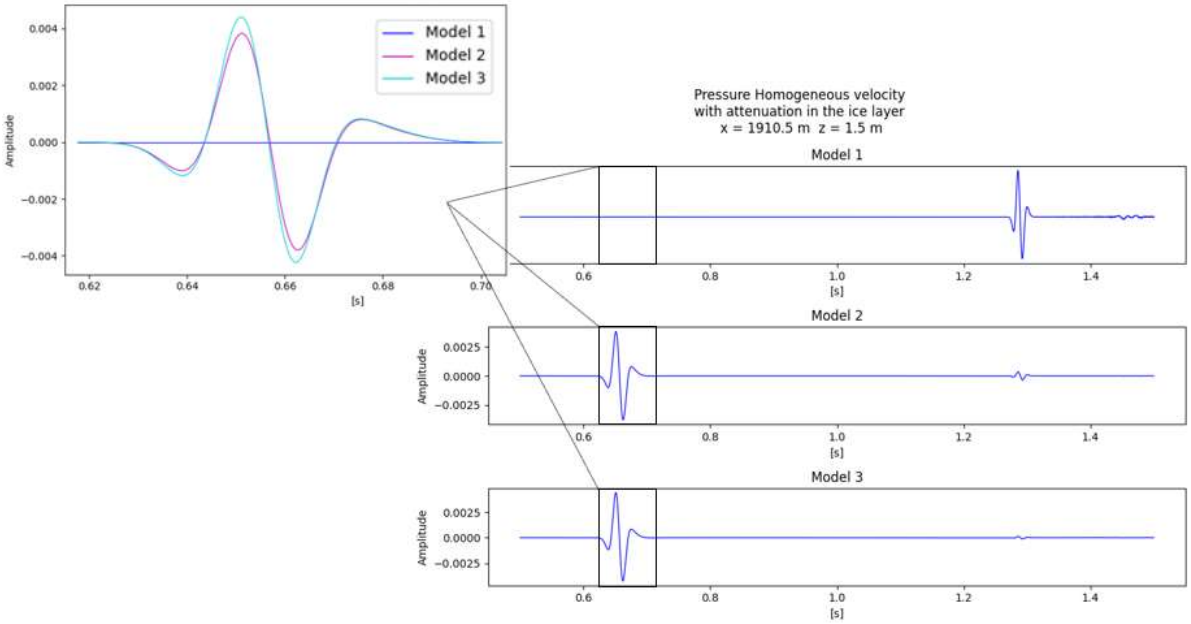

Figure 39. *Seismograms recorded at 1.5 m depth at* $x = 1910.5$ *m, for all three models. The figure in the upper left corner shows a zoom in on the wave pulse of the elastic P-wave, where Model 1 is shown in blue, Model 2 in pink, and Model 3 in light blue.*

Figure 40 shows the wave pulse of the elastic P-wave for Model 2 and Model 3 in the case of a non-attenuating ice layer. The wave form is different, the arrival time slightly earlier, and the amplitude is significantly larger compared to the attenuating case (Figure 39).

The wave pulse of the head wave also shows a difference in pulse shape, when comparing the attenuating (Figure 41) and non-attenuating (Figure 38) cases, but as for the attenuating case, the amplitude is slightly larger for Model 2 than for Model 3.

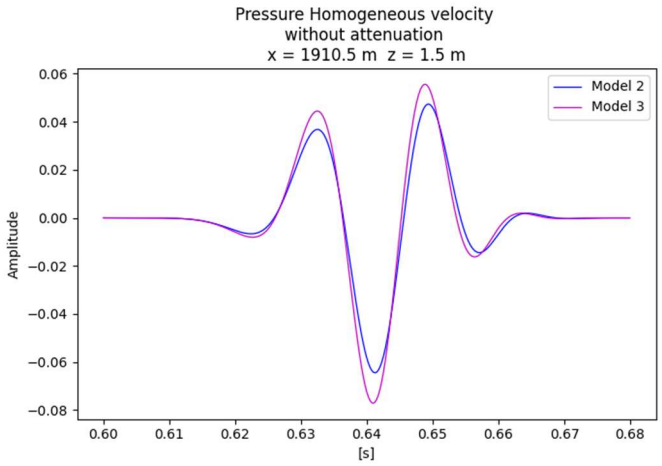

Figure 40. *The wave pulse of the elastic P-wave for Model 2 (blue line) and Model 3 (pink line) without attenuation in the ice layer.*

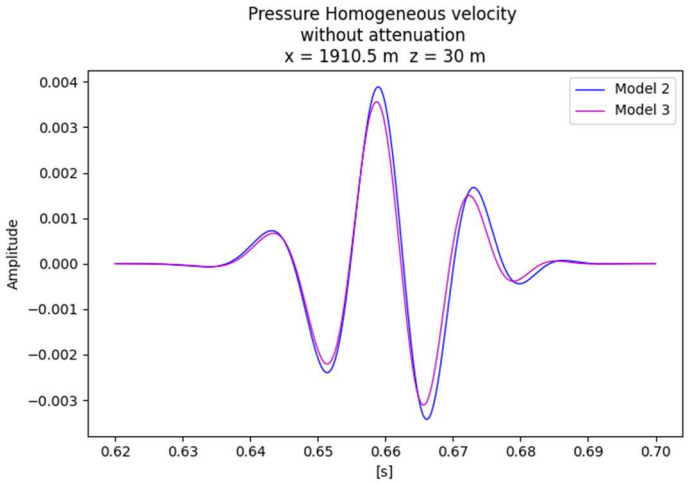

Figure 41. *The wave pulse of the head wave, recorded at 30 m depth for Model 2 (blue line) and Model 3 (pink line) for non-attenuating ice.*

5.1.5. Transmission loss

The transmission loss curves for all three models, both with and without attenuation in the ice layer, are shown in Figure 42. The transmission loss at 30 m depth is shown in Figure 42a, where no significant differences can be observed between the models. However, there are small differences. Without attenuation in the ice layer, the transmission loss at 4 km is 60.67 dB for Model 1, 60.33 dB for Model 2, and 60.26 dB for Model 3. The curve is a bit irregular at greater distances, and there are uncertainties related to the reflection from the absorbing bottom boundary. However, as the curves show the loss in dB, variations around 60 dB correspond to small changes in pressure amplitude only. At approximately 2 km distance, the noise pulse of the reflection is still small enough to the considered insignificant. At

this location, the transmission loss is 50.89 dB for Model 1, 50.58 dB for Model 2, and 50.56 dB for Model 3. The curve starts to be irregular at increasing distances, which might be related to the reflections from the absorbing layer at the bottom, as explained in Section '*4.5.1. Validation of the domain dimensions'*.

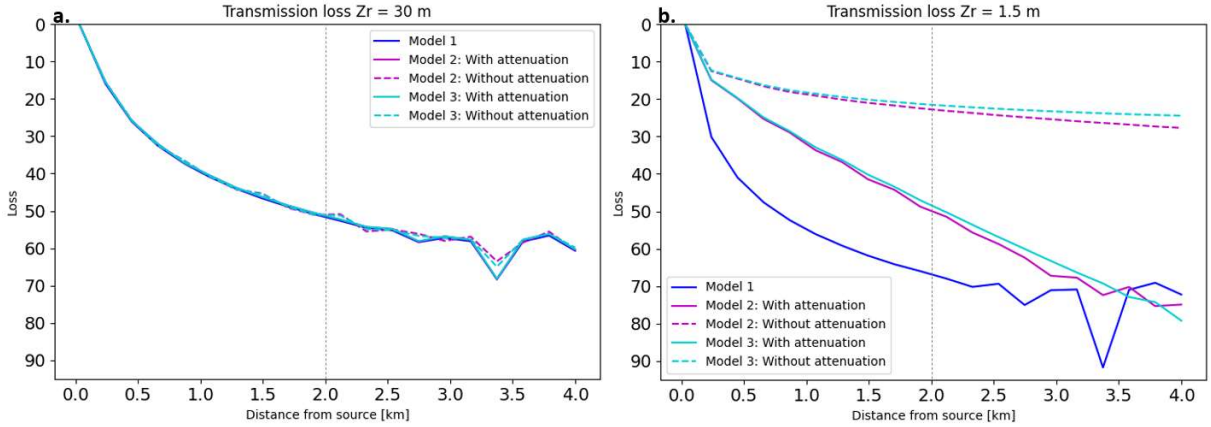

Figure 42. *Transmission loss in dB curves for Model 1 (blue lines), Model 2 (pink lines), and Model 3 (light blue lines) with attenuation (solid lines) and without attenuation (dashed lines) in the ice layer. Figure 42a shows the transmission loss at 30 m depth and Figure 42b shows the transmission loss at 1.5 m depth. The dotted vertical line marks where the extra pulse discussed in Section '4.5.1. Validation of the domain dimensions' appears, although it is still insignificant at this point.*

Figure 42b shows the transmission loss within the ice layer. Less transmission loss can be observed for Model 3 (range-dependent ice), than for Model 2 (range-independent ice). Note that Figure 42b shows transmission loss in the water for Model 1, and in the ice layer for Model 2 and Model 3.

5.2. Simulations with a linearly increasing sound velocity profile

In this section, an upwards refracted sound velocity profile is introduced in the simulations. The sound velocity profile is a simplified upwards refracting profile, which linearly increases in velocity with increasing depth from $v_p = 1482\ m/s$ at the surface to $v_p = 1525\ m/s$ at 500 m depth (Section '*3.4.1. A linearly increasing sound velocity* profile'). The rest of the parameters and the location of the source and receivers are the same as in the previous section. There cannot be seen any noteworthy difference in the figures visualizing the wave field, and therefore they will not be shown in this section.

Increased amplitudes of the acoustic wave are observed when the upwards refracting velocity profile is implemented, as shown in Figure 43. The head wave (Figure 44) does not appear to be affected by the different velocity profiles in the water.

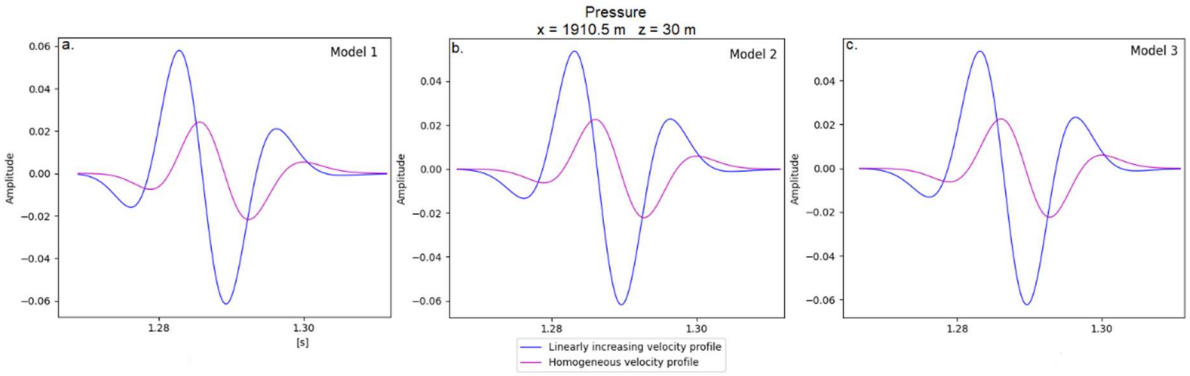

Figure 43. *The wave pulse of the acoustic wave recorded at $x = 1910.5$ m for Model 1 (fig. a.), Model 2 (fig. b.) and Model 3 (fig. c.), for a linearly increasing velocity profile (blue lines) and a homogeneous velocity profile (pink lines). The amplitude is significantly increased in all models when a linearly increasing velocity profile is implemented.*

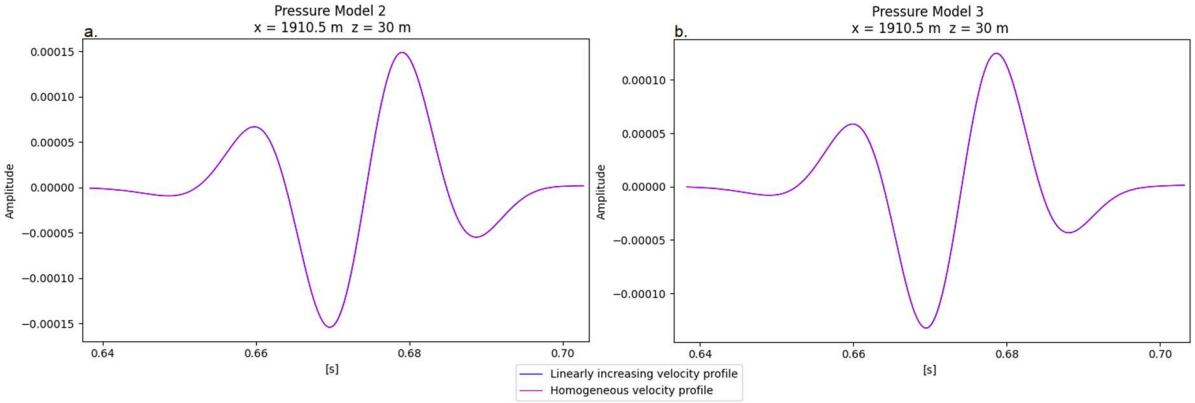

Figure 44. *The wave pulse of the head wave for Model 2 (fig. a.) and Model 3 (fig. b.) for a linearly increasing (blue lines) and a homogeneous velocity profile (pink lines), recorded at the same position as Figure 43.*

The same trends of increased amplitudes are observed within the ice layer. The amplitude of the transmitted acoustic wave becomes larger with an upwards refracting velocity profile for all models (Figure 45). Note the different scales on the figures and the amplitude differences between the models. The largest amplitudes are observed in the absence of ice, and the second largest amplitudes are observed for Model 2 (range-independent ice) for both velocity profiles. Some oscillations can be observed for Model 3 after 1.3 s. The amplitude is so small at this point that it is close to the noise level. The elastic P-wave is not observed to be affected by the different velocity profiles in the water layer, as shown in Figure 46.

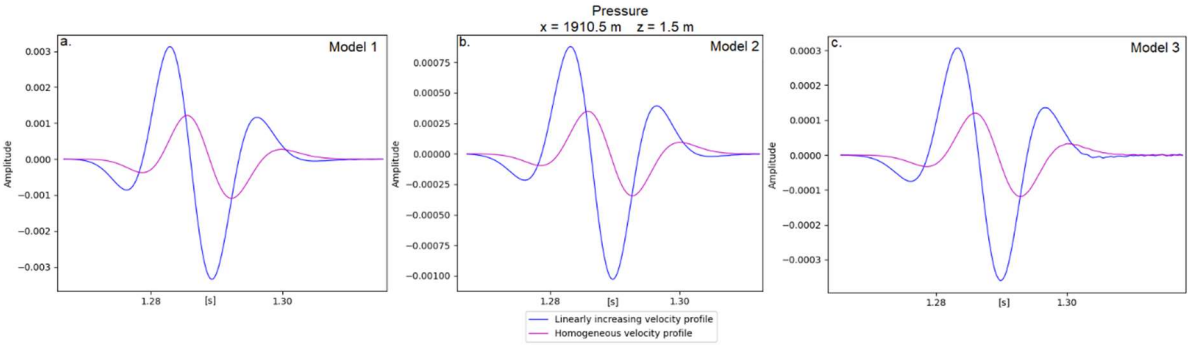

Figure 45. *The wave pulse of the acoustic wave for Model 1 (fig. a.) and the transmitted acoustic wave for Model 2 (fig. b.) and Model 3 (fig. c.), recorded at the same horizontal position as Figure 43 and Figure 44, for a linearly increasing (blue lines) and a homogeneous velocity profile (pink lines). Note the different scales on the axes.*

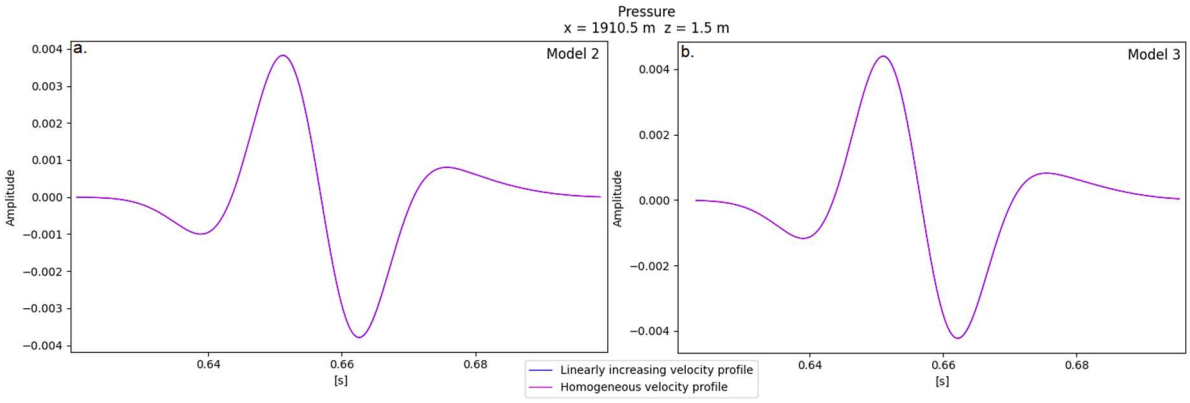

Figure 46. *The wave pulse of the elastic P-wave for Model 2 (fig. a.) and Model 3 (fig. b.), recorded at the same horizontal position as the previous figures in this section (Figure 43, Figure 44, Figure 45), for a linearly increasing (blue lines) and a homogeneous velocity profile (pink lines Note the slightly different scales on the axes.*

Transmission loss curves for all models are shown at 30 m depth in Figure 47a and at 1.5 m depth in Figure 47b. The loss curves at 30 m depth deviate after approximately 500 m, where the loss decreases for the upwards refracting velocity profile (dashed lines), compared to the homogeneous velocity profile (solid lines), for all models. At 4 km, there is a difference of approximately 20 dB in transmission loss for a receiver and source at 30 m depth between the different velocity profiles. The curves are somewhat irregular for increased distances, probably due to reflections from the absorbing layer. No large differences can be observed in transmission loss between the three models for neither velocity profile. However, there are small differences. At 4 km, a 40.60 dB loss is observed for Model 1, 40.20 dB for Model 2, and 40.20 dB for Model 3. At approximately 2 km, there is a 43.39 dB loss observed for Model 1, 43.02 dB for Model 2, and 43.01 dB for Model 3, which means that there is approximately 7.5 dB less transmission loss for the linearly increasing velocity profile compared to the homogeneous profile at this point. The loss curves for the upwards refracting profile show fewer irregularities with distance, which might be explained by fewer waves interacting with the absorbing bottom boundary.

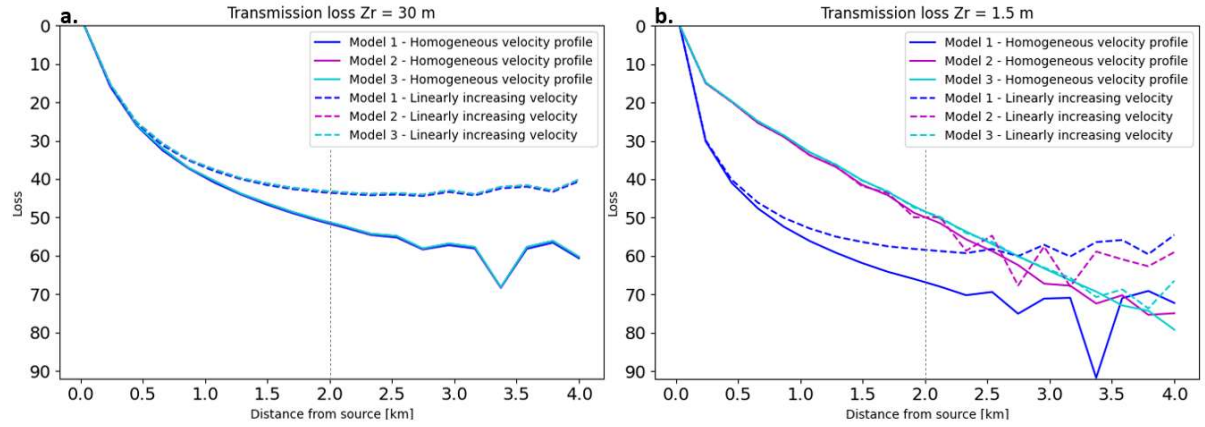

Figure 47. *Transmission curves in dB for Model 1 (blue), Model 2 (pink) and Model 3 (light blue), with a homogeneous sound velocity profile (solid lines) and a linearly increasing sound velocity profile (dotted lines). Figure 47a shows the transmission loss at 30 m depth and Figure 47b the loss at 1.5 m depth. The dotted line marks where the extra pulse can be observed as a small noise pulse.*

The transmission loss in the ice layer is not significantly affected by the difference in sound velocity profile in the water before 2 km range. The loss curves of the models with an upwards refracting profile

does however become more irregular with increasing distance compared to the models with a homogeneous velocity profile. This especially applies to Model 2 (range-independent ice), where the transmission loss also decreases with increasing distances for an upwards refracting sound velocity profile. The same trend can be observed for Model 3 (range-independent ice), but with smaller differences. The increasing irregularity might be linked to the reflections from the absorbing layer (see Section '*4.5.1. Validation of the domain dimensions*').

5.3. Simulations with an Arctic sound speed profile

To implement a more realistic velocity profile, an Arctic sound speed profile is built from CTD-data measured at latitude 83.1303 and longitude 31.7093 (Chierici et al., 2021) as described in Section *'3.4.2. An Arctic sound speed profile from* CTD-data*'*. The velocity profile is ranging from $v_p = 1440.4\ m/s$ to $v_p = 1463.9\ m/s$ and the density profile between $\rho = 1026.61\ kg/m^3$ and $\rho = 1027.95\ kg/m^3$. The rest of the parameters are the same as in the previous section. There are no notable differences in the figures visualizing wave field compared to the previous two cases, and those figures will therefore not be presented.

Seismograms from 30 m depth 1910.5 m into the domain are shown in Figure 48 for all three models. As in the previous two sections is the amplitude of the head wave (Figure 48a) larger for Model 2 (range-independent ice) than for Model 3 (range-dependent ice). As for the previous velocity profiles, the amplitude of the acoustic wave is slightly larger in the absence of ice (Figure 48b), but a small phase shift is observed.

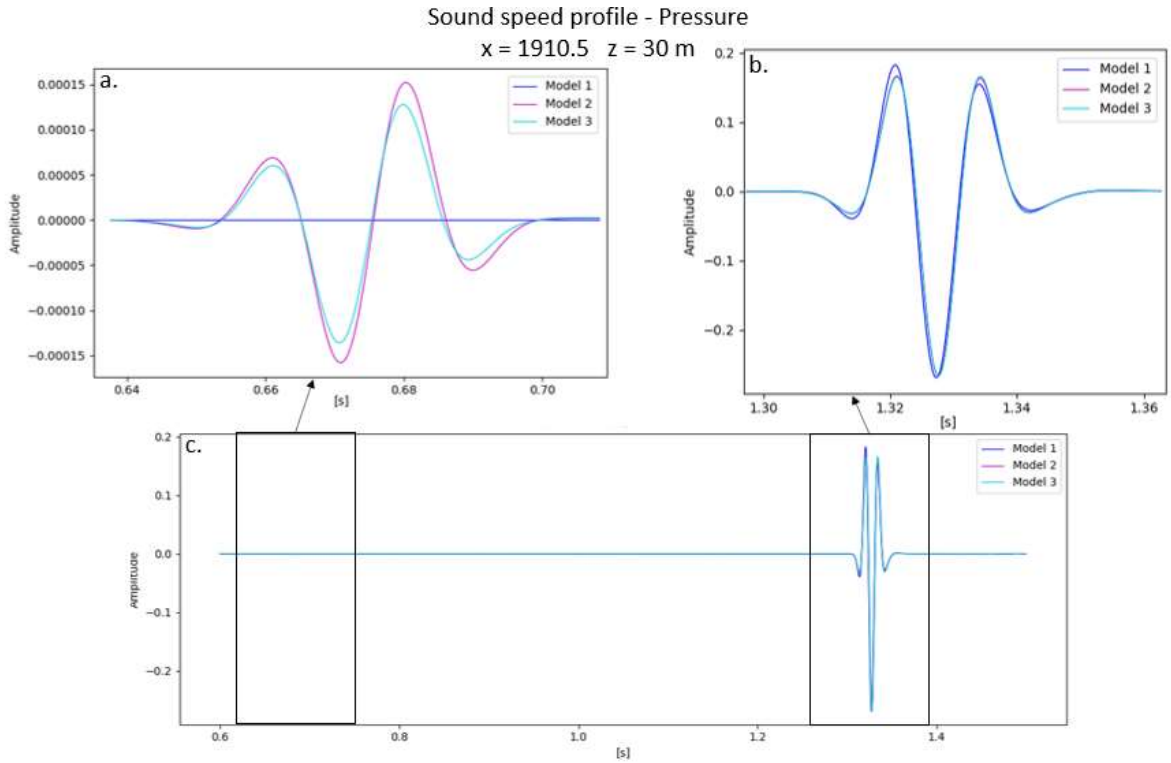

Figure 48. *Seismogram recorded at 30 m depth at* $x = 1910.5$ *m at 30 m for Model 1 (blue lines), Model 2 (pink lines), and Model 3 (light blue lines). A closer view of the head wave is shown in Figure 48a and of the acoustic wave in Figure 48b.*

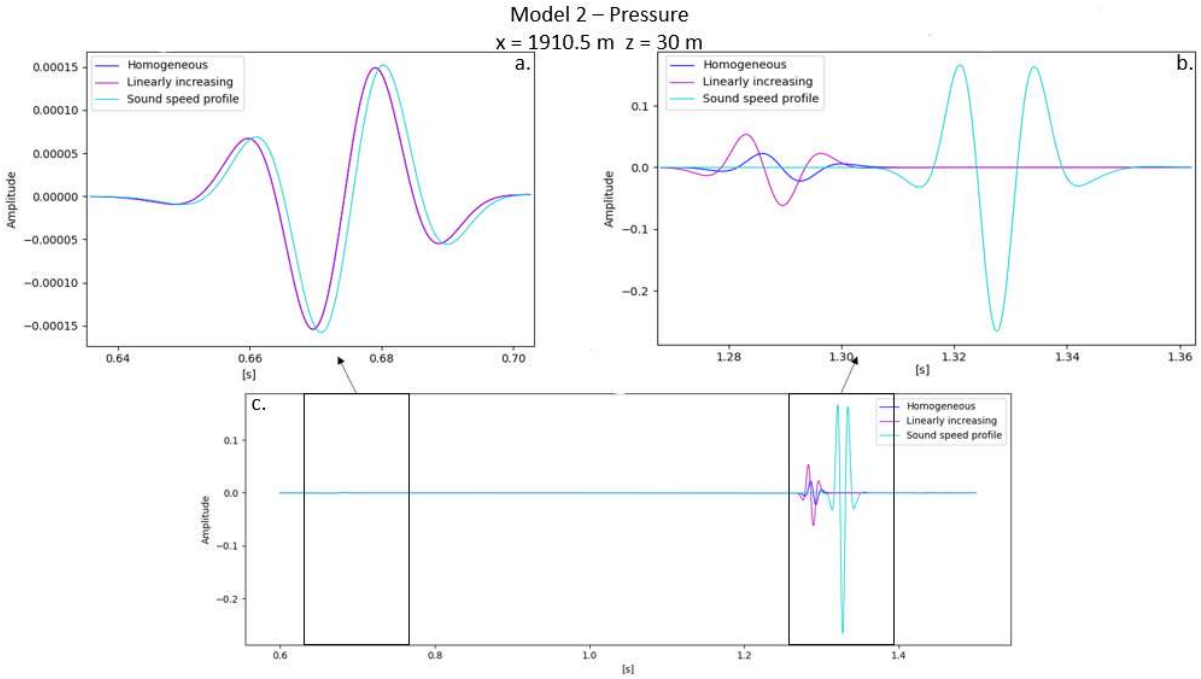

Figure 49. *Seismogram for Model 2 at $x = 1910.5$ m at 30 m depth in Figure c, for a homogeneous (blue lines), linearly increasing (pink lines), and an Arctic sound speed profile (light blue lines), with a zoom in on the head wave (*Figure 49a*) and a zoom in on the acoustic wave (*Figure 49b*). The acoustic wave shows a phase change for the Arctic sound speed profile, which has a strong velocity gradient.*

Seismograms for Model 2 (range-independent ice) recorded at 30 m depth, at $x = 1910.5$ m, are shown for all implemented sound velocity profiles in Figure 49. When the Arctic sound speed profile is implemented, a small delay in arrival time is observed for the head wave (Figure 49a). This delay is expected due to the significantly slower velocities in this profile (see Section *'3.4.2. An Arctic sound speed profile from* CTD-data*'*, Figure 13). The acoustic wave (Figure 49b) propagates directly through the water and thus, shows a larger delay in arrival time. The amplitude of the acoustic wave is significantly larger when the Arctic sound speed profile is implemented, and a phase shift is observed.

Seismograms for all the models recorded at 1.5 m depth, 1910.5 m into the domain, are shown in Figure 50. The elastic P-wave (Figure 50a) and the transmitted acoustic wave (Figure 50b) both show the same features as presented for the other two velocity profiles. Note that Figure 50b shows the acoustic wave for Model 1 (water only).

Seismograms for Model 3 (range-dependent ice) at 30 m depth, for Model 2 and Model 3 at 1.5 meters depth, and for Model 1 at both 1.5 and 30 m depth, are not shown as they are very similar to what already is presented, in terms of both the shapes and features of the wave pulses. The results for both Model 2 and Model 3 at 1.5 m depth show that the wave propagating within the ice layer appears quite unaffected by the velocity profile in the water. Also, only a very small increase in the amplitude of the elastic P-wave and the transmitted acoustic wave is observed when the Arctic sound speed profile is implemented. The relative differences between the models for the amplitude of the transmitted acoustic wave are comparable to what is shown for the acoustic wave in Figure 49b for the different sound velocity profiles. The seismograms for Model 3 (range-dependent ice) at 30 m depth are very similar to Model 2 (Figure 49). The amplitudes of the head wave are observed to be slightly larger for Model 2 than for Model 3, while no noteworthy differences are observed for the acoustic wave. The acoustic wave in

Model 1 shows the same shape and features as is presented for Model 2 and Model 3 above, for both receiver depths.

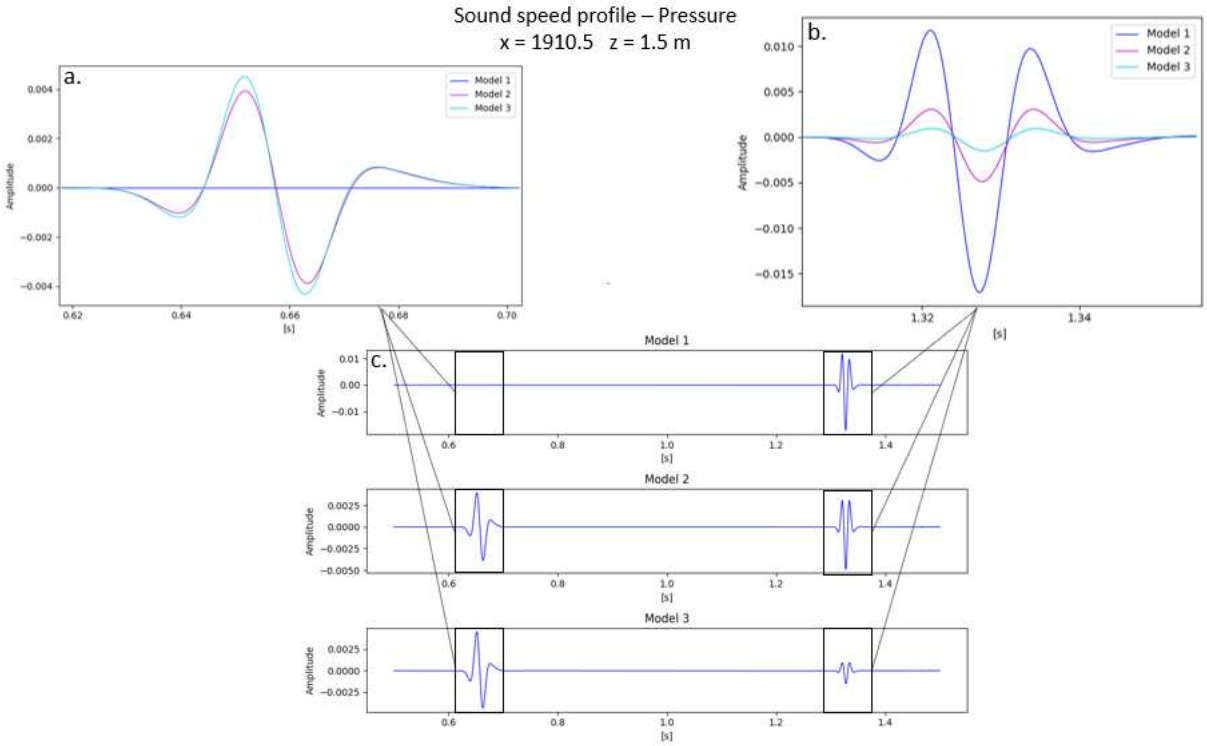

Figure 50. *Seismograms for Model 1 (blue lines), Model 2 (pink lines), and Model 3 (light blue lines) at 1.5 m depth 1910.5 m into the domain, with a zoom in on the wave pulse of the elastic P-wave (fig. a.) and for the transmitted acoustic wave (fig. b.).*

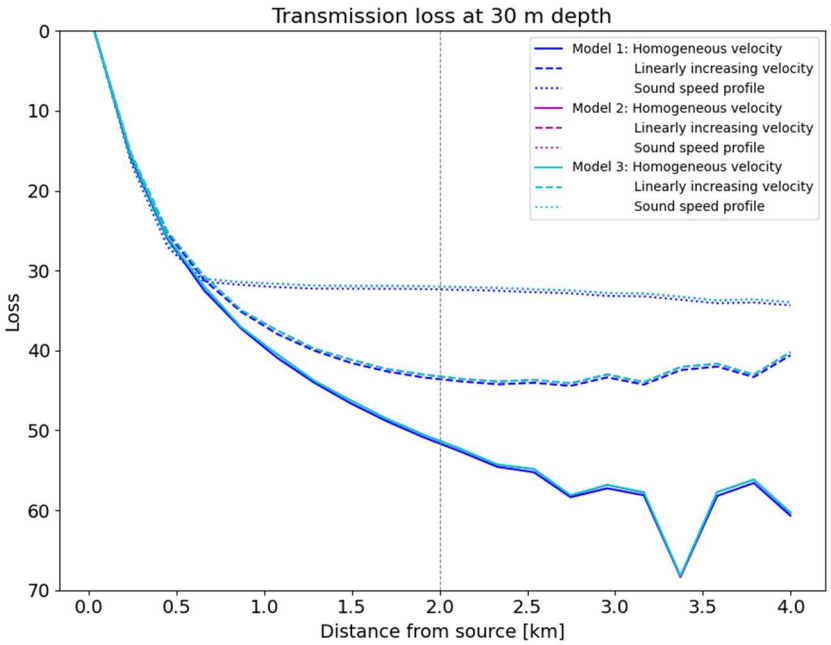

Figure 51. *Transmission loss curves at 30 m depth for Model 1 (blue lines), Model 2 (pink lines) and Model 3 (light blue lines) with the homogeneous velocity profile (solid lines), the linearly increasing velocity profile (dashed lines) and the Arctic sound speed profile (dotted lines). The horizontal dotted line marks the where the extra pulse can be observed as a small noise pulse.*

Transmission loss curves at 30 m depth for all models and all velocity profiles are shown in Figure 51. Corresponding to what is shown in the previous sections, the least transmission loss is observed for the

models with an Arctic sound speed profile (dotted lines), and the second least loss for the linearly increasing profile (dashed lines). The most loss is still observed for the homogeneous profile (solid lines). As in the previous sections, there are no large differences in transmission loss between the ice models. At 4 km, 34.35 dB loss is observed for Model 1, 33.97 dB for Model 2, and 33.95 dB for Model 3. At 2 km are the losses 31.96 dB, 31.95 dB, and 31.94 dB, respectively. When the Arctic sound speed profile is implemented, a rapid loss can be observed until approximately 500 m range, after which the loss increases at a much slower rate.

The transmission loss at 1.5 m depth is shown in Figure 51 for all models and all velocity profiles. Note that Model 1 (blue lines) shows the loss in the water layer, while Model 2 (pink lines) and Model 3 (light blue lines) show the loss within the ice layer. The transmission loss curves for Model 2 and Model 3 are observed to increase fastest during the first approximately 2 km. After that, the loss curve for the models with an upwards refracting sound velocity profile becomes more horizontal compared to the loss curve of the models with a homogeneous sound velocity profile. The least loss is observed for the models with an Arctic sound speed profile. The transmission loss curves for the ice layer are quite irregular at ranges above 2 km, but two trends can be distinguished; less loss is observed for range-independent ice (Model 2) than for ice with a linearly decreasing thickness (Model 3), and the loss appears to decrease the more upwards refracting the velocity profile in the water is. However, there are some uncertainties with the loss curves at increased distances, and the impact on transmission loss is most visible for Model 2, while it is closer to the noise level for Model 3.

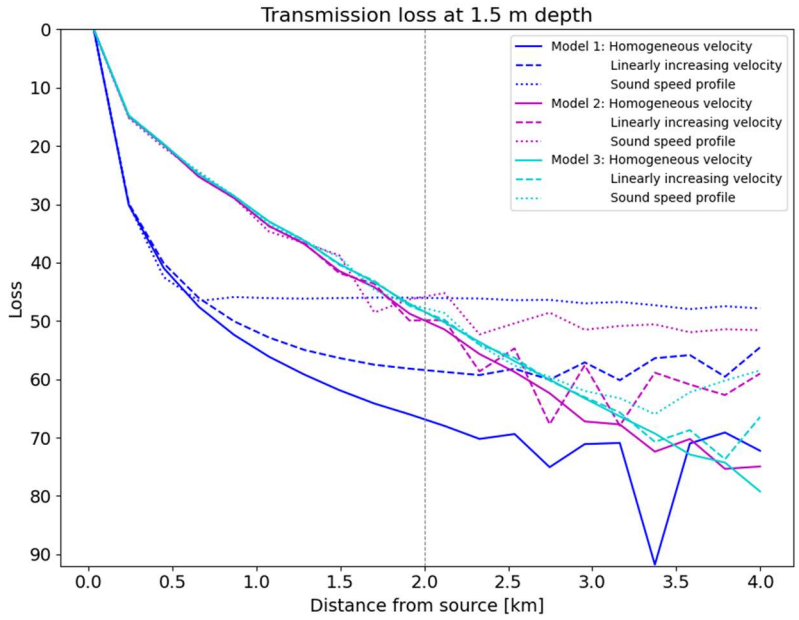

Figure 52. *Transmission loss in dB shown as for Figure 51, but at 1.5 m depth.*

5.4. Simulations with ice roughness and ice ridges

In this section, ice roughness and ice ridges are implemented in different combinations, as described in Section '*3.7.2. Ice models with ice ridges*'. Two ice ridges are located at $x = 996$ m and $x = 2992$ m, one ridge with a 4.9 m deep keel and one with a 7.1 m deep keel. Their horizontal location is varied.

Both a smooth ice-water interface with surrounding 2 m thick ice layer and a rough ice-water interface with a surrounding ice of 2 m mean thickness are used in the following simulations.

All simulations in this section are done with the Arctic sound speed profile built from CTD-data (Section '*3.4.2. An Arctic sound speed profile from* CTD-data') and its corresponding density profile, introduced in the previous section. Also, the same elastic ice parameters as in previous simulations are used. All parameters are summarized in Table 5. Additionally, the domain, the source location, and the horizontal locations of the receivers are the same as in earlier simulations. Two extra receiver sets were placed at 100 m and 150 m depth, but the results from 1.5 m and 30 m depth are mainly shown in this section as well.

	FLUID REGION	SOLID REGION
COMPRESSIONAL VELOCITY v_P	1440.4-1463.9 m/s	3500 m/s
SHEAR VELOCITY v_s	-	1800 m/s
DENSITY ρ	1026.61-1027.95 kg/m^3	900 kg/m^3
COMPRESSIONAL ATTENUATION α_p	-	0.3 dB/ λ
SHEAR ATTENUATION α_s	-	1.0 dB/λ

Table 5. *Parameters in the simulations.*

5.4.1. A smooth ice model with two ice ridges

First, the results for a model with a smooth ice-water interface and two ice ridges are presented. The model has the shallower of the two ice ridges (4.9 m) as the first ridge in the domain, and the deeper (7.1 m) as the second. The simulations are done with time step $dt = 4.9335 \cdot 10^{-5}$ over 59000 steps. The CPU time was 4 h 31 min. Model 2 (3 m thick ice) from the previous section will be used as a reference model to easier distinguish the contribution of the ice ridges. The wave field at time $t = 0.75$ is shown in Figure 53.

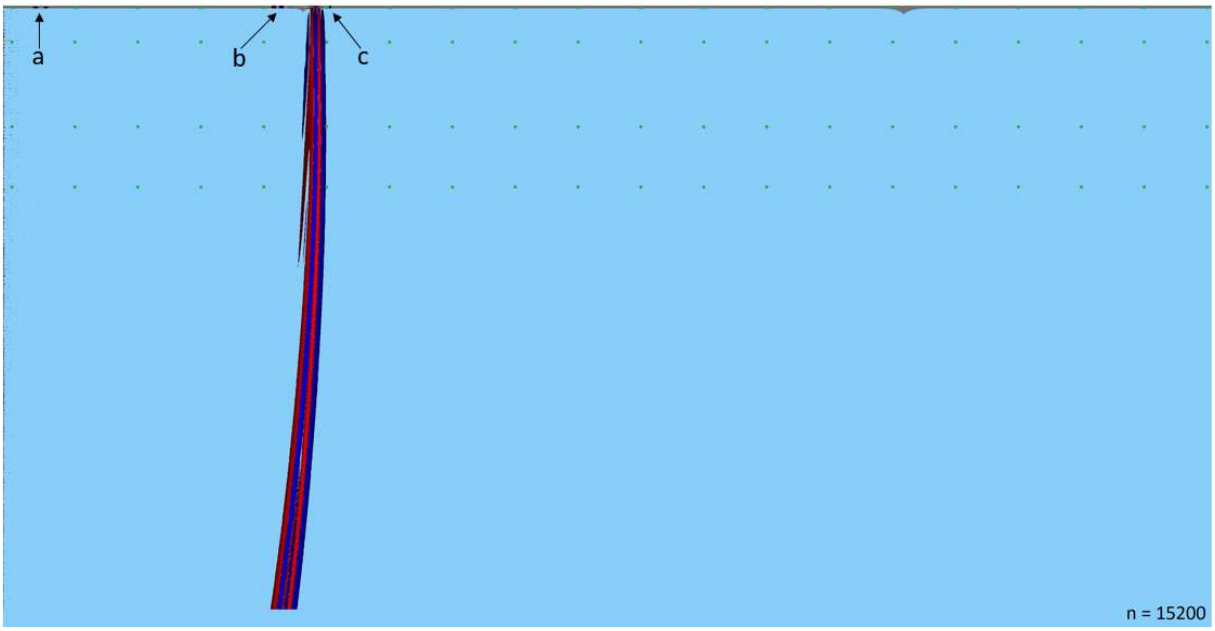

Figure 53. *The wave field at* $t = 0.75$ *in a domain with smooth ice and two ice ridges, one shallow (4.9 m) at 996 m and one deeper (7.1 m) at 2992 m. Arrow a show the backscattered elastic P-wave, arrow b the backscattered transmitted acoustic wave and arrow c the forward scattered transmitted acoustic wave.*

Figure 53 shows the wave field when the acoustic wave just passed the first ice ridge. This causes energy to be transmitted into the ice layer and to be scattered, both backward (arrow b in Figure 53) and forward (arrow c Figure 53). In Figure 53, the elastic P-wave has already passed the first ice ridge (at approx. 0.37 s), which also generated scattering. The backward scattered elastic P-wave shown by arrow a has at this point been reflected at the symmetry axis and will continue through the domain as noise.

Therefore, more waves are generated when an ice ridge is introduced to the simulations. When the acoustic wave passes the ice ridge, a forward and backward scattering of the transmitted wave occurs, generating a small head wave as the scattered waves are refracted into the water. Those waves will be referred to as the head wave of the forward scattered and backscattered transmitted acoustic waves. In addition, the elastic P-wave generates a backward scattered elastic P-wave when it passes the ice ridge, which propagates within the ice layer. This wave will be referred to as the backscattered elastic P-wave, which also refracts into the water layer and generates a backscattered head wave. There cannot be distinguished any forward scattered elastic P-wave, as this wave would propagate at the same velocity as the elastic P-wave, and by so, practically be in the same wave. A wave, which appears to propagate both within the ice and the upper water layer, is also observed after the elastic P-wave and the acoustic wave pass the ice ridge. This wave propagates at a velocity of approximately 1400 m/s. Figure 54 visualizes the waves generated as the acoustic wave, and the elastic P-wave passes the ice ridges. This figure is created in a shallower domain (200 m depth) for a level ice of 3 m thickness with an ice ridge at $x = 520$ m to visualize the wave more clearly. Note that the waves are observed to be more distinct for thicker ice. A figure obtained for the same model with a 2 m thick surrounding ice is shown in Appendix B.II. , Figure 99.

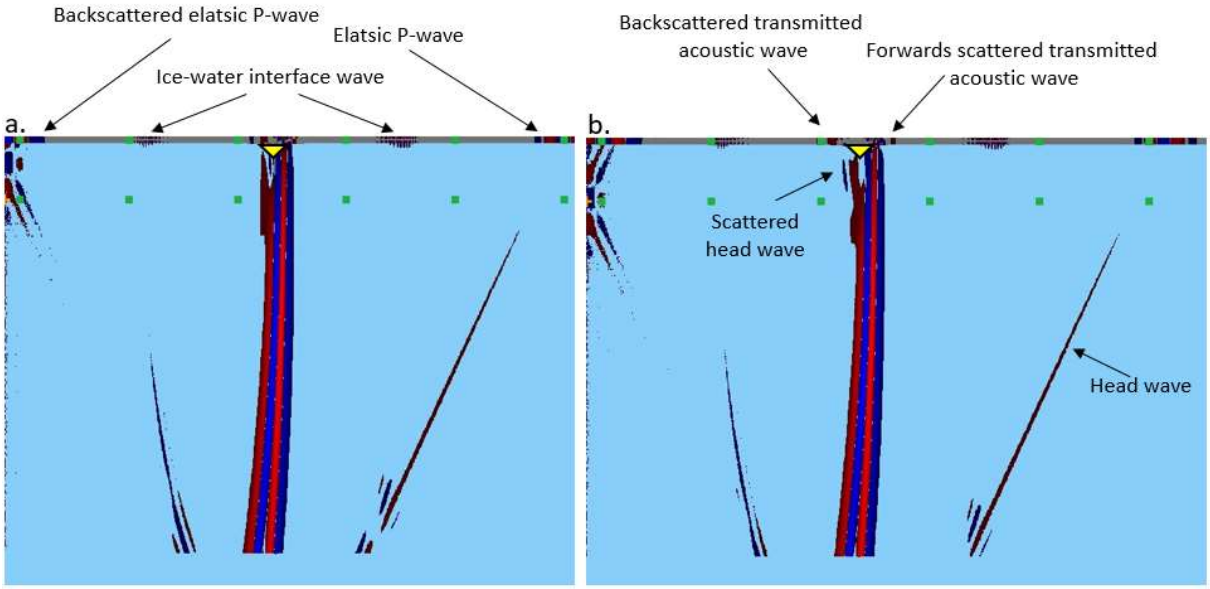

Figure 54. *The wave field of a wave propagating in a 200 m deep domain. Figure 54a shows the wave field over approximately 1100 m range and Figure 54b over approximately 1200 m range. The ice ridge is marked by a yellow triangle for clarity.*

Figure 55 shows the wave field at time $t = 2.13$, right after the acoustic wave has passed the second, deeper ice ridge. Both a backscattered (arrow a) and a forward scattered (arrow b) transmitted acoustic wave are observed. Note that a reflection from the absorbing layer can be observed in the figure.

Figure 55. *The wave field as described in Figure* 53*, but at time* $t = 2.13$*. The acoustic wave has just passed the second ice ridge at this point.*

To compare the effect of the shallower and deeper ice ridge their locations are exchanged, and the simulations are run with the deeper ridge in the first part of the domain ($x = 996$ m) and the shallower as the second ($x = 2992$ m). The figures of the wave field are very similar to what is already shown and will not be presented. The seismograms presented in this, and the following sections, are recorded at the receivers just before and after each ice ridge. The receivers are denoted 1,2,3, and 4, with a prefix denoting their vertical location, where 'i' denotes the receivers in the ice layer and 'w' denotes the receivers in the water layer, as shown in Figure 56.

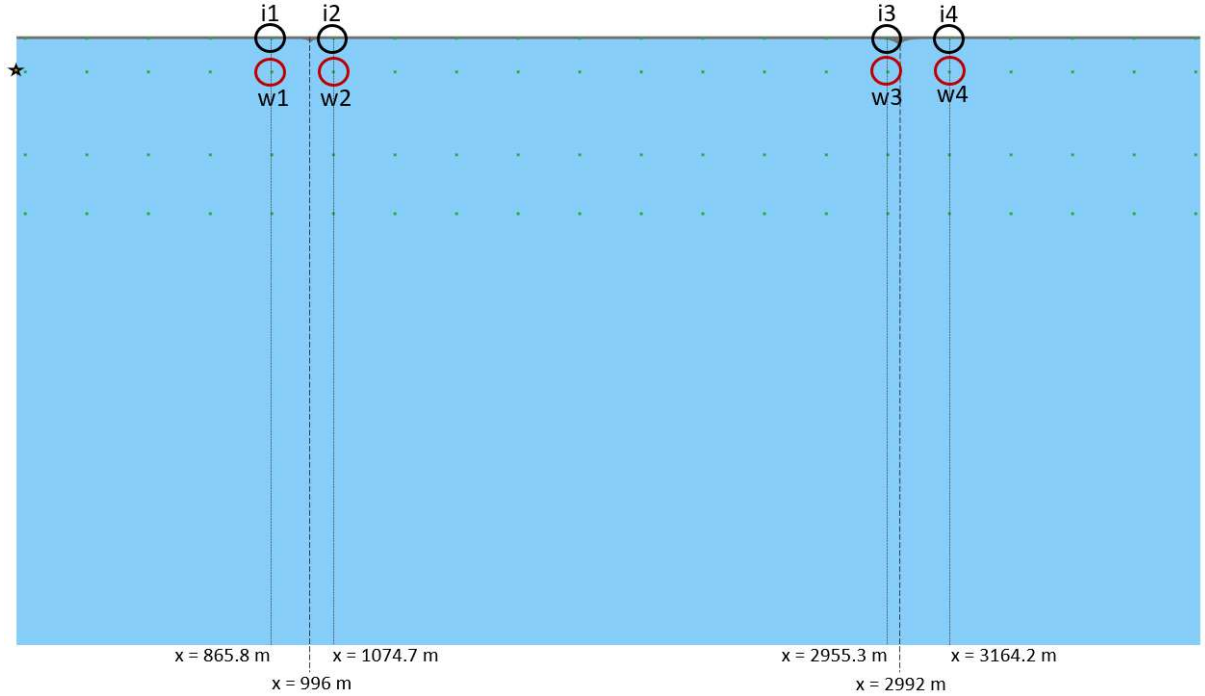

Figure 56. *The eight receivers that will be considered in this section. Receiver i1, i2, i3 and i4 are located at 1.5 m depth in the ice layer, and receiver w1, w2, w3 and w4 are located in the water, at 30 m depth. The green dots mark all receivers in the domain and the star marks the source.*

Seismograms for receiver w1, w2, w3, and w4 are shown in Figure 57, together with Model 2 from the previous section as a reference, where the time window is chosen to show the wave pulse of the acoustic wave. The acoustic wave does not show any notable differences when the two ice ridges are implemented. Neither does it show any difference whether the deeper ridge is located early (pink lines) or late (blue lines) in the domain.

The seismograms for receiver w1, w2, w3, and w4, are shown in Figure 58, with time windows chosen to show the head wave. The head wave (at approx. 0.31 s, 0.37s, 1.0 s, 1.09 s, for the receivers in Figure 58) does not show any large differences for the different ridge locations but is reduced in amplitude compared to Model 2. The elastic P-wave passes the first ice ridge at approximately 0.36 s, and the backscattering is likely shown around 0.4 s in Figure 58A. There is also a wave pulse at approximately 0.44 s in Figure 58A, which could be the wave propagating in the ice-water interface. The receiver is located 131 m from the ridge, and with a velocity of 1400 m/s it should reach the receiver at approximately 0.45 s. Two wave pulses are observed at approximately 1.4 s and 1.45 s in Figure 58C and Figure 58D, respectively. This pulse is not present in the simulation without ice ridges (Model 2, green lines) and is clearly caused by the ridges. In Figure 58C, a slight difference in amplitude of the head wave is observed when the two models with ice ridges are compared to each other, and there is also observed an extra pulse at around 1.35 s, which is not present in the model without ice ridges. Receiver w3 is located before the second ice ridge, which could be a backscattered head wave.

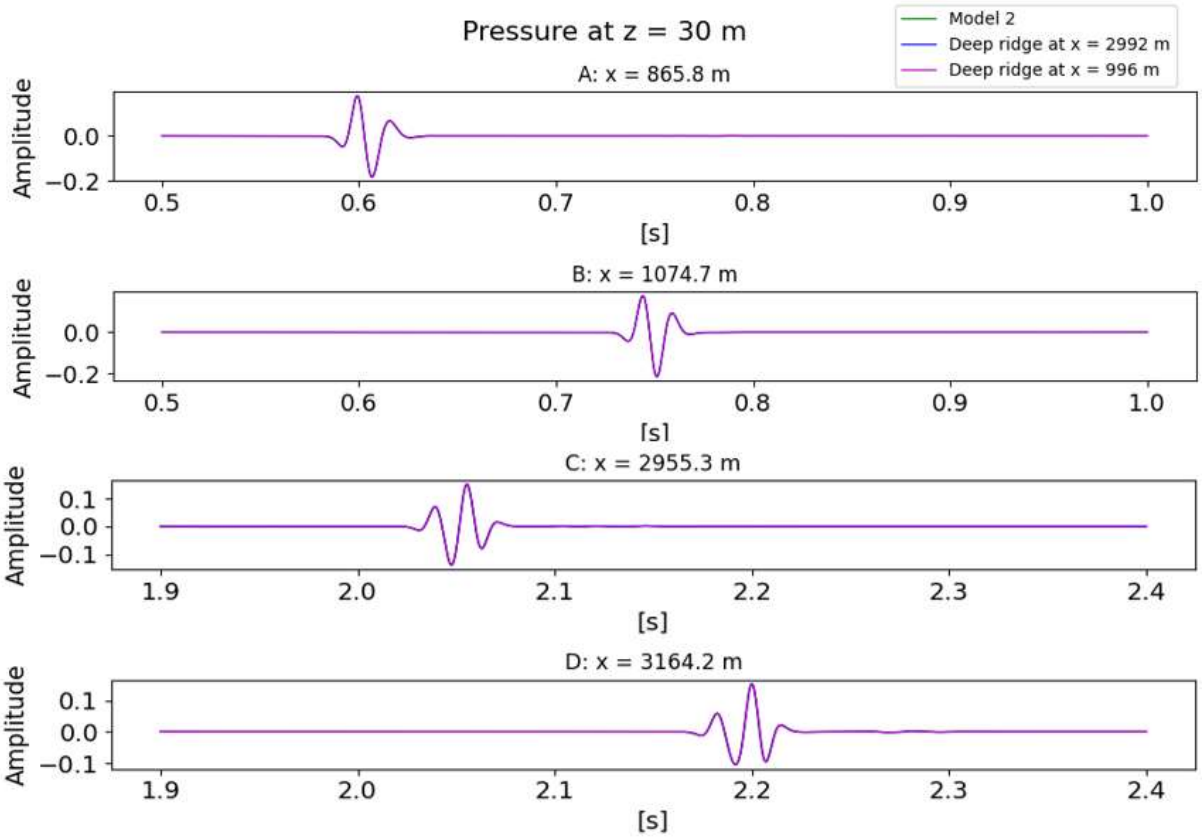

Figure 57. *The seismograms from receiver w1 (fig. A), w2 (fig. B), w3 (fig. C) and w4 (fig. D) showing the wave pulse of the acoustic wave for the model with the deepest ice ridge located first (pink) of the two ridges and last (blue) of the two ridges. Note the different scales on the axes.*

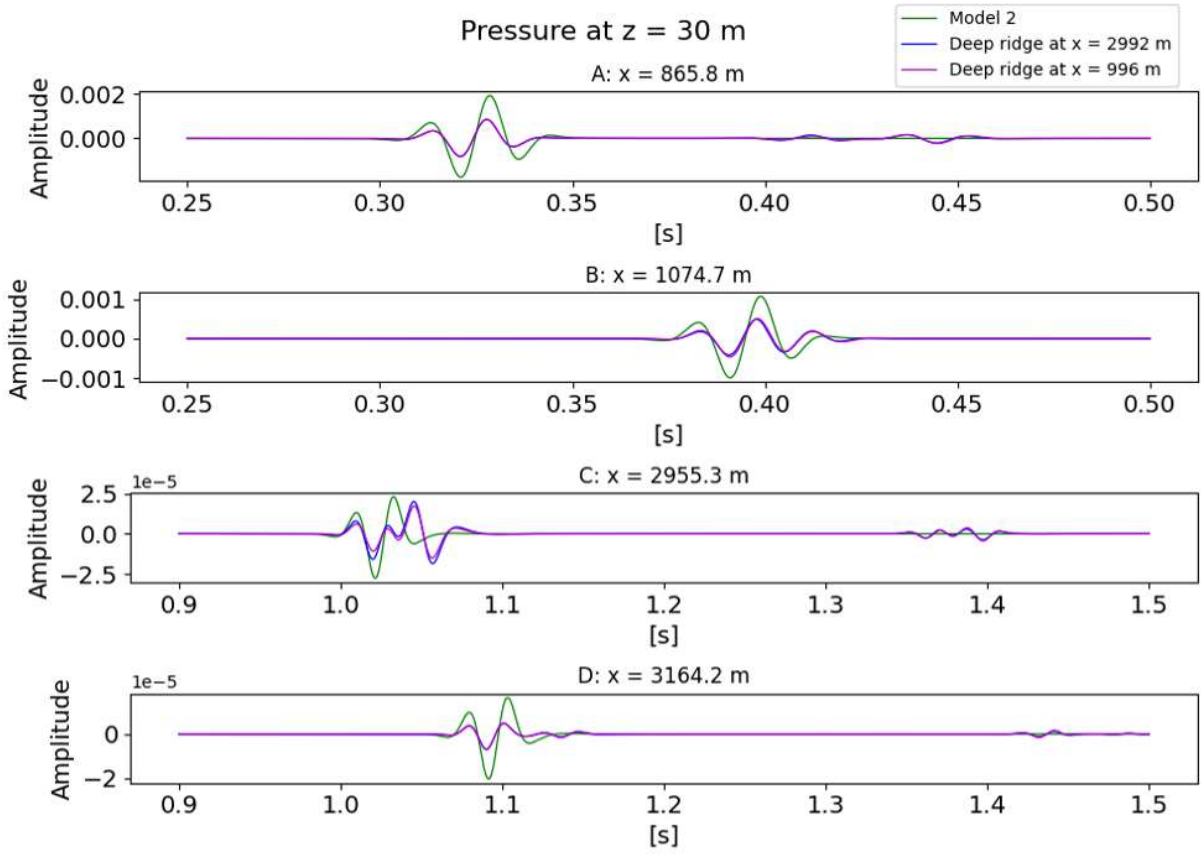

Figure 58. *Same as Figure 57, but the wave pulse of the head wave is shown instead.*

Seismograms from receiver i1, i2, i3, and i4, are shown in Figure 59 and Figure 60. The elastic P-wave can be observed in Figure 59 (at approx. 0.3 s, 0.37 s, 1.0, and 1.05 s for figure A-D, respectively), and shows no remarkable differences due to the difference in ridge depth. It is observed to decrease with increasing distance compared to Model 2, which does not have any ice ridges but 1 m thicker ice. The elastic P-wave reaches the first ice ridge at around 0.36, and the backscattered head wave is likely observed in Figure 59A at approximately 0.4 s. The transmitted acoustic wave is observed at approximately 0.6 s (Figure 59A, Figure 60A) and 0.75 s (Figure 59B, Figure 60B), 2.05 second (Figure 60C), and 2.2 s (Figure 60D). The transmitted acoustic wave shows differences in amplitude depending on the depth of the ice ridge it passes.

The acoustic wave passes the first ice ridge at around 0.72 s (Figure 53) and generates a forward- and backscattered transmitted acoustic wave. This backscattered transmitted acoustic wave could explain the wave pulse at 0.73 s in Figure 60A. The forward scattered acoustic wave could likely be observed at 0.74 in Figure 60B, and approximately 2.09 in Figure 60C. Overall, there are small differences in the amplitude between the two cases of different ridge locations. In both amplitude and pulse shape, the most notable differences appear to be for the scattered transmitted acoustic wave.

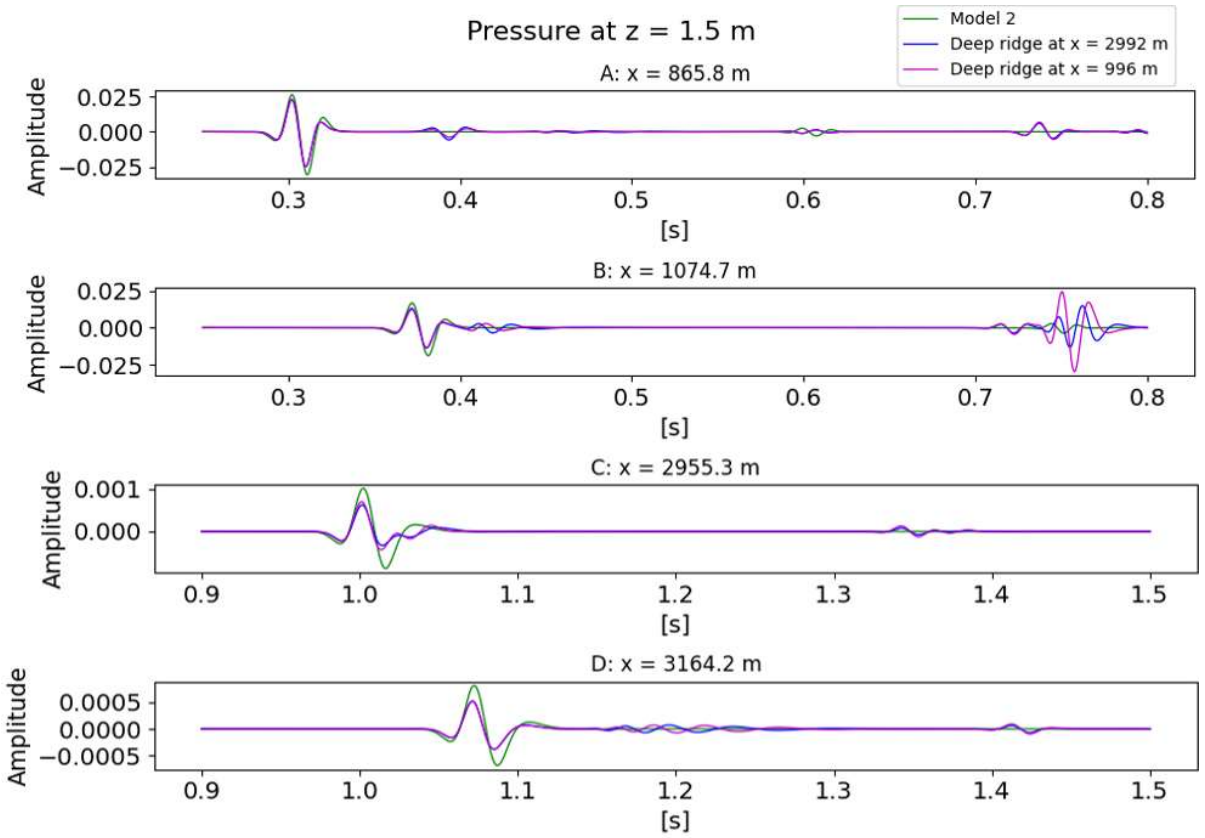

Figure 59. *The seismograms from receiver i1 (fig. A), i2 (fig. B), i3 (fig. C) and i4 (fig. D) showing wave pulse of the elastic P-wave, amongst other waves, in a chosen time window for the model with the deepest ice ridge located first (pink) of the two ridges and last (blue) of the two ridges. Note the different scales on the axes.*

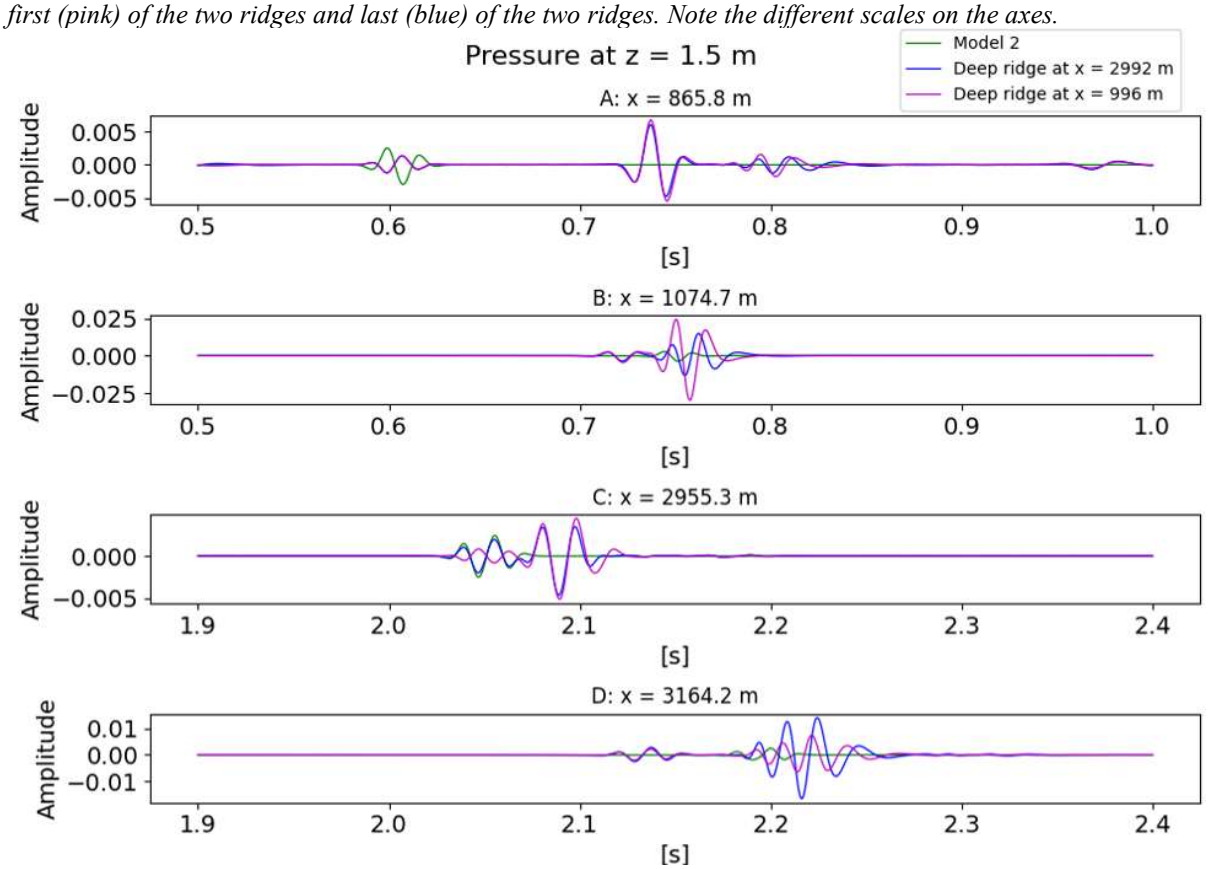

Figure 60. *Same as Figure 59, but with chosen time windows to show the wave pulses of the transmitted acoustic wave. Note the different scale on the axes.*

On the presented seismograms, the amplitude of the transmitted acoustic wave can be observed larger for the deeper ice ridge after the acoustic wave has passed the ridge (e.g., 0.75 s in Figure 60B and 2.2 s in Figure 60D. A crop out of the wave field figures showing the acoustic wave after it passed the first ice ridge in the domain is shown in Figure 61 and Figure 62, between approximately 1070 m and 1700 m at time $t = 0.89$ s. The ice model with the deepest ice ridge at this location is shown in Figure 61, while Figure 62 is showing the ice model with the shallower ice ridge at the same location. A wave propagating in the ice layer and the ice-water interface can be observed, which appears stronger after the deeper ice ridge.

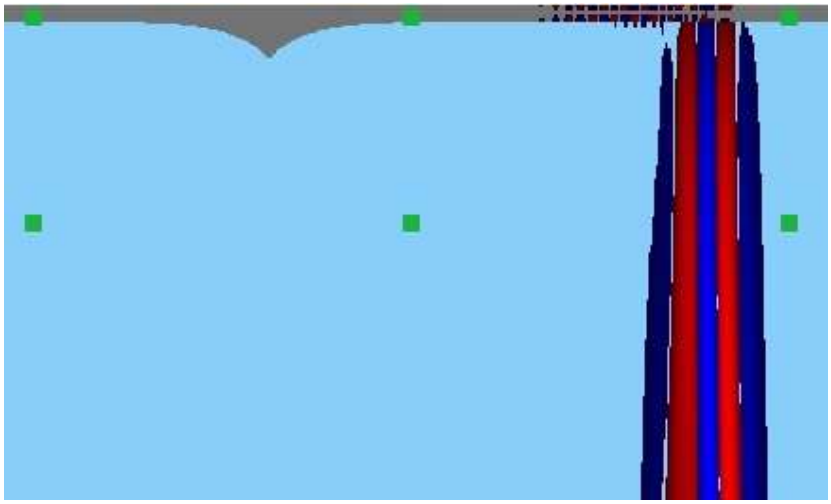

Figure 61. *The wave field at 0.89 s for the ice model with the deepest ridge at x = 996 m. The acoustic wave has passed the ice ridge. A wave propagating in the ice and at the ice-water interface can be observed.*

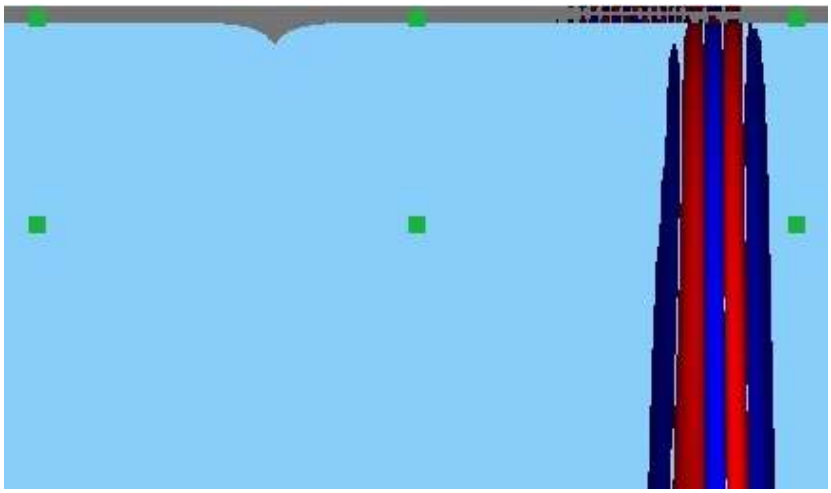

Figure 62. *The wave field at 0.89 s for the ice model with the shallower ice ridge at x=996 m. The wave in the ice layer appears weaker than for the corresponding model with a deeper ice ridge at the same location in Figure 61.Also, the wave seems to propagate more in the ice and not in the ice-water interface.*

Only small differences between the models with two ice ridges and the model without ice ridges are observed in terms of loss. At 4 km is the loss 34.16 dB for both models. Figure 63 shows the transmission loss difference in dB at 30 m depth, using Model 1 (water only) and Model 2 (3 m thick ice) from the previous section as reference models. Negative signs denote decreased loss, while positive signs denote increased loss, compared to the reference model in question. Both models with ridges have approximately 0.19 dB less transmission loss than Model 1 (Figure 63, left side) and approximately 0.19 dB more loss than Model 2 (Figure 63, right side), at 4 km. In connection to the first ridge, there can be observed an increase in the difference between the ice model with the deepest ridge at this location, and Model 2 as reference model, meaning that there is an increased transmission loss at those points. Note that the differences in transmission loss are overall very small.

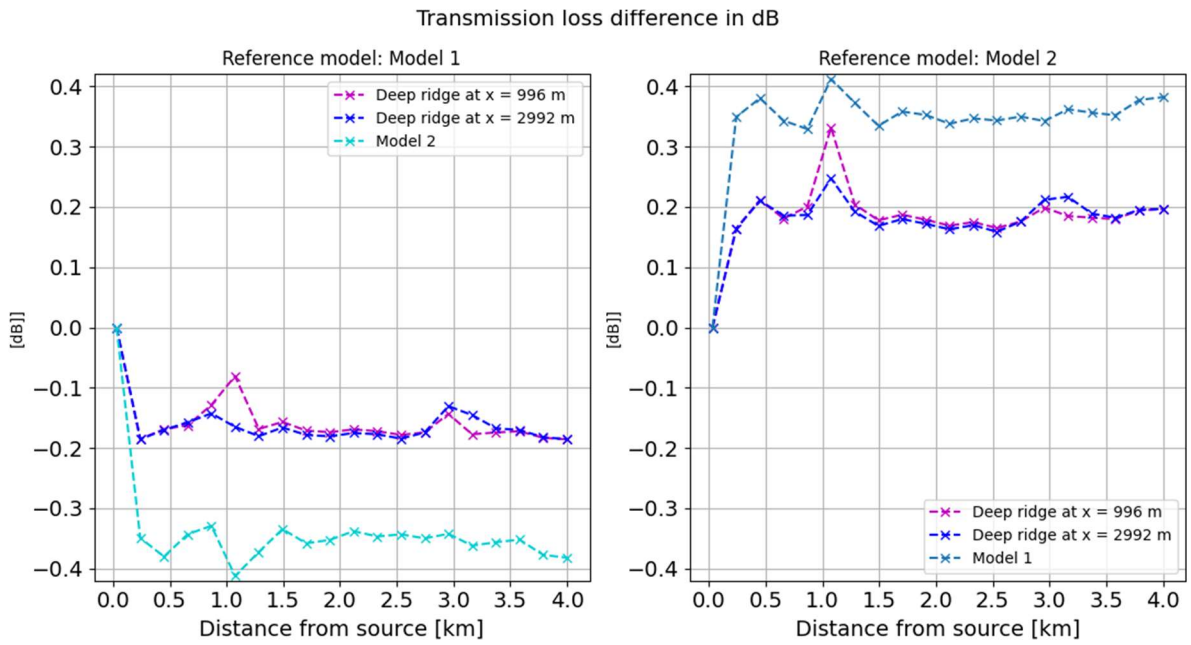

Figure 63. *Transmission loss difference in dB at 30 m depth, with Model 1 (water only) on the left side, and Model 2 (3 m thick ice) on the right side, as reference models. Positive signs denote more loss, and negative signs denote less loss, compared to the reference model in each figure.*

Figure 64 shows transmission loss curves at 1.5 m depth, in the ice layer. The curves are irregular but show an overall decrease in loss for the models with ice ridges (blue and pink lines), compared to the 3 m thick ice layer without any ice ridge (light blue line). A decrease in transmission loss is shown where the deeper ice ridge is located, consistent with the increased transmission loss in Figure 63.

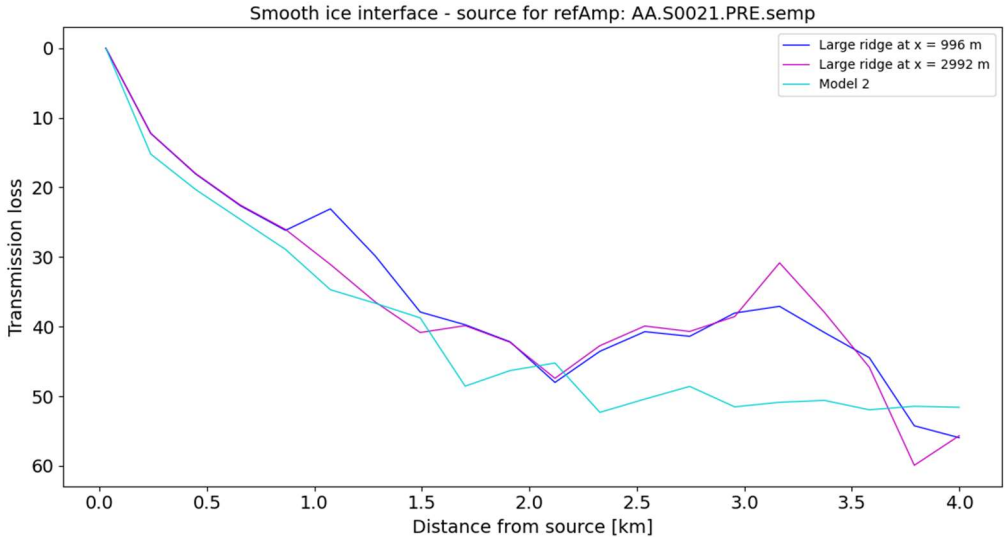

Figure 64. *Transmission loss in dB curves as in Figure 63, but at 1.5 m depth and without Model 1. Note that the labels have different colors than in the previous figures. The model with 3 m thick ice is shown in light blue, the model with a deeper (7.1 m) ice ridge at 996 m is shown in blue, while the ice ridge with a shallow (4.9 m) ice ridge at 996 m is shown in pink.*

To study the impact of source depth on transmission loss, the ice model with the shallowest ice ridge in the first part of the domain was modeled with four different source depths. Figure 65 shows transmission loss curves at 1.5 m and 30 m depth for a source located at 10 m (blue line), 30 m (pink line), 50 m (light

blue line), and 100 m (purple line) depth. The transmission loss recorded at 30 m depth (Figure 65a) is observed to decrease with an increasing source depth. The transmission loss curves within the ice layer (Figure 65b) is a bit irregular but also shows greatest loss for the shallowest source.

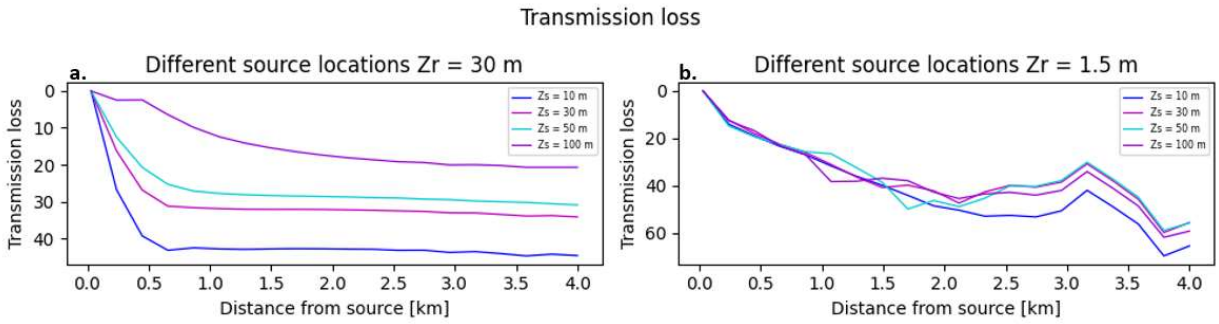

Figure 65. *Transmission loss curves in dB for a receiver at 30 m depth (fig. a.) and within the ice layer (fig. b.), for a source at 10 m (blue lines), 30 m (pink lines), 50 m (light blue lines), and 100 m (purple lines) depth.*

5.4.2. A rough ice model with two ice ridges

In this section, ice roughness is implemented in the simulations, as the only difference from the previous section. The simulation used time step $dt = 2.1916 \cdot 10^{-5}$ s over 130000 steps. The CPU time was 9 h 52 min. Model 2 (3 m thick ice) from the previous section is also used as a reference model in this section. The wave field at time $t = 0.75$ and at $t = 2.13$ s is visualized in Figure 66 and Figure 67, respectively. Both figures show great similarities to the figures of the wave field in the domain with a smooth ice-water interface (Figure 53, Figure 55). However, more backscattered waves (e.g., arrow a in Figure 66) and noise are observed at the symmetry axis in the simulations with rough ice.

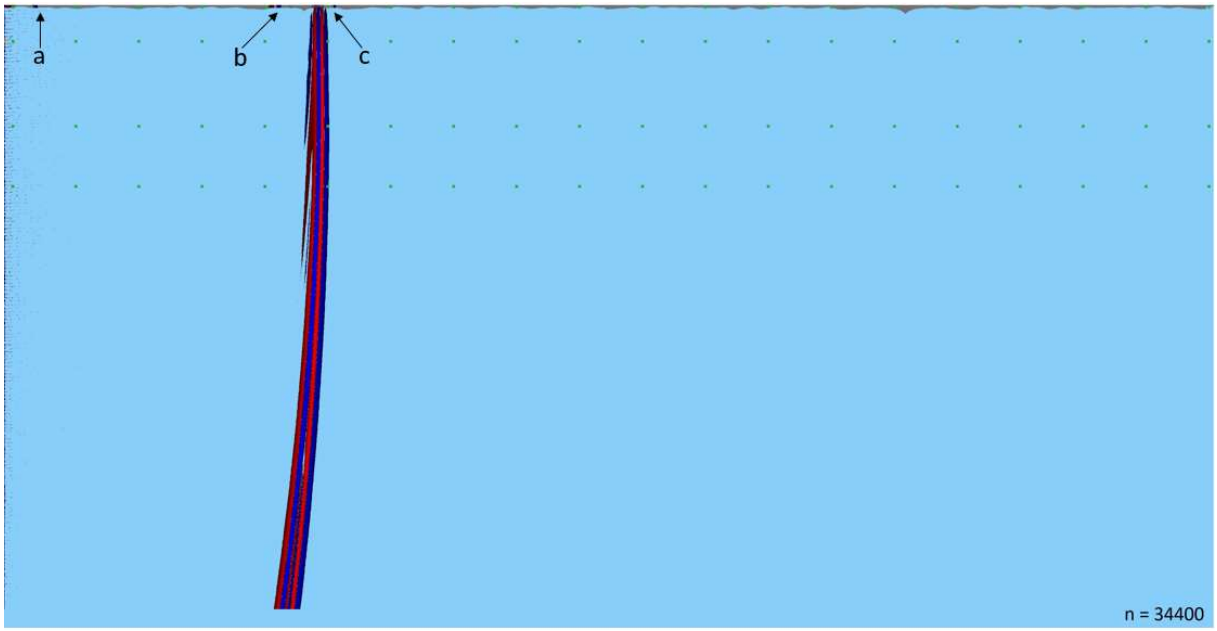

Figure 66. *The wave field at* $t = 0.75$. *The domain has two ridges, a shallower at* $x = 996$ *m and a deeper at* $x = 2992$ *m, and a rough ice-water interface. Arrow a show the backscattered elastic P-wave, arrow b the backscattered transmitted acoustic wave and arrow c the forward scattered transmitted acoustic wave.*

As in the previous section, there is no difference in the wave pulse of the acoustic wave caused by the different ridge locations. Also, the amplitude corresponds to what was shown in the previous section, and therefore, the seismograms showing the acoustic waves separately are not presented in this section.

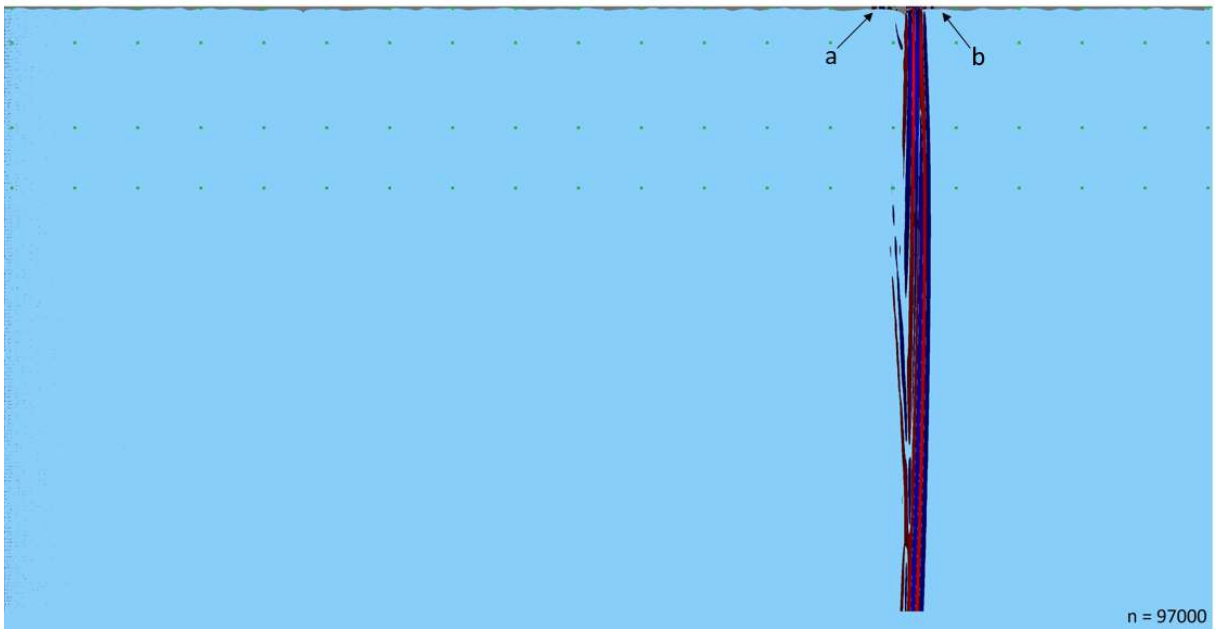

Figure 67. *The wave field as in Figure* 66*, but at time* $t = 2.13$ *s.*

The wave pulse of the head wave is shown for station w1, w2, w3, and w4. in Figure 68.

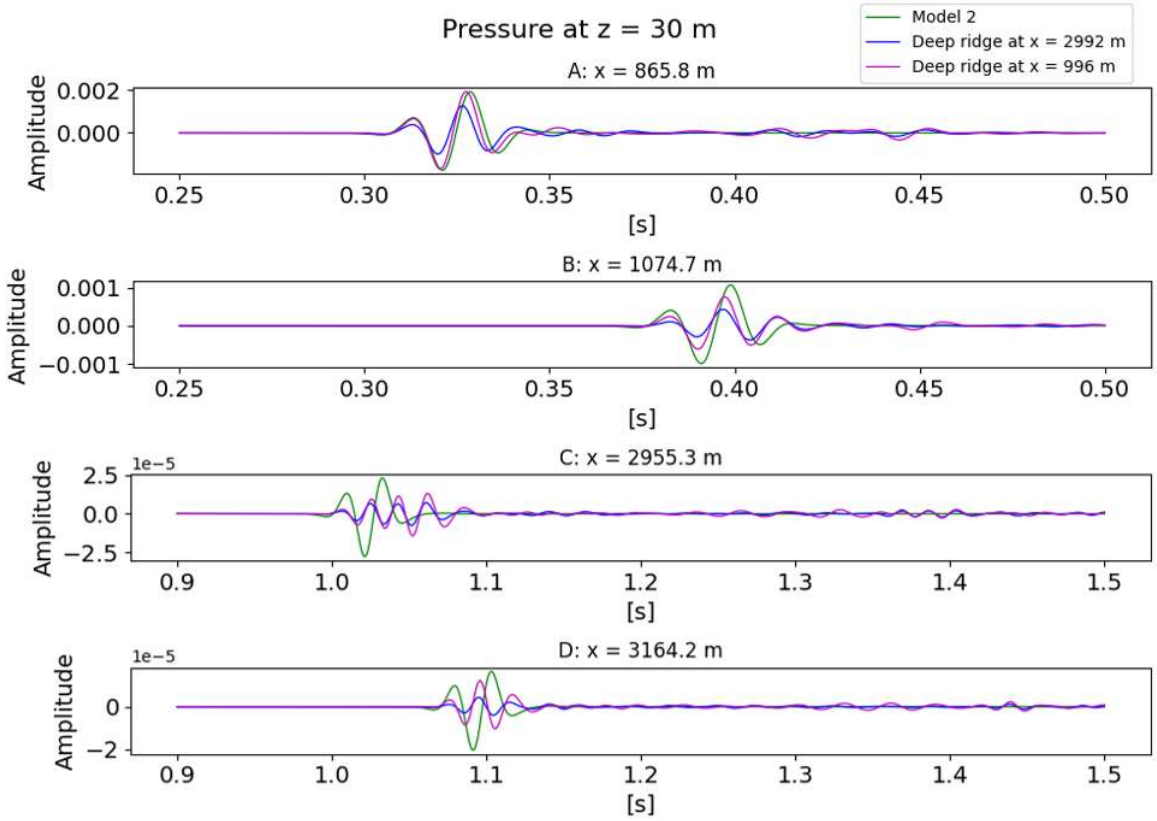

Figure 68. *The seismograms from receiver w1 (fig. A), w2 (fig. B), w3 (fig. C) and w4 (fig. D), showing the wave pulse of the head wave for the model with the deepest ice ridge located first (pink lines) and last (blue lines) parts of the domain with a rough ice-water interface. Note the different scales on the axes.*

In Figure 68, a larger amplitude is observed for the simulation where the deeper ridge is located in the first part of the domain (pink lines). In general, the rough ice-water interface generates many extra oscillations on the seismograms. Note that a larger amplitude of the head wave is observed for the model with a deep ice ridge in the first part of the domain (pink lines). This can also be observed before the wave has passed the first ice ridge.

Figure 69 and Figure 70 show seismograms recorded at 1.5 m depth on chosen time intervals. The elastic P-wave (Figure 69) is, as the head wave, observed to have larger amplitudes when the deeper ridge is located in the first part of the domain (pink lines). Also, note the differences in the transmitted acoustic wave recorded at receiver i2 (78 m after the first ridge) between the models (at approx. 0.75 s, Figure 70b), where a larger amplitude is observed for the ridge with the deeper ridge at this location. This can also be observed after the second ice ridge, where the amplitude of the transmitted wave becomes largest for the model with the deepest ridge at this location (at approx. 2.2 s in Figure 70D)

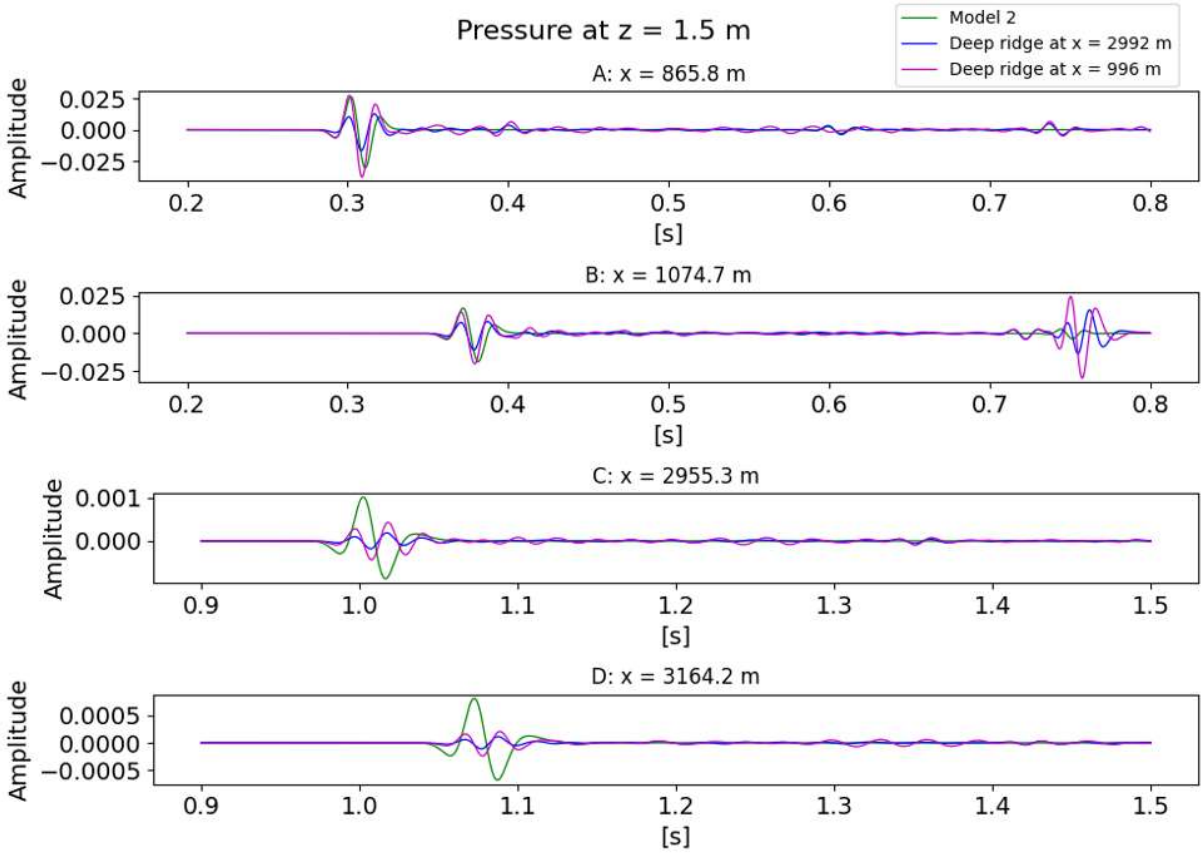

Figure 69. *Seismograms from receiver i1 (fig. A), i2 (fig. B), i3 (fig. C) and i4 (fig. D), in a time window showing the elastic P-wave.*

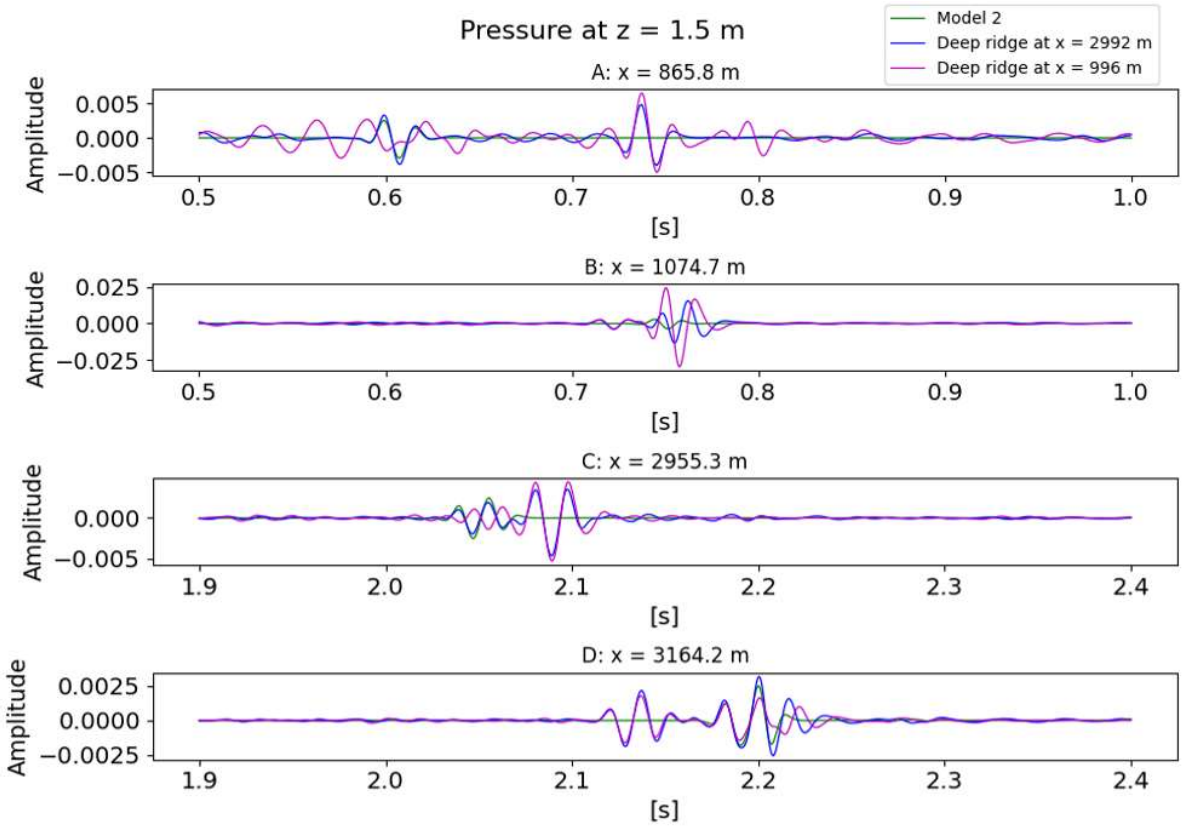

Figure 70. *Seismograms as in Figure 69, but for time intervals around the arrival of the transmitted acoustic wave.*

Figure 71 shows the transmission loss curves in the ice layer. The transmission loss curves displays sharp variations. One can, however, observe a decreased loss in connection to the location of the ice ridges, at around 1 and 3 km, where the least loss is observed for the models with the deeper ice ridge at the location in question.

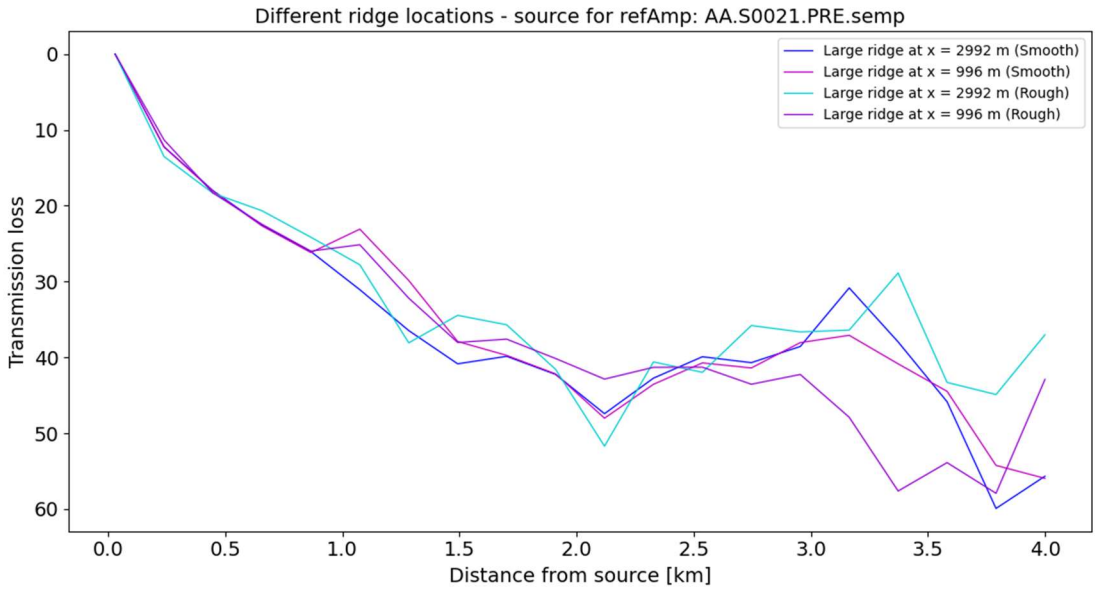

Figure 71. *Transmission loss curves in dB at 1.5 m depth for the four ice models. Two models with the deeper ice ridge in the first part of the domain, one smooth (pink line) and one rough (purple line), and two models with the deeper ice ridge in the second part of the domain, one smooth (blue line) and one rough (light blue line).*

As in all the previous cases, there are only small differences between the models for the transmission loss at 30 m depth. Figure 72 shows transmission loss differences in dB with Model 1 (water only) and Model 2 (3 m thick ice) from Section '*5.3. Simulations with an Arctic sound speed* profile' as reference models. It is observed that the model with the deep ridge in the second part of the domain (blue lines) has a larger transmission loss than both Model 2 and the model with a reversed location of the ice ridges. The model with the deepest ice ridge in the first part of the domain (pink lines) is observed to have less transmission loss than Model 2. Note that the differences in transmission loss are very small.

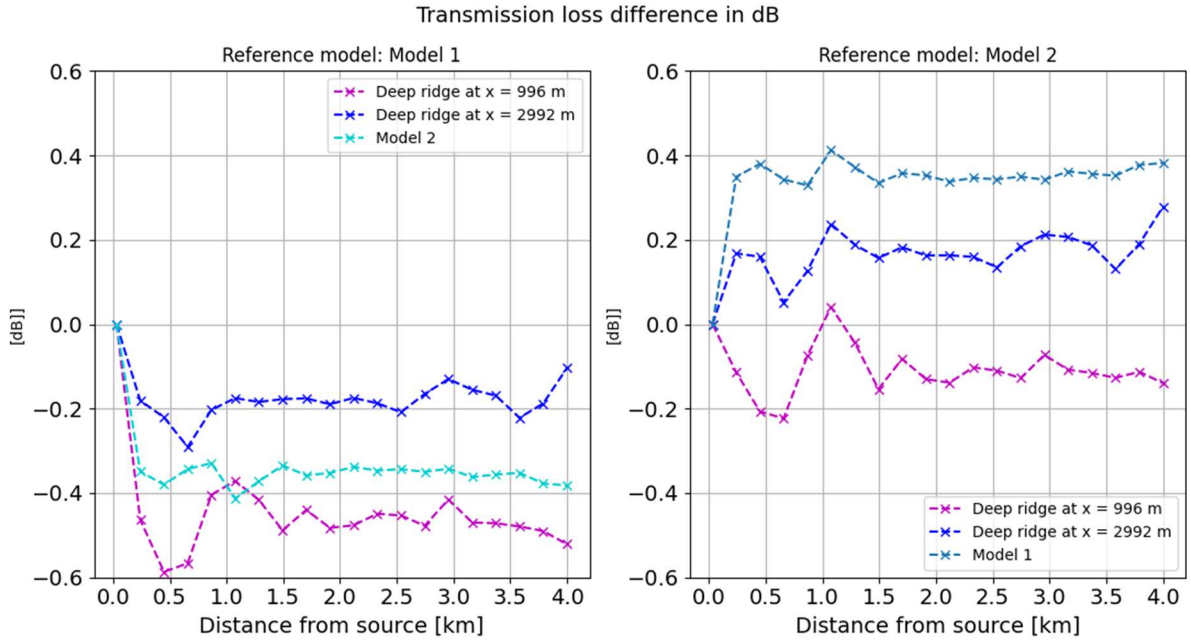

Figure 72. *Transmission loss differences in dB at 30 m depth, with Model 1 (water only) and Model 2 (3 m thick ice) as reference models. Positive signs denote more loss, and negative signs denote less loss, compared to the reference model in each figure. The model deepest ridge at the first part of the domain has blue lines, while the model with the deepest ridge in the second part of the domain has pink lines. Both models have a rough ice-water interface.*

5.4.3. The effect of ice roughness and ice ridges

To get a better view of the contribution from ice ridges and ice roughness, two models with ice ridges will be compared to the model with an ice layer of 3 m thick homogeneous ice with a smooth ice-water interface (Model 2 in Section '*5.3. Simulations with an Arctic sound speed* profile'). The models with ice ridges have the shallower ridge keel in the first part of the domain (at $x = 996$ m) and the deeper keel in the second part (at $x = 2992$ m), one with a smooth and one with a rough ice-water interface.

The seismograms recorded at 30 m depth just before and after the first ice ridge are shown in Figure 73 (receiver w1) and Figure 74 (receiver w2).

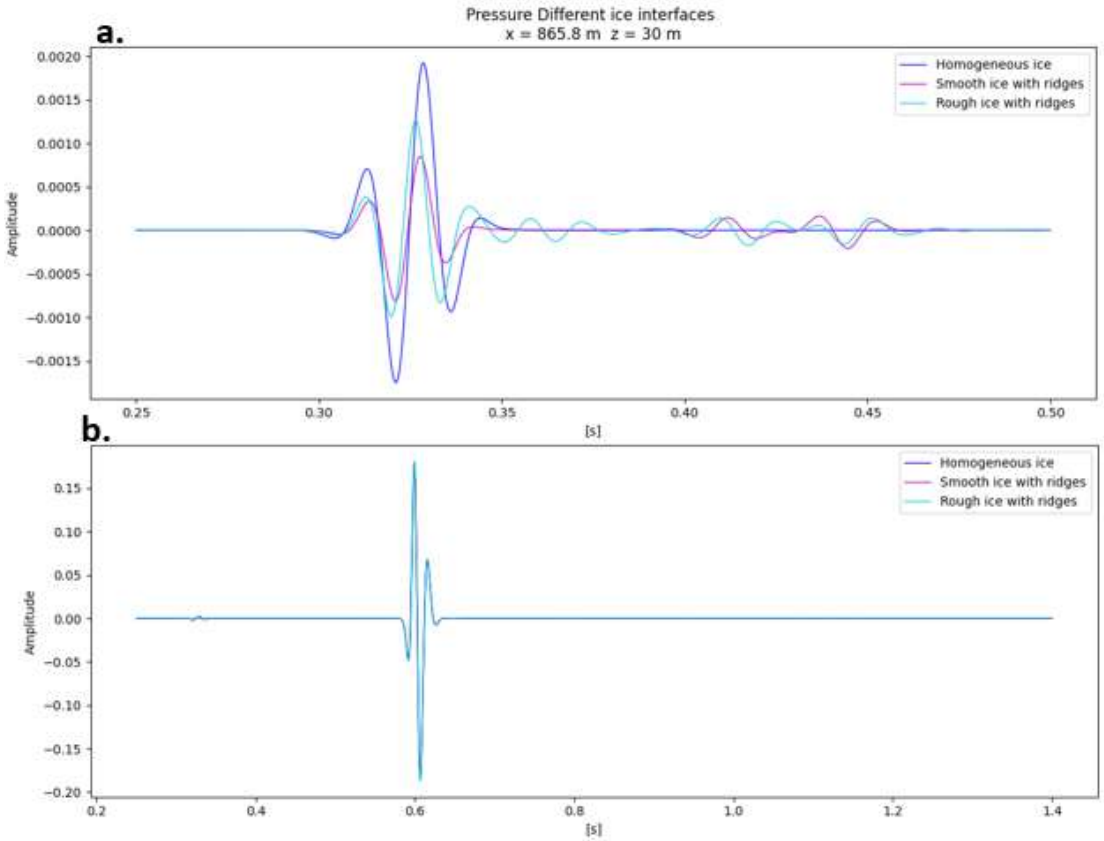

Figure 73. *The seismograms from receiver w1, where Figure 73a shows the head wave and Figure 73b the acoustic wave for a model with 3 m thick smooth ice (blue lines), and two models with ice ridges, one with a smooth (pink lines) and one with a rough (light blue lines) ice-water interface.*

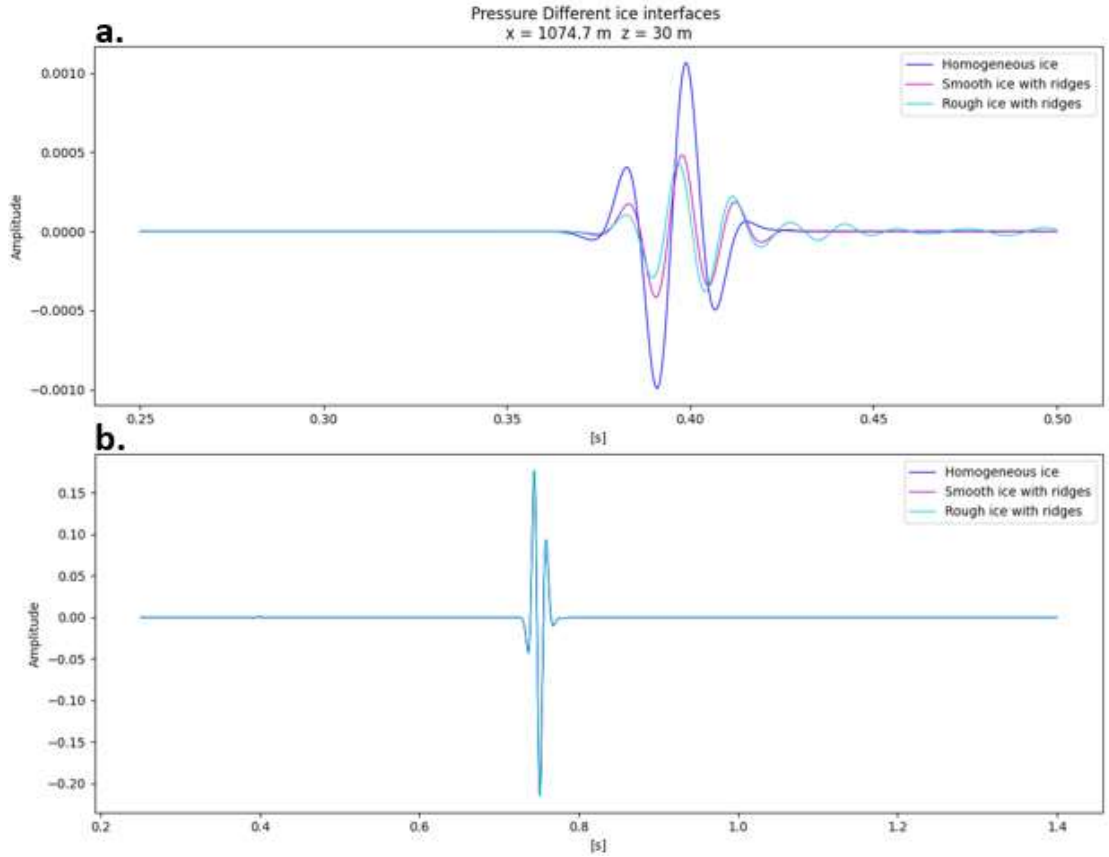

Figure 74. *Seismograms as in Figure 73, but from receiver w2.*

In Figure 73, the seismograms recorded at the receiver placed approximately 130 m before the first ice ridge. The amplitude of the head wave is larger for 3 m thick homogeneous ice (blue line), and the smallest for the model with ice ridges and a smooth ice-water interface (pink line). Smaller oscillations are observed around the head wave for the model with ice roughness and two ridges (light blue line). The backward scattered head wave (at approx. 0.4 s) and the following wave propagating in the ice-water interface (at approx. 0.44 s) are observed to be affected by the ice roughness.

For the seismograms recorded approximately 78 m after the first ice ridge (Figure 74), the amplitude is, as in the previous section, largest for homogeneous ice, but the difference between the smooth and rough model with ice ridges has decreased. The acoustic wave (Figure 74b) does not show any large difference between the models, but small differences are present. The amplitude of the acoustic wave is 0.178 for Model 2, 0.179 for the smooth ice model, and 0.181 for the rough ice model.

The seismograms recorded 130 m before the first ice ridge 1.5 m depth (receiver i1) are shown in Figure 75. The amplitude of the elastic P-wave (Figure 75a) is largest for 3 m thick homogeneous ice and smallest for the ice model with ice roughness. The backscattered acoustic wave is observed in Figure 75b, which shows a larger amplitude for the smooth ice model with two ridges. The transmitted acoustic wave is shown in Figure 76, where largest amplitude is observed for the rough ice model with two ridges and the smallest for the smooth ice model with two ridges.

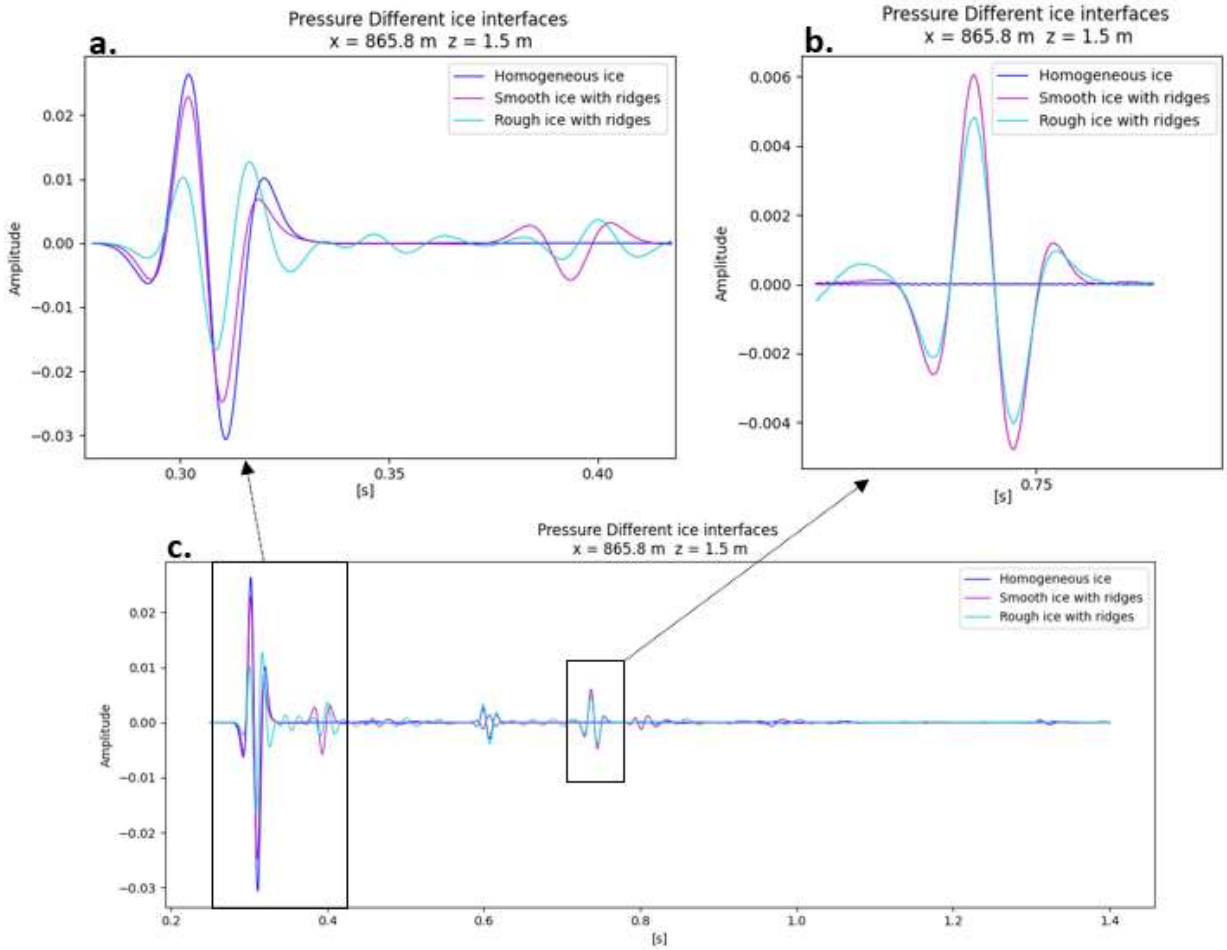

Figure 75. *Seismograms from receiver i1, where Figure 75a shows the elastic P-wave and Figure 75b the backscattered transmitted acoustic wave for a model with 3 m thick smooth ice (blue lines), and two models with ice ridges, one with a smooth (pink lines) and one with a rough (light blue lines) ice-water interface.*

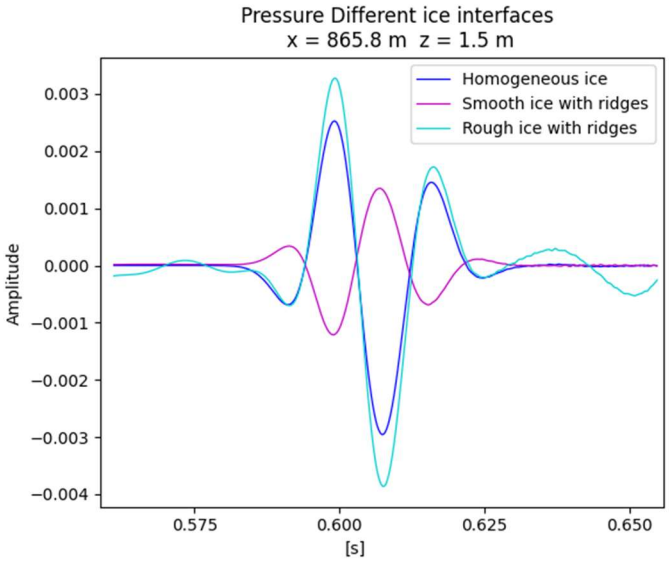

Figure 76. *A zoom in on Figure 75c at approximately 0.6 s, showing the wave pulse of the transmitted acoustic wave at receiver i1.*

Seismograms for receiver i2 are shown in Figure 77. The pulse of the elastic P-wave (Figure 77a) shows the same features as before the ice ridge (Figure 75a) but with decreased amplitudes. Figure 77b shows the transmitted acoustic wave (at approx. 0.74) and the forward scattered acoustic wave (at approx. 0.76 s).

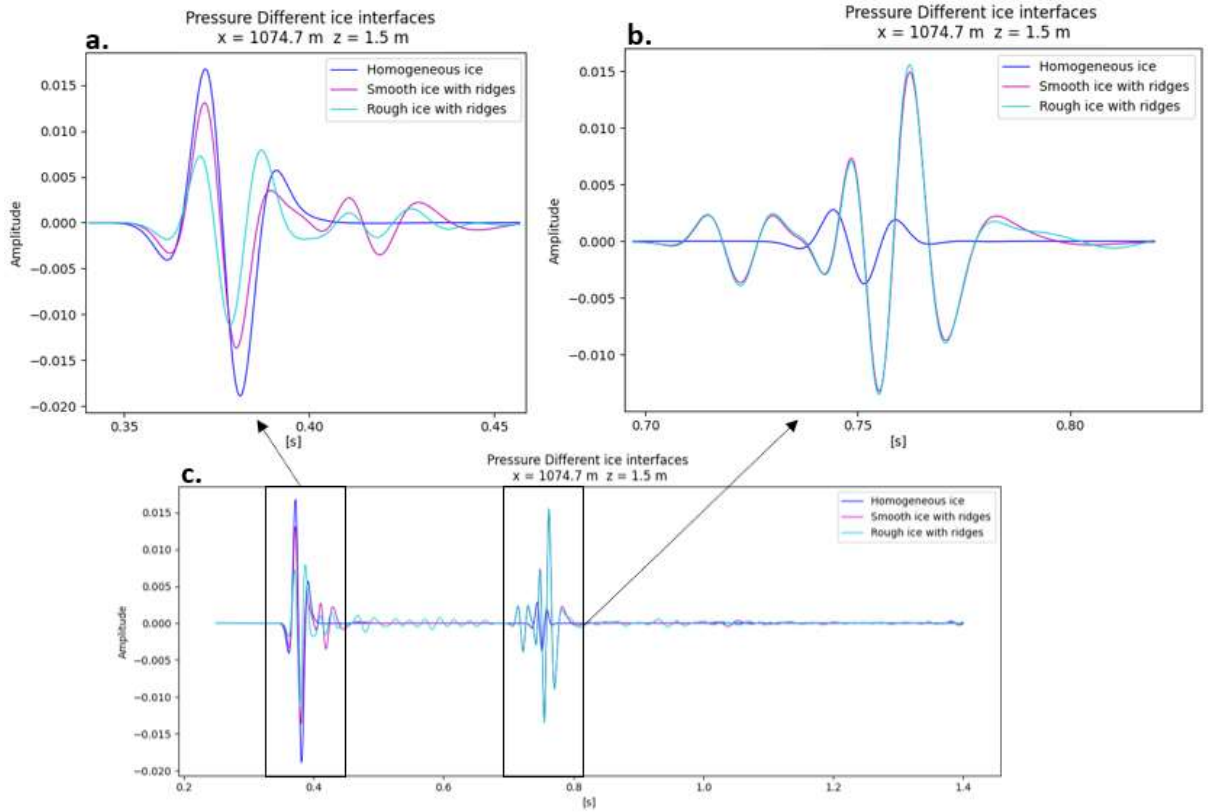

Figure 77. *Seismograms from receiver i2. The elastic P-wave is shown in Figure 77a, and the transmitted acoustic wave is shown in Figure 77b for a model with 3 m thick smooth ice (blue lines), and two models with ice ridges, one with a smooth (pink lines) and one with a rough (light blue lines) ice-water interface.*

Transmission loss differences at 30 m depth with Model 1 (water only) and Model 2 (3 m thick homogeneous ice) as reference models are shown in Figure 78. Note that the differences in all cases are

small, and that the transmission loss is almost the same for both the smooth (pink lines) and rough (light blue lines) models with two ice ridges. However, both models with ice ridges show a slightly larger transmission loss than Model 2.

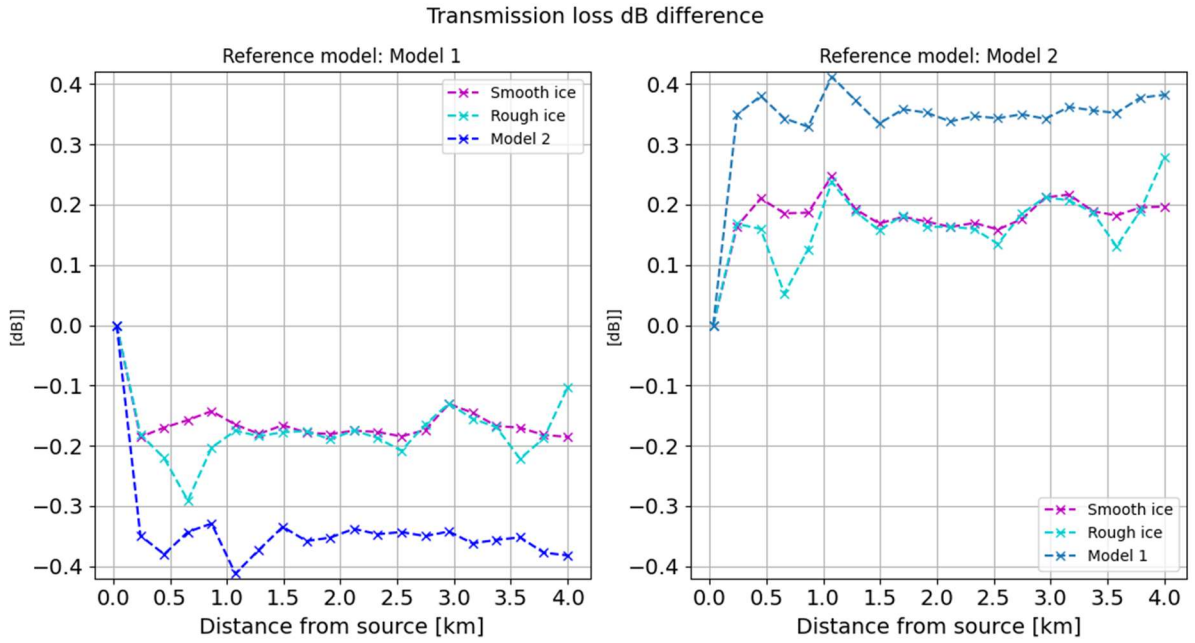

Figure 78. *Transmission loss differences at 30 m depth with Model 1 (water only) and Model 2 (3 m thick ice) as reference models. Positive signs denote more loss, and negative signs denote less loss, compared to the reference model in each figure.*

The transmission loss curves from 1.5 m depth are shown in Figure 79. The ice models with two ice ridges shows less transmission loss than the model with 3 m constant thickness at increasing distances. The curves are irregular, but no large difference between the smooth and the rough ice model with two ice ridges is shown.

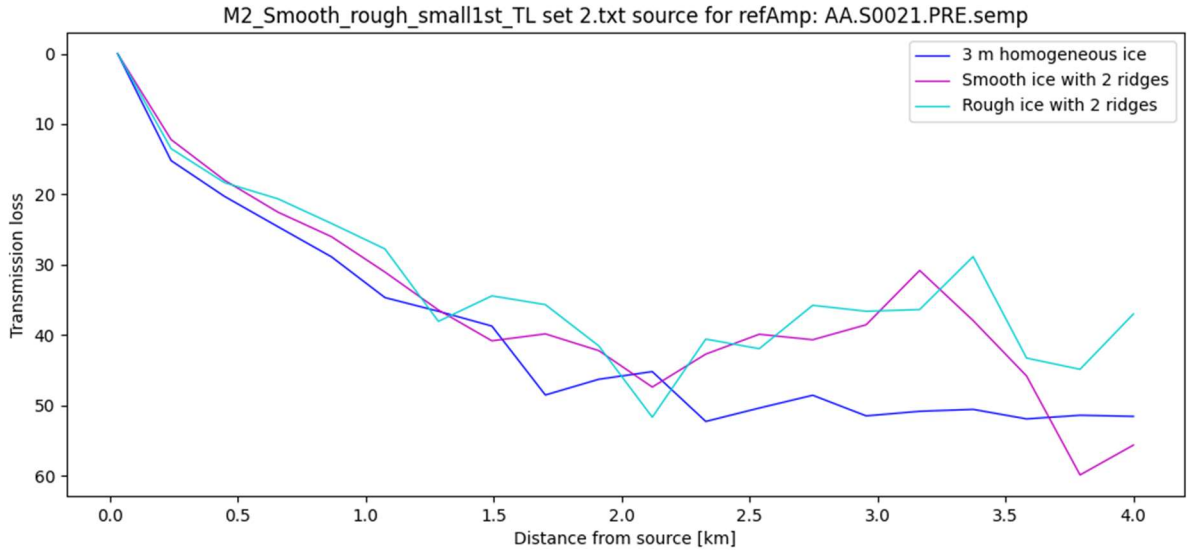

Figure 79. *Transmission loss in dB at 1.5 m depth for 3 m thick ice (blue line), smooth ice with two ice ridges (pink line), and rough ice with two ice ridges (light blue line).*

5.4.4. The effect of the sound velocity profile

To study the effect of an upwards refracting Arctic sound speed profile on waves interacting with ice ridges, the results of the previous section, using upwards refracting profiles, are compared to runs with a homogeneous velocity profile ($v_p = 1482\ m/s$), using the same ice models. For the models with a homogeneous velocity profile, the CPU times were 5 h 43 min and 10 h 56 min for the smooth and rough ice model, respectively.

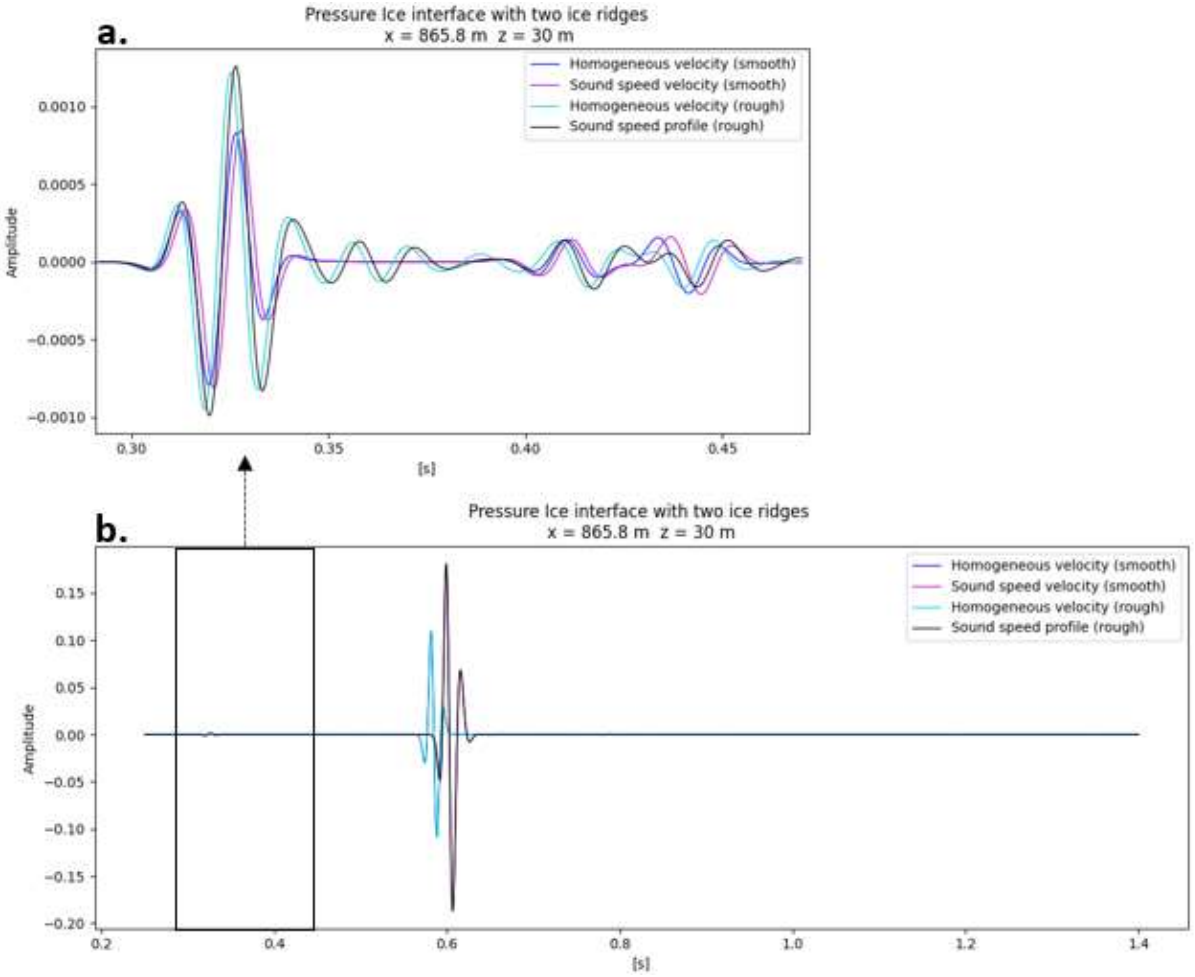

Figure 80. *Seismogram from receiver w1, showing two models with a homogeneous velocity profile; one with smooth (blue lines) and one with rough ice (light blue lines), and two models with an Arctic sound speed profile; one with smooth (pink lines) and one with rough (black lines) ice.*

Figure 80a shows the head wave recorded at receiver w1, where larger amplitudes for the models with a rough ice-water interface are observed, no matter the velocity profile. The difference in amplitude reduces after the head wave has passed the first ice ridge, and the models with a smooth ice-water interface can instead be shown to be slightly larger at this point (Figure 81). However, the difference is very small, and all models are quite similar at this point. The amplitude of the acoustic wave is significantly larger for the models with an Arctic sound speed profile both before and after the first ice ridge (Figure 80b, Figure 81b), and the relative difference increases with distance. Due to the different velocities in the water, time shifts are observed.

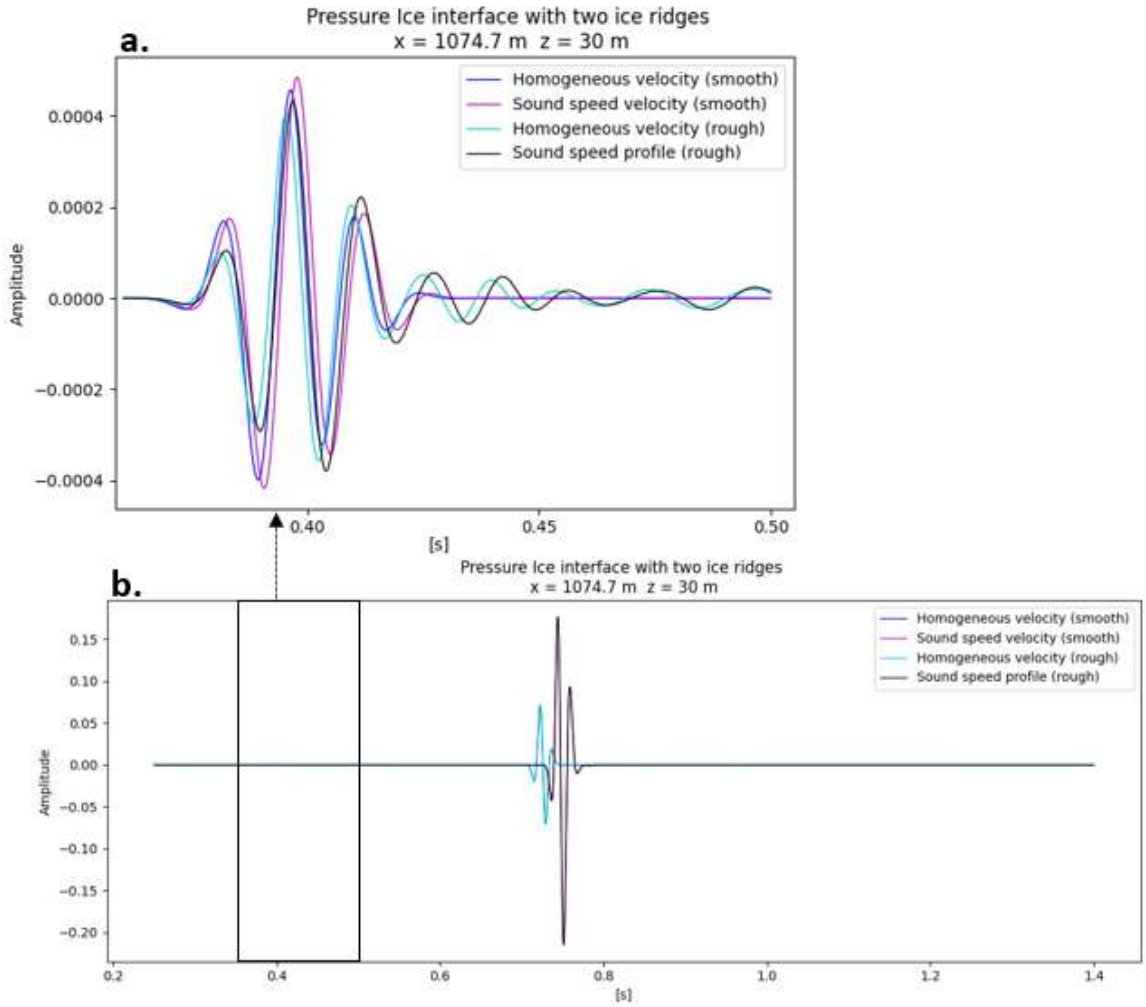

Figure 81. *Same as in Figure 80, but for receiver w2.*

The difference in amplitude of the acoustic wave between the models of different velocity profiles continues to grow throughout the domain. Figure 82 shows a significantly larger amplitude for models with an Arctic sound speed profile, no matter the shape of the ice-water interface after 2955.3 m. The head wave appears to be most affected by the ice roughness, where much smaller amplitudes are observed for rough ice in Figure 83. Note that the scales in Figure 82 and Figure 83 are very different.

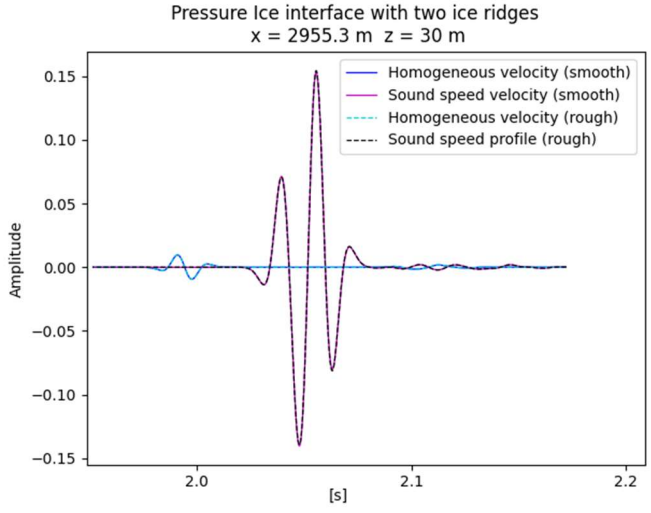

Figure 82. *The wave pulse of the acoustic wave recorded at receiver w3, showing the two models with a homogeneous velocity profile; one with smooth (blue lines) and one with rough ice (light blue lines), and the two models with an Arctic sound speed profile; one with smooth (pink lines) and one with rough (black lines) ice.*

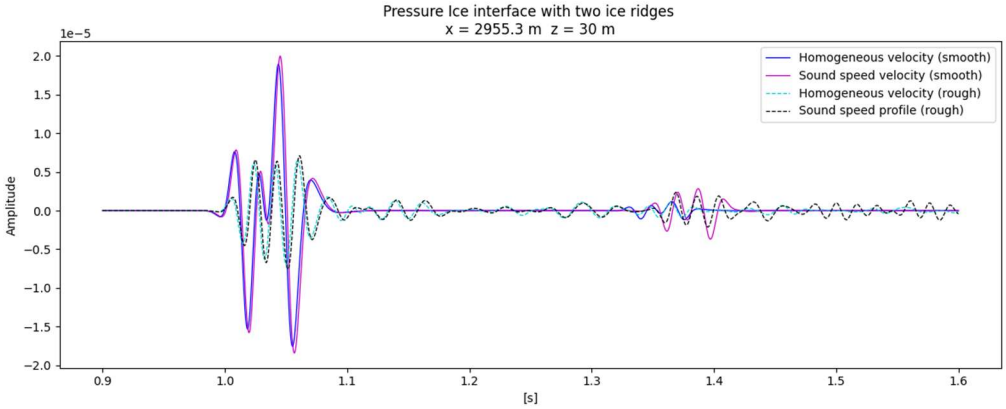

Figure 83. *Same as Figure 82, but in a different time interval, showing the head wave at approximately 1 s.*

The amplitude of the elastic P-wave is observed to reduces when ice roughness is applied to the ice model, no matter the velocity profile (Figure 84a). The combination of an Arctic sound speed profile and rough ice generates the largest amplitudes for the transmitted acoustic wave (Figure 84b, black lines), and the model with rough ice and a homogeneous velocity profile shows the second largest amplitude. The backscattered transmitted acoustic wave shows increased amplitudes for the models with an Arctic sound speed profile (Figure 84b).

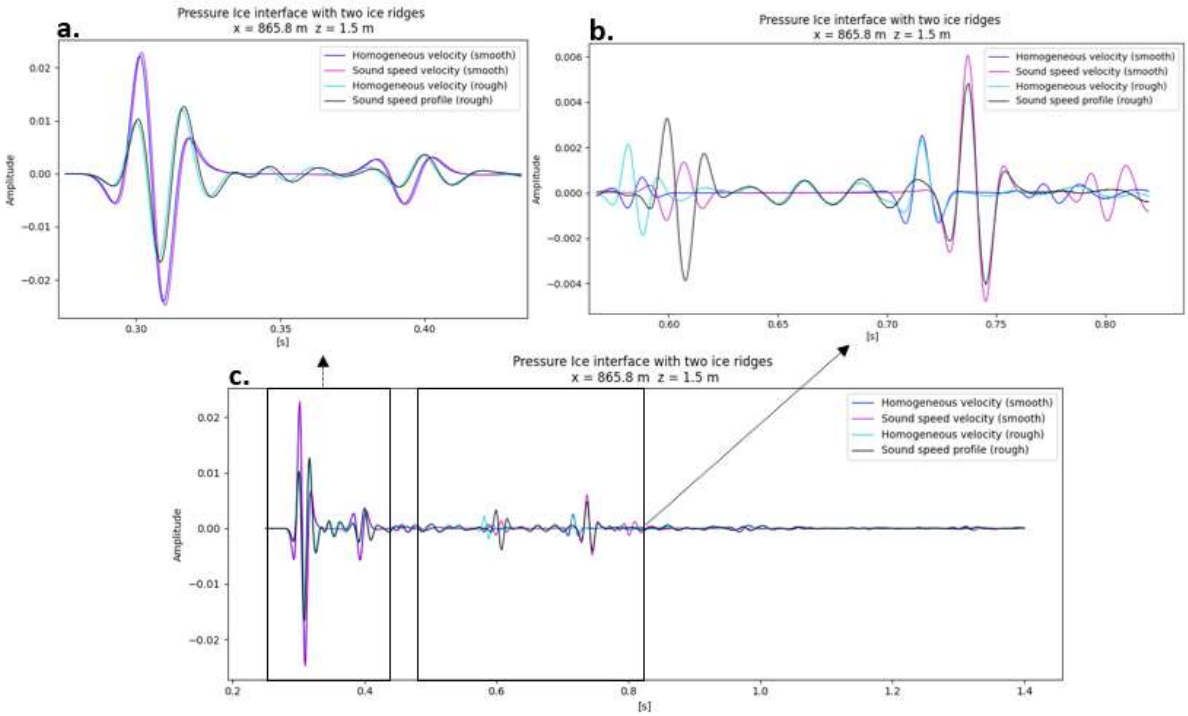

Figure 84. *Seismogram from receiver i1, showing the model with a smooth ice interface with a homogeneous velocity profile (blue) and an Arctic sound speed profile (pink) and the model with a rough ice interface and a homogeneous velocity profile (green) and an Arctic sound speed profile (black). Note the different scales.*

Figure 85 shows the seismograms recorded at the receiver located approximately 78 m after the first ice ridge (receiver i2). The amplitude of the elastic P-wave (Figure 85a) is reduced since receiver i1 but has a similar shape. The transmitted acoustic wave (Figure 85b) shows increased amplitudes for the Arctic sound speed profiles, no matter the ice-water interface.

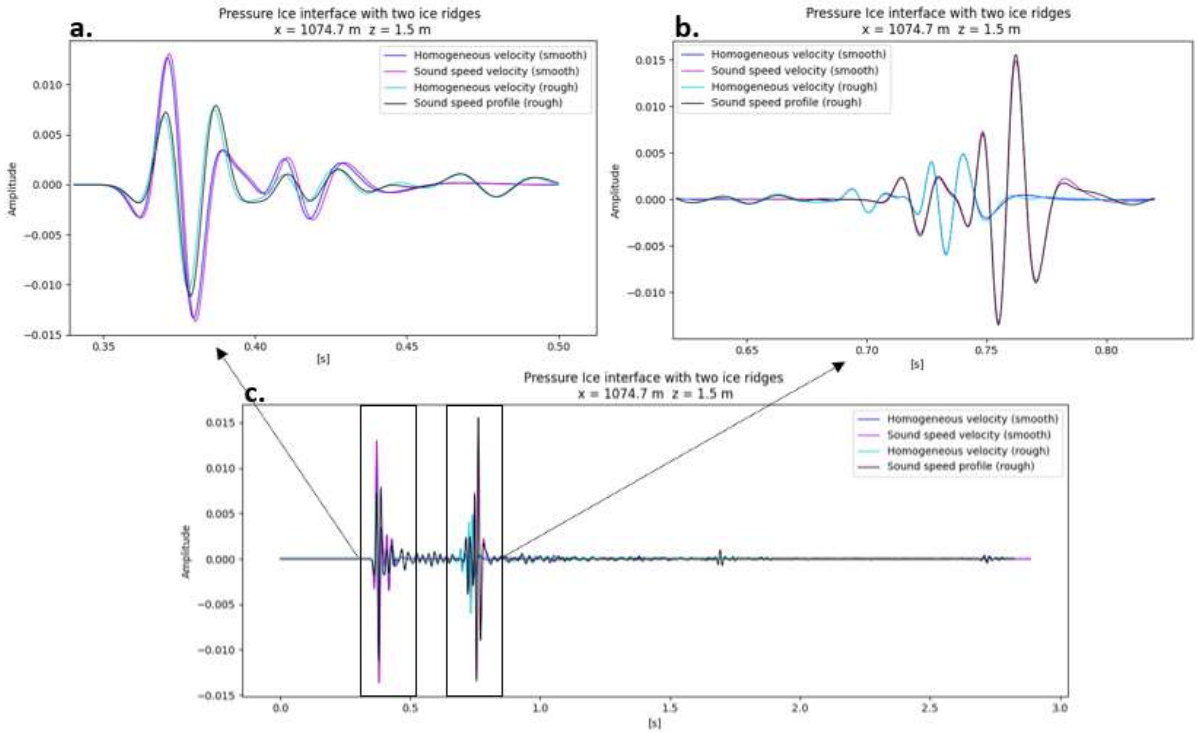

Figure 85. *Seismograms as in Figure 84 , but from receiver i2.*

For the smooth and rough ice, the transmission loss at 4 km for the models with a homogeneous velocity profile is 60.45 dB and 60.41 dB, respectively. This is larger than what is observed for the models with an Arctic sound speed profile, which is 34.16 dB and 34.25 dB for smooth and rough ice, respectively. However, the differences in transmission loss between smooth and rough ice models are small in both cases.

Chapter 6
Discussion

6.1. Modeling acoustic wave propagation in an ice-covered Arctic Ocean with SPECFEM2D

This section will briefly discuss the implementation of ice roughness and ice ridges in the ice models in the axisymmetric version of SPECFEM2D. It will also address the issue with reflections of backscattered waves at the symmetry axis and discuss the reflection at the absorbing bottom boundary.

6.1.1. Implementing ice roughness and ice ridges in SPECFEM2D

As mentioned in the introduction, the complexity of a realistic sea ice layer and its highly variable geometry distinguished by ice ridges and ice roughness along the propagation path (e.g., Jensen et al., 2011, p. 307) is often a challenge for numerical tools.

With the internal mesher in SPECFEM2D, the ice layer is defined by a chosen number of (x, z) points, describing the surface and bottom interface of the layers. This gives the ability to define the features in the ice layer in a free manner, as SPECFEM2D, in theory, can implement any ice model. Comparing SPECFEM2D to OASES, which Hope et al. (2017) used to investigate the impact of ice roughness on high-frequency acoustic propagation, OASES instead uses a statistical approach to implement both ice thickness and ice roughness. The ice thickness is implemented as a Gaussian distribution around the mean, and the ice roughness is implemented as small perturbations around a mean thickness, with a correlation length and an RMS value around the mean. OASES requires the RMS value to be small compared to the wavelengths (Hope et al., 2017). Hope et al. (2017) calculated the characteristic correlation length from an ice segment in the Nansen basin, and found a corresponding roughness RMS value of 1.52 m. As this was too large compared to the wavelengths (1.59-4 m), they used an RMS value of 0.6 m instead. Theoretically, it would be possible to implement ice roughness with a large RMS value compared to the wavelength in SPECFEM2D, as the interface is freely defined by the chosen points. It might, however, be beneficial to use an external mesher, e.g. Gmsh (Geuzaine & Remacle, 2009), for more complex geometries, to ease the implementation of a nicely fitted mesh around the ice features and avoid stretching or compression of the grid cells.

In this thesis, the ice roughness was created by a Fourier transform of the roughness amplitude spectrum, calculated with a Gaussian power spectrum and the characteristic correlation length in Hope et al. (2017). The rough ice-water interface was created by adding the ice roughness around a smooth ice interface with two ice ridges. In OASES, the roughness is isotropic and transversely invariant and thus, has the same statistical properties in all directions. Ice ridges stretches out along one direction, and

cannot be considered isotropic (Hope et al., 2017). As the ice roughness with the internal mesher in SPECFEM2D is described by a chosen set of (x, z) points, the ice layer can vary along the propagation direction in SPECFEM2D, ice ridges were easily defined. As the axisymmetric 2.5D version is used, the features of the ice layer will, however, be symmetric around the symmetry axis and the ice ridges and ice roughness will take a circular shape.

Comparing SPECFEM2D to parabolic equation approximations (e.g., Collis et al., 2016), an advantage of SPECFEM2D is that the axisymmetric version of SPECFEM2D takes backscattering into consideration, and the backscattered waves are properly modeled (Bottero, 2018). One requirement for the parabolic equation approximation is that the backscattered energy is small enough compared to the forward scattered energy to be ignored (Thomson & Brooke, 2008). The results of this thesis have shown backscattering by both the acoustic and elastic waves to occur at the ice ridges. Probable Scholte waves propagating in the ice-water interface were also observed after the elastic P-wave passed the ice ridges. In this thesis, only two ice ridges are implemented, which might be an underestimate. Diachok (1976) found 9.5 ridges/km as the best fit for data collected in the western part of the Arctic Ocean, and 11.5 ridges/km for data from the eastern Arctic Ocean. The RMS value in the thesis (0.6 m) is also an underestimate, and a more realistic ice layer might generate more scattering.

However, an issue related to the backscattered waves in the axisymmetric simulations in SPECFEM2D is the reflection that occurred at the symmetry axis. This boundary is non-absorbing and was observed to cause the waves reaching the symmetry axis to reflect, whereafter they continued to propagate through the domain as noise. As explained in (Bottero, 2018), this is a limitation that occurs as the axisymmetric models assumed symmetry around the symmetry axis. This symmetry leads to a zero radial component for displacement at the symmetry axis, and the boundary at the symmetry axis therefore behaves as a perfectly reflecting Dirichlet boundary condition. The geometry of the axisymmetric domain also causes backscattered energy to grow towards the symmetry axis, and this issue will be most pronounced when the source of scattering is near the symmetry axis. In the simulations, the reflections at the symmetry axis became more pronounced when ice roughness was implemented to the model with two ice ridges. The noise at the symmetry axis also became more visible. Ice roughness generates scattering (e.g., LePage & Schmidt, 1994), and thus, more waves interact with the symmetry axis. The effect of this issue has not been investigated nor quantified, and therefore there are uncertainties in the presented results related to those artificial waves. The transmission loss curves presented in this thesis are calculated from all waves recorded at each receiver, and consequently, those artificial reflections are included in the seismograms and affect the presented transmission loss curves to an unknown extent. To reduce this impact, a suggestion may be to use only a selected time interval of the seismograms for the transmission loss curves. This issue of reflection of backscattered waves at the symmetry axis must be considered a limitation when modeling acoustic wave propagation in an ocean with ice roughness and ice ridges with the axisymmetric SPECFEM2D. A suggestion to reduce, or at least delay, this issue, could be to implement a smooth ice layer close to the symmetry axis and move the heterogeneities away from the symmetry axis. However, this would require an extended domain, and would consequently be more time consuming.

A 3D simulation would not have a symmetry axis, and thus, would have solved the issue with the reflected backscattered waves. The ice features, as ice ridges, would neither be symmetric around the

symmetry axis nor have the circular shape. However, 3D simulation has a higher computational cost than a 2.5D simulations, and is particularly costly for the large dimensions needed to model long-range propagation in the ocean (Bottero, 2018).

6.1.2. Reflections from the absorbing boundary

Initially, a domain of 100x4000 m was chosen for the simulations. As the perfectly matched layers were placed inside the domain, the initial domain had an actual depth of 85 m. As explained in Section '*4.5.1. Validation of the domain dimensions*', the models were validated against the seismo-acoustic propagation model OASES and an exact solution.

The initial domain of 100x4000 was observed to be challenging, as a noise pulse arose at approximately 500 range. However, a nice correspondence was shown between SPECFEM2D and the exact solution before for 500 m. Attempts to change to a finer (1x1 m) and coarser (10x10 m) grid did not improve the results. Therefore, the depth of the domain was instead increased to 500 m, while keeping the initial grid size (3x3 m). This attempt was successful and good correspondence between OASES, the exact solution, and SPECFEM2D could be observed at shorter ranges. However, a noise pulse of negligible size was still present at 1910.5 m range and 30 m depth. At an increased range of 2955.3 m, the main pulse in the water still showed good correspondence to the reference curve. However, the noise pulse was observed to grow with increased distances and is not insignificant for larger ranges. This noise pulse is interpreted as a reflection from the absorbing boundary.

Perfectly matched layers are most efficient for waves with normal incidence angle to the PML, while grazing angles are generally more difficult to handle. Therefore, large distances between the source and receivers can be challenging (Komatitsch & Martin, 2007).Long-range wave propagation problems require very elongated domains, which can be challenging for absorbing boundaries to handle. Therefore, the numerical domain must be extended to avoid artificial reflections from the boundaries (Xie et al., 2016). In this thesis, the domain is indeed elongated. The initial domain became 85x3985 m, as the 5 elements thick PMLs were placed inside the domain, hence the horizontal length is almost 47 times the vertical length. Better results were found for a 500x4000 m domain, thus for a horizontal length of 8 times the vertical depth. In addition, the distance between the source and the receiver is quite large. Therefore, one can assume that the grazing angles in the simulations might become challenging for the perfectly matched layer, which might be an explanation for the observed reflections at the absorbing bottom layer.

Small elements inside the PML can contribute to numerical instabilities within the absorbing layer. This issue can be avoided by using a stretching formulation within the PMLs, which postpones the instabilities for an as long time as needed for the simulation (Xie et al., 2014). The absorbing layers implemented in the 2.5D version of SPECFEM2D are the improved perfectly matched layers developed by Xie et al. (2014) and Xie et al. (2016), which enables modeling in very elongated domains (Bottero, 2018). The mathematical formulation of the damping profile within the perfectly matched layers in SPECFEM2D requires the velocities and densities to be constant in the direction normal to the PML inside each absorbing layer. Therefore, an external velocity or density profile must be redefined and set

to be constant at these locations (Centre national de la recherche scientifique & Princeton University, 2021). Unfortunately, this was not done for the external profiles in this thesis. Thus, the velocity and density are not constant in the vertical direction inside the bottom absorbing boundary, which leads to mathematical challenges for the damping profile. This makes it legitimate to assume that the absorbing efficiency will be affected in some way. However, this cannot explain the origin of the bottom reflection from the absorbing layer presented in Section '*4.5.1. Validation of the domain dimensions*', as a constant velocity and density profile is used in those simulations.

It is not certain what causes the reflection at the bottom perfectly matched layer to arise. However, the domain in this thesis might be challenging for perfectly matched layers, as it is elongated, has the source on the symmetry axis and non-normal incident angles at the absorbing layers. Increasing the domain depth did improve the results but did not remove the reflections completely at large ranges. For ranges considered in this thesis, the noise pulse is relatively small, and even though there are some uncertainties related to this artificial reflection in the results obtained at greater distances, the impact is supposedly quite small. However, as this reflection grows with increasing distances, it is suggested that this issue is investigated further before performing long-range wave propagation simulations in boundless ice-water domains. A suggestion is to investigate whether an increased PML thickness in terms of number of elements or larger grid cells in the layer could reduce the reflections.

6.2. Comparison to the shallow water models in Collis et al. (2016)

In this section, the results from Section '*5.1. Simulations with a homogeneous velocity profile*' and '*5.2. Simulations with a linearly increasing sound velocity profile*' are compared to the predicted transmission loss curves of the elastic parabolic solution presented in Collis et al. (2016). Collis et al. (2016) models wave propagation in shallow water with a sea floor at 100 m depth for a time-harmonic 50 Hz point source and a receiver, both at 30 m depth, over 10 km range. Three model configurations were used, one domain with water only, one domain with a range-independent 3 m thick ice layer, and one domain with a range-dependent ice layer linearly decreasing from 3 m thickness to 0.5 m thickness after 10 km.

Their model configurations in terms of ice layers were recreated in this thesis, and the same elastic ice parameters and water density were used. However, the domain differs and the results in SPECFEM2D were obtained in a 4000x500 m domain. Two sound velocity profiles were used in the water layer in Collis et al. (2016), one homogeneous velocity profile ($v_p = 1500\,m/s$) and one velocity profile linearly increasing with depth ($v_p = 1482\,m/s$ to $v_p 1525\,m/s$). The predicted transmission loss curves obtained by Collis et al. (2016) are shown in Figure 86.

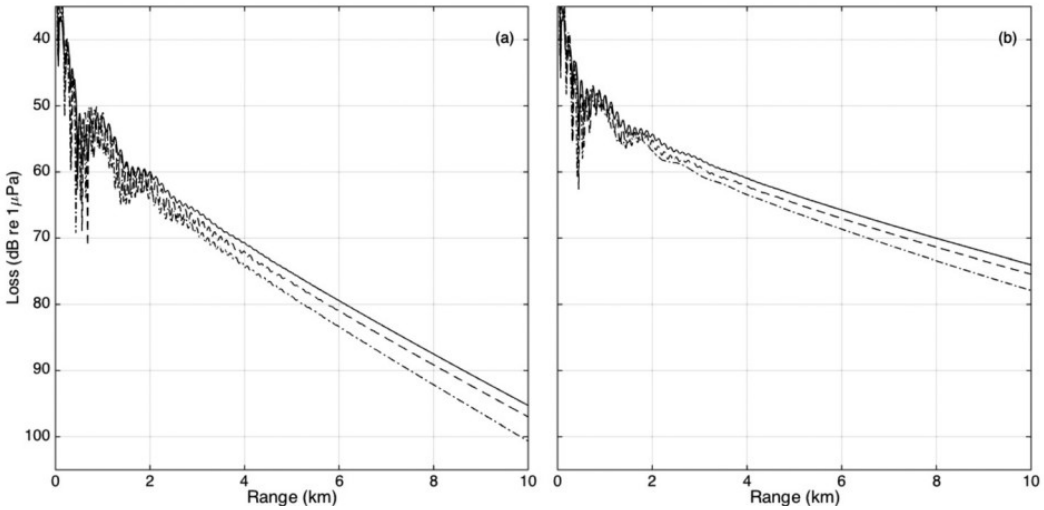

Figure 86. *Results obtained by Collis et al. (2016) showing the predicted transmission loss of their elastic parabolic equation for three models; one model with water only (dashed-dotted lines), one with a range-independent ice layer (solid lines) and one with a range-dependent ice layer (dashed lines). Figure 86a shows transmission loss for a homogeneous velocity profile and Figure 86b for a linearly increasing velocity profile.*

Transmission loss curves obtained in SPECFEM2D are shown in Figure 87, where the approximate intervals of the transmission loss obtained in Collis et al. (2016) are shown by the red (homogeneous velocity profile) and green (linearly increasing velocity profile) intervals, as read from Figure 86. Note that the right-hand axis corresponds to the loss curves presented in Collis et al. (2016), given in dB/ 1μPa. A first thing to notice is that the predicted transmission loss presented in Collis et al. (2016) is approximately 20-25 dB less transmission loss at 2 km for both velocity profiles.

The main difference between the results presented in this thesis, and those obtained by Collis et al. (2016), is that Collis et al. (2016) models wave propagation in shallow water and have a sea floor at 100 m depth. The sea floor is attenuating ($\alpha_p = 0.76\ dB/\lambda$ and $\alpha_s = 1.05\ dB/\lambda$) and has P- and S-wave velocities of $v_p = 2000\ m/s$ and $v_s = 1000\ m/s$. Waves propagating in a shallow water environment are trapped in a channel between the surface and the bottom, and thus, are exposed to repetitive interactions at both ends (Urick, 1983, pp. 172-177) . Attenuation and reflection at the sea floor impact acoustic propagation in shallow water domains (Gavrilov & Mikhalevsky, 2006; Hope et al., 2017), while data has shown that it is insignificant for deep basins (Gavrilov & Mikhalevsky, 2006). As Collis et al. (2016) models wave propagation in a shallow water domain, there will be both reflection and transmission at the sea floor. In this thesis, the sea floor is removed. Instead, an absorbing layer is applied at the bottom boundary and all waves propagating to the bottom boundary are theoretically absorbed. Consequently, the contribution of waves reflected at the sea floor is excluded, while all bottom loss is included in the results presented in this thesis. Therefore, one cannot directly compare the transmission loss curves presented in this thesis with the loss curves presented in Collis et al. (2016).

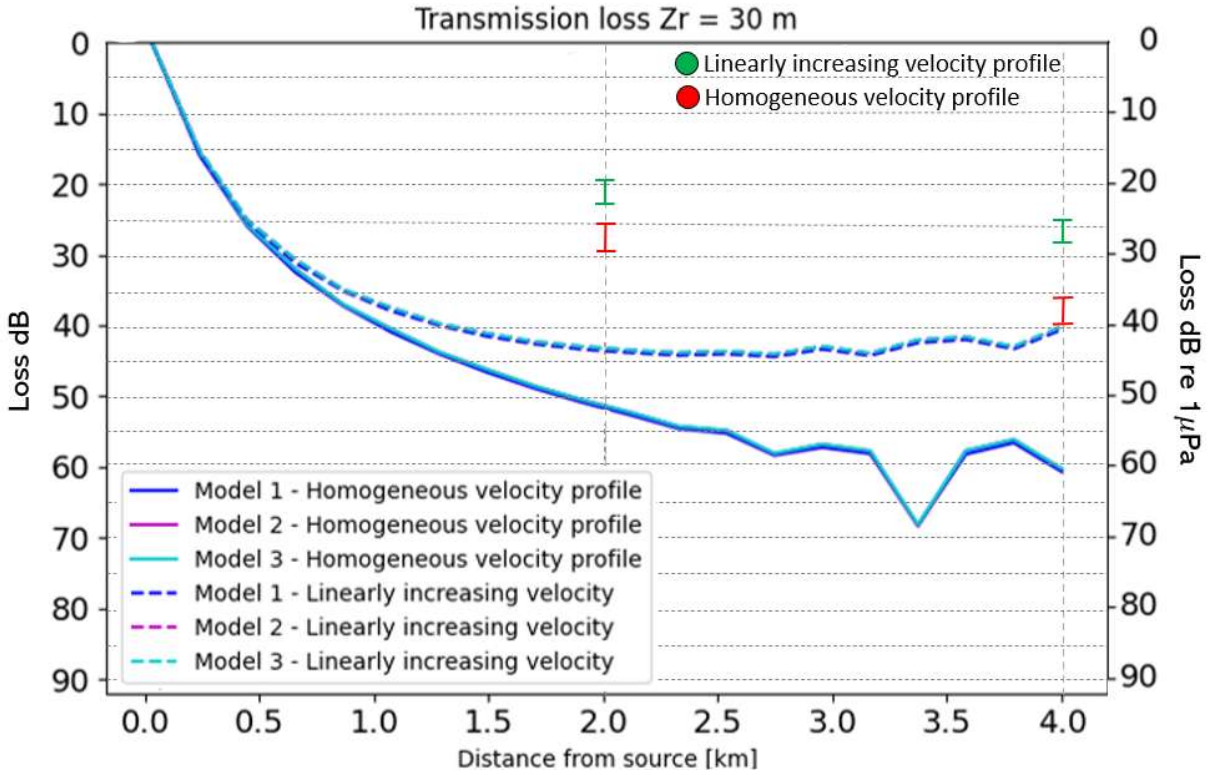

Figure 87. *Edited from Figure 47, showing transmission loss curves in dB for Model 1 (blue), Model 2 (pink) and Model 3 (light blue), with a homogeneous sound velocity profile (solid lines) and a linearly increasing sound velocity profile (dotted lines). Approximate values from Collis et al. (2016) for their linearly increasing velocity profile is shown between the green interval, and for their homogeneous velocity profile in red intervals. The right-hand axis corresponds to the values from Collis et al. (2016), while the left-hand axis corresponds to the results presented in this thesis.*

Additionally, one cannot quantitatively compare the results presented in Collis et al. (2016) and in this thesis as the velocity gradient of the linearly increasing sound velocity profile is different. As the same velocity range is used over different depths, the velocity gradient becomes stronger in the shallower domain in Collis et al. (2016). Also, their homogeneous velocity profile is faster than the homogeneous velocity profile in this thesis. However, in terms of the effect of the different sound velocity profiles, the results presented in this thesis are consistent with the results in Collis et al. (2016). In both cases, the transmission loss considerably decreases when an upwards refracting linearly increasing velocity profile is introduced.

Concerning the effect of the ice layer, it turned out to be somewhat difficult to interpret the results of Collis et al. (2016) as the description in the main text does not correspond to what is shown in the figure and corresponding figure caption. The figure, and its caption, states *least loss for 3 m thick range-independent ice* (solid lines in Figure 86) and *most loss for the domain with water only*. In contrast, the main text says *least loss for the range-dependent ice* (dashed lines in Figure 86), while most loss is still stated for water only. They present the same trends among the ice models for both a homogeneous velocity profile (Figure 86a) and an upwards refracting velocity profile (Figure 86b), but with less transmission loss for all models in the latter case.

In this thesis, the observed influence of sea ice on transmission loss at 30 m depth is marginal. This is not consistent with the results presented in Collis et al. (2016). The results of this thesis suggest that the ice layer does not significantly contribute to decreased transmission loss for a receiver and 50 Hz source

at 30 m depth (e.g., Figure 87) at shorter ranges. This applies to both velocity profiles and is consistent throughout all simulations conducted. Nevertheless, small differences in transmission loss are observed between the models, but the relative differences in transmission loss presented in this thesis are significantly smaller than what is presented by Collis et al. (2016). In this thesis, most loss is observed for Model 1 (water only), second most for Model 2 (range-independent ice), and least loss for Model 3 (range-dependent ice), both in the case of a homogeneous and an upwards refracting velocity profile. This is not consistent with what is shown in Figure 86, where the least loss is shown for the range-independent ice (i.e., Model 2). It is, however, consistent with the description in the main text in Collis et al. (2016), which describes the least loss to be for the range-dependent ice layer (i.e., Model 3).

Assuming the discussion about which ice models generate the most loss is ignored, and the relative difference between the models instead is addressed, a difference of roughly 3.5 dB and 2.5 dB can be read from Figure 86 (Collis et al., 2016) at 4 km for the homogeneous and linearly increasing velocity profile, respectively. The total difference between the models in SPECFEM2D is small, 0.41 dB and 0.4 dB, for the homogeneous and linearly increasing velocity profile, respectively.

As Collis et al. (2016) model shallow-water wave propagation in an ice-covered domain, the waves are repeatedly interacting with the sea ice. Those repetitive wave interactions at the sea ice can be assumed to increase the influence of the ice layer on transmission loss. Following the explanation in Collis et al. (2016), the least loss is observed for the ice model with linearly decreasing thickness because the angle of reflection is reduced, thereby decreasing the loss to the sea floor. Thus, the stronger influence of the sea ice in the shallow water domain in Collis et al. (2016) might be explained by the repetitive wave interactions at the ice layer. Also, the larger relative difference in loss between the ice models can be explained by the decreased sea floor loss for the ice model with linearly decreasing ice thickness.

In this thesis, all waves are absorbed at the bottom boundary, independent of the incidence angle. Therefore, a decreased bottom loss cannot explain why least loss is observed for Model 3 (range-dependent ice) and this loss must instead be related to the ice layer itself. The observed difference between the models is much smaller in this thesis compared to Collis et al. (2016), indicating that the ice layer has less impact on transmission loss in deep water domains than in shallow water domains over shorter ranges.

6.3. The effect of ice ridges on acoustic wave propagation

Only minor differences in transmission loss at 30 m depth have been observed in this thesis, caused by the different configurations of the ice layer. The modeled ice thickness in all ice models is thin compared to the acoustic wavelengths (~29-70 m), 2-3 m thick in general, and 4.9-7.1 m thick at the ice ridges. The relationship between the incident wave at the sea ice interface and the final reflection going back into the water is related in a generalized reflection coefficient presented in Hope et al. (2017). This generalized reflection coefficient shows that a 2-3 m thick smooth ice layer will generate a final contribution of full reflection for almost all incidence angles at 50 Hz. The ice layer is basically too thin to be noticed as a layer by the incident wave. For a rough sea ice interface with a roughness RMS value of 0.6 m, frequencies above approximately 100 Hz are required to generate a generalized reflection

coefficient below 1, for almost all angles of incidence. However, waves of approximately 28° incidence angle will experience some loss due to the sea ice layer at 50 Hz, both for a smooth and a rough ice layer. This indicates that no major differences in transmission loss can be expected in the simulations performed in this thesis. However, although no major differences are observed in this thesis, suggesting that the ice layer not significantly impacts the transmission loss over a 4 km range, small differences in transmission loss are observed, which should not be neglected.

In this thesis, minor differences in transmission loss at 30 m depth are observed at 4 km range when two ice ridges are implemented in a smooth 2 m thick ice layer (34.16 dB), compared to a smooth ice layer of 3 m constant thickness (33.97 dB). Also, back- and forward scattering is observed as the waves pass by the ice ridges. The most notable differences in the seismograms presented in this thesis are shown within the ice layer, where several back- and forward scattered waves are observed. The amplitude of the transmitted acoustic wave is shown to increase as the depth of the ice ridge increase, which could indicate that ice ridges enhance energy transmission into the ice layer. Also, a local increase in transmission loss is observed at the location of the ice ridges, which was most pronounced when the deeper of the two ice ridges was located in the first part of the domain. The local increase in ice thickness at the ice ridge may explain some of the enhanced transmission of energy into the ice layer at those locations. The generalized reflection coefficient in Hope et al. (2017) can be scaled with the ice thickness, and a reflection coefficient below 1 would occur at lower frequencies for thicker ice.

One interesting observation in this thesis is the wave propagating at the ice-water interface. Forward modeling performed by Landschulze (2018) showed that Rayleigh waves, Scholte waves, and flexural waves are often present in the Arctic ice layer simultaneously. The Rayleigh waves propagate on top of the ice layer and in the adjacent air, the flexural waves within the ice layer, and the Scholte waves at the ice-water interface. The Scholte waves propagate with velocities lower than the P-wave velocity in the fluid layer (Glorieux et al., 2001), which corresponds with the observed velocity in the simulations, where the ice-water interface wave propagates at a velocity of approximately 1400 m/s. The flexural wave propagates slightly faster than the Scholte wave (Landschulze, 2018), and the part of the interface wave which propagates in the ice layer could be explained as a flexural wave. Most of the energy of a Scholte wave is kept in the water layer, and it does not attenuate along the horizontal direction. Instead, it decays exponentially into the water and ice layer (Glorieux et al., 2001). In this thesis, ice ridges have been observed to generate back- and forward scattered transmitted waves and ice-water interface waves. Therefore, an additional transmission loss is expected in the water layer at 30 m depth. LePage and Schmidt (1994) studied the impact of wave scattering from rough ice. They found that scattering into flexural waves in the ice layer is a very important process to consider when calculating acoustic propagation loss in the Arctic. In this thesis, the observed increase in transmission loss at 4 km for two ice ridges in a 2 m smooth level ice is 0.19 dB, compared to an ice model with 3 m thick smooth ice. However, as already mentioned, two ice ridges in four km may likely be an underestimate, and possible to assume that the transmission loss in the water would increase with an increasing number of ice ridges. In addition, the waves within the ice layer and in the ice-water interface appeared stronger at deeper ice ridges, indicating that deeper ice ridges likely would have increased the transmission loss in the water.

6.4. The effect of ice roughness (and ice ridges)

In this thesis, the effect of ice roughness on acoustic transmission loss for a 50 Hz source and receiver at 30 m depth is observed to be very small over shorter ranges. Two models with ice roughness were implemented, each with two ice ridges. The difference between the models was the location of the deeper and shallower ice ridge, and the roughness profile of the ice surrounding each ice ridge. Both ice roughness profiles are implemented with the same parameters but differ slightly due to the random phase.

Compared to a model with 3 m thick smooth ice, the rough ice model with the deepest ridge at 996 m showed a decrease in transmission loss, while the model with the deepest ice ridge at 2992 m showed an increase. In addition, for the rough ice model with the deepest ridge at 996 m, the amplitudes on the seismograms, both in the ice and at 30 m depth in the water, shows larger amplitudes for almost all wave pulses, also before the waves wave reached the first ice ridge.

It is difficult to determine the reason for the difference in observed transmission loss between the rough ice models. As the model with the deepest ridge closest to the symmetry axis experiences less loss than the three other models with ice ridges, one suggestion is that it might be related to reflections of backscattered waves at the symmetry axis. However, as the amplitudes of the rough ice model with the deepest ridge at 996 m are larger than for the other ice models with ice ridges, also before the waves have reached the first ridge, this indicates that the ice ridge is not the reason.

Another suggestion is that the observed difference between the rough ice models is related to the different ice roughness profiles implemented in the ice models. Although the ice roughness is created with the same Gaussian amplitude power spectrum, RMS value, and characteristic correlation length, the phase is random. Thus, the ice roughness is not identical around both ice ridges. The ice roughness extends to somewhat greater depths around the deeper ice ridge, and the ice is much thicker at the very beginning of the domain when the deepest ridge is located at 996 m (see Figure 16, Figure 17). As previously mentioned in the thesis, an increase in energy transmission into the ice layer at the ice ridges have been observed. Therefore, an increase in transmission loss would be more expected due to the difference in ice roughness profiles, than a decrease. As this ice model is the only of four models with ice ridges that experience less loss than a model with a 3 m thick smooth ice layer, it indicates that it might be numerically caused. Therefore, this model will be excluded from further discussion, and only the model with the shallower ice ridge in the first part of the domain will be considered further on in the discussion.

LePage and Schmidt (1994) modeled Arctic low-frequency propagation with a normal mode solution. Their results show that the additional transmission loss for 40 Hz frequency, caused by a rough sea-ice cover, is expected to be very small at short ranges. For a source at 95 m depth, LePage and Schmidt (1994) present an additional transmission loss caused by ice roughness for 50 Hz of approximately 0.02-0.06 dB/km, depending on how the ice roughness is modeled, compared to a smooth ice layer. In this thesis, an additional transmission loss of 0.28 dB is observed at 4 km when ice roughness is implemented in an ice model with two ice ridges, compared to the same model without ice roughness. The same difference at 2 km is 0.18 dB. Comparing the rough ice model with two ice ridges to the smooth ice

model with two ice ridges, an increase in transmission loss of 0.09 dB is observed at 4 km for the rough ice model.

LePage and Schmidt (1994) point out that the transmission loss strongly depends on the different experiments. Parameters such as the shape of the sound speed profile, source depth, and ice roughness characteristics are important factors affecting the modeled transmission loss. Regardless, their results might be assumed to be able to give a fair reference on how much loss can be expected due to a rough ice-water interface. In this thesis, the observed differences in transmission loss caused by rough ice are fairly comparable to what is presented in LePage and Schmidt (1994).

LePage and Schmidt (1994) suggest that the transmission loss caused by scattering into flexural waves is important to consider when modeling Arctic transmission loss. Additionally, they showed that the scattering at rough ice-water interfaces strongly depends on the roughness spectrum of the modeled roughness and the scattering into flexural waves in the ice layer increases for increased slopes of the features in the rough ice layer. This thesis suggests that the presence of ice ridges in the Arctic Ocean will enhance the transmission of energy into the ice layer and, by so, increase the transmission loss in the water. Moreover, ice ridges have also been observed to generate both forward and backward scattered waves, as well as waves propagating in the ice-water interface. As explained earlier, the ice-water interface wave is likely a Scholte wave in the water and possibly a flexural wave in the ice. In this thesis, the transmission loss is observed to increase by 0.07 dB/km for a rough ice model with two ice ridges compared to a 3 m thick ice layer. When both models have two ice ridges, the rough ice model have an increase of 0.0225 dB/km in transmission loss, relative to the model with smooth ice. This could indicate that larger features such as ice ridges are more important to transmission loss in the water than the ice roughness, as they are seemingly more efficient in transferring energy into flexural waves and Scholte waves.

Modeled additional transmission loss caused by ice roughness is highly dependent on the experiment configurations. Modeled wave scattering at a rough sea ice interface strongly depends on the shape of the roughness profile and scattering into flexural waves increases for shorter roughness correlation lengths. The shape of the sound velocity profile and the source depth also significantly impact the modeled transmission loss (LePage & Schmidt, 1994). In this thesis, the shape of the sound velocity profile is shown to impact the transmission loss in the water considerably. For a 50 Hz source and a receiver at 30 m depth, the shape of the sound velocity profile appears to have the most impact on the observed transmission loss over shorter ranges. The source depth is also observed to significantly impact the transmission loss at 30 m depth, where the transmission loss is observed to increase with decreasing source depth. Therefore, it is rather difficult to compare modeled transmission loss accurately. However, the results in LePage and Schmidt (1994) give an indication of the expected additional transmission loss due to ice roughness, which corresponds fairly to what is observed in this thesis.

Although the ice layer generally has shown to only have a minor influence on the acoustic transmission loss at 30 m depth in this thesis, it is fair to assume that a larger impact is possible for higher frequencies and longer ranges (Fricke, 1993; e.g., Gavrilov & Mikhalevsky, 2006; Hope et al., 2017; Yang, 1989). It is also important to keep in mind that there are some uncertainties in the presented transmission loss in this thesis, related to the reflections of backscattered waves and the reflection at the absorbing bottom boundary. As mentioned earlier, the transmission loss curves are calculated from the full seismograms,

and not for a particular arrival. Consequently, any artificial wave recorded at the receiver is also included in the loss curves. The acoustic wave in the water appears rather unaffected by the different ice layers, but the waves within the ice layer becomes more complex with rough ice and ice ridges. Some of those waves are also refracted down into the water. Although the seismograms at 30 m depth are dominated by the acoustic wave in the water, the differences in transmission loss in the results are small. Therefore, the small refractions from the waves reflected at the symmetry axis might also impact the presented transmission loss curves to some extent.

6.5. The effect of the sound velocity profile

It is well understood that the characteristic upwards refracting sound velocity profile in the Arctic Ocean largely impacts the acoustic wave propagation in the region, as it creates a channel of very efficient long-range wave propagation beneath the ice layer (e.g., Jensen et al., 2011; Urick, 1983).

In this thesis, the transmission loss at 30 m depth has clearly been observed to decrease when an upwards refracting sound velocity profile is implemented. The transmission loss is observed to decrease more for larger gradients in the profile. For a model with water only, the transmission loss decreased by 7.5 dB when a sound velocity profile with linearly increasing velocity was implemented and by 18.9 dB when an Arctic sound speed profile was implemented. For a model with 3 m thick ice, the decrease was 7.56 dB and 18.6 dB for each velocity profile, respectively.

The shape of the sound velocity profile impacts the transmission loss in the Arctic Ocean, and small changes in the profile affect the wave propagation (Gavrilov & Mikhalevsky, 2006). In addition, it can affect the scattering loss at rough sea ice interfaces, as sound velocity profiles with a stronger velocity gradient in the upper layer experience higher loss than profiles with a weaker velocity gradient in the upper layer for the same ice roughness (LePage & Schmidt, 1994).

Two ice models with two ice ridges, one with a rough and one with a smooth ice-water interface, were implemented for a homogeneous velocity profile and an Arctic sound speed profile. The amplitude of the acoustic wave was observed to be significantly larger when an Arctic sound speed profile was implemented and was not affected by whether the ice-water interface was rough or smooth. Furthermore, the amplitude of the head wave was observed to be larger for rough ice than for smooth ice before the first ice ridge, no matter the velocity profile, whereas it became smaller for rough ice than for smooth ice with increasing distances. This indicates that an increase in transmission loss can be expected for rough ice compared to smooth ice, no matter the sound velocity profile. However, the difference in amplitude of the acoustic wave is significantly larger than the amplitude of the head wave. Therefore, the expected difference in transmission loss due to ice roughness is small, while the expected difference in transmission loss due to the Arctic sound speed profile is large.

An increased transmission loss of 0.09 dB is observed at 4 km for a rough ice model with two ice ridges, compared to a smooth model with two ice ridges, when a realistic Arctic sound speed profile is implemented. For the same ice models with a homogeneous velocity profile, 0.04 dB less loss is observed for the rough ice model. In total, the transmission loss at 4 km is observed to decrease by

approximately 26 dB when a realistic Arctic sound speed profile is implemented in the ice models, compared a homogeneous velocity profile.

The results in this thesis confirm that the shape of the sound velocity profile in the water significantly impacts the transmission loss in the water. Furthermore, it suggests that the sound velocity profile in the water is the most important parameter controlling acoustic transmission at short ranges for a 50 Hz source and receiver at 30 m depth in an ocean with a thin 2-3 m thick ice layer.

6.6. Modeled acoustic wave propagation within the ice layer

This section will briefly discuss the wave propagation observed within the ice layer. The amplitude of the head wave was observed to be slightly larger for a constantly 3 m thick smooth ice layer than for a smooth ice layer with linearly decreasing thickness in all simulations. The opposite was shown for the amplitude of the elastic P-wave, which was slightly larger for a 3 m thick ice layer than for an ice layer with linearly decreasing thickness. Although the amplitude differences are small, this suggests that more energy is kept within the linearly decreasing upwards sloping ice layer, compared to the flat, 3 m thick ice layer. The amplitudes of the transmitted acoustic wave have been observed to be larger for a constantly 3 m thick ice layer, than for an ice layer with linearly decreasing thickness. This indicates that a thicker non-sloping ice layer enhances the energy transmission from the acoustic wave into the ice layer. At the same time, the wave refracted from the elastic P-wave into the water is stronger, which means that the 3 m thick ice layer both transmits and refracts more energy than an ice layer with decreasing thickness. As the amplitude of the transmitted acoustic wave is larger relative to the refracted head wave, in total, more energy is transmitted into the ice layer than what is refracted down into the water layer. This corresponds to what is observed in the water layer, as more transmission loss is observed in the water when the ice layer has a constant thickness. The acoustic wave is observed to be slightly smaller when an ice layer is implemented, but the observed difference is very small, and it does not differ between the two ice models. This suggests that the minor differences shown in transmission loss in the water are caused by the transmission of energy into the ice layer.

When ice roughness and ice ridges are implemented in the ice models, the most pronounced effects are observed on the seismograms recorded within the ice layer itself. In the water, the acoustic wave does not show any difference due to the ice ridges and ice roughness, and even if the head wave is shown to be affected by the ice roughness, the most effect was still visible within the ice layer itself. The waves generated by the ice ridges were best observed within the ice layer. Even though the seismograms become complicated when the ice roughness and ice ridges are implemented, it might be possible to use this information. A possibility might be to locate ice ridges by recording acoustic wave propagation within the ice layer, as the wave pulses of the scattered waves are clearly shown on these seismograms. It would have been easier to differentiate between the waves on the seismograms by looking at displacement. Displacement seismograms are also available in SPECFEM2D, but it has not been possible to study those in this thesis due to the time limit.

The different sound velocity profiles in the water appear to somehow affect the transmission loss in the ice layer. The smooth ice model with 3 m thick ice, the rate of transmission loss appears to reduce around

2 km range when an Arctic sound speed profile is implemented. For the same ice model, less loss is also observed for the sound velocity profile with linearly increasing velocity, but not as much. The impact of the different sound velocity profiles is also somewhat visible for the model with a linearly decreasing ice thickness, but the differences are smaller.

As earlier mentioned, when ice ridges and ice roughness are implemented in the ice models, backscattered waves in the ice layer are reflected at the symmetry axis and continue to propagate through the domain as noise. As the transmission loss curves are calculated from the full seismograms, this noise is also included in the loss curves. Most effect of the ice roughness is observed within the ice layers, and it is likely that the transmission loss curves in the ice layer are affected by this noise to a larger extent than the loss curves within the water.

6.7. In the aspect of Arctic climate change

The Arctic region experiences rapid climate changes, and the surface air temperature has likely increased more than double the global average during the last 20 years (Meredith et al., 2019). In a recent study, Xuanji et al. (2022) studied satellite data in the Arctic between the years 1982-2020 and showed an approximate decrease of 52 % in ice thickness and 63 % in ice extent, estimating an ice-free Arctic Ocean in 2061-2064, if the same trend continues. Sea ice-covered areas are decreasing in extent, and the ice becomes both younger and thinner (Lindsay & Schweiger, 2015; Meredith et al., 2019; Stroeve & Notz, 2018), and the shape and depth of the ice ridges are changing in the Arctic Ocean. Multi-year ice has been observed to contain more and deeper pressure ridges with less steep sides than first-year ice. Therefore, less multi-year ice could lead to less ice ridges in the Arctic Ocean (Wadhams & Toberg, 2012).

In this thesis, the ice layer has not been observed to impact the acoustic transmission loss at 30 m depth to a large extent, no matter the configuration of the ice model. Nonetheless, as previously mentioned, a larger impact is likely observed for higher frequencies or greater distances (e.g., Gavrilov & Mikhalevsky, 2006; Hope et al., 2017; Yang, 1989).

The mean thickness of the ice layers in this thesis is between 2 to 3 m. Assuming that this demonstrated impact in this thesis is small because the ice thickness is thin compared to the wavelengths, it could suggest that the acoustic propagation loss would be less and less impacted by the ice roughness and ice layer with the shift towards younger and thinner ice in the Arctic Ocean. The data of the ice segment used by (Hope et al., 2017) was collected in the Nansen basin in 2005 and had a mean thickness of 2.4 m. Gavrilov and Mikhalevsky (2006) refer to observations and suggest a mean thickness in the Nansen basin to be 3-4 m in the winter and 2-3 m in the summer. The annual mean ice thickness in the Arctic has been observed to be as low as 1.13 m in 2020 (Xuanji et al., 2022). This suggests that the ice thickness used in the simulations in this thesis is a reasonable choice.

The elastic ice parameters for velocity and density used throughout this thesis are parameters in the range of what is traditionally used in acoustic wave propagation studies, e.g., Collis et al. (2016); Fricke (1993); Gavrilov and Mikhalevsky (2006); LePage and Schmidt (1994) all use P-wave velocities between 3000-3500 m/s, S-wave velocities of 1600-1800 m/s, and densities between 900 and 910 kg/m^3.

Gavrilov and Mikhalevsky (2006) used attenuations of $\alpha_p = 0.45\ dB/\lambda$ and $\alpha_s = 0.9\ dB/\lambda$, compared to $\alpha_p = 0.3\ dB/\lambda$ and $\alpha_s = 1.0\ dB/\lambda$ used both in Collis et al. (2016) and in this thesis. As mentioned in the introductory chapter, porosity, brine content, and the material properties to withstand stress and strain influence the acoustic wave propagation. Those properties vary from multi-year and first-year ice, where first-year ice has decreased sound velocities due to increased brine content. Also, for first-year ice, the S-wave velocity can become less than the sound velocity in the underlaying water, and by so, the transmission of energy into the ice layer can increase (Worcester & Ballard, 2020). With the changing climate in the Arctic Ocean and the shifting from older multi-year ice towards younger ice, it might be relevant to review the ice parameters to examine whether they are still appropriate choices, or if they require to be updated. This is not in the scope of this thesis but might be a suggestion for further studies.

Although the total impact was observed to be small, the results in this thesis suggest that ice ridges contribute to an increased transmission loss in the water and can generate interface waves, such as the Scholte wave. By comparing the ice models with different locations of the shallower respectively deeper ice ridge, a slight increase in transmission loss could be observed at the location of the deeper ice ridge. A decreased amount of multi-year ice, and the consequently less deep ice ridges in the Arctic Ocean (Wadhams & Toberg, 2012; Worcester & Ballard, 2020), can then be suggested to contribute to decreased transmission loss by the sea ice over ranges considered in this thesis. The reduced amount of multi-year ice and its deep ridges enables higher frequencies to propagate longer distances, although reasonably low frequencies still are necessary for long-range propagation (Worcester & Ballard, 2020).

The shape of the sound speed profile and the source depth affect the Arctic wave propagation and are important for the measured transmission loss (Gavrilov & Mikhalevsky, 2006; LePage & Schmidt, 1994), and also small changes in the profile can lead to significant changes in the acoustic propagation (Gavrilov & Mikhalevsky, 2006). The results in this thesis suggest that the sound velocity profile is the most important parameter controlling acoustic transmission loss for a 50 Hz source and receiver at 30 m depth over shorter ranges. However, only large variations in the shape of the sound velocity profile have been implemented. The potential effect of small-scale variations in salinity or temperature has not been in the scope of this thesis. Even if the sound velocity profile in the Arctic Ocean typically is upwards refracting, there can be a wide variation in the shape of the profile in different regions (Gavrilov & Mikhalevsky, 2006).

Furthermore, the climate in the Arctic Ocean is rapidly changing and the ice-cover has been continuously shifting towards younger and thinner ice during the last decades (Stroeve & Notz, 2018). If this trend continues, the influence of the sea ice on acoustic transmission loss might decrease and therefore, the importance of the sound velocity profile may increase. Also, Xuanji et al. (2022) states that there is a possibility of an ice-free Arctic Ocean during September month already by year 2061-2064. Thus, it may be possible that closer monitoring and mapping of variations in the sound velocity profile could be more meaningful to future wave propagation modeling in the Arctic Ocean.

6.8. Suggestions for future work

For further work, a suggestion is to refine the implemented ice layer in the models. For example, it could be relevant to review the traditionally used elastic ice parameters, to investigate if there is a requirement for updated parameters for the ice layer due to the changing ice conditions in the Arctic Ocean. It could also be motivated to implement an ice layer with a more realistic roughness RMS value to investigate whether this could increase the observed transmission loss caused by the ice layer. Further, it could be suggested to increase the range to investigate the impact of a relatively thin ice layer on long-range propagation and increase the frequency in the simulations.

Another suggestion for further work is to study how small-scale changes in the parameters controlling the sound velocity profile might affect the acoustic wave propagation in the Arctic Ocean.

Additionally, the reason and full effect of the observed reflection from the absorbing bottom boundary and how this can be removed, could be investigated further. The reflections of the backscattered waves at the symmetry axis could also benefit from further attention, to clarify their significance on the measured transmission loss in the domain. A suggested solution to remove the reflected backscattering is given in Bottero (2018).

Chapter 7

Conclusion

The main objective of this thesis was to implement an ice layer on top of a water layer in the axisymmetric version of the spectral element package SPECFEM2D, to model acoustic wave propagation in the deep Arctic Ocean. The aim was to find out whether SPECFEM2D is a suitable tool for such numerical modeling.

As stated in the introduction, modeling a realistic ice-cover includes complex geometries such as ice ridges and ice roughness. This thesis has shown that the axisymmetric version of SPECFEM2D is a good candidate for numerical simulations in such environments. SPECFEM2D offers the ability to implement the ice layer and its features in a very free manner, although it might be beneficial to use an external meshing program for more complicated ice layers. Nevertheless, one limitation is the reflections of backscattered waves at the symmetry axis. This is problematic when modeling wave propagation in a domain with ice roughness and ice ridges implemented, as both those elements produce backscattering. There is also potential for improvement related to the reflections from the perfectly matched layer, but it is possible that there is a rather simple solution, as an increased domain depth.

Initially, three models comparable to the models presented in Collis et al. (2016) were set up. Two models, one with water only and one with 3 m thick ice, were validated against the seismo-acoustic propagation model OASES and an exact solution. In general, a good correspondence was shown for a 500 m deep domain up to approximately 2 km range, after which a reflection from the bottom PML could be observed, growing with distance. At increased ranges the reflection from the absorbing boundary becomes so large than it cannot be considered insignificant. Therefore, there are uncertainties in the results related to this artificial reflection.

As a subsidiary objective,

The influence of sea ice on acoustic wave propagation was compared between the results presented in this thesis and the results presented for the shallow water domain in Collis et al. (2016). The ice models in Collis et al. (2016) were observed to influence the acoustic transmission loss to a greater extent than what is observed in this thesis. Both the difference between a model with an ice layer compared to a model of water only, and the difference between the ice models themselves was significantly larger in Collis et al. (2016). In terms of the effect of an upwards refracting sound velocity profile, the transmission loss was observed to considerably decrease for a linearly increasing sound velocity profile compared to a homogeneous sound velocity profile, both in Collis et al. (2016) and this thesis.

Another subsidiary objective was to implement ice roughness and ice ridges in the models. The ice roughness amplitude spectrum was calculated with a Gaussian power spectrum with a characteristic correlation length of 19.1 m and a roughness RMS of 0.6 m. Two ice ridges with concave profiles were implemented, one of 4.9 m depth and one of 7.1 m depth. The mean ice thickness was 2 m, and a realistic Arctic sound velocity profile built from CTD data collected in the nearby surrounding of the Nansen basin was implemented. The influence of both ice roughness and ice ridges on transmission loss for a 50 Hz source and receivers at 30 m depth was observed to be marginal. Instead, the sound velocity

profile in the water is indicated to be the most important parameter controlling acoustic wave propagation.

Although the contribution was small in both cases, the ice ridges were observed to influence the acoustic transmission loss more than the ice roughness. In addition, scattering into ice and ice-water interface waves was observed at the ice ridges. This may indicate that larger elements in the ice layer may be more important than the ice roughness itself, as they enhance the transmission of energy into the ice layer. Even though the influence of ice roughness and ice ridges on acoustic transmission loss is observed to be small in this thesis, it is plausible that the influence may increase for higher frequencies, longer ranges, and thicker ice.

Nevertheless, the results obtained in this thesis suggest that the most important parameter controlling acoustic transmission loss for a 50 Hz source and receivers at 30 m depth over short ranges is the sound velocity profile. The effect of ice roughness and ice ridges has been observed to be most pronounced within the ice layer itself. The influence of ice ridges and ice roughness is present in the observed transmission loss curves at 30 m depth but to a much smaller extent than the effect of the sound velocity profile. With the rapidly changing climate in the Arctic Ocean and the continuous shifting towards thinner and younger ice, it might be proposed that close monitoring and mapping of the shape of the sound velocity profile could be more valuable for future wave propagation modeling in the Arctic Ocean.

References

Assi, H., & Cobbold, R. S. C. (2016). A perfectly matched layer formulation for modeling transient wave propagation in an unbounded fluid–solid medium. *J Acoust Soc Am*, *139*(4), 1528-1536. https://doi.org/10.1121/1.4944793

Ballard, M. S. (2019). Three-dimensional acoustic propagation effects induced by the sea ice canopy. *J Acoust Soc Am*, *146*(4), EL364-EL368. https://doi.org/10.1121/1.5129554

Ben-Menahem, A., & Singh, S. J. (1981). *Seismic waves and sources*. Springer-Verlag.

Berenger, J.-P. (1994). A perfectly matched layer for the absorption of electromagnetic waves. *Journal of computational physics*, *114*(2), 185-200. https://doi.org/10.1006/jcph.1994.1159

Bottero, A. (2015, 18.04.2018). *computeTL.py*. GitHub. Retrieved 24.01.2022 from https://github.com/geodynamics/specfem2d/blob/devel/EXAMPLES/paper_axisymmetry_example/computeTL.py

Bottero, A. (2018). *Full-wave numerical simulation of T-waves and of moving acoustic sources* [Doctoral dissertation, Aix-Marseille Université CNRS]. HAL theses. https://tel.archives-ouvertes.fr/tel-01893011

Brekhovskikh, L. M., & Lysanov, Y. P. (2003). *Fundamentals Of Ocean Acoustics* (3rd Edition ed.). New York, NY: Springer-Verlag. https://doi.org/10.1007/b97388

Buck, B. M., & Greene, C. R. (1964). Arctic Deep-Water Propagation Measurements. *Journal of the Acoustical Society of America*, *36*(8), 1526-1533. https://doi.org/10.1121/1.1919237

Centre national de la recherche scientifique, & Princeton University. (2021, 04.10.2021). *SPECFEM2D User Manual Version 7.0*. Retrieved 22.11.2021 from https://specfem2d.readthedocs.io/en/latest/

Chaljub, E., Capdeville, Y., & Vilotte, J.-P. (2003). Solving elastodynamics in a fluid–solid heterogeneous sphere: a parallel spectral element approximation on non-conforming grids. *Journal of computational physics*, *187*(2), 457-491. https://doi.org/10.1016/S0021-9991(03)00119-0

Chaljub, E., Komatitsch, D., Vilotte, J.-P., Capdeville, Y., Valette, B., & Festa, G. (2007). Spectral-element analysis in seismology. In *Advances in wave propagation in heterogeneous earth* (Vol. 48, pp. 365-419). Elsevier Science & Technology. https://doi.org/10.1016/S0065-2687(06)48007-9

Chierici, M., Jones, E., & Fransson, A. (2021). *Water column data on dissolved inorganic nutrients (nitrite, nitrate, phosphate and silicic acid) from the Nansen LEGACY joint cruise KH 2018707 with R.V. Kronprins Haakon, 8-20 August 2018* Institute of Marine Research. https://doi.org/https://doi.org/10.21335/NMDC-839276558

Colladon, J. D., & Strum, C. F. (1827). Suite du Mémoire sur la Compression des Liquides. In *Annales de chimie et de physique: 36. 1827* (pp. 225-257). Paris. https://www.digitale-sammlungen.de/en/view/bsb10071735?page=,1

Collins, M. D. (1993). A split-step Padé solution for the parabolic equation method. *Journal of the Acoustical Society of America*, *93*(4), 1736-1742. https://doi.org/10.1121/1.406739

Collis, J. M., Frank, S. D., Metzler, A. M., & Preston, K. S. (2016). Elastic parabolic equation and normal mode solutions for seismo-acoustic propagation in underwater environments with ice covers. *J Acoust Soc Am*, *139*(5), 2672-2682. https://doi.org/10.1121/1.4946991

Davis, N. R., & Wadhams, P. (1995). A statistical analysis of Arctic pressure ridge morphology. *J. Geophys. Res*, *100*(C6), 10915-10925. https://doi.org/10.1029/95JC00007

Diachok, O. I. (1976). Effects of sea-ice ridges on sound propagation in the Arctic Ocean. *The Journal of the Acoustical Society of America*, *59*(5), 1110-1120. https://doi.org/10.1121/1.380965

Faccioli, E., Maggio, F., Quarteroni, A., & Tagliani, A. (1996). Spectral-domain decomposition methods for the solution of acoustic and elastic wave equations. *Geophysics*, *61*(4), 1160-1172. https://doi.org/10.1190/1.1444036

Fofonoff, N. P., & Millard Jr, R. C. (1983). *Algorithms for the computation of fundamental properties of seawater* (UNESCO Technical Papers in Marine Sciences, 44). UNESCO. https://doi.org/10.25607/OBP-1450

Frank, S. D., & Ivakin, A. N. (2018). Long-range reverberation in an Arctic environment: Effects of ice thickness and elasticity. *J Acoust Soc Am*, *143*(3), EL167-EL173. https://doi.org/10.1121/1.5025841

Fricke, J. R. (1993). Acoustic scattering from elemental Arctic ice features: Numerical modeling results. *The Journal of the Acoustical Society of America*, *93*(4,4 I), 1784-1796. https://doi.org/10.1121/1.406720

Gavrilov, A. N., & Mikhalevsky, P. N. (2006). Low-frequency acoustic propagation loss in the Arctic Ocean: Results of the Arctic climate observations using underwater sound experiment. *The Journal of the Acoustical Society of America*, *119*(6), 3694-3706. https://doi.org/10.1121/1.2195255

Geuzaine, C., & Remacle, J.-F. (2009). Gmsh: a three-dimensional finite element mesh generator with built-in pre- and post-processing facilities. *International journal for numerical methods in engineering*, *79*(11), 1309-1331. https://doi.org/10.1002/nme.2579

Glorieux, C., Van de Rostyne, K., Nelson, K., Gao, W. M., Lauriks, W., & Thoen, J. (2001). On the character of acoustic waves at the interface between hard and soft solids and liquids. *Journal of the Acoustical Society of America*, *110*(3), 1299-1306. https://doi.org/10.1121/1.1396333

Hope, G., Sagen, H., Storheim, E., Hobæk, H., & Freitag, L. (2017). Measured and modeled acoustic propagation underneath the rough Arctic sea-ice. *J Acoust Soc Am*, *142*(3), 1619-1633. https://doi.org/10.1121/1.5003786

Hutt, D. (2012, May 21-25). An Overview of Arctic Ocean Acoustics.*AIP Conference Proceedings* [Advances in ocean acoustics]. 3rd International Conference on Ocean Acoustics (OA), Beijing, Peoples R China.

Igel, H. (2016a). The Finite-Element Method. In *Computational Seismology* (pp. 153-181). Oxford: Oxford University Press. https://doi.org/10.1093/acprof:oso/9780198717409.003.0006

Igel, H. (2016b). The Spectral-Element Method. In *Computational Seismology* (pp. 182-210). Oxford University Press. https://doi.org/10.1093/acprof:oso/9780198717409.003.0007

Jensen, F. B., Kuperman, W. A., Porter, M. B., & Schmidt, H. (2011). *Computational Ocean Acoustics* (2 ed.). Springer, New York, NY. https://doi.org/10.1007/978-1-4419-8678-8

Komatitsch, D., Barnes, C. R., & Tromp, J. (2000). Wave propagation near a fluid-solid interface; a spectral-element approach. *Geophysics*, *65*(2), 623-631. https://doi.org/10.1190/1.1444758

Komatitsch, D., & Martin, R. (2007). An unsplit convolutional perfectly matched layer improved at grazing incidence for the seismic wave equation. *Geophysics*, *72*(5), SM155-SM167. https://doi.org/10.1190/1.2757586

Komatitsch, D., Ritsema, J., & Tromp, J. (2002). The Spectral-Element Method, Beowulf Computing, and Global Seismology. *Science*, *298*(5599), 1737-1742. https://doi.org/10.1126/science.1076024

Komatitsch, D., & Tromp, J. (2003). A perfectly matched layer absorbing boundary condition for the second-order seismic wave equation. *Geophys. J. Int*, *154*(1), 146-153. https://doi.org/10.1046/j.1365-246X.2003.01950.x

Komatitsch, D., & Tromp, J. (2017, 26.10.2021). *define_external_model.f90*. GitHub. Retrieved 05.01.2022 from https://github.com/geodynamics/specfem2d/blob/devel/src/specfem2D/define_external_model.f90

Komatitsch, D., & Vilotte, J.-P. (1998). The spectral element method; an efficient tool to simulate the seismic response of 2D and 3D geological structures. *Bulletin of the Seismological Society of America*, *88*(2), 368-392.

Landschulze, M. (2018). Seismic wave propagation in floating ice sheets - a comparison of numerical approaches and forward modelling. *Near Surface Geophysics*, *16*(5), 493-505. https://doi.org/10.1002/nsg.12013

Langtangen, H. P., & Mardal, K.-A. (2019). *Introduction to Numerical Methods for Variational Problems* (Vol. 21). Cham: Springer International Publishing AG. https://doi.org/https://doi.org/10.1007/978-3-030-23788-2

LePage, K., & Schmidt, H. (1994). Modeling of low-frequency transmission loss in the central Arctic. *The Journal of the Acoustical Society of America*, *96*(3), 1783-1795. https://doi.org/10.1121/1.410257

Li, S., Yuan, S., Liu, S., Wen, J., Huang, Q., & Zhang, Z. (2021). Characteristics of low-frequency acoustic wave propagation in ice-covered shallow water environment. *Applied Sciences*, *11*(17), Article 7815. https://doi.org/10.3390/app11177815

Lindsay, R., & Schweiger, A. (2015). Arctic sea ice thickness loss determined using subsurface, aircraft, and satellite observations. *The cryosphere*, *9*(1), 269-283. https://doi.org/10.5194/tc-9-269-2015

Maday, Y., & Patera, A. T. (1989). Spectral element methods for the incompressible Navier-Stokes equations. *State-of-the-Art Surveys on Computational Mechanics*, 71-143.

Maslanik, J. A., Fowler, C., Stroeve, J., Drobot, S., Zwally, J., Yi, D., & Emery, W. (2007). A younger, thinner Arctic ice cover: Increased potential for rapid, extensive sea-ice loss. *Geophys. Res. Lett*, *34*(24). https://doi.org/10.1029/2007GL032043

Mavko, G., Mukerji, T., & Dvorkin, J. (2020). Elasticity and Hooke's Law. In *The rock physics handbook* (3rd edition. ed., pp. 37-120). Cambridge: Cambridge University Press. https://doi.org/10.1017/9781108333016.003

Mellen, R. H. (1966). Underwater sound in the Arctic Ocean. *U.S. Navy Journal of Underwater Acoustics*, *16*, 247-259. https://apps.dtic.mil/sti/citations/AD0484962

Mellen, R. H., & Marsh, H. W. (1963). Underwater Sound Reverberation in the Arctic Ocean. *Journal of the Acoustical Society of America*, *35*(10), 1645-1648. https://doi.org/10.1121/1.1918774

Meredith, M., Sommerkorn, M., Cassotta, S., Derksen, C., Ekaykin, A., Hollowed, A., Kofinas, G., Mackintosh, A., Melbourne-Thomas, J., Muelbert, M. M. C., Ottersen, G., Pritchard, H., & Schuur, E. A. G. (2019). *Polar Regions* (PCC Special Report on the Ocean and Cryosphere in a Changing Climate, Issue. I. Press. https://www.ipcc.ch/srocc/chapter/chapter-3-2/

Metzger, A. T., Mahoney, A. R., & Roberts, A. F. (2021). The Average Shape of Sea Ice Ridge Keels. *Geophysical Research Letters*, *48*(24), Article e2021GL095100. https://doi.org/10.1029/2021GL095100

Metzner, E. P., Salzmann, M., & Gerdes, R. (2020). Arctic Ocean Surface Energy Flux and the Cold Halocline in Future Climate Projections. *Journal of Geophysical Research-Oceans*, *125*(2), Article e2019JC015554. https://doi.org/10.1029/2019jc015554

Mikhalevsky, P. N. (2001). Acoustics, Arctic. In J. H. Steele (Ed.), *Encyclopedia of Ocean Sciences (Second Edition)* (pp. 92-100). Academic Press. https://doi.org/https://doi.org/10.1016/B978-012374473-9.00314-3

Mikhalevsky, P. N., & Gavrilov, A. N. (2001). Acoustic thermometry in the Arctic Ocean. *Polar research*, *20*(2), 185-192. https://doi.org/10.1111/j.1751-8369.2001.tb00055.x

National Snow and Ice Data Center. (1998). *Submarine Upward Looking Sonar Ice Draft Profile Data and Statistics, Version 1* Boulder. https://doi.org/https://doi.org/10.7265/N54Q7RWK

Nummelin, A., Ilicak, M., Li, C., & Smedsrud, L. H. (2016). Consequences of future increased Arctic runoff on Arctic Ocean stratification, circulation, and sea ice cover. *Journal of Geophysical Research-Oceans*, *121*(1), 617-637. https://doi.org/10.1002/2015jc011156

Patera, A. T. (1984). A spectral element method for fluid dynamics: Laminar flow in a channel expansion. *Journal of computational physics*, *54*(3), 468-488. https://doi.org/10.1016/0021-9991(84)90128-1

Patris, J., Komatitsch, D., Sepulveda, M., Santos, M., Glotin, H., Malige, F., Buchan, S., Asch, M., & Ieee. (2019, Jun 17-20). Mono-hydrophone localization of baleen whales: a study of propagation using a spectral element method applied in Northern Chile.*Oceans-Ieee* [Oceans 2019 - marseille]. OCEANS - Marseille Conference, Marseille, FRANCE.

Priolo, E., Carcione, J. M., & Seriani, G. (1994). Numerical-simulation of interface waves by high-order spectral modeling techniques. *Journal of the Acoustical Society of America*, *95*(2), 681-693. https://doi.org/10.1121/1.408428

Rossing, T. D. (Ed.). (2007). *Springer Handbook of Acoustics*. New York: Springer. https://doi.org/https://doi.org/10.1007/978-0-387-30425-0.

Schmidt, H., & Jensen, F. B. (1985). A full wave solution for propagation in multilayered viscoelastic media with application to Gaussian beam reflection at fluid-solid interfaces. *The Journal of the Acoustical Society of America*, *77*(3), 813-825. https://doi.org/10.1121/1.392050

Seriani, G., & Priolo, E. (1994). Spectral element method for acoustic wave simulation in heterogeneous media [Article]. *Finite Elements in Analysis and Design*, *16*(3-4), 337-348. https://doi.org/10.1016/0168-874X(94)90076-0

Seth, S., & Wysession, M. (2003). *An Introduction to Seismology, Earthquakes, and Earth Structure*. Blackwell Publishing.

Simon, B., Isakson, M., & Ballard, M. (2018). Modeling acoustic wave propagation and reverberation in an ice covered environment using finite element analysis. 175th Meeting of the Acoustical Society of America,

Stroeve, J., & Notz, D. (2018). Changing state of Arctic sea ice across all seasons. *Environ. Res. Lett*, *13*(10), 103001. https://doi.org/10.1088/1748-9326/aade56

Strub-Klein, L., & Sudom, D. (2012). A comprehensive analysis of the morphology of first-year sea ice ridges. *Cold regions science and technology*, *82*, 94-109. https://doi.org/10.1016/j.coldregions.2012.05.014

Tesei, A., Maguer, A., Fox, W. L. J., Lim, R., & Schmidt, H. (2002). Measurements and modeling of acoustic scattering from partially and completely buried, spherical shells. *Journal of the Acoustical Society of America*, *112*(5), 1817-1830. https://doi.org/10.1121/1.1509425

Thomson, D. J., & Brooke, G. H. (2008). Parabolic equation techniques in underwater acoustics. In N. A. Kampanis, V. A. Dougalis, & J. A. Ekaterinaris (Eds.), *Effective Computational Methods for Wave Propagation* (pp. 135-173). Chapman & Hall/CRC. https://doi.org/https://doi.org/10.1201/9781420010879

Tolstoy, I., & Clay, C. S. (1966). *Ocean acoustics : theory and experiment in underwater sound*. New York: McGraw-Hill.

Tromp, J., Komatitsch, D., & Liu, Q. Y. (2008). Spectral-element and adjoint methods in seismology. *Communications in Computational Physics*, *3*(1), 1-32. <Go to ISI>://WOS:000252368000002

Urick, R. J. (1983). *Principles of underwater sound* (D. Heiberg & J. Davis, Eds. 3rd ed.). McGraw-Hill.

Wadhams, P., & Toberg, N. (2012). Changing characteristics of arctic pressure ridges. *Polar science*, *6*(1), 71-77. https://doi.org/10.1016/j.polar.2012.03.002

Worcester, P. F., & Ballard, M. S. (2020). Ocean acoustics in the changing Arctic. *Physics Today*, *73*(12), 44-49. https://doi.org/10.1063/pt.3.4635

Xie, Z., Matzen, R., Cristini, P., Komatitsch, D., & Martin, R. (2016). A perfectly matched layer for fluid-solid problems: Application to ocean-acoustics simulations with solid ocean bottoms. *Journal of the Acoustical Society of America*, *140*(1), 165-175. https://doi.org/10.1121/1.4954736

Xie, Z. N., Komatitsch, D., Martin, R., & Matzen, R. (2014). Improved forward wave propagation and adjoint-based sensitivity kernel calculations using a numerically stable finite-element PML. *Geophysical journal international*, *198*(3), 1714-1747. https://doi.org/10.1093/gji/ggu219

Xu, C. X., Tang, J., Piao, S. C., Liu, J. Q., & Zhang, S. Z. (2016). Developments of parabolic equation method in the period of 2000-2016. *Chinese Physics B*, *25*(12), Article 124315. https://doi.org/10.1088/1674-1056/25/12/124315

Xuanji, W., Yinghui, L., Jeffrey, R. K., & Richard, D. (2022). A New Perspective on Four Decades of Changes in Arctic Sea Ice from Satellite Observations. *Remote sensing (Basel, Switzerland)*, *14*(8), 1846. https://doi.org/10.3390/rs14081846

Yang, T. C. (1989). Low-frequency transmission loss in the Arctic SOFAR channel for shallow sources and receivers. *The Journal of the Acoustical Society of America*, *85*(3), 1139-1147. https://doi.org/10.1121/1.397443

Appendix A

A.I. The bulk modulus in a plain strain case

As described in '*Chapter 2.1.1Solid region*', stress and strain are related by Hooke's Law. The stress tensor is expressed in terms of infinitesimal strain and the tensor of elastic moduli in Equation (2). The tensor of elastic moduli contains 81 values of c_{ijkl} in total. Due to symmetry, the number of independent coefficients is greatly reduced. For uniform materials, it reduces to 36, and for isotropic materials, it reduces to 21 values, of which only two are independent. This is closer explained in Ben-Menahem and Singh (1981, pp. 18-19). Using the Lamé parameters, an expression for c_{ijkl} in a isotropic material can be written as (Ben-Menahem & Singh, 1981, pp. 18-19; Seth & Wysession, 2003, pp. 29-115):

$$c_{ijkl} = \lambda\delta_{ij}\delta_{kl} + \mu\left(\delta_{ik}\delta_{jl} - \delta_{il}\delta_{jk}\right) \tag{58}$$

Using Equation (58), Equation (2) can be rewritten as:

$$\boldsymbol{T}_{ij}(\boldsymbol{u}) = c_{ijkl}\boldsymbol{\varepsilon}_{kl}(\boldsymbol{u}) = \lambda\varepsilon_{kk}\delta_{ij} + 2\mu\varepsilon_{ij} \tag{59}$$

where δ_{ij} is the Kronecker delta. The dilation of the medium is expressed by a summation of the diagonal elements in the strain tensor (Seth & Wysession, 2003, pp. 29-115):

$$\varepsilon_{kk} = \varepsilon_{11} + \varepsilon_{22} + \varepsilon_{33} = \Delta \tag{60}$$

For a plain strain case, there is no strain in the third direction, thus $\varepsilon_{33} = 0$. Then, Equation (59) can be written into five expression for the stress tensor (Ben-Menahem & Singh, 1981, p.34-36):

$$\begin{aligned} T_{11} &= \lambda\Delta + 2\mu\varepsilon_{11} = (\lambda + 2\mu)\varepsilon_{11} + \lambda\varepsilon_{22} \\ T_{12} &= \lambda\Delta + 2\mu\varepsilon_{11} = 2\lambda\varepsilon_{12} \\ T_{21} &= T_{12} \\ T_{22} &= \lambda\Delta + 2\mu\varepsilon_{22} = \lambda\varepsilon_{11} + (\lambda + 2\mu)\varepsilon_{22} \\ T_{33} &= \lambda(\varepsilon_{11} + \varepsilon_{22}) \end{aligned} \tag{61}$$

The bulk modulus $K = -\frac{dP}{d\Delta}$ characterizes a material's resistance to pressure and expresses the ratio of the applied pressure to the caused volume change. This change in stress and volume can be expressed as (Seth & Wysession, 2003, pp. 29-115):

$$d\boldsymbol{T}_{ij}(\boldsymbol{u}) = -dP\delta_{ij} = \lambda d\Delta\delta_{ij} + 2\mu d\varepsilon_{ij} \tag{62}$$

In 3D, where $i = j = (1,2,3)$, the expression of the change in pressure becomes:

$$-3\,dP = 3\lambda\,d\Delta + 2\mu\,d\Delta \tag{63}$$

In the 2D plain strain case, the pressure change instead takes the expression:

$$-2\,dP = 2\lambda\,d\Delta + 2\mu\,d\Delta \tag{64}$$

Therefore, the bulk modulus κ in the 2D plain strain case becomes:

$$\kappa = -\frac{dP}{d\Delta} = \lambda + \mu \tag{65}$$

A.II. The quality factor in a plain strain case

The quality factor Q quantifies how much energy that is lost in a medium during one cycle. The inverse quality factor Q^{-1} is directly proportional to attenuation α (Seth & Wysession, 2003, pp. 119-212). The inverse quality factor be expressed as (Ben-Menahem & Singh, 1981, p. 848)

$$\frac{1}{Q} = \frac{1}{2\pi}\frac{-\Delta E}{E} \tag{66}$$

Here E is the maximum of stored energy and ΔE is the energy lost during one cycle of 2π. The decay of a wave can be expressed as (Seth & Wysession, 2003, pp. 119-212):

$$A(t) = A_0\,exp\left(-\frac{\omega_0}{2Q}t\right) \tag{67}$$

An attenuating wave can be expressed as a wave with a complex frequency, ω^* (Seth & Wysession, 2003, pp. 119-212):

$$A(x,t) = A_0\,exp(i(\omega + i\omega^*)t) \tag{68}$$

Here $\omega^* = \frac{\omega_0}{2Q}$. The velocity of the attenuating wave can then be described as a complex velocity $C = \frac{\omega + i\omega^*/2Q}{k} = c + ic^*$, if the attenuation is assumed to be small. Then, the inverse quality factor can be expressed as (Seth & Wysession, 2003, pp. 119-212):

$$\frac{1}{Q} = \frac{2c^*}{c} \tag{69}$$

Seismic waves are expressed in terms of their elastic modulus, where the S-wave is $v_s = \sqrt{\frac{\mu}{\rho}}$, where ρ is density and μ is shear modulus (Seth & Wysession, 2003, pp. 58-59). The complex S-wave velocity then takes the shape (Seth & Wysession, 2003, pp. 119-212):

$$v_s + iv_s^* = v_s\left(1 + \frac{i}{2Q_s}\right) = \sqrt{\frac{\mu + i\mu^*}{\rho}} = v_s\sqrt{1 + \frac{i\mu^*}{\mu}} \tag{70}$$

Which approximated by the first term of the Taylor series leads to:

$$v_s + iv_s^* \approx v_s\left(1 + \frac{i\mu^*}{2\mu}\right) \tag{71}$$

By combining Equation (71) with Equation (69), the expression for the inverse quality factor for S-waves becomes:

$$\frac{1}{Q_s} = \frac{\mu^*}{\mu} \tag{72}$$

The P-wave velocity $v_p = \sqrt{\frac{M}{\rho}} = \sqrt{\frac{\lambda+2\mu}{\rho}}$ where $M = \rho v_p^2 = \lambda + 2\mu$ is the P-wave modulus (Mavko et al., 2020, p. 38). Using the bulk modulus for the 2D plain strain case $\kappa = \lambda + \mu$, the expression for the P-wave velocity can be written as $v_p = \sqrt{\frac{\kappa+\mu}{\rho}}$, and the expression for the inverse P-wave quality factor becomes:

$$\frac{1}{Q_p} = \frac{\kappa^* + \mu^*}{\kappa + \mu} \tag{73}$$

A.III. The image solution used for model validation

Trond Jenserud at the Norwegian Defence Research Establishment (FFI) contributed with the reference curves obtained by an exact solution to validate the SPECFEM2D models (Section '*4.5. Validation*', Figure 18, and Figure 19). The exact solution used to validate the models was an image (ray) solution for a fluid half-space with a pressure free upper boundary. For a homogeneous waveguide of depth h with free boundaries the image ray solution is given as Tolstoy and Clay (1966, pp. 65-101):

$$p(r,z,t) = \frac{\rho}{4\pi}\sum_{n=0}^{\infty}\left(\frac{1}{R_n}\ddot{g}\left(t - \frac{R_n}{c}\right) - \frac{1}{R_n'}\ddot{g}\left(t - \frac{R_n'}{c}\right)\right) \tag{74}$$

Here p is pressure, c velocity, and $\ddot{g}$ the double derivate with respect to time of a time dependent source. R_n and R_n' are ray paths. For a fluid half-space with a free surface, only the direct ray and the rays reflected at the surface contribute, and Equation (74) becomes:

$$p(r,z,t) = \frac{\rho}{4\pi}\left(\frac{1}{R_0}\ddot{g}\left(t - \frac{R_0}{c}\right) - \frac{1}{R_0'}\ddot{g}\left(t - \frac{R_0'}{c}\right)\right) \tag{75}$$

Here R_0 is the direct ray and R_0' the surface reflected wave, given by:

$$R_0 = \sqrt{(z - z_0)^2 + r^2} \tag{76}$$

$$R_0' = \sqrt{(z + z_0)^2 + r^2} \tag{77}$$

Where the source depth is z_0, the receiver depth z, and r the distance from the source. Because a Gaussian source function $g(t)$ is used in SPECFEM2D (Section *'4.2. Source function'*), the pressure becomes a Ricker pulse.

Appendix B

B.I. 2D vs 2.5D simulations

The first modeling step was to run two models in a 2D and a 2.5D domain to compare the results. The domain in this section is 4000x100 m, containing 1333 horizontal and 33 vertical elements, and the perfectly matched layers are placed within the domain. This makes the actual domain of the simulations to be 3970x85 m for 2D simulations and 3985x85 m for 2.5D simulations, using a 5 elements thick absorbing layer.

It is important to note that those simulations were done before the validation of the model, and thus, the extra pulse arising after 500 m range in a domain of 100 m depth was still unknown (see Section *'4.5.1. Validation of the domain dimensions'*). Therefore, there are uncertainties in the results in this section, related to the extra pulse, and the results will be used for a relative comparison between 2D and 2.5D models only.

The source is located at $x = 30$ for 2D simulations, which makes the source location be 15 m into the actual domain, as the first 15 m are an absorbing layer. For the 2.5D simulations, the source is located on the symmetry axis, at $x = 0$ m. The models in this section all have a homogeneous velocity profile and the ice layers are non-attenuation. The velocity and density profiles of the simulations are given in Table 6. There are two sets of receivers used, one set at 1.5 m depth and one at 30 m depth, where each set contains 20 receivers each, evenly placed between $x = 30$ and $x = 4000$ m.

	FLUID REGION	SOLID REGION
COMPRESSIONAL VELOCITY v_P	1482 m/s	3500 m/s
SHEAR VELOCITY v_s	-	1800 m/s
DENSITY ρ	1000 kg/m^3	900 kg/m^3

Table 6. *Parameters in the simulations.*

B.I.I. Model 1 - water only

Model 1 consists of a 100 deep water layer, where the last 15 m are redefined to be an absorbing layer. The simulation was run with time step $dt = 1.727 \cdot 10^{-4}$ s for $N = 16000$ steps. A visualization of the wave field in pressure at time $t = 0.086$ s for the 2D simulation is shown in Figure 88, and for the 2.5D simulation in Figure 89. The absorbing layer can be observed on the bottom and the left axis in the 2D simulation, as the wave is vanished at this point. Because of the different source locations in the two models, the wave in the 2D simulation has traveled 15 m more into the domain than the wave in the 2.5D simulation at this point.

Figure 88. *The wave field at time $t = 0.086$ s in the 2D domain. The green dots are receivers.*

Figure 89. *The wave field at time $t = 0.086$ s in the 2.5D domain.*

The wave pulses of the acoustic wave, recorded at 30 m depth at the second receiver (at $x = 238.9$ m), in the 2D (pink line) and 2.5D (green line) simulations, are shown in Figure 90. Note the different scales in the figures. A time delay in the 2.5D simulation compared to the 2D simulation is observed. Both arrival times correspond to what is expected. The different source locations and source types must be kept in mind, as the 2D simulation has a line source at $x = 30$ meters, and the 2.5D simulation has a point source at $x = 0$ meters. A small wave pulse is observed at approximately 0.1 s and 0.11 s, for the 2D and 2.5D simulations, respectively.

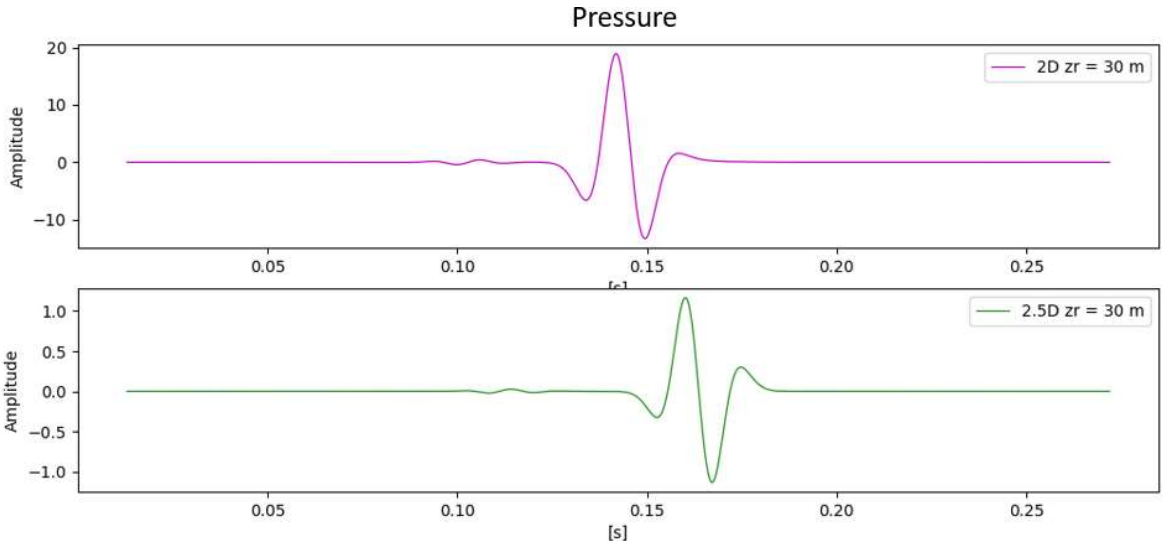

Figure 90. *Seismograms from the second receiver ($x = 238.9$ m) at 30 m depth in the 2D (pink lines) and 2.5D (green lines) domain. Note the different scales on the axes.*

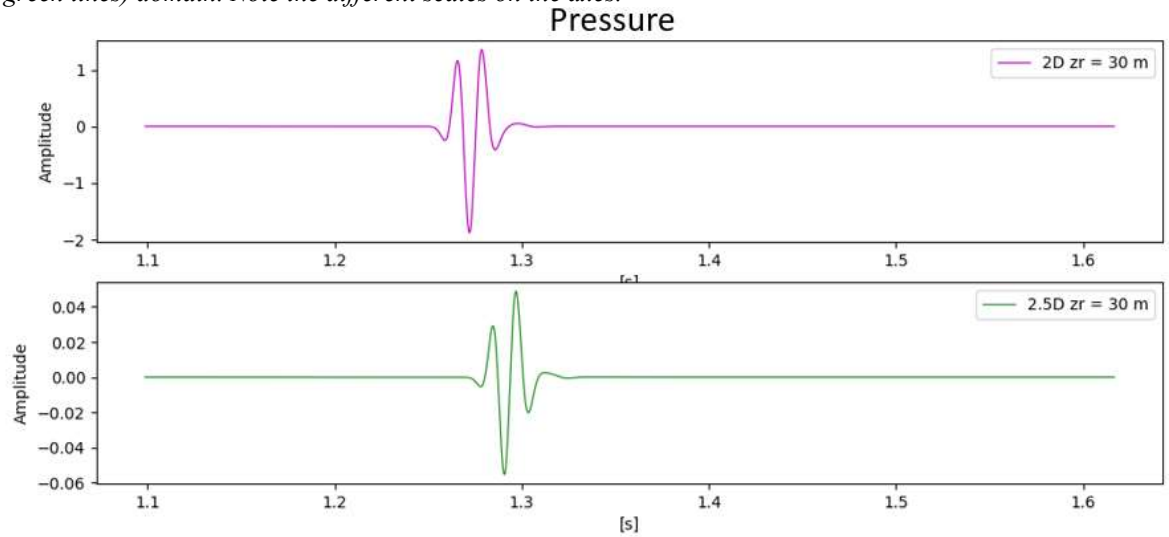

Figure 91. *Seismograms same as in Figure 90, but from the 10th receiver, at $x = 1910.5$ m.*

Figure 91 shows the seismograms from the 10th receiver ($x = 1910.5$ m). A difference in the wave pulses is observed. As for the previous station, the arrival times correspond with what is expected. The simulations are satisfying, and ice layers will be added to the simulations.

B.I.II. Model 2 - a range-independent ice layer

Model 2 consists of a range-independent ice layer with a constant thickness of 3 m, above 97 m thick water layer, of which the last 15 m are an absorbing layer as described earlier. The 2D simulation was run with time step $dt = 7.4 \cdot 10^{-4}$ and $N = 36500$ time steps, while the 2.5D simulation with the same time step over for $N = 38700$. The reason was that the 2D simulation was shown to be slightly too short in total time, which was changed for the 2.5D simulations. However, this only affects the last receiver.

Figure 92 and Figure 93 show a visualization of the wave field for the 2D and 2.5D simulations, respectively. A tail of energy following the acoustic wave within the ice layer can be observed in the 2D simulation. This is also present in the 2.5D simulation, but it appears much weaker than the other waves in the simulation. This wave tail initially appears mainly in the ice layer but grows downwards into the adjacent water layer and can probably be explained as noise. No attenuation is applied in the ice layer in this section. Also, note some noise on the symmetry axis in the 2.5D domain. Both the acoustic wave and the head wave appear weaker in the 2.5D simulation (compare Figure 92b and Figure 93b), in the absence of figure scales it is hard to quantify the difference.

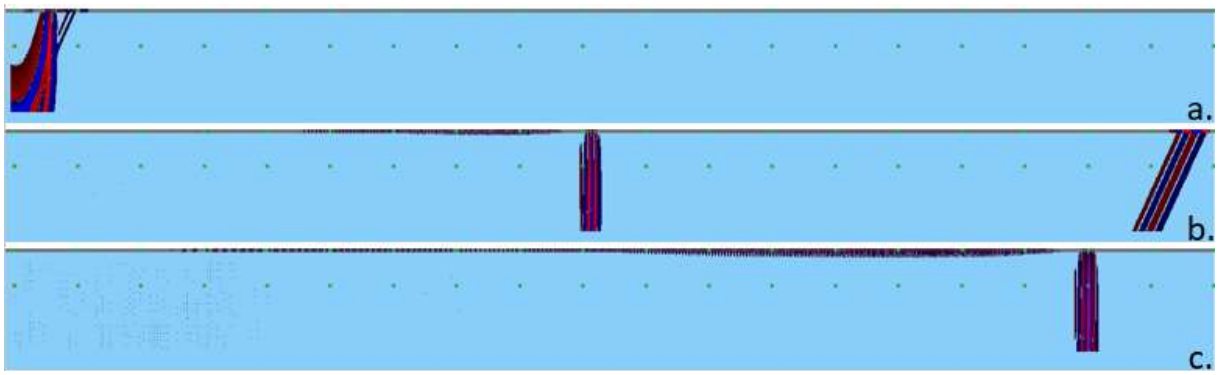

Figure 92. *Figures of the wave field in the 2D simulation at time* $t = 0.104$ *(fig. a.),* $t = 1.317$ *(fig. b.) and* $t = 2.427$ *s (fig. c.).*

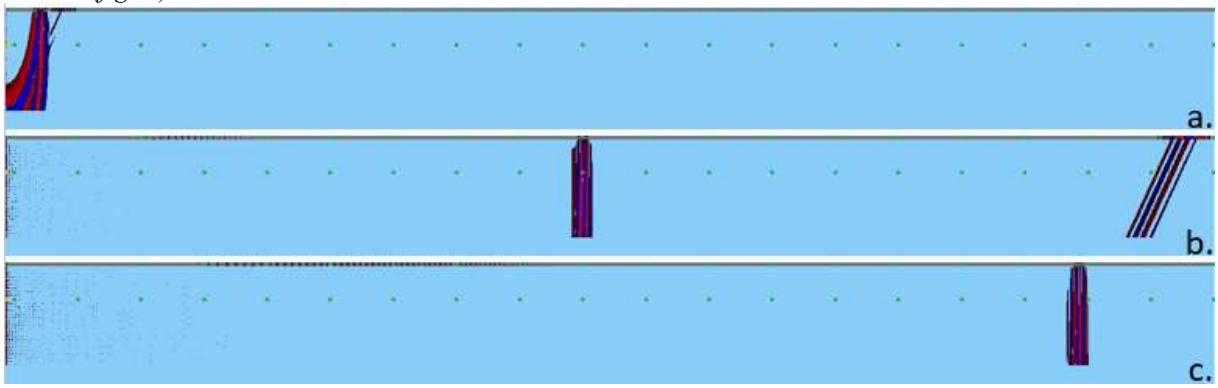

Figure 93. *The wave field shown as in Figure* 92*, but for the 2.5D simulation.*

The seismograms recorded at the 3rd ($x = 447.9$ m) and 10th ($x = 1910.5$ m) receiver, at 30 m depth, shown in Figure 94. Again, note the difference in amplitude between the 2D (blue lines) and the 2.5D (pink lines) simulations. The head wave appears to have a slightly larger amplitude relative to the amplitude of the acoustic wave in the 2D simulation, compared to the 2.5D simulation. This answers well to what is observed in Figure 92b and Figure 93b.

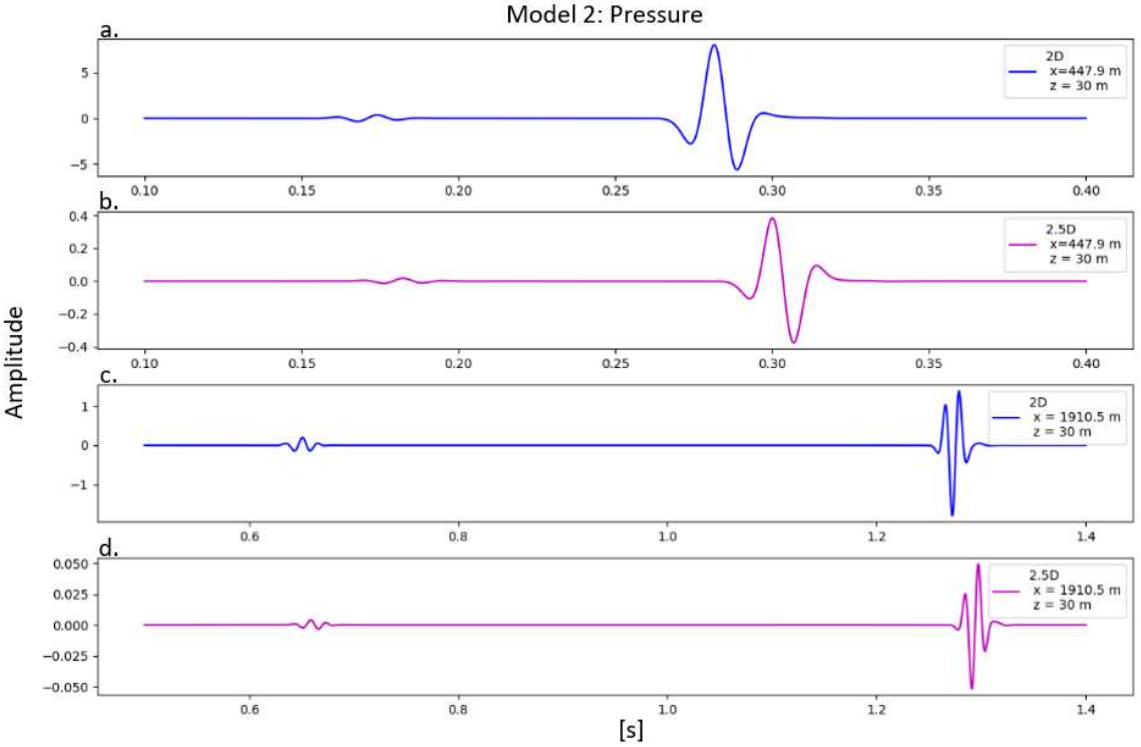

Figure 94. *Seismograms from the 3rd ($x = 447.9$ m, fig. a and fig. b.) and the 10th ($x = 1910.5$ m, fig. c. and fig. d.) receiver at 30 m depth for the 2D simulation (blue lines) and 2.5D simulation (pink lines).*

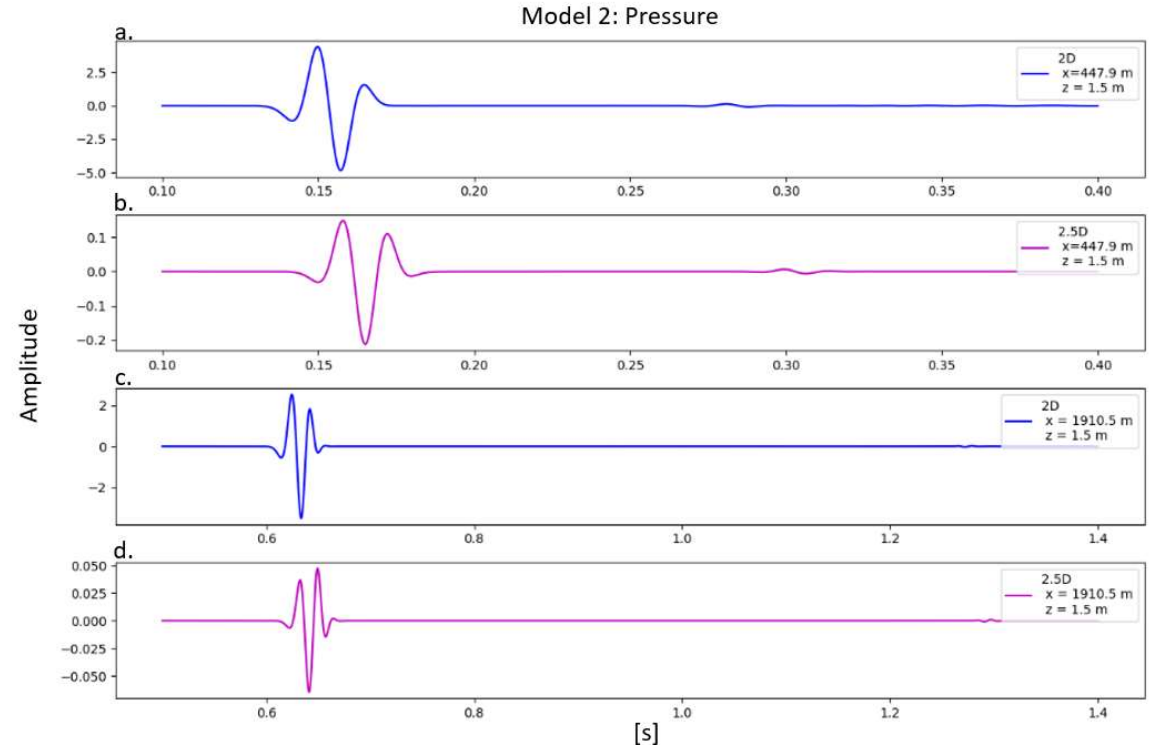

Figure 95. *Seismograms same as in Figure* 94*, but at 1.5 m depth.*

Figure 95 shows the seismograms from the 3rd ($x = 447.9$ m) and 10th ($x = 1910.5$ m) receiver, recorded at 1.5 m, and shows the pulses of the elastic P-wave. A difference in pulse shape and a phase shift is observed.

B.I.III. Model 3 - a range-dependent ice layer

Model 3 has a range-dependent ice layer with a thickness linearly decreasing from 3 m thickness to 2 m thickness throughout the domain. The 2D simulation was run with time step $dt = 4.934 \cdot 10^{-5}$ over $N = 54500$ time steps, and the 2.5D simulations used the same time step but over $N = 57500$ time steps. As in the previous section, the reason for the difference in the total of time steps is that the 2D simulation had a slightly too short simulation run time.

The wave field is shown at $\mathrm{t} = 1.312$ s for the 2D and 2.5D simulations in Figure 96 and Figure 97, respectively. The head wave in the 2.5D simulation visually appears weaker in Model 3 compared to Model 2 (Figure 92 and Figure 93) for both simulations, even though it is hard to evaluate the pressures without a scale.

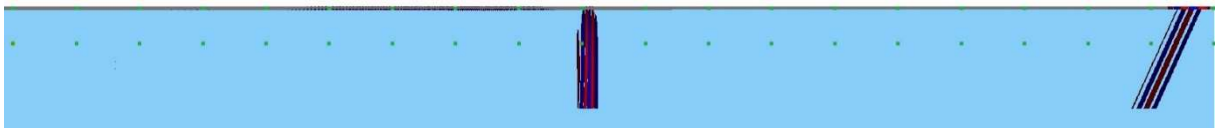

Figure 96. *The wave field at time* $t = 1.312$ *s in the 2D simulation.*

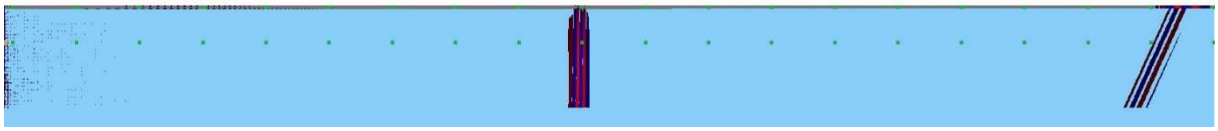

Figure 97. *The wave field at the same time as Figure* 96*, but for the 2.5D simulation.*

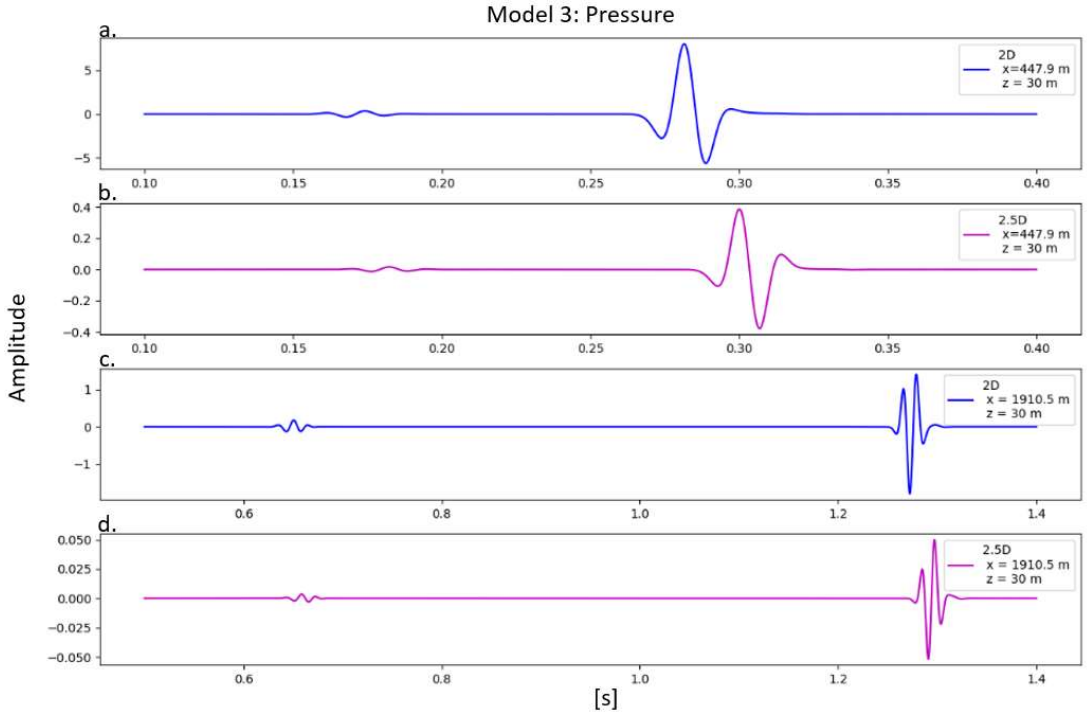

Figure 98. *Seismograms from the receivers at x = 447.9 m (fig. a. and fig. b.) and x = 1910.5 m (fig. c. and fig. d.) at 30 m depth for Model 3, for the 2D simulation (blue lines) and 2.5D simulation (pink lines).*

The seismograms for both simulations recorded at 30 m depth at range $x = 477.9$ m and $x = 1910.5$ m are shown in Figure 98. The figures for Model 3 are very similar to the ones for Model 2, therefore only one figure is presented in this section.

The simulations in the 2.5D domain gave satisfying results, and the remaining simulations in this thesis will be performed in 2.5D.

B.II. Additional figures

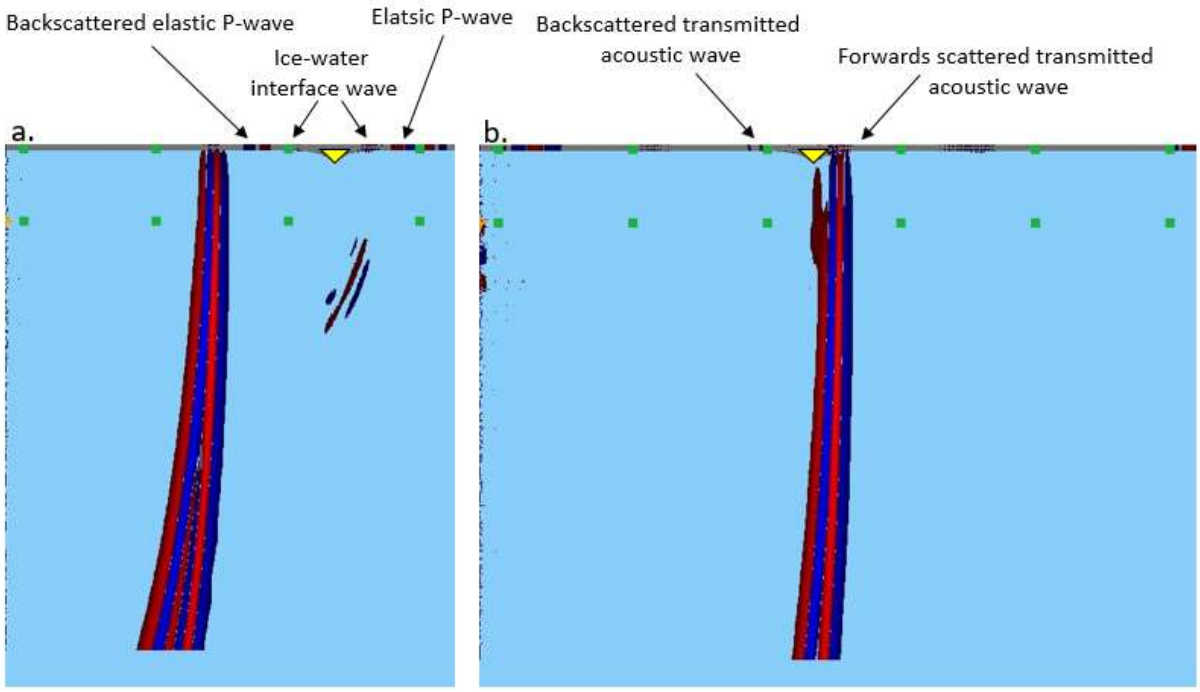

Figure 99. *The wave field of a wave propagating in a 200 m deep domain with 2 m thick ice surrounding an ice ridge at 520 m. The ice ridge is marked by a yellow triangle for clarity. The arrows show the waves generated as the elastic P-wave (Figure 99a) and the acoustic wave (Figure 99b) pass the ice ridge as explained in Section '5.4.1. A smooth ice model with two ice ridges'.*